

Microstrip patch antennas with broad beamwidth

Présentée le 21 avril 2023

Faculté des sciences et techniques de l'ingénieur
Groupe SCI STI AS
Programme doctoral en génie électrique

pour l'obtention du grade de Docteur ès Sciences

par

Ismael VICO TRIVIÑO

Acceptée sur proposition du jury

Dr S.-R. Cherkaoui, président du jury
Prof. A. Skrivervik, directrice de thèse
Prof. A. Sharaiha, rapporteur
Prof. M. Ammann, rapporteur
Prof. F. Rachidi-Haeri, rapporteur

Visible solo para aquel que sepa donde mirar

- El Laberinto del Fauno, Guillermo del Toro

A mis padres, a mi hermana, y a mis abuelos

Acknowledgements

During the last years, I have always thought about the day I would sit down to write these words, and to thank everyone that has accompanied me until now. Not only to the people that has been with me during the Thesis, but also to those who have been an inspiration or have believed in me when I could not do it by myself. I have no words to express the deep gratitude and admiration that I have for Prof. Anja Skrivervik, as a scientist, as supervisor and as a person. She is and has been an enormous inspiration in so many aspects, and I feel extremely fortunate to have been able to work with her these years. Thank you for everything, Anja.

I also want to thank everyone from the LEMA times. Even if many were leaving when I arrived to the lab, I am glad I could share some time with them. Big thanks to Prof. Juan Mosig, for his kindness and the incredible team spirit he created in LEMA. Thanks to Esteban, Noe, Joana Silva, Joana Maria, Mina, Nevena, Tatjana, Anton, Mercedes and Eulalia. Special thanks to Santiago for being so supportive and always available to discuss. And big thanks to Jovanche, for making my arrival to the lab so smooth, being so kind and so supportive, and for his invaluable help co-supervising my Master Thesis. Big thanks to my colleagues from Flyability: Steven, Ludo, Adrien, Patrick, Raffael, Arnaud Garnier; for being so helpful during my time in the company and the Thesis, and also to the amazing ReX team: Josh, Rémi, Ágathe, Yann and Arnaud Janvier.

When MAG started, we had the best incorporation that one could imagine in a team. Daniela has always been the joy of the lab, always having the right words in the right moments to make everyone laugh regardless the situation. She has also been the most patient teacher to help me learning French. Merci beaucoup pour tout Daniela. Thanks to my colleagues in ELBO: Jamal, Mohammad, Eric, Denys, Aleks, Baha, Eva, Mingxiang, Tingyong, Yuanyan, Behnaz, Erik, Sujith, Giselle, Germán, Jakub, Gurjot, Kerem, Jonas and Robin. Thanks to Hannes for all the nice conversations. Special thanks to Miroslav, for always being so supportive since the first moment I arrived in the lab. And last but definitely not least, my deepest gratitude to Danelys, who has held me by the hand in my best and worst moments these years, and always managed to magically dissipate any problem over a 10-min coffee. I would not be writing these words today without your support. Muchas gracias Dane.

There are some people that leave a mark on you across the years, and give you the tools to grow as a person and as a professional. En primer lugar, muchas gracias, Cristina Morales, por verme, por guiarme con tanto cariño y comprensión, y por creer en mí y enseñarme a hacerlo yo mismo. Pasen los años que pasen siempre te estaré agradecido. A Luz García, quien con su buen hacer como profesora, me hizo cambiar de opinión y escoger la especialidad que me ha llevado a escribir esta Tesis. Gracias a ella y a Carmen Martínez por su supervisión de mi proyecto de fin de grado. A Pablo Padilla por ser siempre tan cercano y por estar siempre disponible y dispuesto a ayudar.

I have been so lucky to share these years with some amazing people, to whom I express my deepest gratitude. A Ana, por salvarme de la peor tormenta de nieve en décadas y haber estado siempre ahí desde entonces. A Adri, gracias por todos estos años de amistad, y por seguir ahí pase lo que pase hasta cambiando de país y de idioma. Gracias, Marta, por ser única y hacerme reír como nadie. A Irene por tu carisma y tu buena energía que transmites a todos. A Sandra por tratarme siempre con tanto cariño y saber siempre escucharme. A Alberto, gracias ser mi familia y por entenderme mejor que nadie. A Pablo y Fernando, porque con vosotros las risas diluyen todos los males. Gracias a María, Rosi y Eva, por estar siempre conmigo casi desde que tengo memoria. Gracias, Carlota por tu inestimable ayuda todos estos años. A mi Yaiza, que con su gran corazón me enseñó que un amigo se puede convertir en familia. Merci Jérôme, pour ta positivité contagieuse, et ta patience infinie

à m'aider à améliorer mon français. À Jordan pour son énergie inépuisable. Thank you, Ícaro, for your shining personality and your kindness. I want to thank you all for being part of my life.

Y para terminar, esta Tesis no habría sido posible sin la ayuda incondicional de mi familia. Gracias a mi madre, que nunca escatimó el más mínimo esfuerzo en mi educación y por su desbordante creatividad que siempre fue una inspiración. Gracias a mi padre, por su incondicional y ciega confianza en mí, y su infinita curiosidad que consiguió transmitirnos a sus dos hijos. Gracias a mi hermana, de quien siempre he admirado su impulso irrefrenable de aprender y crecer, haciendo muchos sacrificios y enfrentándose a muchos miedos pero siempre con constancia y perseverancia. Siempre he sabido que esta tesis sería para mi abuela Presenta y a mi abuelo Antonio, que se sacrificaron y esforzaron tanto por darnos las mejores oportunidades, ahorrando desde que mi hermana y yo nacimos para que pudiéramos tener estudios. Todo esto empezó con vosotros. Muchas gracias, y allá donde estéis, espero que estéis orgullosos.

Ismael Vico Triviño

Lausanne, December 22nd 2022

Abstract

Microstrip antennas offer a broad set of advantages such as low profile, light weight, easy fabrication and low cost. As these are desirable or even critical for a broad range of applications, there has been a large interest for these antennas in the antenna community. In applications like drones or satellite communications, the especially stringent constraints on weight and size make microstrip antennas a good option, despite their intrinsic performance limitations such as their narrow bandwidth. The radiation pattern of these antennas is directive which for some of these cases, translates to an insufficient beamwidth if one uses only one antenna. In the literature, one can find an extensive analysis on gain and bandwidth enhancement of microstrip antennas, but the research on broadening the beam of these antennas is not as popular. In this thesis, we focus on the beamwidth enhancement of microstrip antennas, and more specifically on antennas for small drones and satellites.

Most of the work in the thesis is dedicated to the antennas for a drone protected by a carbon fibre superstructure which enables it to fly indoors. This drone is used for industrial inspections, and to reach places that are dangerous or inaccessible to humans. In these environments, the reliability of the connection between the drone and the controller is critical in order not to lose the drone where it cannot be recovered. This is especially challenging in indoor scenarios and for this specific type of drone, because of the multipath effect and the perturbation of the propagation of the signal by the conductive cage protecting the drone. The antennas used should be light, compact and inexpensive, and provide a quasi-isotropic coverage around the UAV. The number of antennas is limited to two by the transmission system, and therefore, for a reliable connection, the typical beamwidth of a patch of 70° is insufficient. The antennas should also radiate circularly polarized patterns to minimise the effect of the cage, the potential cross polarisation losses, and the multipath effect.

In this thesis, we analyse the limitation of the gain at low elevation angles for microstrip patch antennas, providing an overview and guidance on different techniques to improve the beamwidth. We illustrate some of these techniques through various designs of compact and light antennas with application for drones. The proposed antennas for the communication with the drone consist of a patch, which naturally radiates in broadside, combined with several extra parasitic elements excited by the patch that radiate in end-fire. This research results in a $\lambda/3$ antenna with a CP and broadened beam. We perform and describe a system validation of the antenna in a real scenario comparing with the original set of antennas in the drone. The test, based on the SNR of the link, shows that the reliability of the system is significantly improved compared to the original configuration of the antennas. This is especially remarkable in NLOS, which is precisely the scenario for which the antennas were conceived.

We extend the research on wide beam microstrip antennas, to the use of parasitic elements to enhance the beamwidth and achieve broad-beam and/or iso-flux patterns, with applications to pico-satellites. Using passive elements in an array-like structure allows to increase the low elevation gain and even achieve conical patterns. This last feature is very convenient for pico-satellites in Low Earth Orbit, where a well-tuned conical pattern provides uniform coverage on the illuminated region of the Earth.

With this thesis we contribute with an analysis on the different techniques to broaden the beamwidth of microstrip antennas. It tackles each different approach from a didactic perspective that allows to understand and identify the main aspects of each design, providing unified guidelines to the beamwidth broadening of patch antennas. It helps to establish compromises between size, weight, bandwidth and beamwidth for this type of antennas, which are dependent on the application. We present two examples of these compromises: the antennas designed for the drone, which prioritize having a minimum weight, sacrificing other parameters, and

the antennas for the satellites that call for broadbeam or conical patterns, and are less restrictive in weight and size. All the designs presented in this thesis keep a very low-profile, which is not commonly seen in the literature due to the intrinsic limitations on the beamwidth of patch antennas.

Keywords

broad-beam, wide-beam, microstrip antennas, patch antennas, UAV communications, drone communications, satellite communications, parasitic elements, isoflux patterns, broadbeam patterns, low profile

Resumé

Les antennes microruban offrent de nombreux avantages tels qu'un profil bas, une fabrication facile, un poids léger et un faible coût. Ces caractéristiques sont très pratiques pour une large gamme d'applications et par conséquent ont attiré un grand intérêt dans la communauté des antennes. Pour les applications telles que le contrôle à distance de drones ou les communications par satellite, les contraintes particulièrement strictes de poids et de taille font des antennes microruban une bonne option, malgré leurs inhérentes limitations telles que leur bande passante étroite. Le diagramme de rayonnement de ces antennes est directif, ce qui se traduit dans certains cas, par une largeur de faisceau insuffisante si l'on n'utilise qu'une seule antenne. Dans la littérature, on peut trouver une analyse très complète sur l'amélioration du gain et de la bande passante de ces antennes, ce qui n'est pas le cas pour l'élargissement de leur faisceau.

La majeure partie de cette thèse se concentre sur des antennes conçues pour un drone protégé par une structure en fibre de carbone, permettant d'opérer celui-ci dans des environnements complexes. Ce drone est utilisé pour des inspections industrielles, et pour atteindre des endroits dangereux ou inaccessibles aux personnes. Dans ces environnements, la fiabilité de la connexion entre le drone et le contrôleur est importante afin de ne pas perdre le drone là où il ne pourra pas être récupéré. Ceci est particulièrement critique à l'intérieur des bâtiments, spécifiquement pour ce type de drone, à cause de l'effet multi-trajets et la perturbation de la propagation du signal par la cage conductrice protégeant le drone. Les antennes utilisées doivent être légères, compactes et peu coûteuses. En outre, elles doivent assurer une couverture quasi-isotrope autour du drone. Le nombre d'antennes est limité à deux par le système de transmission, et donc, pour une connexion fiable, la largeur du faisceau typique d'un patch, de l'ordre de 70° est insuffisante. Les antennes doivent également rayonner à polarisation circulaire pour minimiser l'effet de la cage, les pertes potentielles de polarisation croisée et l'effet multi-trajets.

Dans cette thèse, nous analysons la limitation du gain aux faibles angles d'élévation pour les antennes patch microruban, en fournissant un aperçu et des conseils sur les différentes techniques pour élargir leur largeur de faisceau. Nous illustrons certaines de ces techniques à travers différentes conceptions d'antennes compactes et légères pour les drones. Les antennes proposées pour la communication avec le drone sont constituées d'un patch à rayonnement transversal, associé à plusieurs éléments parasites à rayonnement longitudinal, qui sont activés par le patch. Cette recherche aboutit à une petite antenne, de taille $\lambda/3$, avec un CP et un faisceau élargi. Nous effectuons et décrivons une validation des antennes au niveau du système de transmission dans une situation réelle en comparant leur performance avec celle des 'antennes d'origine du drone. Le test, qui utilise le rapport signal sur bruit (SNR) de la communication radio entre le drone et la télécommande, montre que la fiabilité du système est considérablement améliorée par rapport à la configuration d'origine des antennes. Ceci est particulièrement remarquable pour des communications sans ligne de vision, ce qui est précisément le scénario pour lequel les antennes ont été conçues.

Nous poursuivons avec la recherche sur les antennes microruban à faisceau large avec l'utilisation d'éléments parasites pour améliorer la largeur de faisceau et obtenir des diagrammes à faisceau large et/ou coniques, avec des applications pour pico-satellites. L'utilisation d'éléments passifs dans une structure en forme de réseau permet d'augmenter le gain dans la direction longitudinale et même d'obtenir des diagrammes de rayonnement coniques. Cette dernière caractéristique est très pratique pour les pico-satellites en orbite terrestre basse (LEO), où un diagramme conique bien réglé offre une couverture uniforme sur une région ciblée de la Terre.

Avec cette thèse, nous contribuons à une analyse des différentes techniques pour élargir la largeur de faisceau des antennes microruban. Nous abordons les différentes approches d'un point de vue didactique afin de

comprendre et d'identifier les principaux aspects de chaque technique, tout en fournissant des lignes directrices unifiées pour l'élargissement de faisceau des antennes patch. Cette démarche permet d'établir des compromis, dépendants du type d'application, entre la taille, le poids, la bande passante et la largeur de faisceau pour ce type d'antennes. Nous présentons deux exemples de ces compromis: les antennes conçues pour le drone, qui privilégient un poids minimum, au détriment d'autres paramètres, et les antennes pour des pico-satellites qui nécessitent des diagrammes à faisceaux larges ou coniques, et qui sont moins contraignantes en poids et en taille. Toutes les conceptions présentées dans cette thèse conservent un profil très bas, ce qui n'est pas courant dans la littérature en raison des limitations intrinsèques de la largeur de faisceau des antennes patch.

Mots-clés

faisceau élargi, antennes microruban, drones, communications satellite, éléments parasites, diagramme isoflux, antennes à profil bas

Contents

Acknowledgements	iv
Abstract.....	vi
Resumé.....	viii
List of Figures	xiii
List of Tables.....	xxii
1 Introduction	1
1.1 Overview on broadbeam microstrip antennas and their applications.....	1
1.1.1 Printed antennas for UAVs	2
1.1.2 Isoflux or broadbeam patterns for satellite communications	3
1.2 Motivation.....	4
1.2.1 Antennas for increased reliability of cage-protected drones.....	4
1.2.2 Antennas with broadbeam patterns antennas for satellite IoT terminals	7
1.3 Antenna requirements	8
1.3.1 Antenna system and antenna element requirements for the cage protected drone.	8
1.3.2 Requirements for broadbeam antennas for satellite IoT terminals	9
1.4 Organization of the thesis	9
1.5 Research contributions	10
1.6 Teaching and student projects	11
2 State of the art on broad-beam microstrip patch antennas	13
2.1 Brief summary on microstrip antennas	13
2.2 The pattern of patch antennas and their beamwidth.....	15
2.2.1 Modifications of the canonical geometry	17
2.2.2 Extra radiators to improve end-fire gain and increase the beamwidth.....	22
2.3 Comparative tables of contributions.....	29
3 On the beamwidth of microstrip antennas and how to increase it.....	33
3.1 Physical explanation on the pattern of microstrip patches and their beamwidth	33
3.1.1 Antenna operation and analysis of pattern shape and effective aperture.....	33
3.1.2 Fundamentals of the beamwidth of canonical microstrip antennas: summary	37
3.2 Analysis of the main parameters of a patch regarding its pattern.....	38
3.2.1 Effect of the ground and substrate size	38
3.2.2 Effect of the substrate thickness	39

3.2.3	Effect of the substrate permittivity on the beamwidth. Relation to the effective area of an antenna	41
3.3	Techniques to increase the beamwidth changing the antenna geometry.....	44
3.3.1	Bending the substrate.....	44
3.3.2	Using 3D ground structures.....	46
3.4	Using additional radiating elements for improved low elevation gain	49
3.5	Summary and compromises on improving the beamwidth	50
4	Compact and lightweight LP and CP broad-beam microstrip antennas: compromises and explanation through designs and examples	53
4.1	Summary on the antenna system constraints and requirements	53
4.2	LP broadband patch using higher order modes.....	55
4.3	Compact broadband LP patch antennas using ground slots	59
4.3.1	Concept of increasing the beamwidth using slots with end-fire patterns.....	59
4.3.2	Design of a LP patch antenna with slotted ground for a quantitative assessment of the performance.....	62
4.3.3	Prototype of a LP patch with ground slots	67
4.4	Compact broadband circularly polarized patch antennas using ground slots.....	70
4.4.1	Concept. Broadband CP patches combining patches with ground slots	70
4.4.2	Design of a CP patch antenna with slotted ground for a quantitative assessment of the beamwidth improvement	72
4.4.3	Prototypes. CP patch with ground slots with feeding network.....	75
4.5	Conclusions from this chapter. Broad-beam LP and CP low profile antennas	85
5	Analysis of the cage and system measurements of the antennas assembled on the drone	89
5.1	Analysis of the cage effect using canonical antennas and MoM.....	89
5.1.1	Analysis of the cage effect using canonical antennas and MoM.....	89
5.1.2	Analysis of a sector of the cage using a directional antenna	92
5.2	Analysis of the power transferred through the cage and the polarization of the radiated wave using infinite periodic array theory.....	93
5.2.1	Definition of the experiment	94
5.2.2	Transmitted power through the structure. Perpendicular incidence	97
5.2.3	Transmitted power for non-perpendicular incidence.....	99
5.2.4	Conclusions	100
5.3	System measurements. Validation of CP broadband patch with ground slots.....	101
5.3.1	Definition of the system measurements.....	101

5.3.2	Positioning of the antennas on the drone and comparison between dipoles and CP patches	111
5.3.3	System measurements. Comparison of dipoles, LP patches, and CP patches: effect of the polarization.....	117
5.3.4	System measurements: Comparison of antennas inside and outside the cage: effect of the cage	120
5.3.5	Conclusions	122
6	Broadening the beamwidth of microstrip antennas using multiple elements for larger footprint antennas	125
6.1	Basic array theory as an analogy to increase the beamwidth with additional elements...	125
6.1.1	Basic two-elements array. Directing the beam towards a given direction.....	126
6.1.2	Three element patch arrays to tune the beamwidth	127
6.1.3	Patch antenna with two parasitic elements for broad beamwidth	129
6.2	Broadbeam patch using parasitic elements – concept and design rules	131
6.2.1	Description and analysis of the beamwidth enhancement	131
6.2.2	Modifying the pattern by tuning critical parameters: gap_w, pad_w and pad_l.....	134
6.2.3	Compromise between size, performance and compatibility for CP antennas.....	135
6.2.4	Summary of the results.....	136
6.3	Broadbeam patch using parasitic elements. Modification of the parasitic elements and dual band operation	137
6.3.1	Modification of the dual-band CP element.....	137
6.3.2	Beamwidth Improvement - Results	139
6.3.3	Discussion on the results	140
6.4	Conclusions.....	140
7	Conclusions	143
7.1	Summary and conclusions.....	143
7.2	Future work.....	147
	References.....	149
	Curriculum Vitae	153

List of Figures

Figure 1. Illustration of a patch antenna and its radiation pattern.....	1
Figure 2. Omnidirectional printed antennas embedded in the wings of a UAV [3].....	2
Figure 3. Illustration of the downlink communication of a satellite with some ground terminals, where the coverage of the satellite is uniform at ground level, radiating more power in directions where the path loss is higher.	3
Figure 4. Antenna using a dielectric cavity (left) to achieve an isoflux pattern (right) [9].....	4
Figure 5. Top view (left) of the antenna proposed in [10] and its isoflux pattern (right) [10].	4
Figure 6. Drone protected by a cage, that provides collision resilience [11].....	5
Figure 7. Drone with the antennas placed inside the cage. The waves radiated by the antennas inside of the cage are modified and attenuated by the cage, thus reducing the range of operation and the reliability of the link.	5
Figure 8. Comparison of the radiation pattern between the isolated dipole (left) and the one enclosed with the protective structure (right).....	6
Figure 9. The carbon fiber cage is made of pentagons attached together. In the Figure we can see one of the pentagons highlighted in green.....	6
Figure 10. Radio link from the remote controller to the drone [11].	7
Figure 11. Uplink communication from a ground terminal that is communicating with several satellites in orbit thanks to an extended broadbeam or isoflux pattern.....	8
Figure 12. Operation of a microstrip patch antenna [1].....	13
Figure 13. Cavity model of a rectangular microstrip, where magnetic current densities in the two radiating slots that can be used to compute the total radiated pattern by the patch [1].	14
Figure 14. Stacked patches with aperture coupling for higher bandwidth of microstrip patches [19].....	14
Figure 15. Miniaturized PIFA patch antenna using shorting ground and transversal slots.	15
Figure 16. Radiation pattern of a patch antenna on an infinite ground plane. Results obtained for a canonical patch with an infinite ground plane boundary at 2.45GHz using Ansys Electronics Desktop [22].....	16
Figure 17. Conical or isoflux pattern (top) and AR (bottom) [23].....	16
Figure 18. Geometry of the design proposed in [30] to achieve broad AR beamwidth	18
Figure 19. Geometry of the pin-loaded antenna presented in [33].....	18
Figure 20. AR beamwidth for the two main cuts of the antenna presented in [33] and for various pin radii.....	19
Figure 21. CP patch antenna with broadened beamwidth using conductive posts [35].	19
Figure 22. Using 3D ground structures to modify the shape of the fringing fields and extend the beamwidth [36].	20

Figure 23. Geometry of the antenna presented in [38]. Side view (a) and top view (b).....	20
Figure 24. Geometry of the antenna presented in [40]	21
Figure 25. Geometry of the antenna presented in [42]. Isometric view (a) and side view (b).....	21
Figure 26. Microstrip ring and its pattern when exciting modes TM ₂₁ and TM ₄₁ [43].....	22
Figure 27. Geometry of the antenna (left) and its surface current distribution (right) [44]	23
Figure 28. Magnetic fields under the patch for different order modes (left) and the needed feeding to excite CP for higher order modes (right). The black dots are the feeding points [46].	23
Figure 29. AR beamwidth of 140deg using hybrid perturbation method [35]	24
Figure 30. Geometry of the antenna (left) and its pattern with and without the parasitic ring (right) [48]	24
Figure 31. Geometry of the antenna proposed in [49], with a modified patch and two parasitic elements (left) and principle of operation of the modified patch using magnetic currents (right).....	25
Figure 32. Effects of the parasitic patches and the extended ground plane on the antenna directivity (and beamwidth). Radiation pattern of the standalone antenna (left), pattern with patches (right). Both at 34.5GHz [49].	25
Figure 33. Geometry of the antenna (left) and radiation pattern and AR over angle (right) [50]	25
Figure 34. Geometry of the antenna presented in [51] that uses two types of parasitic elements to broaden the antenna beamwidth.....	26
Figure 35. Comparison of patterns for a regular patch antenna and the proposed antenna in the E- plane (left) and the H-plane (right) [51].....	26
Figure 36. Geometry of the antenna presented in [52] (left), and its radiation pattern with and without the parasitic stacked patch (right).	27
Figure 37. Geometry of the antenna in [55] (left) and its AR over angle (right).....	27
Figure 38. Geometry of the antenna consisting of crossed dipoles combined with vertical parasitic elements [56]	28
Figure 39. Surface current distribution at 1.0GHz and 1.65GHz [56].....	28
Figure 40. Functioning of a rectangular patch in one of its fundamental mode.....	33
Figure 41. LP (left) and CP pattern (right) in copol, at 2.45GHz.....	34
Figure 42. Effect of a perfect electric conductor on the fields [1].....	35
Figure 43. A patch antenna showing two arbitrary E field components in Far Field.....	35
Figure 44. Radiation pattern, in copol, for the two main cuts of a patch on an infinite ground plane.	36
Figure 45. Radiation pattern in Copol (left) and its corresponding AR aperture (right) for the two main cuts of the antenna example used in Section 3.1.1	37
Figure 46. Radiation patterns for the two main cuts, $\phi=0^\circ$ (left) and $\phi=90^\circ$ (right) of a patch antenna.	39
The spurious radiation caused by the PCB edges occurs because of the surface waves in the substrate. Their decay is slower than for waves propagating in free space: inversely proportional to the distance, and not to the square of the distance as in free space. The surface waves are then not sufficiently attenuated when they reach	

the edges of the board. As their magnitude is non-negligible, the radiation from the edges interferes with the radiation of the patch, modifying the radiation pattern depending on the size of the board and the permittivity of the substrate. The latter also changes the propagation speed of the surface waves and therefore the phase shift between the radiation from the two radiating mechanisms: the patch and the edges of the board; therefore modifying their interference and shape of the total pattern [61]. Also, the low losses of the substrate (in the case of the results in Figure 47, the loss angle of 0.0009 for Rogers RT5880) are very low to sufficiently attenuate the surface waves.	39
Figure 48. Reflection coefficient in magnitude (left) and Smith Chart (right) for various substrate heights. The substrate is Rogers RT5880.	40
Figure 49. Reflection coefficient in magnitude (left) and Smith Chart (right) for various substrate heights. The substrate is Rogers TMM10.	40
Figure 50. Side view of the E fields in complex magnitude in the two radiating slots of a patch with 1mm thickness (left) and 5 mm thickness (right). The substrate is Rogers TMM10, with a relative permittivity of 9.2. The fields are shown in the E-plane, to see the behaviour of the radiating edges of the patch.	40
Figure 51. Radiation pattern of a patch antenna using RT5880 (left) and TMM10 (right) for various substrate thicknesses.	41
Figure 52. Top view of four patches using different substrates. The substrate thickness is of 1mm in all the cases. Antennas designed and simulated using Ansys Electronics Desktop [22].	42
Figure 53. Reflection coefficient in magnitude (left) and Smith Chart (right) for various substrates with different permittivities.	42
Figure 54. E-field complex magnitude for the lowest (left) and highest (right) permittivity substrates at $\phi=90^\circ$ cut, where we can see the behaviour of the radiating edges.	42
Figure 55. Radiation patterns in $\phi=0^\circ$ (left) and $\phi=90^\circ$ (right) cuts for the antennas in Figure 52.	43
Figure 56. Variation of the gain (left) and HPBW (right) with the various substrate permittivities.	43
Figure 57. Regular patch (left) and bent patch (right). The bending radius is of 200 mm.	44
Figure 58. Effective aperture "equalization". Broadside to endfire ratio changes from 35 to 3.4.	45
Figure 59. Reflection coefficient in magnitude (left) and Smith Chart (right) of a bent patch and a regular planar patch.	45
Figure 60. E field complex magnitude distribution for the planar (left) and bent patches (right). At 2.45GHz.	45
Figure 61. Radiation pattern $\phi=0^\circ$ (left) and $\phi=90^\circ$ (right).	46
Figure 62. Example of a broadbeam microstrip antenna using 3D ground structure [66].	47
Figure 63. Proposed geometry mimicking a 3D ground structure using several substrate layers. Both use a substrate RO3210 with a permittivity of 10.2 and a loss angle of 0.003. Each substrate layer has a thickness of 5mm. Antenna designed and simulated using Ansys Electronics Desktop [22].	47
Figure 64. Reflection coefficient of the simple ground antenna and the layered ground antenna.	47
Figure 65. Complex magnitude distribution of the E field.	48
Figure 66. Radiation patterns for the cuts at $\phi=0^\circ$ (left) and $\phi=90^\circ$ (right).	48
Figure 67. Additional radiating elements/current distributions for enhanced vertical effective aperture [69].	49

Figure 68. The signal radiated by the antennas inside of the cage is being attenuated by the cage, thus reducing the strength of the signal being emitted and therefore range of operation.	54
Figure 69. Geometry of the hybrid antenna using higher order modes. The antenna size is $140 \times 140 \times 6.35 \text{ mm}^3$ [70].	55
Figure 70. Geometry and main dimensions of the geometry proposed in Figure 69 (left), and the current distribution (right) [70].	55
Figure 71. In this figure we show the $\Phi = 90^\circ$ pattern cuts (in copol) of the disk (left) and the ring (right). These two patterns complement each other to broaden the beamwidth.	56
Figure 72. Reflection coefficient (left) and gain pattern over for the lower, center, and higher frequency of the band [70].	56
Figure 73. Gain in Copol and Xpol for the antenna proposed in Figure 69. $\Phi = 0^\circ$ (left) and $\Phi = 90^\circ$ (right) [70].	57
Figure 74. Effect of varying u_{strip_W} on the reflection coefficient (left) and the radiation pattern @2.45GHz (right).	57
Figure 75. Effect of substrate thickness on the reflection coefficient (left) and how a thinner substrate leads to a more unstable radiation pattern over frequency (right), for a thinner substrate (4mm instead of 6.35mm). ..	58
Figure 76. Gain in copol of the proposed antenna, a regular patch, and a dipole at cuts $\Phi = 0$ (left) and $\Phi = 90$ (right) [70].	58
Figure 77. Standalone vivaldi antenna (left) and its corresponding pattern with good end-fire gain. The size is of $50 \times 50 \text{ mm}$ and it operates at 2.4GHz.	59
Figure 78. Combination of 4 Vivaldi antennas fed with microstrip lines (left) to achieve the desired monopole-like radiation pattern (right).	60
Figure 79. Slot antenna (left) on the same ground as the Vivaldi in Figure 77 and its corresponding radiation pattern (right).	60
Figure 80. Evolution of the Vivaldi antennas to simple rectangular slots (left) to achieve the desired monopole-like radiation pattern (right)	61
Figure 81. Matching (left) and radiation pattern stability over frequency (right) of the slots from the design in Figure 80.	61
Figure 82. Adding a patch in the gap between the slots to combine their patterns providing a beamwidth of 220°	62
Figure 83. Patch antenna with ground slots. The substrate is Rogers TMM10 with a permittivity of 9.2, and a thickness of 1.27mm. The lateral size of the antenna is $47.8 \times 47.8 \text{ mm}^2$, and the dimension of the slots is of 14mm.	62
Figure 84. E fields of the LP antenna with slots in Figure 83. E-field vector (left) and complex magnitude (right).	63
Figure 85. 3D LP pattern (left), and the co-pol cut in the YZ plane (right) with a HPBW of 190°	63
Figure 86. Bandwidth of a single patch (red) and the patch with slots 5% (yellow), for exactly the same size. The bandwidth is increased by x5 times.	64

Figure 87. Effect of the slot width on the input impedance (left) and the radiation pattern (right). The variations are for a slot length of 14mm, a separation patch-gap of 0mm and a patch size of 19.8mm. These results refer to the antenna in Figure 88.	64
Figure 89. Radiation pattern cuts at $\phi=0^\circ$ (left) and $\phi=90^\circ$ (right) for various slot widths . The variations are for a slot length of 14mm, a separation patch-gap of 0mm and a patch size of 19.8mm.	65
Figure 90. Effect of the slot length on the input impedance. The variations are for a slot width of 1mm, a separation patch-gap of 0mm and a patch size of 19.8mm.	65
Figure 91. Radiation pattern cuts at $\phi=0^\circ$ (left) and $\phi=90^\circ$ (right) for various slot lengths . The variations are for a slot width of 1mm, a separation patch-gap of 0mm and a patch size of 19.8mm.	65
Figure 92. Effect of the slot-patch gap in the reflection coefficient.	66
Figure 93. Effect of the slot-patch gap on the pattern. The variations are for a slot length of 14mm, a slot width of 1mm and a patch size of 19.8mm.	66
Figure 94. Reflection coefficient for various substrate thicknesses . The variations are for a slot length of 14mm, a separation of 0mm and a patch size of 19.8mm.	66
Figure 95. Radiation pattern cuts at $\phi=0^\circ$ (left) and $\phi=90^\circ$ (right) for various substrate thicknesses . The variations are for a slot length of 14mm, a separation of 0mm and a patch size of 19.8mm.	67
Figure 96. Geometry of the antenna prototype. The dimensions are $45.2 \times 45.1 \times 1.27 \text{ mm}^3$, with a Rogers TMM 10i substrate. The length of the slots is 13mm and the sides of the squared patch are 19.2mm.	67
Figure 97. Fabricated LP patches. Top view (left) and bottom view (right).	68
Figure 98. Measured and simulated S11 of the LP patches prototypes. Its bandwidth is of ~100 MHz, broader than the 83.5 MHz required in the band.	68
Figure 99. Measurement of the LP prototype in the anechoic chamber. The support introduces reflections that are ultimately seen in the measurement of the pattern as ripples.	69
Figure 100. Measurement and simulation results in the $\phi=0^\circ$ cut (left) and $\phi=90^\circ$ cut (right). The HPBW is of 190° for the optimized plane. The patterns are shown @2.45GHz, and the peak gain is 4.6dBi.	69
Figure 101. Patch with four ground slots and two lumped ports that excite circular polarization in the antenna.	70
Figure 102. Illustration of the E field (red) and the current in the ground (black) in the antenna at different phases. The ports are marked with green circles.	71
Figure 103. Pattern of the antenna from Figure 101 when exciting only one of its linear polarizations (current density along X axis). These results are obtained for an antenna of $47.1 \times 47.1 \times 1.27$ made of TMM10. The patch is $19.5 \times 19.5 \text{ mm}$ and the slot length 11.5mm.	71
Figure 104. Pattern of the antenna from Figure 101 when exciting CP on it. These results are obtained for an antenna of $47.1 \times 47.1 \times 1.27$ made of TMM10. The patch is $19.5 \times 19.5 \text{ mm}$ and the slot length 11.5mm.	72
Figure 105. Antenna with optimized geometry to reduce its size and increase the beamwidth in both planes and circular polarization. The size of the antenna is of $48.2 \times 48.2 \times 1.27 \text{ mm}^3$, patch_w = 19.8mm, there is no gap between the patch and the slots, the corners are trimmed with a chamfer distance of 20mm and the feeding of the ports is located at 8.5mm from the center of the patch.	72

Figure 106. Realized gain patterns in copol and crosspol for the two main cuts, for the antenna without slots (left) and with slots (right). Results at 2.45GHz.	73
Figure 107. Reflection coefficient in magnitude (left) and in the Smith Chart (right).....	73
Figure 108. The realized gain pattern of the antenna without slots (left) and with slots (right). Both are obtained for the cut at $\Phi = 90^\circ$, the performance at $\Phi = 0^\circ$ is equivalent. Results at 2.45GHz.	74
Figure 109. AR of the antenna without slots (left) and with slots (right). Results at 2.45GHz.	74
Figure 110. Geometry of the first prototype, including two substrate layers of Rogers TMM10.	75
Figure 111. Top layer (left) and bottom layer (right) for the prototype.	75
Figure 112. Gluing of the two PCBs (feeding network and antenna) together.	76
Figure 113. Fabricated prototype. Feeding network (left) and patch (right)	76
Figure 114. Reflection coefficient measurement setup (left) and results (right)	77
Figure 115. Axial ratio simulated and measured in both cuts	77
Figure 116. Modified design with the cable underneath the antenna.....	78
Figure 117. Complex magnitude of the current density at 2.35GHz with lumped port (left) and a cable with length of 20mm (right).....	78
Figure 118. Effect of the cable in the lower frequencies without (left) and without (right) an H boundary on the cable for various cable lengths	79
Figure 119. Design of antenna using bazooka balun on the coaxial cable (left) and its AR (right).....	79
Figure 120. Design of the final prototype. Top (left) and bottom view (right).	80
Figure 121. Simulation result. Reflection coefficient (left) and pattern (right) of the final designs.....	81
Figure 122. Simulation results. AR vs freq (left) and vs angle (right).	81
Figure 123. Final prototype of the circularly polarized broad beam patch antenna.....	81
Figure 124. Measured and simulated S11 of the final prototype. Bandwidth $\sim 250\text{MHz} > 100\text{ MHz}$	82
Figure 125. Final prototype of the CP broad-beam antenna in the measurement setup in the anechoic chamber.	83
Figure 126. Measured pattern (left) and gain (right) of the final prototype. HPBW of 90° , and 6dB beamwidth of 150° . Gain of 2.1dBi @2.4 GHz, 3.2dBi @2.46 GHz and 3.1dBi @2.48 GHz. The gain variation with two antennas combined is of 6dB, below the maximum required of 10dB.....	83
Figure 127. Measured axial ratio of the final prototype vs frequency (left) and vs angle (right). The AR bandwidth is of 200MHz and the AR is below 6dB for 120-140°.	83
Figure 128. Comparison of the pattern of three antennas: proposed antenna (measured), and two regular patches using a substrate with a permittivity of 2.3 and 9.2.	84
Figure 129. Cage with a resonant dipole that we move along the Y axis.	90
Figure 130. 3D radiation pattern of the resonant dipole along the X axis, centred in the cage (left) and moved 170mm from the centre, towards the cage and along the Y axis (right)	90

Figure 131. Gain of the dipole without cage (a), at -17cm from the centre (b), at -8.5cm from the centre (c), and at the centre (d). We are displacing the dipole in the hemisphere contained from theta 0° to 180°	91
Figure 132. Gain variance computed moving the resonant dipole along the X, Y and Z axes of the cage, from its centre.....	91
Figure 133. Near field plot of the dipole centred inside the cage (left) and at 12cm from the centre (right)	92
Figure 134. Fields distribution on the XY plane for a Yagi (left) and a Yagi with a portion of cage (right).....	93
Figure 135. Fields distribution on the XY plane for a Yagi and full cage with H boundary (left) and with PEC cage and H boundary only on the rod parallel to the Yagi, in black (right)	93
Figure 136. Illustration of a cut of the cage with an isotropic antenna in its center. We can assume that the waves have the same amplitude and phase when they arrive to the cage.....	94
Figure 137. Simplification of a simplified hexagon to a smaller cell with parallel segments.....	95
Figure 138. Definition of the cell on ANSYS Electronics Desktop (left), and definition of one pair of master/slave boundaries (right).....	95
Figure 139. Definition of the Floquet ports and calculation of the 10 first modes analysed in the structure.....	96
Figure 140. Modes modes excited by the two Floquet ports of the periodic structure.....	97
Figure 141. S21 for all 10 ports at a perpendicular incidence Theta scan=0°	97
Figure 142. S112 , S212 and S112 + S212 for mode 1	98
Figure 143. Intermodal transmission. It describes the power received in port 2 in mode 1 from all the other ports.....	99
Figure 144. S21 for all 10 modes at an incidence of Theta_scan=20°.....	99
Figure 145. S21 for all 10 modes at an incidence of Theta_scan=40°.....	100
Figure 146. S112 + S212 of mode 1 for various angles of incidence	100
Figure 147. Setup LOS. Drone and controller in the corridor (left) and sketch of the measurement setup (right).	102
Figure 148. Setup NLOS. Remote controller inside a laboratory (left) and sketch of the measurement scenario (right).....	102
Figure 149. Drone prepared for measurements, with the three axes of rotation.....	103
Figure 150. Ratio of increased distance in free space for an increment of EIRP (transmitted power, antenna gain or both).....	104
Figure 151. Antennas in original orientation and position, on inner frame.....	106
Figure 152. Dipoles on support	106
Figure 153. CP Patches on support.	107
Figure 154. Dipoles optimal position and orientation.....	107
Figure 155. Positioning and orientation of the LP patches inside the cage for the tests.....	108
Figure 156. Positioning and orientation of the CP patches inside the cage for the tests.....	108
Figure 157. Dipoles inside cage.....	109

Figure 158. Dipoles outside cage.....	109
Figure 159. CP Patches inside cage.....	110
Figure 160. CP Patches outside cage.....	110
Figure 161. Average SNR over two measurements in the YAW, ROLL and PITCH rotation in LOS for the Setups BD-Orig, BD-Sup and CPP-Sup.....	111
Figure 162. Reliability metrics for the worst-case threshold (left) and the adjusted threshold (right) for the three antenna setups in LOS, for the Setups BD-Orig, BD-Sup and CPP-Sup.....	112
Figure 163. NLOS. Comparison of SNR for the Setups BD-Orig, BD-Sup and CPP-Sup.....	114
Figure 164. Comparison of reliability indicator for the Setups BD-Orig, BD-Sup and CPP-Sup.....	114
Figure 165. Comparison of reliability indicator before (left) and after adding 1dB to the measurements (right), for the Setups BD-Orig, BD-Sup and CPP-Sup.....	115
Figure 166. Comparison in LOS: average SNR over two measurements in the YAW, ROLL and PITCH rotation for BD-Orig, BD-Opt, LPP-Opt, CPP-Opt.....	117
Figure 167. Comparison in LOS. Comparison of reliability indicator for BD-Orig, BD-Opt, LPP-Opt, CPP-Opt.	118
Figure 168. Comparison in LOS: average SNR over two measurements in the YAW, ROLL and PITCH rotation for various positions and orientations	119
Figure 169. Comparison in NLOS. Comparison of reliability indicators for BD-Orig, BD-Opt, LPP-Opt, CPP-Opt.	119
Figure 170. Sketch of the interaction of the antennas inside and outside the cage, and their placement for the tests. The cage cross section shows the various pentagons highlighted with different colors.....	121
Figure 171. Comparison in NLOS: average SNR over two measurements in the YAW, ROLL and PITCH rotation for various positions and orientations	121
Figure 172. Comparison in NLOS. Comparison of reliability indicators for BD-Ins, BD-Out, CPP-Ins, CPP-Out.	121
Figure 173. Two elements array, pin-fed with lumped ports (left), and illustration of the pointing of the radiation pattern when using a linear array with a phase delay between elements (right).....	126
Figure 174. Radiation pattern in of a two-element patch array in the two main cuts at $\phi = 0^\circ$ (left) and $\phi = 90^\circ$ (right). The results are at @2.45GHz.	126
Figure 175. Array of three patches. The substrate is made of FR4 and its thickness is of 2.4mm.	127
Figure 176. Patterns generated by the combination of Patch 1 and 2 in absence of patch 3 (red) and by the combination of Patch 2 and 3 in absence of Patch 1 (blue).	127
Figure 177. Radiation pattern of the 3-element array for its two main cuts at $\phi=0^\circ$ (left) and $\phi=90^\circ$ (right). This is made for the two lateral antennas with a 10% of the power of the central patch.....	128
Figure 178. Normal S11 and Active S11 to show coupling.....	128
Figure 179. Total radiation pattern for a patch with parasitic elements designed to achieve broad beamwidth. The pattern results from combining the effect of the two sub-antennas (patch + parasitic elements).	129

Figure 180. Central patch antenna is active and the two lateral patches are identical but not fed.	129
Figure 181. Different arrangement of the patches and the dependence with the element separation.	130
Figure 182. $\Phi = 0^\circ$ (left) and $\Phi = 90^\circ$ (right) pattern cuts for a patch with parasitic elements identical to the patch placed along the Y axis.	130
Figure 183. Example of a rectangular patch with parasitic elements to enhance the beamwidth in the YZ plane [74].	131
Figure 184. Reflection coefficient. Bandwidth of 97 MHz [74]	132
Figure 185. Directivity for the lower, middle, and upper frequencies within the band [74].	132
Figure 186. Cross polar discrimination in the YZ plane. XPD is larger than 30dB in the entire upper hemisphere [74].	133
Figure 187. Fabricated prototype (left) and comparison of normalized pattern in simulation and measurements at the center of the band and in the YZ plane (right) [74].	133
Figure 188. Gap_w sweep [74]	134
Figure 189. Pad_L (left) and Strip_w sweeps (right) [74]	134
Figure 190. Surface currents on the geometry with additional pads, to excite circular polarisation and extend the beamwidth in the XZ and YZ planes [74]	135
Figure 191. Copol of the XZ and YZ cuts with only one mode activated in the geometry of Figure 190 [74].	136
Figure 192. RHCP (Copol) and LHCP (Xpol) for the XZ cut (left) and YZ cut (right). The peak directivity is 2.7dBi [74]	136
Figure 193. Proposed antenna geometry without parasitic elements (left) and with parasitic elements (right). The shape of the parasitic elements is modified and diagonal slots to excite dominant CP and dual band operation.	138
Figure 194. Simulated (left) S_{11} parameter and (right) broadside realized RHCP gain of (gray) a conventional patch antenna (not shown here), and the proposed antenna: (blue) without and (orange) with parasitic elements.	138
Figure 195. Radiation patterns of the proposed antenna at two frequencies and angular cuts (left), and comparison with the antenna without parasitic elements (right). Note the gain improvement of 1 – 2 dBi at angles $60 - 75^\circ$	139

List of Tables

Table 1. Requirements for the antennas for the collision-robust drone.....	9
Table 2. Requirements for satellite antennas in the L band with dual-band and broad beam.....	9
Table 3. Summary of the techniques that modify the structure of patches to broaden the beamwidth.....	29
Table 4. Summary of the techniques that combine several radiators or modes to broaden the beamwidth.	30
Table 5. Comparative table of advantages and disadvantages of the different approaches.....	51
Table 6. Dimensions of the geometry in Figure 70.....	56
Table 7. Comparison of the HPBW and peak gains for the YZ and XZ pattern cuts at 2.45GHz for various antennas.....	59
Table 8. Mechanical requirements and actual values of the prototype.....	82
Table 9. Comparison of all the CP antennas presented in the Chapter.....	86
Table 10. Comparison of all the LP antennas presented in the Chapter.....	87
Table 11. Comparison of all antennas included in the test	105
Table 12. Global probabilities for worst case threshold and worst case + margin in LOS, for the Setups BD-Orig, BD-Sup and CPP-Sup.....	112
Table 13. Average SNR improvement for the CP patches (setup CPP-Sup) compared to the dipoles in the setups D-Orig and D-Opt, and FSEII.	113
Table 14. Global probabilities for worst case threshold and worst case + margin in NLOS, for the Setups BD-Orig, BD-Sup and CPP-Sup.....	114
Table 15. CPP-Sup compared to BD-Orig and BD-Sup.....	115
Table 16. Global probabilities for worst case threshold and worst case + margin in NLOS +1dB, for the Setups BD-Orig, BD-Sup and CPP-Sup.....	116
Table 17. CPP-Sup compared to BD-Orig and BD-Sup adding +1dB of extra transmit power thanks to lower gain of the patches.	116
Table 18. Final conclusions on the reliability of the dipoles and the CP patches.....	116
Table 19. Final conclusions on the free space equivalent distance improvement of the CP patches compared to the dipoles.....	117
Table 20. Comparison in LOS. Global probabilities for worst case threshold and worst case + margin in LOS, for BD-Orig, BD-Opt, LPP-Opt, CPP-Opt.....	118
Table 21. Comparison of LPP-Opt and CPP-Opt to BDD-Opt in LOS. Average SNR improvement and (FSEII).	118
Table 22. Comparison in NLOS. Global probabilities for worst case threshold and worst case and adjusted thresholds, for BD-Orig, BD-Opt, LPP-Opt, and CPP-Opt.....	119

List of Tables

Table 23. Comparison of LPP-Opt and CPP-Opt to BDD-Opt in NLOS. Average SNR improvement and (FSEII).	120
Table 24. Comparison in NLOS. Global probabilities for worst case threshold and worst case + margin, for BD- Ins, BD-Out, CPP-Ins, CPP-Out.	122
Table 25. Average change of SNR and FSEII, comparing BD-Out to BD-Ins and CPP-Out to CPP-Ins. The bigger the change, the more significant the effect of the cage.	122
Table 26. Feeding of the three patches to obtain the results of Figure 177.	128
Table 27. Values used in the example	131
Table 28. Antenna beamwidth (in °).	139

1 Introduction

1.1 Overview on broadbeam microstrip antennas and their applications

Microstrip patch antennas offer a large number of mechanical advantages like being lightweight, inexpensive, low profile and easy to manufacture and conformable. These advantages are critical for many applications, making them desirable despite their relatively low efficiency and narrow bandwidth. Thus, the antenna community has devoted several decades to addressing these limitations and increasing the impedance bandwidth and the efficiency of microstrip patch antennas. They consist of a metallic patch on a dielectric substrate and a ground plane, as shown in Figure 1. This architecture takes advantage of the easy and mature fabrication process for printed circuit boards (PCBs).

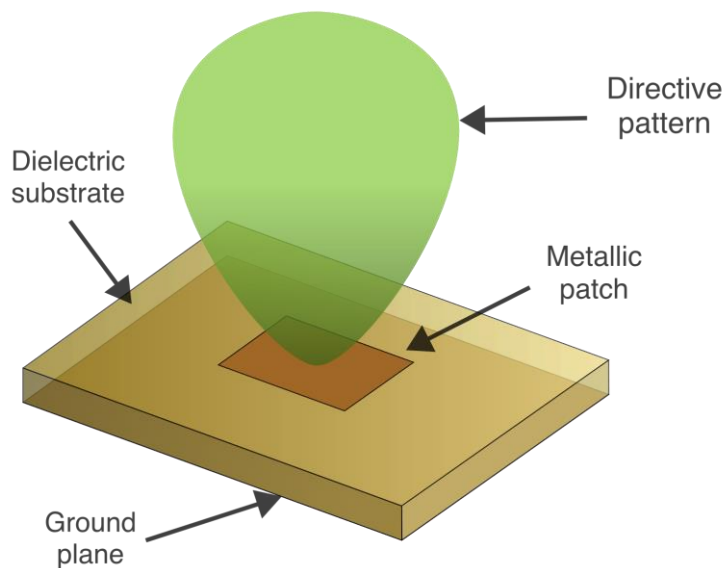


Figure 1. Illustration of a patch antenna and its radiation pattern.

The radiation pattern of patch antennas is directive and its peak gain is pointing the direction normal to the surface of the board. The more directive the pattern of an antenna is, the narrower is its beamwidth, that is quantified using the aperture of the beam at half power from the peak, called Half Power Beam Width (HPBW). In the case of microstrip patches, the HPBW is typically around 70°. [1]

While a directive pattern is convenient for many applications that require medium or high gain, there are others that benefit from broader beamwidth patterns, at the expense of lower peak gain, as satellite communications and remote piloting of Unmanned Aerial Vehicles (UAVs or drones).

1.1.1 Printed antennas for UAVs

The weight is one of the critical aspects of UAVs as it has a direct impact on their battery life, one of their most limiting factors. Printed antennas are very convenient and commonly used in communications with UAVs thanks to their reduced weight and cost. They offer other advantages, like their easy integration, as they can be bent conformally to a surface or integrated in the structure of the UAV [2]. Their low profile is also beneficial because it reduces the air drag, which ultimately improves the stability of the drone and also their battery life.

In short, the common requirements for drone antennas are to be small, low profile, low weight and to have an omnidirectional coverage. The latter can be achieved using omnidirectional antennas, or combining several antennas with sectorial coverage. One example of printed omnidirectional antennas that are highly integrated in the structure of a UAV is shown in Figure 2, where the printed monopoles are embedded in the wings of the drone [3].

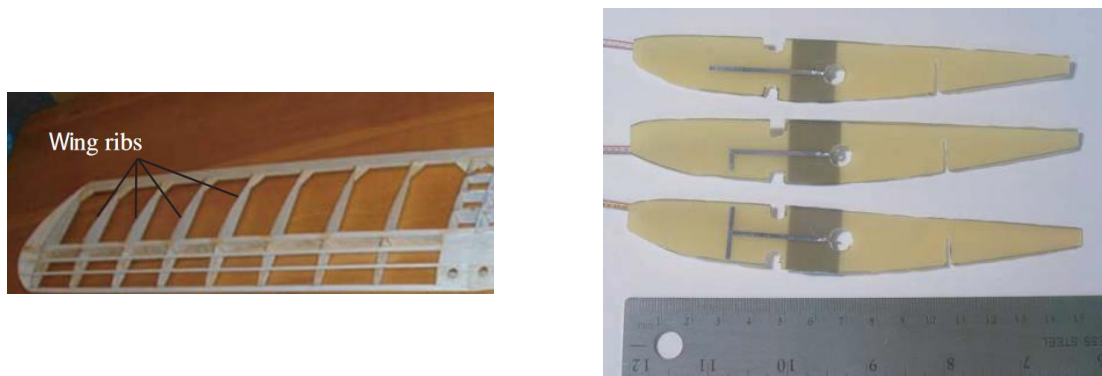


Figure 2. Omnidirectional printed antennas embedded in the wings of a UAV [3].

The transmission system and the performance of the antennas are two critical aspects that define the maximum range that a drone can be flown from a remote controller. The output power and sensitivity of the transmission system have more influence on the maximum range, while the antennas have a stronger effect on the reliability of the communication. The latter comes from the fact that the position and orientation of the drone changes continuously while it flies. A uniform coverage, omnidirectional or ideally isotropic is needed to minimize variance of the gain and maintain the quality of the link as the drone maneuvers. The radiation pattern of the antennas is very dependent on the structure of the UAV, as its structure and components can modify it. Therefore, custom antenna designs are sometimes needed for a specific drone, and thus each case should be analyzed and addressed individually.

For cases where omnidirectionality is not achieved with a single element, the use of several antennas is to be considered. Diversity techniques are used to improve the pattern of the antennas, by combining several radiation patterns and switching between them as needed [4]. This approach is broadly used for UAV applications [5], [6] and for MIMO (Multiple Input Multiple Output) scenarios in general [7].

1.1.2 Isoflux or broadbeam patterns for satellite communications

Microstrip antennas have been very broadly used in satellite communications thanks to their low profile, low cost and easy integration. In these cases, the link is established between a satellite in orbit and ground stations or terminals on the surface of the Earth. A scenario where a satellite is required to illuminate a uniform coverage area on the ground to communicate with several ground terminals is shown in Figure 3. The path loss to reach each of the terminals increases with the angle seen from the satellite. To grant an uniform coverage, microstrip antennas with broadbeam or isoflux patterns [8] have been broadly studied and applied by the antenna community.

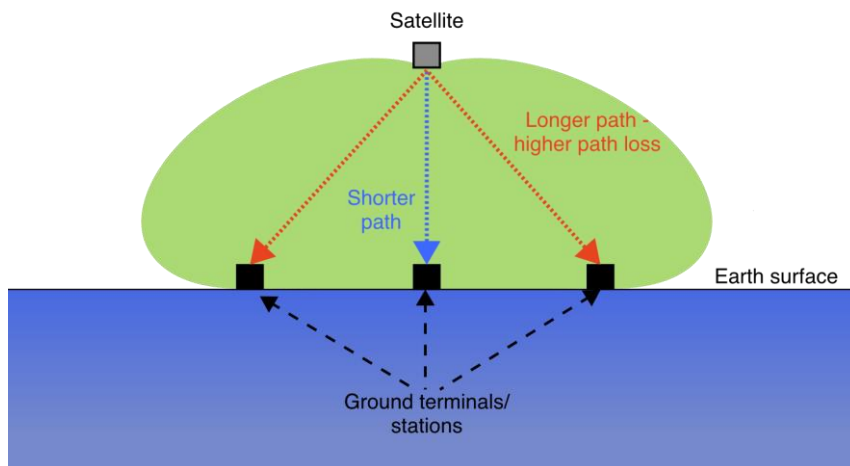


Figure 3. Illustration of the downlink communication of a satellite with some ground terminals, where the coverage of the satellite is uniform at ground level, radiating more power in directions where the path loss is higher.

Isoflux patterns do not have their peak directivity in broadside but symmetrically tilted away from this direction. One example of antennas radiating isoflux patterns is shown in Figure 4, that has its peak at $\theta = \pm 40^\circ$ [9]. Another antenna with isoflux pattern shown in Figure 5 [10] combines four elements arranged in a ring shape to provide the desired pattern.

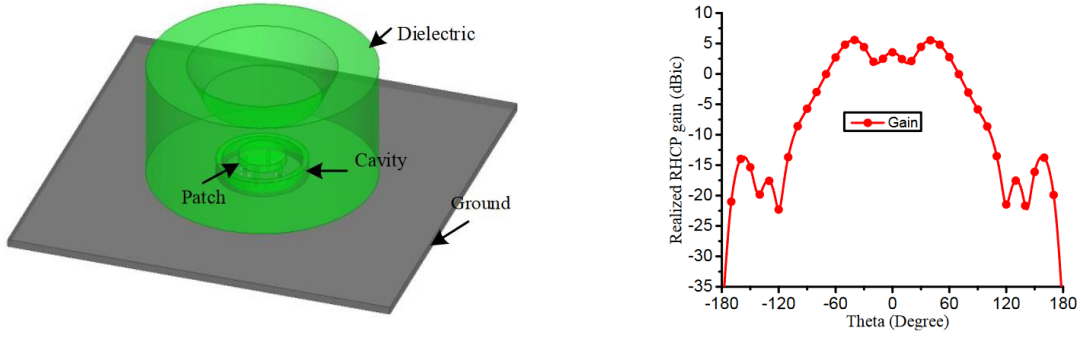


Figure 4. Antenna using a dielectric cavity (left) to achieve an isoflux pattern (right) [9]

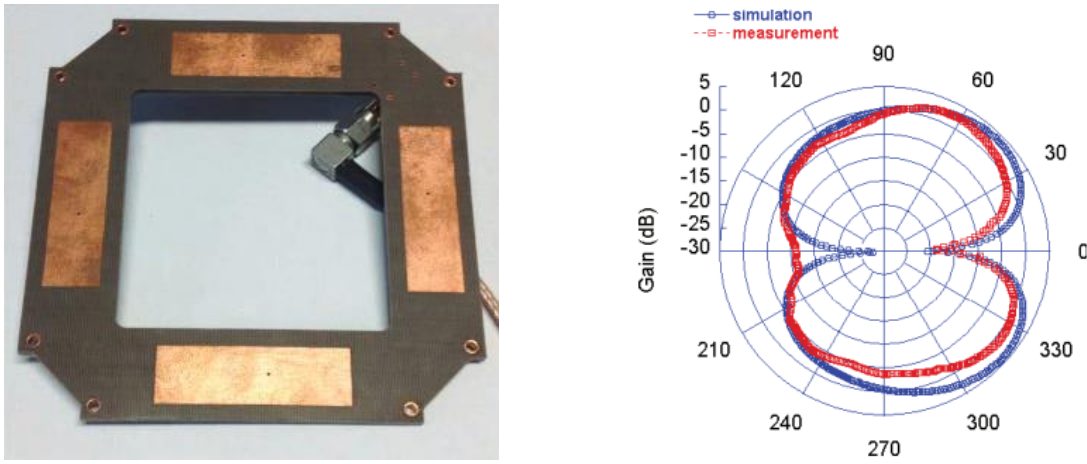


Figure 5. Top view (left) of the antenna proposed in [10] and its isoflux pattern (right) [10].

1.2 Motivation

1.2.1 Antennas for increased reliability of cage-protected drones

UAVs are revolutionizing many sectors of the industry in the last years, such as industrial inspections, search and rescue or simply to be used in inaccessible places that may be dangerous for people. However, they are also sensitive to crashing, as their propellers can break easily if they touch an obstacle, potentially leading to losing the drone. To tackle this issue, Flyability SA [11] developed a collision tolerant drone protected by a cage that prevents the drone from crashing. This feature allows to use the drones in scenarios where a more traditional non-collision-robust drone is risky or even impossible to use.



Figure 6. Drone protected by a cage, that provides collision resilience [11]

The cage is made of carbon fiber, which offers excellent advantages in terms of mechanical resistance to collisions and weight. Carbon fiber is electrically conductive and, in consequence, the protective cage affects considerably the quality of the radio link, as the antennas are also inside the cage. The degradation occurs in terms of the range at which the drone can fly, but also of reliability of the link, the latter being especially critical as these drones are supposed to be flown in inaccessible places. This is of particular importance for drones operated indoors and beyond line of sight, where obstacles may strongly degrade the quality of the link abruptly. The use of the carbon fiber-based superstructure for protection of a drone is a development introduced to the market by Flyability, and as such there has not been much research on this topic and on how to improve its electromagnetic behavior.



Figure 7. Drone with the antennas placed inside the cage. The waves radiated by the antennas inside of the cage are modified and attenuated by the cage, thus reducing the range of operation and the reliability of the link.

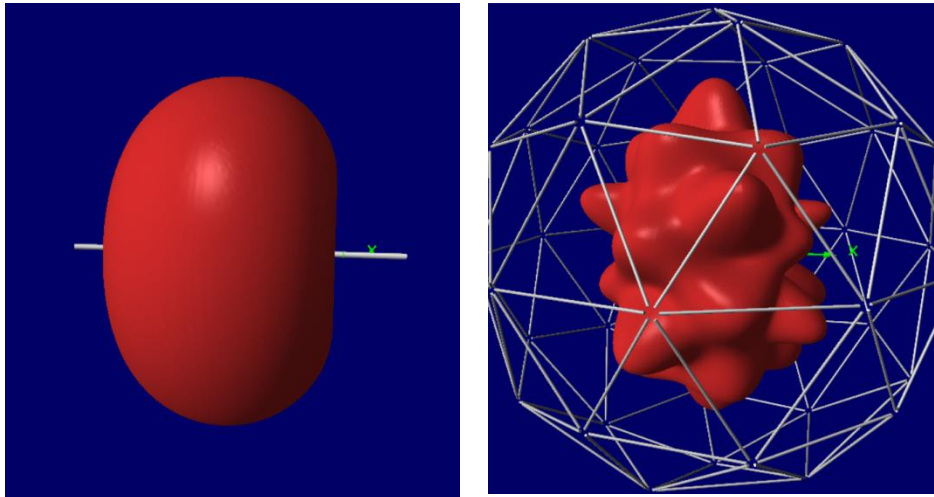


Figure 8. Comparison of the radiation pattern between the isolated dipole (left) and the one enclosed with the protective structure (right).

In Figure 8, we can get an overview on how the cage is affecting to the propagation of the waves through it. It shows the pattern of a regular resonant dipole with and without the cage surrounding it. The cage perturbs the radiation pattern differently in each direction the geometry of the cage. It has a geodesic shape of 40cm of diameter, made of pentagons as we can see in Figure 9. The pentagons have segments of two sizes: 131mm or 1.07λ , and 115mm or 0.94λ . These are close to one full wavelength in the operating band of the transmission system: the ISM band at 2.4GHz. When the pentagons are assembled together, they also form larger hexagons from the larger segments. The different shapes and lengths of the segments lead to the non-uniform distortion of the pattern shown in Figure 8.

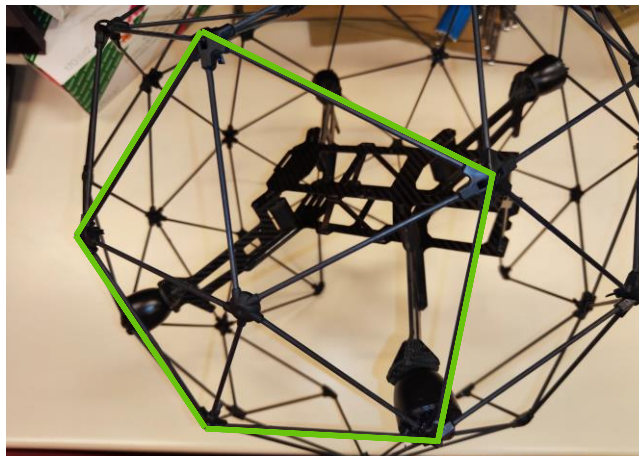


Figure 9. The carbon fiber cage is made of pentagons attached together. In the Figure we can see one of the pentagons highlighted in green.

The radio link is illustrated in Figure 10. We can summarize the particularities of the collision tolerant drone protected by the cage from the point of view of the radio link as follows:

- It is flown indoors and in unpredicted environments with high multipath effect.
- The cage perturbs the propagation of the waves. The effect is highly dependent on the shape of the cage. The protective structure cannot be modified as it is critical to the robustness of the UAV.
- The drone uses a transmission system with two antennas using a maximum selection diversity scheme and operates in the ISM band at 2.4GHz.

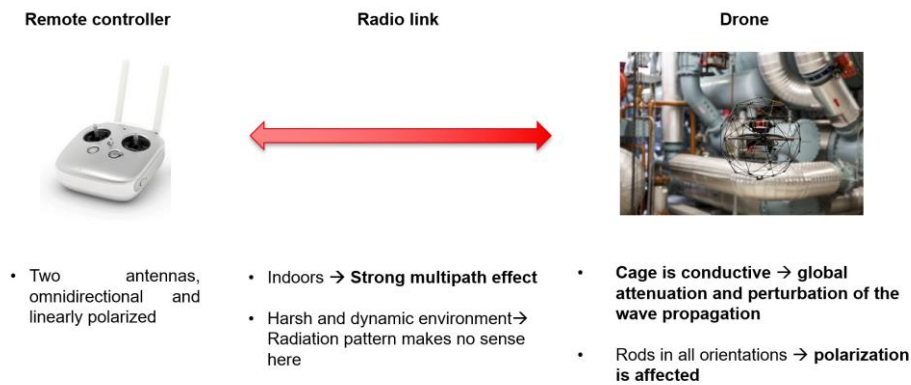


Figure 10. Radio link from the remote controller to the drone [11].

The work on the antennas for this drone is condensed in the Chapters 4 and 5 of this Thesis.

1.2.2 Antennas with broadbeam patterns antennas for satellite IoT terminals

The satellite Internet of Things (IoT) networks are growing very rapidly nowadays, with both traditional and new satellite companies being involved in its development and deployment to provide connectivity even in the most remote areas [12].

The size of the Satellite-IoT terminals is directly dependent on the antenna size, which needs then to be reduced as much as possible. In addition, having a good gain in low elevation angles increase the number of satellites to which the terminal can connect and is important to reduce the latency of the system. This scenario is depicted in Figure 11. Isoflux or broadbeam radiation patterns are required in these cases. Antennas with dual band operation, usually with a small frequency ratio (FR), are also needed to enable full-duplex communication between the terminals and the satellites [13]. Some of the existing CP and dual band antennas in the L-band have a FR of approximately 1.05 are helix antennas (high profile) [14], complex multi-layer structures, such as stacked-patch [15], or ring-patch structures [16].

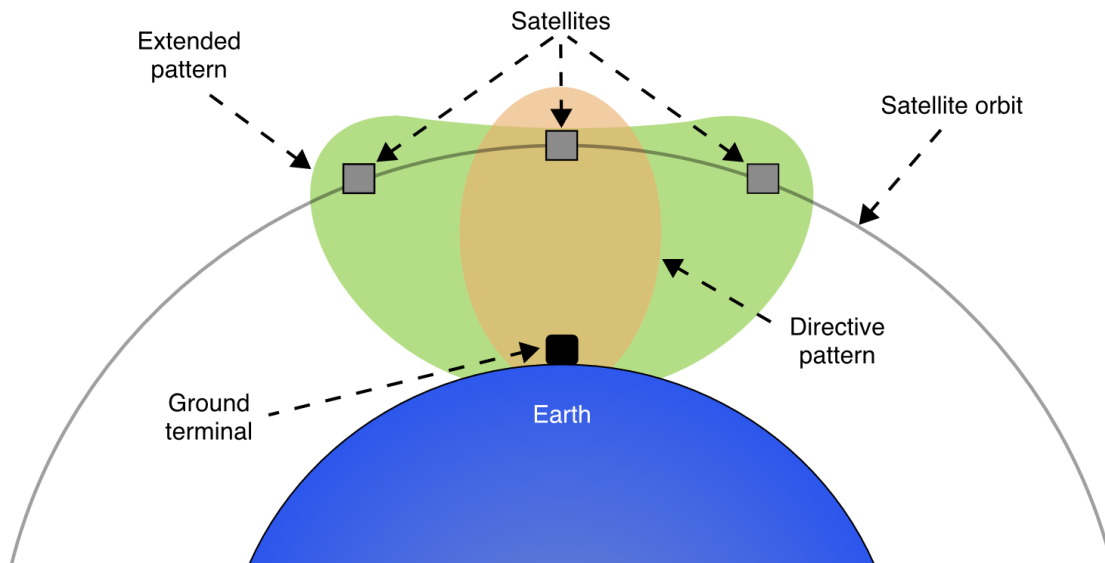


Figure 11. Uplink communication from a ground terminal that is communicating with several satellites in orbit thanks to an extended broadbeam or isoflux pattern.

Relatively small antennas with broad beamwidth, dual band, CP and low cost are then required for IoT satellite communications. Keeping a low profile with these designs is preferred for these antennas, in applications where the aerodynamics of the terminal are very important, such as commercial fleet management for land transport (car, vans), and tracking of drones.

1.3 Antenna requirements

1.3.1 Antenna system and antenna element requirements for the cage protected drone

The goal is to increase the reliability of the radio link by reducing the effect of the cage. This improvement should be accomplished by using only two antennas as this is a limit set by the transmission system. The antennas on the remote controller are linearly polarized. Using antenna elements on the drone with circular polarization or polarization diversity would thus be beneficial to prevent high polarization losses. This also prevents that the cage degrades significantly one single linear polarization.

Therefore, we want a small circularly polarized, low profile, lightweight antenna, and with a gain variation as small as possible and no greater than 10dB with the two antennas combined. The transmission system uses a maximum selection scheme for the antenna diversity, which means that the pattern of the antennas is not combined, as they do not operate at the same time.

In Table 1 we gather the antenna system requirements for the collision-robust drone:

Parameter	Requirement
Matching impedance	50 Ohm.
Operating frequency range	2.4-2.5 GHz (ISM band).
Matching	Better than -10 dB over the operating frequency range.
Number of antenna elements	Set to 2 by the transmission system.
Maximum gain variation	10dB.
Antenna element weight	10g.
Antenna element pattern	Broad beam, as close as possible to hemispherical, minimizing the gain variation.
Antenna element polarization	Circular polarization to reduce cross polarization losses.
Antenna element size	40x40mm per antenna and 8000mm ³ .
Antenna positioning	Facing one of the apertures in the cage.

Table 1. Requirements for the antennas for the collision-robust drone.

These requirements are used for the work in Chapter 4 and 6.

1.3.2 Requirements for broadbeam antennas for satellite IoT terminals

The requirements for the antennas for the IoT terminals are less restrictive in terms of weight than the drones. The requirements are summarized in Table 2 and are used for the antennas in Chapter 6.

Parameter	Requirement
Matching impedance	50 Ohm.
Operating frequency range	Dual band: 1.55GHz and 1.65GHz
Matching	Better than -10 dB over the operating frequency range.
Antenna element pattern	Broad beam or isoflux, cover from -70° to 70°. HPBW broader than 160° are not practically useful
Antenna element polarization	RHCP

Table 2. Requirements for satellite antennas in the L band with dual-band and broad beam.

1.4 Organization of the thesis

- **Chapter 2. State of the art on broadbeam microstrip antennas.**

This Chapter compiles a collection of publications on broad beamwidth microstrip antennas and classifies them depending on the technique that they use to broaden the beamwidth.

- **Chapter 3. On the beamwidth of microstrip antennas and how to increase it.**

In this Chapter, we focus on the pattern of patch antennas, starting from the basics and providing detailed explanation on the physical principle of each of the main techniques to broaden the beamwidth of patch antennas.

- **Chapter 4. Compact and lightweight LP and CP broad-beam microstrip antennas: compromises and explanation through designs and examples.**

This Chapter focuses on the technique of using additional elements to increase the beamwidth of very lightweight and small microstrip antennas. These antennas are designed for their use on the collision-tolerant drone and serve as an example to illustrate how to establish compromises between beamwidth, bandwidth, size and weight using this technique.

- **Chapter 5. Analysis of the cage and system measurements of the antennas assembled on the drone**

This Chapter contains the analysis of the cage of the drone and the system measurements to validate the performance of the antennas designed in Chapter 4.

- **Chapter 6. Broadening the beamwidth of microstrip antennas using multiple elements for larger footprint antennas**

This Chapter tackles the analyses of the beam broadening using additional radiators for applications with less limitations on weight and size than drones, like antennas for ground terminals for satellite communications. Thanks to their bigger size, we can provide a more didactic explanation about this type of antenna.

- **Chapter 7. Conclusions.**

This Chapter gathers the final conclusions of the Thesis.

1.5 Research contributions

With this Thesis we contribute to the community with a self-contained overview on microstrip patch antennas with enhanced beamwidth. While the literature on bandwidth and gain enhancement for these antennas is mature and consistent, the contributions on broadbeam microstrip antennas are less abundant and more scattered. The techniques that enhance the beamwidth are essentially forcing the antennas against their natural trend to be more directive. Broadbeam microstrip antennas can be very attractive for many applications, as we have seen in Section 1.2, and a consistent and complete analysis of the different techniques can be very useful to the antenna community.

With Chapter 2, we provide a comprehensive compilation and overview on the different techniques to broaden the beamwidth of microstrip antennas that one can find in the literature. This gives an initial idea on the different types of techniques, how they can be grouped following their principle of operation, and to have an index on various designs for different frequencies, sizes, and beamwidths.

Having a good understanding about any antenna is crucial to do a successful design, and this is especially applicable to designs that are less canonical as is the case of broadbeam patches. With Chapter 3, we start from a detailed explanation about the pattern of patch antennas, focusing on the physical conditions that are related to their beamwidth. We also explain what are the fundamentals behind each of the main techniques used to increase the beamwidth. The contribution of this Chapter is to provide a didactic manual about the different techniques that provides the tools to decide what type of design is more suitable for each application, and to be able to understand what are the key points of each technique.

In Chapter 4, we explain how additional elements can be used to modify the pattern of a patch without increasing its profile. The use of this technique is very versatile and it has many degrees of freedom, depending on the design requirements. With this Chapter we expand the knowledge on this technique and provide novel designs with which we can explain how to establish compromises between beamwidth, bandwidth, size and weight, focusing on the latter.

Chapter 5 focuses on the assessment of the antennas proposed in Chapter 4 through system measurements that include the effect of the protective cage and the effect of the multipath channel. This Chapter gathers several analyses that can help to set benchmarks to assess the reliability of antennas in indoor environments and affected by any surrounding structure. Also, it is useful as it gives hints on how to integrate microstrip antennas in complex structures in general, and for a broad and stable coverage in particular.

To finalize, Chapter 6 focuses on the detailed explanation of the technique using additional radiators to enhance the beamwidth of patches. This approach is very versatile but it can also get very complex to understand and tune due to the several radiators interacting with each other and the many interdependent parameters. With this Chapter we provide a structured analysis that allows to get a deeper understanding of the main parameters to tune these designs.

1.6 Teaching and student projects

The contributions to teaching as assistant are the following:

- **Microwaves, the basics of wireless communications.** 2018-2020
- **Rayonnement et Antennes.** 2020-2022
- **Microwave laboratories.** 2018-2022
- **TP en technologies de l'information.** 2018-2022

During the Thesis, the author has assisted supervision of the following student projects:

- **Alberto José Moreno Montes:** Course 2018-2019. Master project on implantable antennas.
- **Jonas Müller:** Course 2018-2019. Semester project on implantable antennas.
- **Kerem Cekmeceli:** Course 2020-2021. Semester project on implantable antennas.
- **Gurjot Singh Bhatia:** Course 2020-2021. Master project on implantable antennas.
- **Robin Bonny:** Course 2021-2022. Semester project on broadbeam microstrip antennas

2 State of the art on broad-beam microstrip patch antennas

2.1 Brief summary on microstrip antennas

A microstrip patch antenna consists of a ground plane and a patch on both sides of a dielectric substrate, which provides mechanical support and robustness to the structure. The operation of patch antennas consists of a voltage difference between the ground plane and the patch, as one can see in Figure 12. Their radiation can be better understood by means of the cavity model, in which we can approximate the patch by a dielectric substrate enclosed by electric walls (patch and ground plane) and magnetic walls that emulate open circuits (the slots). In Figure 13, one can observe the equivalent magnetic current densities of the two radiating slots, and their corresponding E field distribution in the slots.

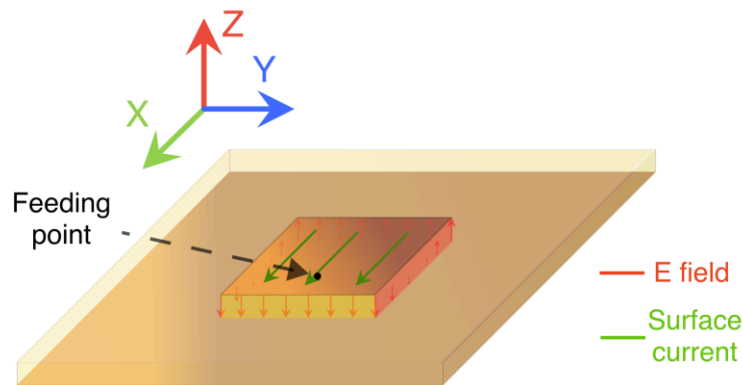


Figure 12. Operation of a microstrip patch antenna [1]

From the depiction of the fields in a patch shown in Figure 13, one can observe that the most important part of the fields lies in the slots below the patch and inside the substrate. Therefore, the electrical properties of the material used as a substrate, its size and thickness have a strong influence on the operation of the antenna. The two parameters to consider regarding the material are its permittivity and losses. The permittivity modifies the electrical size of the antenna, and the substrate losses limit the radiation efficiency. They are quantified by the relative permittivity, ϵ_r , and the loss angle $\tan\delta$, respectively. A higher permittivity substrate compresses the wavelength inside of the material, which allows to decrease the physical size of the antenna keeping the same resonant frequency. However, as more power density is contained in the substrate, the losses increase, degrading the radiation efficiency of the antenna [17] and the peak gain. The miniaturization of the antennas using higher permittivity substrates often permits to decrease the weight of the antenna, what is convenient for applications where this is critical, as for example antennas on drones. However, this size reduction leads to narrower bandwidth, accentuating the already limited bandwidth of patch antennas [17].

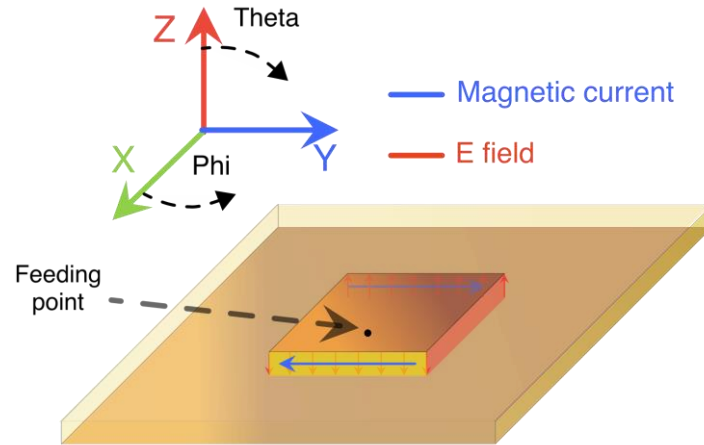


Figure 13. Cavity model of a rectangular microstrip, where magnetic current densities in the two radiating slots that can be used to compute the total radiated pattern by the patch [1].

There are several techniques to **increase the bandwidth** of patch antennas. One can use substrates with lower permittivity, thicker substrates, add stacked patches, add extra elements to the antenna, and/or use a feeding technique that does not rely on contact. Stacked patches, as shown in Figure 14, for example, improve the bandwidth if they are close, and the gain if they are more distant. There is a transition area where the pattern is irregular [18].

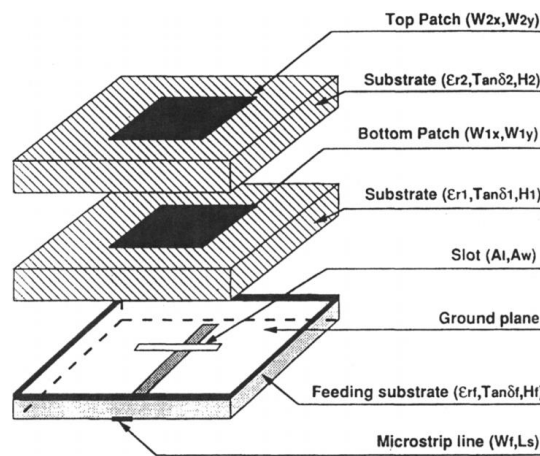


Figure 14. Stacked patches with aperture coupling for higher bandwidth of microstrip patches [19]

Apart from using high permittivity materials, other techniques can be used to miniaturize microstrip antennas such as cutting slots transversally to the direction of the current. It increases the electrical distance that the current has to travel from one side of the patch to another [20], which allows to shrink the length of the patch. An antenna that occupies more volume would have a wider bandwidth [18].

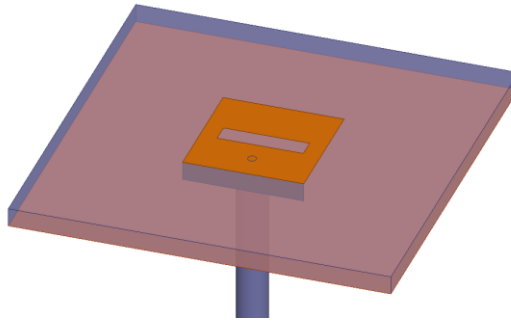


Figure 15. Miniaturized PIFA patch antenna using shorting ground and transversal slots.

Another way of miniaturizing microstrip antennas is by cutting them in half and short circuiting one of its edges to the ground plane. The resulting antenna is a Planar Inverted F Antenna (PIFA). Since the voltage at the middle of a resonant patch is zero, this modification does not change the operating frequency of the antenna, but its size is reduced by half [21]. Depending on the length of the short circuit, the size reduction can be further tuned. An example of a PIFA is depicted in the Figure 15.

The mechanisms in this Section are well-known, but reminding them is important to use them as a base to apply the knowledge to broaden the beamwidth of patch antennas. They are addressed more in details in Chapter 3, as these are also linked to the effective area, size and of course the gain.

2.2 The pattern of patch antennas and their beamwidth

Another characteristic of patch antennas is their directional pattern, which has a maximum in the direction perpendicular to the surface of the board (broadside direction). The field lines illustrating the radiation of the patch can be seen in Figure 12. The radiation occurs at two of these slots, while the other pair of non-radiating edges cancel out and do not contribute to the radiation pattern. The waves launched by the two radiating slots add up in phase in the direction perpendicular to the surface of the antenna (broadside). The radiation from the slots and the presence of the ground plane, that blocks the radiation to the lower hemisphere, leads to the typical directional pattern of a patch antenna, depicted in Figure 16. This directional pattern provides a peak directivity of around 7-9dBi. A higher peak directivity means inevitably that the power is more concentrated spatially and therefore the antenna covers a smaller section of space. In terms of antenna parameters this translates in a narrower beamwidth, which is often quantified using the angular aperture at half power of the pattern, or HPBW (Half Power Beamwidth). The HPBW of conventional patches is around 70-90°, which may suffice for some applications where the coverage at low elevation angles is not critical. However, there are other cases as satellite or mobile communications for which a broad coverage can be required.

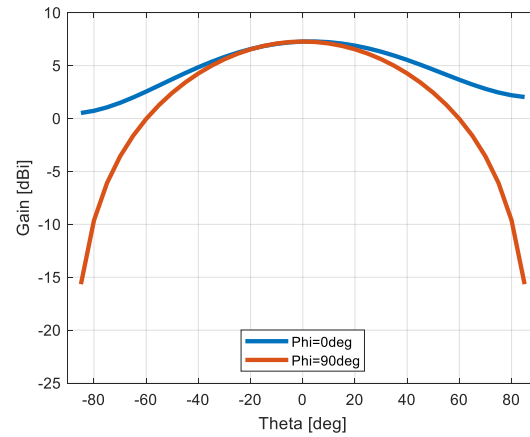


Figure 16. Radiation pattern of a patch antenna on an infinite ground plane. Results obtained for a canonical patch with an infinite ground plane boundary at 2.45GHz using Ansys Electronics Desktop [22].

It is important to distinguish two types of patterns, especially for satellite applications in LEO constellations: broadbeam or isoflux. The references [9], [23], [24] present isoflux patterns, and they state their utility to compensate for the path losses and provide a uniform coverage on the illuminated area on the ground. An isoflux pattern has a local minimum in the broadside direction, as the one we can observe in Figure 17. Strictly, isoflux patterns are not necessarily broad beam if they have a big null in the broadside direction, but the need of enhancing the gain at lower elevation angles is the same as for broadbeam designs. Therefore, the techniques used are often similar to achieve both types of patterns. For other applications like GPS localization, the antennas require also broad 3dB AR beamwidth (120°) to provide a reliable CP coverage in the illuminated earth area [25].

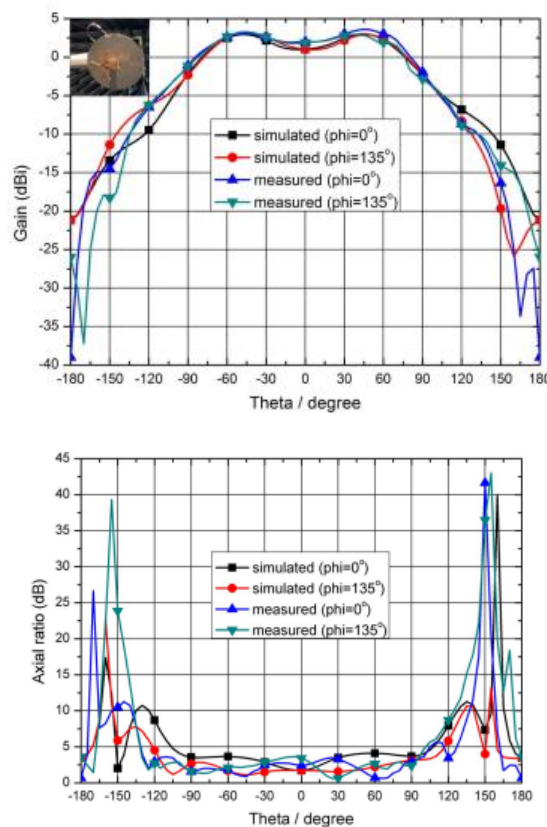


Figure 17. Conical or isoflux pattern (top) and AR (bottom) [23]

There are some parameters in a design of a patch antenna that play a role in its directivity and beamwidth. These are mainly the ground plane size, the thickness/permittivity of the substrate and the antenna size. Intuitively, when the **size of the ground plane** is decreased, there is a higher portion of the power that radiates in the lower hemisphere, potentially increasing the beamwidth of the patch but degrading the front to back ratio (F/B). The radiation pattern for finite grounds also depend on the specific size of the ground and of the spurious radiation from the edges of the board. The **thickness** of the substrate controls the effective height of the patch with respect to the ground. For thicker substrates, the fringing fields are less concentrated to the ground and therefore the beamwidth is increased [18]. When the permittivity is higher this allows to decrease the size of the antenna, which is linked to its effective aperture. The effective area of an antenna is proportional to its gain and its beamwidth as one can see in equation (1.1) [1]. A smaller antenna has a smaller effective area, lower directivity and in consequence broader beamwidth [1], [26], [27].

$$A_{em} = \frac{\lambda}{4\pi} D_0 \quad (1.1)$$

In [28] the authors show how the thickness of the substrate does not change significantly the gain or the beamwidth. Therefore, for large beamwidth improvements other techniques are required, that modify more substantially the geometry of a canonical patch antenna. These effects are explained more in detail in Chapter 3.

2.2.1 Modifications of the canonical geometry

In this subsection, we gather several techniques found in the literature which modify the canonical structure of a patch antenna to broaden its beamwidth. Some of the contributions address the broadening of the directivity pattern, while others focus on the AR beamwidth for CP antennas.

In [29], the authors provide an analysis of conformal arrays and the effect of the substrate bending on the individual elements of the array (patches). They show how the bending enlarges the beamwidth in one plane. Enhancing the beamwidth in the two main planes or in a revolution symmetry around the broadside direction complicates significantly the fabrication and integration of these antennas, and sacrifices their low profile.

A less aggressive modification, that keeps the antenna low profile is presented in [30]. The authors take as a reference a rectangular patch working at 1.575GHz and with a total size of $0.37\lambda_0 \times 0.37\lambda_0 \times 0.016\lambda_0$. To achieve circular polarization, they use a variation of the traditional method of trimming the edges of a rectangular patch. They subtract circular slots; which diameter increases progressively. The sense of the polarisation can be changed depending on the sense the radius of the slots grows. With this technique, the authors achieve a 3dB AR beamwidth of 170° while keeping a low profile, single feeding and with no extra cost or fabrication complexity compared to canonical patches. The antenna total HPBW remains around 100° . The work presented in [31] also focus on increasing the 3dB AR beamwidth and uses a similar principle. It consists of a CP antenna with added circular elements on the corners that allow to enhance the 3dB AR beamwidth up to 180° . Other techniques using defected or modified structures (patch or ground) are used in [24] and [32] where they enhance the 3dB AR beamwidth up to 180° .

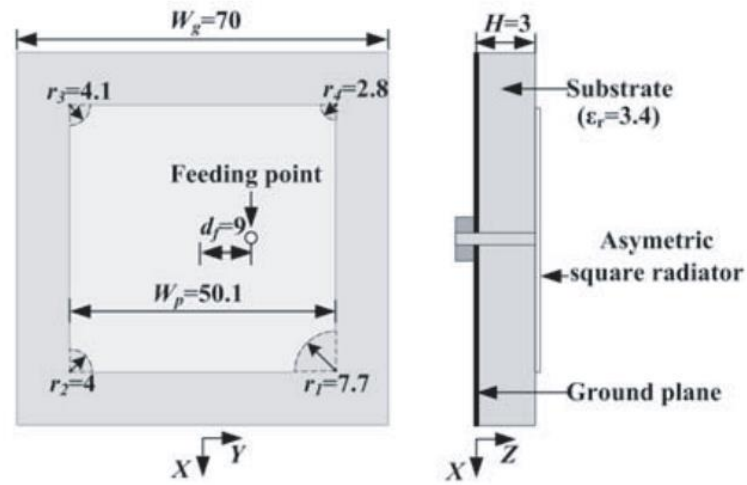


Figure 18. Geometry of the design proposed in [30] to achieve broad AR beamwidth

In [33], the proposed antenna uses pins connecting the ground and the patch to excite circular polarization and increase the beamwidth. The two central pins are used to generate the CP, while the external pins are used to enhance the 3dB AR beamwidth up to 160° , as one can observe in Figure 20.

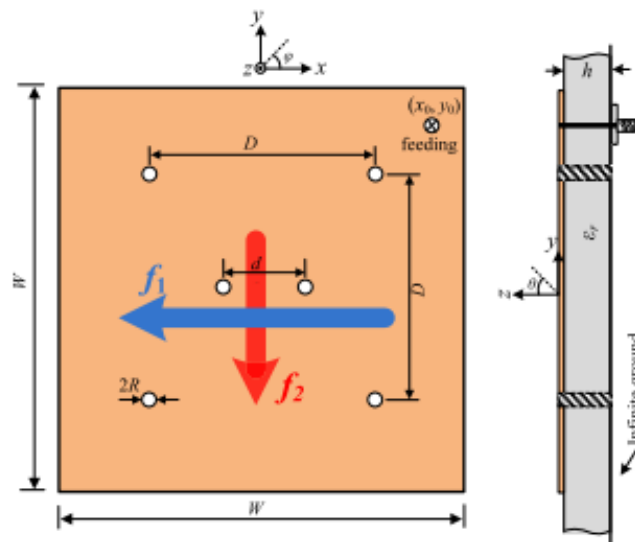


Figure 19. Geometry of the pin-loaded antenna presented in [33].

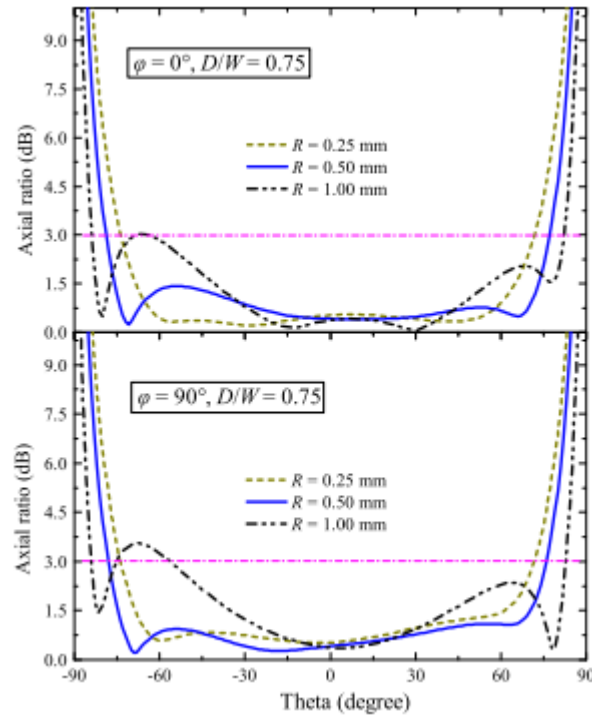


Figure 20. AR beamwidth for the two main cuts of the antenna presented in [33] and for various pin radii.

In [34], the authors use conductive posts around a patch to modify its fringing fields and therefore its pattern. This principle complicates the geometry of the antenna and the fabrication, but the achieved HPBW is of 120° , what is already an increase of around $30\text{--}40^\circ$ compared to a regular rectangular patch. The same idea has been used in [35], where they use vertical vias around a patch to increase the beamwidth. This design uses trimmed corners to achieve circular polarisation, as can be observed in Figure 21. The vias combined with a parasitic ring lead to a HPBW of 160° and 3dB AR beamwidth of 80° .

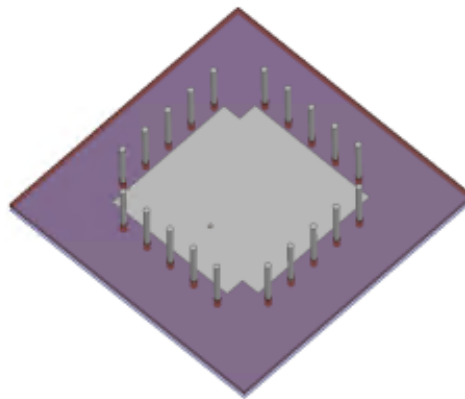


Figure 21. CP patch antenna with broadened beamwidth using conductive posts [35].

In [36] an antenna with a 3D ground structure is presented, which relies on the same principle of modifying the fringing fields of the patch. It allows to the fringing fields to get redirected to a ground with a different size and shape. The beamwidth achieved with this a procedure could be used for microstrip patch antennas that need to be assembled on a metallic structure if the latter is designed accordingly.

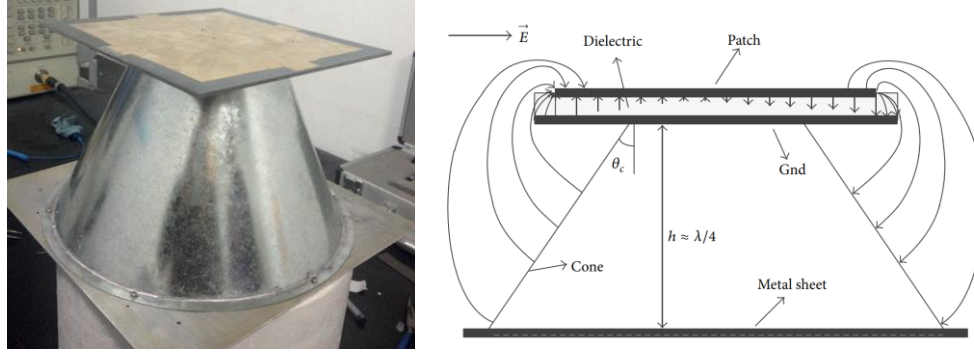


Figure 22. Using 3D ground structures to modify the shape of the fringing fields and extend the beamwidth [36].

The antenna presented in [37] works in two bands and can achieve 180° and 130° degrees in the high and low frequencies (2.03GHz and 1.45 GHz), respectively. It uses a longer substrate beyond the ground plane that takes advantage of the surface waves in the substrate to radiate in the end-fire directions.

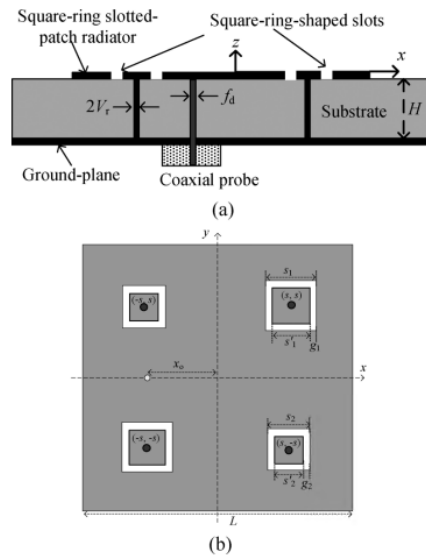


Figure 23. Geometry of the antenna presented in [38]. Side view (a) and top view (b).

Other technique used in the literature is trimming slots in the patches or in the ground to modify the fields. In [38] a CP square-slotted ring for GNSS applications is presented. It uses four squared rings slots, leading to a 3dB AR beamwidth of 140. In [39] the authors use a defected ground to get a 3dB AR beamwidth of 220°, and cut slots on the patch to achieve CP. The antenna presented in [40] uses several slots fed sequentially, as can be seen in Figure 24. The achieved 3dB AR beamwidth is of 110°.

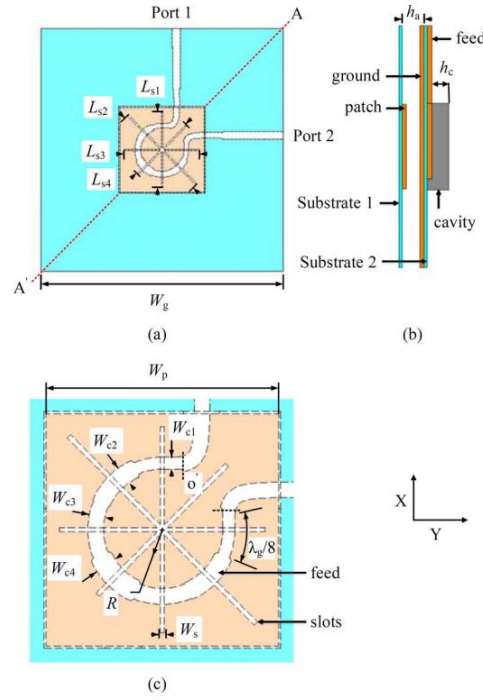


Figure 24. Geometry of the antenna presented in [40]

The antenna proposed in [41] consists of patch with a L-shaped slot. The authors focus on enhancing the AR beamwidth, increasing it to around 100° . The paper also provides a detailed explanation on the functioning and tuning of the slots.

In [42], the authors propose a fern fractal antenna that provides a HPBW of 100° and a very high 3dB AR beamwidth of 187° . The antenna geometry is shown in Figure 25, and as one can see the antenna is very compact as it works at 3.7GHz, even if its profile is relatively thicker.

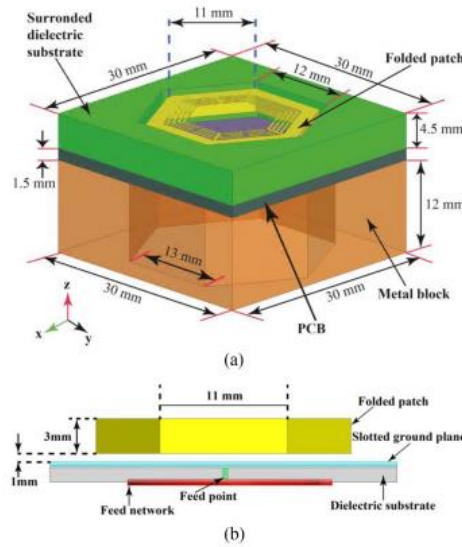


Figure 25. Geometry of the antenna presented in [42]. Isometric view (a) and side view (b).

The conclusion that we can draw from this subsection is that to achieve a significant beamwidth enhancement a big structural change that often requires to sacrifice some of the mechanical advantages of microstrip antennas is required. In the next subsection we explore other options that maintain a lower profile.

2.2.2 Extra radiators to improve end-fire gain and increase the beamwidth

2.2.2.1 Adding additional virtual radiators to patches / combination of different modes

From the modification of the geometry one can see that increasing the beamwidth of microstrip antennas while maintaining their low profile and other mechanical advantages is not an easy task. Therefore, in the literature many authors propose to launch other modes combined with the dominant mode of regular patches to broaden the beamwidth. These modes could be launched by adding physical elements that support them, modifying a given geometry to launch two or more modes, or a combination of both.

One of the techniques to improve the gain in low elevation angles is **using higher order modes**, with which one can achieve monopole-like radiation patterns. These patterns combined with the broadside radiation pattern of a regular patch can increase the beamwidth. Several contributions take advantage of this effect to achieve increased [43]–[45]. The use of different modes can be combined with different antenna geometries to achieve a specific pattern for each radiating element that in total generates a broader radiation pattern. For example, in [43], the authors explain the behavior and pattern of the first higher order modes of a microstrip ring antenna, where one can see how the TM_{21} mode, for example, generates a monopole-like or conical pattern.

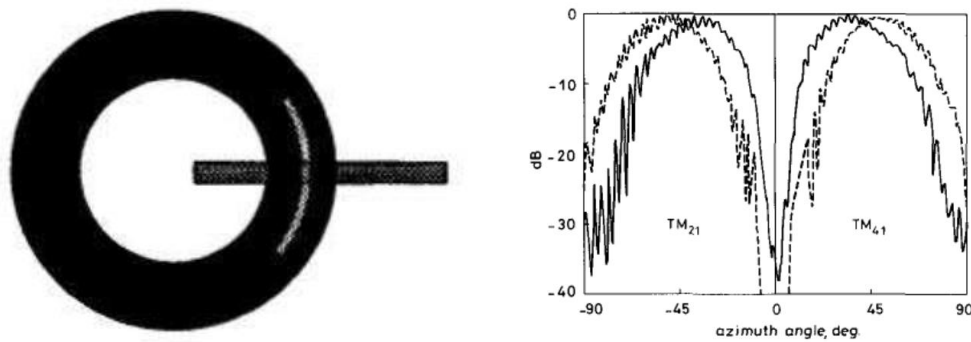


Figure 26. Microstrip ring and its pattern when exciting modes TM_{21} and TM_{41} [43]

The authors in [44] offer a detailed explanation on the manipulation of the modes in a circular patch to launch the desired modes. It is tuned to work at the TM_{31} mode, thus generating a monopole like pattern on a compact and low-profile antenna. The geometry and current distribution for the TM_{31} modes are shown in Figure 27.

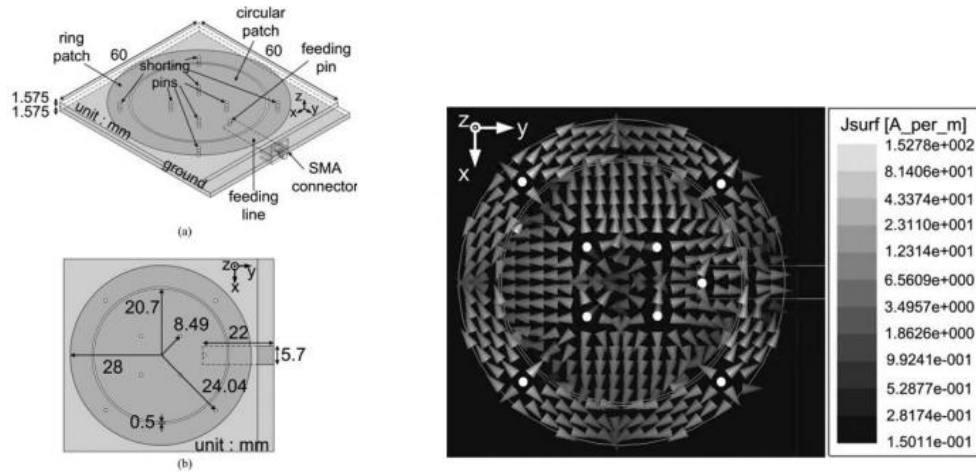


Figure 27. Geometry of the antenna (left) and its surface current distribution (right) [44]

To complete the review of monopole-like or conical radiation patterns, it is important to understand how to excite CP in higher order modes. In [46] we can find an excellent explanation on how to locate the feeding points for each of the higher order modes and also what phase delay to excite in each feeding point.

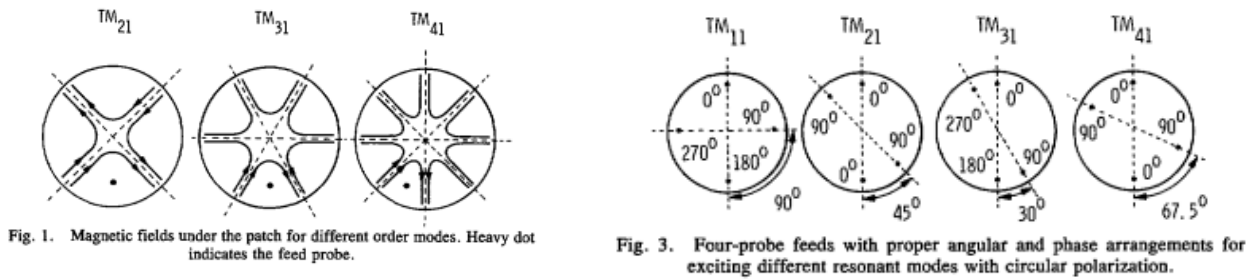


Fig. 1. Magnetic fields under the patch for different order modes. Heavy dot indicates the feed probe.

Fig. 3. Four-probe feeds with proper angular and phase arrangements for exciting different resonant modes with circular polarization.

Figure 28. Magnetic fields under the patch for different order modes (left) and the needed feeding to excite CP for higher order modes (right). The black dots are the feeding points [46].

These antennas using higher order modes can generate monopole-like or conical (isoflux) patterns that can be combined with the patches as is presented in the following sub-section.

2.2.2.2 Adding additional physical radiators to patches

In this part we present all the solutions that use physical additional elements to launch modes with radiation predominant in end fire direction. A CP antenna is presented in [47], which uses a parasitic ring, separated from the antenna substrate using an annular superstrate. The antenna achieves a HPBW of 170° and 3dB AR beamwidth of 165°. In [35] they use a similar idea, adding a parasitic ring on top of a driven ring, both separated by a layer of foam to achieve a AR beamwidth of 140° and a power beamwidth of 160° (see Figure 29).

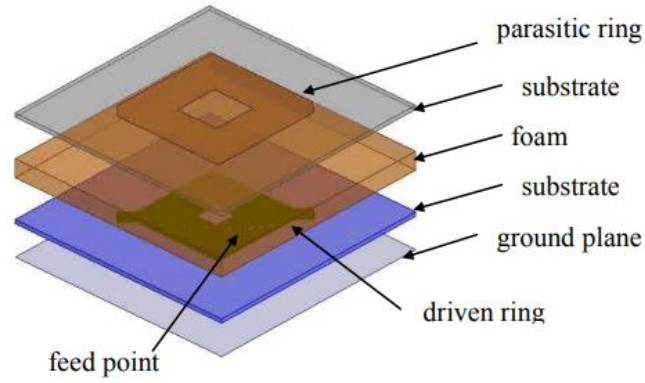


Figure 29. AR beamwidth of 140deg using hybrid perturbation method [35]

The antenna in [48] operates at 2.49GHz and uses a central disk and a parasitic ring to achieve a HPBW of 140°. The antenna uses two layers that are separated by spacers, losing the advantage of having low profile.

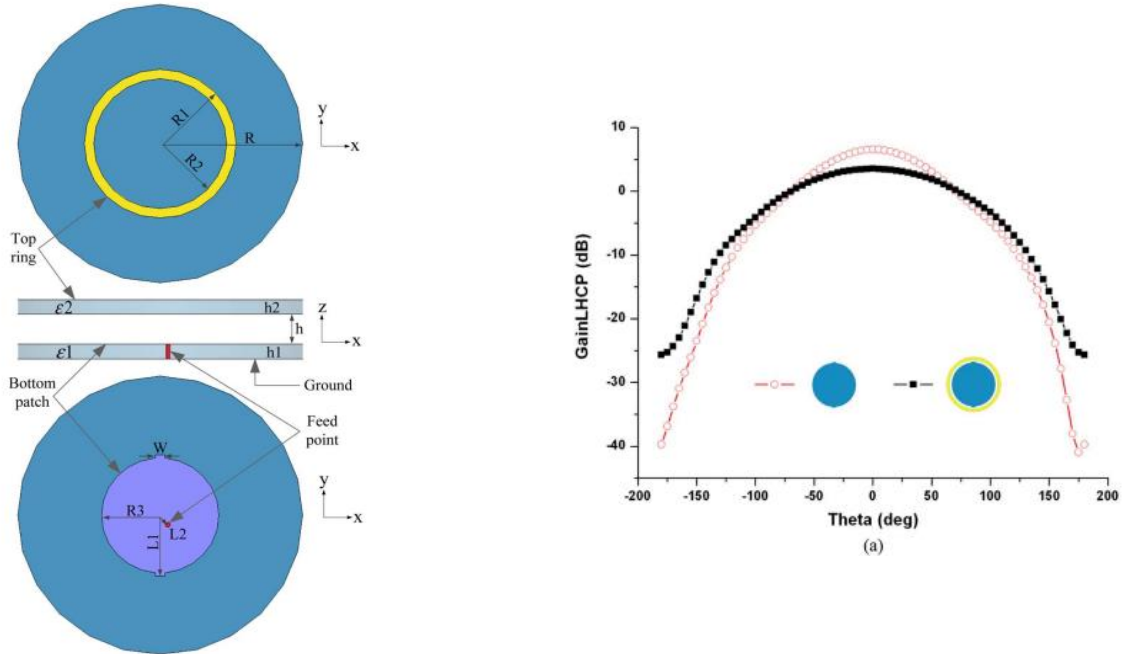


Figure 30. Geometry of the antenna (left) and its pattern with and without the parasitic ring (right) [48]

In [49], the authors tackle the beamwidth widening by decreasing the directivity of the antenna. They tune the equivalent magnetic currents of the several radiating parts of a modified patch to create a destructive interference in broadside that favours the radiation in lower elevation angles. The antenna works between 34.1 and 38.9 GHz with a bandwidth of 13.1%, and offers a HPBW between 100° and 125° in the entire band. The geometry and principle of operation of the modified patch can be seen in Figure 31. From the results in Figure 32 we can see how the design of the active antenna already helps to broaden the beamwidth and decrease the directivity, and the effect is enhanced with the parasitic elements.

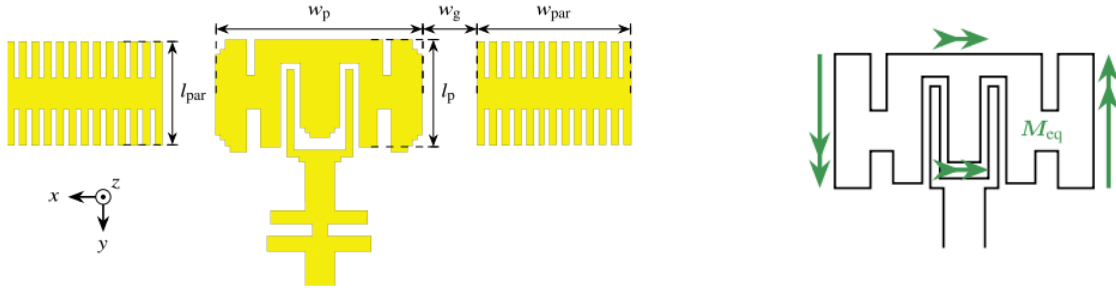


Figure 31. Geometry of the antenna proposed in [49], with a modified patch and two parasitic elements (left) and principle of operation of the modified patch using magnetic currents (right).

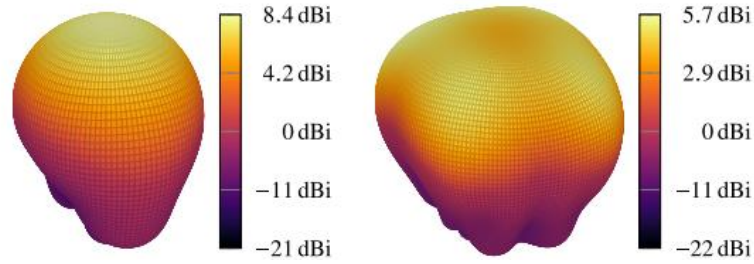


Figure 32. Effects of the parasitic patches and the extended ground plane on the antenna directivity (and beamwidth). Radiation pattern of the standalone antenna (left), pattern with patches (right). Both at 34.5GHz [49].

The antenna in [50] uses a Reactive impedance structure (RIS) that works as a reflector to provide a HPBW of 147° and the AR beamwidth of 180° . It uses parasitic elements following a circle around the main patch. The effect of the parasitic elements in the beamwidth is clear from Figure 33. This antenna is proposed as a good candidate for GNSS and CNSS applications.

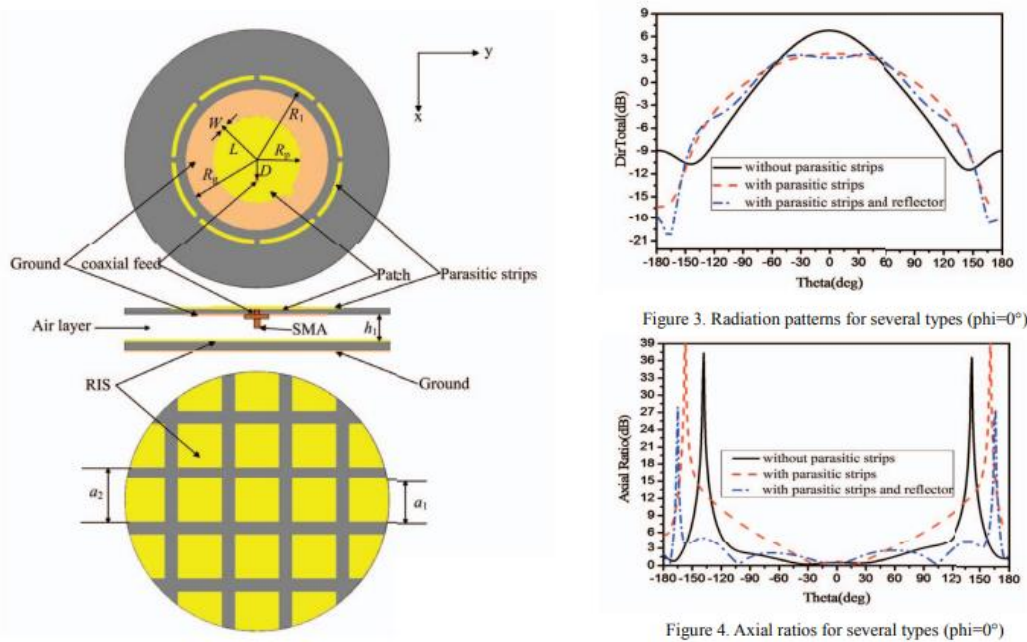


Figure 33. Geometry of the antenna (left) and radiation pattern and AR over angle (right) [50]

In [51], they use parasitic elements (a ring and six patches) to increase the beamwidth in two planes. The ring optimizes one plane and the patches the other, which allows to control the E and H plane patterns separately. The antenna is linearly polarised and the HPBW is of $150^\circ - 170^\circ$.

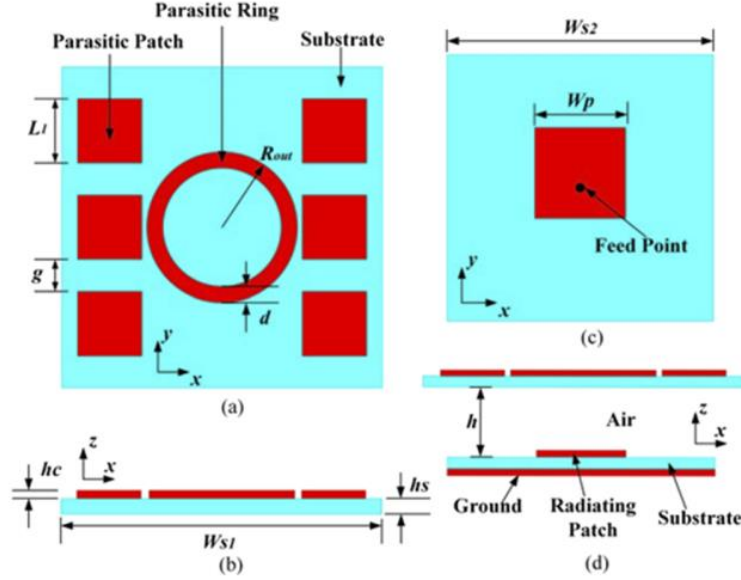


Figure 34. Geometry of the antenna presented in [51] that uses two types of parasitic elements to broaden the antenna beamwidth.

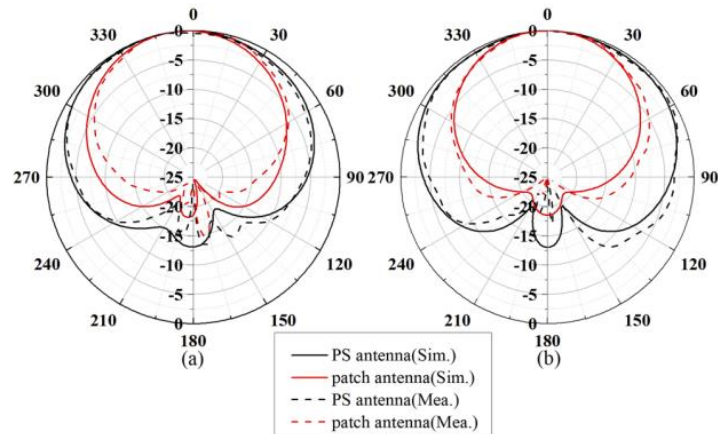


Figure 35. Comparison of patterns for a regular patch antenna and the proposed antenna in the E- plane (left) and the H-plane (right) [51]

The design in [52] uses a stacked patch design, with both patches arranged vertically as seen in Figure 36. Using an analogy with arrays, they tune the interference between the elements to increase the gain at low elevation angles by 1.2dB. This antenna is proposed for Controlled Reception Pattern Antenna (CRPA).

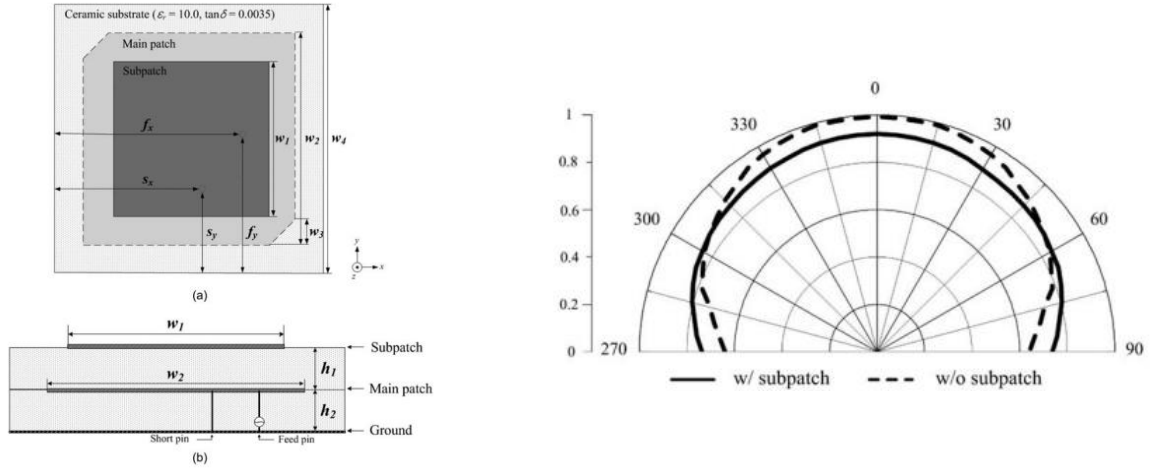


Figure 36. Geometry of the antenna presented in [52] (left), and its radiation pattern with and without the parasitic stacked patch (right).

In [53], an antenna composed by four radiators in circular arrangement enhanced AR beamwidth is presented. They use a Meandered-Line Ring Cavity (MLRC) to reduce the cross polarization in low elevation angles to achieve a wide 3dB AR beamwidth of 190° and a HPBW of 110° . A very similar antenna is presented in [54], which does not use the MLRC technique and therefore has a narrower 3dB AR beamwidth of 130° .

The antenna in [55] uses two pairs of asymmetric slots loading the main patch. The slots created between the smaller patches and the principal patch can be tuned to excite circular polarization and to widen the 3dB AR beamwidth up to 188° . The geometry of the antenna is shown in Figure 37.

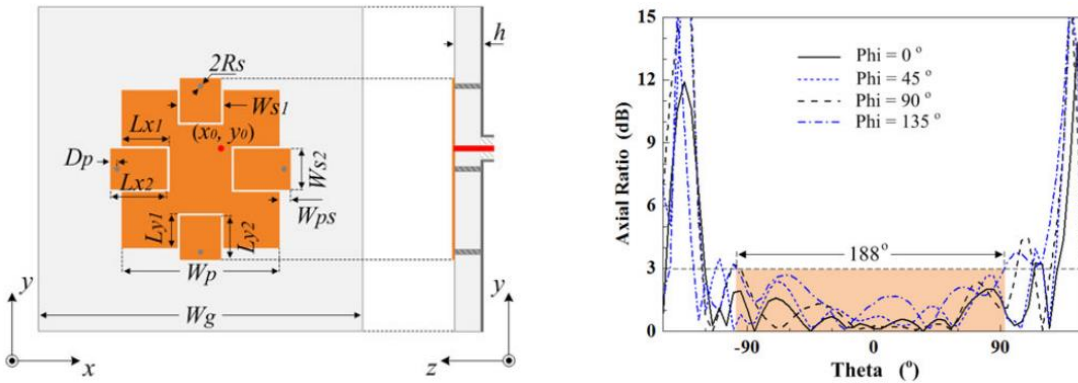


Figure 37. Geometry of the antenna in [55] (left) and its AR over angle (right).

An antenna consisting of two pairs of crossed dipoles and vertical parasitic elements is presented in [56]. The parasitic elements increase the vertical section and help to improve the gain in low elevation. The geometry is shown in Figure 38 and the current distribution on the crossed dipoles at $t=0$ and $t=T/4$ is shown in Figure 39. This antenna provides a 3dB AR beamwidth of 120° and HPBW of more than 110° .

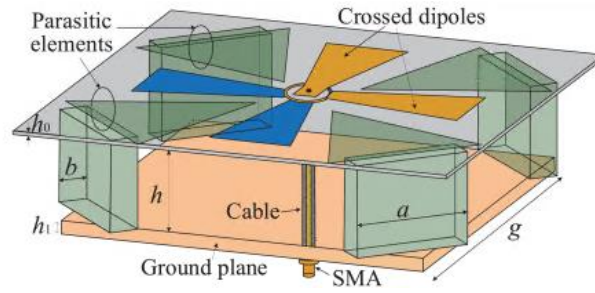


Figure 38. Geometry of the antenna consisting of crossed dipoles combined with vertical parasitic elements [56]

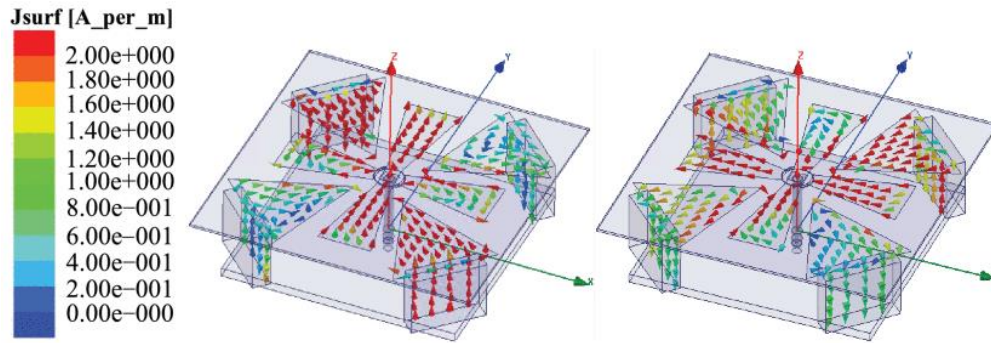


Figure 39. Surface current distribution at 1.0GHz and 1.65GHz [56]

We can observe that a common trend for all the designs using additional elements to increase the HPBW: increasing the profile of the antenna. They usually add air gaps or foam to separate the parasitics or even add vertical elements that help to increase the vertical component of the fields in low elevation angles and increase the beamwidth.

2.3 Comparative tables of contributions

We summarize the main aspects of the papers cited in this Chapter in the following Tables to have a more compact overview on the State of the Art on microstrip antennas with broad beamwidth.

Modified structure or fringing fields						
Paper	Technique	Frequency (GHz)	Size	Polarization	3dB AR beamwidth (°)	HPBW (°)
[30]	Patch with progressively trimmed corners	1.52 GHz-1.65GHz	$0.37 \lambda \times 0.37 \lambda \times 0.16 \lambda$	CP	156	100
[31]	Patch with added circles on the corners	1.6 GHz	$0.373 \lambda \times 0.373 \lambda \times 0.016 \lambda$	CP	180	N/A
[33]	Shorting pins to reduce electrical size and increase beamwidth	2.4 GHz	$1.6 \lambda \times 1.6 \lambda \times 0.02 \lambda$	CP	160	-
[32]	Defected patch	1.27GHz	$0.25 \lambda \times 0.25 \lambda \times 0.009 \lambda$	CP	170	110
[34]	Using posts to modify the fringing fields	4.7 GHz	$0.37 \lambda \times 0.37 \lambda \times 0.18 \lambda$	LP	N/A	120
[35]	Vias to increase vertical component of fields and parasitic ring. Hybrid perturbation for CP	2.06 GHz	$0.67 \lambda \times 0.67 \lambda \times 0.1 \lambda$	CP	80	160
[36]	3d ground structure, a big cone with small ground	400 MHz	$0.42 \lambda \times 0.42 \lambda \times 0.3 \lambda$	CP	89	152
[37]	Larger substrate that takes advantage of the surface waves and stacked patches	Dual band 1.45 GHz and 2 GHz	$0.67 \lambda \times 0.67 \lambda \times 0.02 \lambda$ @2GHz	CP	140	130-180
[38]	Symmetrically cut square-ring slots on the patch	1.6 GHz	$0.32 \lambda \times 0.32 \lambda \times 0.027 \lambda$	CP	140	N/A
[39]	Slotted hexagonal patch with defected ground structure	5 GHz	$0.5 \lambda \times 0.5 \lambda \times 0.026 \lambda$	CP	220	N/A
[40]	Four cross slots sequentially fed	3.7 GHz	$0.33 \lambda \times 0.33 \lambda \times 0.043 \lambda$	CP	110	60
[41]	Patch with L-shaped slot	2.3 GHz	$0.38 \lambda \times 0.38 \lambda \times 0.012 \lambda$	CP	95	93
[42]	Fern fractal patch exciting TM ₁₁ and TM ₂₁	3.65 GHz	$0.36 \lambda \times 0.36 \lambda \times 0.22 \lambda$	CP	187	100
[57]	Modified monopole	5.5 GHz	$0.56 \lambda \times 0.50 \lambda \times 0.029 \lambda$	CP	94	N/A

Table 3. Summary of the techniques that modify the structure of patches to broaden the beamwidth.

Additional elements/modes						
Paper	Technique	Frequency GHz	Size	Polarization	3dB AR Beamwidth (°)	HPBW (°)
[35]	Vias to increase vertical component of fields and parasitic ring. Hybrid perturbation for CP.	2.06 GHz	$0.67\lambda \times 0.67\lambda \times 0.1\lambda$	CP	80	160
[48]	Parasitic ring and spacing with air gap	2.49 GHz	$0.57\lambda \times 0.57\lambda \times 0.11\lambda$	CP	N/A	150
[49]	Modified patch and parasitic elements to create destructive interference in broadside	34-39 GHz	Patch $0.57\lambda \times 0.3\lambda$ @39GHz Parasitics $0.3\lambda \times 0.3\lambda$ @39GHz	LP	N/A	100-125
[50]	RIS reflector with an air-gap and a patch with parasitic elements	2.49 GHz	Diameter of 0.60λ and height of 0.12λ	CP	180	147
[47]	Parasitic ring distant from the patch using an annular superstrate	1.268 GHz	$0.34\lambda \times 0.37\lambda \times 0.18\lambda$	CP	165	169
[51]	Parasitic patches and ring. Each element enhances the beamwidth in one plane	5 GHz	$0.87\lambda \times 0.87\lambda \times 0.18\lambda$	LP	N/A	150 - 170
[53]	Use Meander-Line Ring Cavity to reduce the cross pol at low elevation angles and increase the ARBW. Radiation created from crossed slots	1.2 GHz	Diameter of 0.26λ and thickness of 0.064λ	CP	190	110
[54]	Crossed slots for CP excited from 4 patches	1.2 GHz	Diameter of 0.36λ and thickness of 0.064λ	CP	131	114
[52]	Uses additional elements combined vertically	1.575 GHz	$0.26\lambda \times 0.26\lambda \times 0.05\lambda$	CP	N/A	165
[56]	Crossed dipoles with parasitic elements	1 GHz - 2 GHz	$0.65\lambda \times 0.65\lambda \times 0.1\lambda$ @2GHz	CP	120	110
[55]	Grounded smaller patches in the same layer than the patch	1.575 GHz	$0.21\lambda \times 0.21\lambda \times 0.016\lambda$	CP	188	-

Table 4. Summary of the techniques that combine several radiators or modes to broaden the beamwidth.

One can observe how using additional elements (Table 4) the achievable beamwidth is broader than for the techniques that modify the antenna structure (Table 3). From these two tables we can understand the complexity of designing a broadbeam patch antenna with a small footprint, and especially with a very low profile. The Tables provide a good overview on designs prioritizing the broadening of the beamwidth over the size [51], and others that provide a good compromise between both [52].

3 On the beamwidth of microstrip antennas and how to increase it

In this Chapter, we address the physical limitations of the beamwidth for microstrip antennas, and provide a short overview on the techniques to enhance the beamwidth. We contribute with a set of guidelines and basic explanation of each technique, useful for antenna engineers to choose the most suitable to their application, and have a basic understanding of their operation to implement and adapt their design. These guidelines are based on various figures of merit: beamwidth (gain), bandwidth, size, thickness and fabrication complexity.

3.1 Physical explanation on the pattern of microstrip patches and their beamwidth

Microstrip antennas are a technology very mature in the antenna community, and therefore there is an extensive amount of contribution in the literature explaining in detail their functioning. It is known that microstrip antennas are bad end-fire radiators, excepting tapered-slot antennas [58]. In this section, we focus only on the aspects related to the antenna beamwidth, and more specifically in their limited gain and AR at low elevation angles. We start with a short reminder on the basics of microstrip antennas, focusing on their principle of operation as much as it is related to their pattern. We need this as a reference to develop the rest of the analyses in the Section.

3.1.1 Antenna operation and analysis of pattern shape and effective aperture

We start analysing a basic rectangular patch with two feeding points that can be used to excite circular polarization, as depicted in Figure 40. The orientation of this geometry with respect to the coordinate system is consistent through the entire thesis, and is used to define the pattern cuts and the polarization directions. If we stick to feeding the patch at only one of the two feeding points (along the X axis, for example), the antenna works in a linear polarization that follows the X axis. The radiating and non-radiating slots for that mode are highlighted in yellow and red, respectively. The corresponding surface currents are shown with green arrows, and the resulting fields between the patch and the ground with red arrows. If we excite the orthogonal mode, the operation is the same, but it happens along the Y axis.

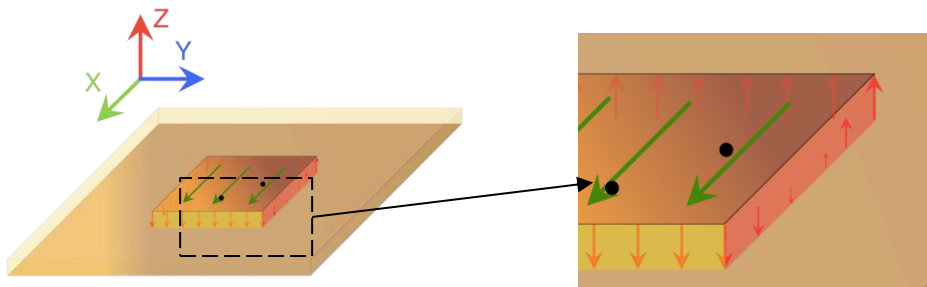


Figure 40. Functioning of a rectangular patch in one of its fundamental mode.

We simulate an antenna that follows the geometry in Figure 40 to see its radiation characteristics and use it as a reference through the Chapter. We use a substrate of 1mm of thickness and made of Rogers RT5880, with a relative permittivity of 2.2 and a loss angle of 0.0009. We excite both linear and circular polarization using two orthogonal lumped ports, feeding them with the same amplitude and a relative phase shift of 90°. The ground size is around two times the size of the patch.

The two main cuts of the antenna radiation pattern are shown in Figure 41, at $\Phi=90^\circ$ and $\Phi=0^\circ$ (YZ and XZ planes) and in linear and circular polarization. We can observe that the HPBW is narrower than 80° in both cases, and a bit narrower for the CP antenna. The latter is a consequence of the functioning of a CP antenna, which launches two modes. We can think of the CP antenna as two separate radiators launching a single mode combined on the same physical support. When there is more than one radiator, the total pattern is the contribution of all the “virtual” antennas (modes), and as their peak gain is in the same direction (broadside), the pattern is more directive. The relation of the peak gain (or beamwidth) with the number of modes launched by an antenna is explained extensively in [27]. We take these values as the reference for the HPBW of a regular microstrip patch.

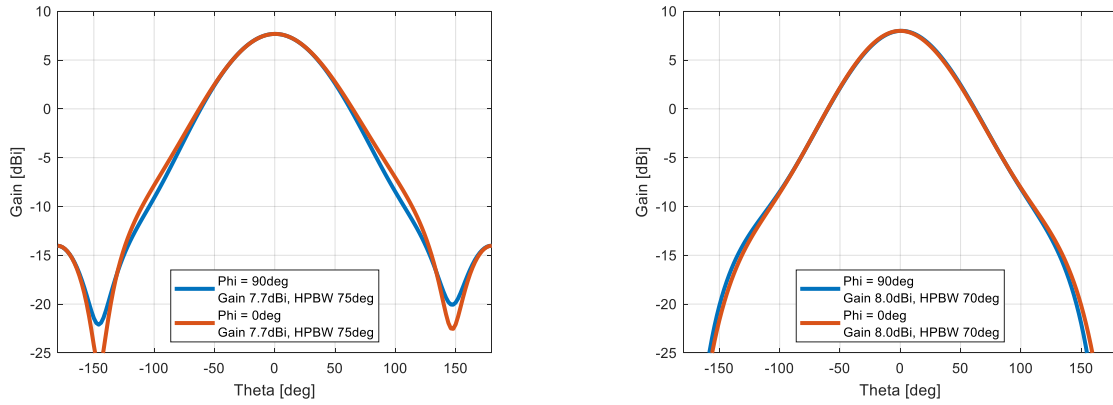


Figure 41. LP (left) and CP pattern (right) in copol, at 2.45GHz.

As we can see from Figure 41, the peak gain of the patches occurs in broadside ($\theta=0^\circ$), which is the direction at which the effective area is maximum, gain and effective area being directly proportional. Like the gain, the effective aperture also depends on the point of observation in the far field, depending thus on θ and ϕ in spherical coordinate. The relation between directivity and gain is described by equation (1). Following this reasoning, the effective aperture of patches is much smaller in endfire than in broadside and this directly contributes to the limited gain at low elevation angles. The equation (3.1), describes the relation between the directivity (gain) and the maximum aperture A_{em} [1].

$$A_{em}(\theta, \varphi) = \left(\frac{\lambda^2}{4\pi} \right) D_0(\theta, \varphi) \quad (3.1)$$

Another cause of the directional pattern of microstrip antennas is the presence of the ground plane. An infinite ground plane does not allow the radiation to propagate towards the lower hemisphere, which increases by a factor of 2 (+3dB) the gain in the upper hemisphere. Large ground planes are recommended to have a stable input impedance and to avoid radiation from the ground, but for practical reasons they are usually just a bit larger than the patch, which results in a less directive pattern.

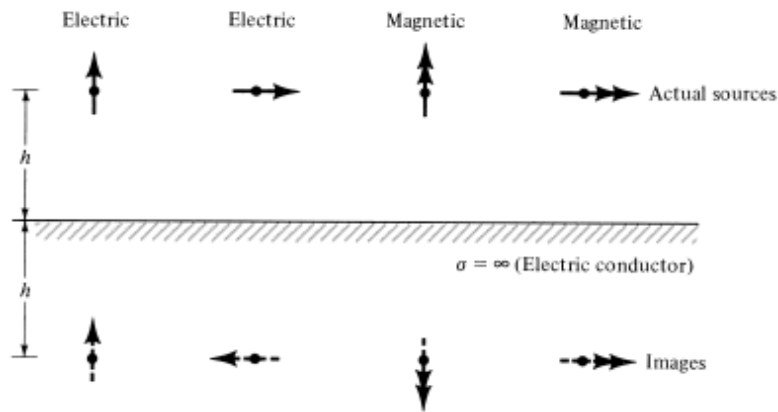


Figure 42. Effect of a perfect electric conductor on the fields [1].

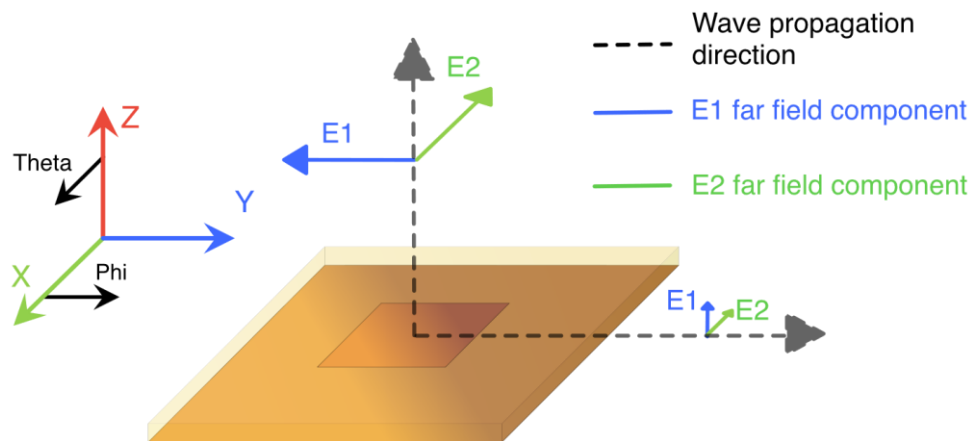


Figure 43. A patch antenna showing two arbitrary E field components in Far Field

To better understand the effect of the ground, let us remember the boundary conditions of a perfect electric conductive (PEC) plane, shown in Figure 42. A PEC plane forces the E fields immediately next to its surface to be 0. Let us apply this to a patch, depicted in Figure 43, radiating two arbitrary orthogonal E field components in the far field. If we focus on the component E2, which would be the E field in far field radiated by an antenna polarized along the X axis. In low elevation, and for reasonably large ground planes, the horizontal component (parallel to the ground) of the E field is diminished due to the boundary conditions of the ground plane, reducing in consequence the amplitude of the horizontal component of the E field in far field as well. This effect

is very clearly observed in patches on an infinite ground plane, as the horizontal E field component is zero, as seen in Figure 44. The copol in $\phi=90^\circ$ is parallel to the ground for the antenna with polarization along the X axis, and therefore the E-field at $\theta=90^\circ$ is zero. At $\phi=0^\circ$, the copolarization is perpendicular to the ground plane, which results in an increased gain in low elevation and better beamwidth. These are for the extreme case of an infinite ground plane, but even for smaller grounds, this is contributing to the poor gain in low elevation angles.

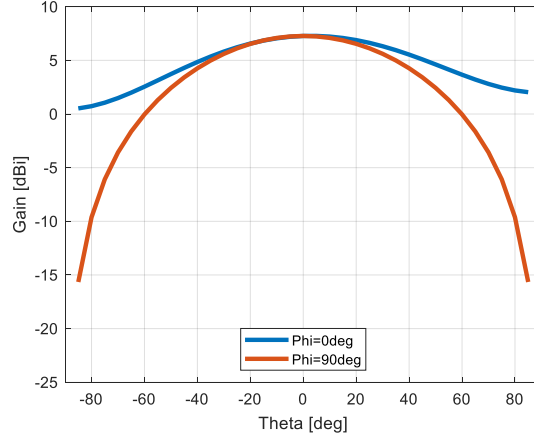


Figure 44. Radiation pattern, in copol, for the two main cuts of a patch on an infinite ground plane.

Grasping the concept of the maximum aperture in relation to the physical area of an antenna is visually intuitive. However, the definition of the maximum aperture given in equation (3.1) is a simplified version, as it does not include the contributions of the mismatch losses, polarization, and efficiency, which also affect the effective aperture. The mismatch losses and the efficiency are not relevant to the shape of the pattern, only to its absolute value. However, polarization is critical as it is needed even to define the type of pattern that characterizes an antenna.

Let us consider two antennas like the one in Figure 43, operating in linear polarization and pointing at each other. Even if the two are well aligned, if their polarizations are orthogonal, no signal is received in the receiving antenna. This clearly states the importance of the polarization in the pattern, and how the polarization should be included in the pattern to really illustrate the way the antenna distributes its radiation in space. Equation (3.2) includes the two parameters that can change the shape of the pattern: the polarization and the directivity. This applies to any kind of antenna, not only microstrip.

$$A_{eff}(\theta, \varphi) = \eta(1 - |\Gamma|^2) \left(\frac{\lambda^2}{4\pi} \right) D_0(\theta, \varphi) |\hat{e}_w(\theta, \varphi) \cdot \hat{e}_a|^2, \quad (3.2)$$

where η is the efficiency, $(1 - |\Gamma|^2)$ accounts for the mismatch losses, $\hat{e}_w(\theta, \varphi)$ is the polarization of a wave impinging on the antenna and \hat{e}_a the polarization of the antenna.

Using a copol – xpol patterns is sufficient to fully characterize the performance of a LP antenna. In the case of CP antennas, to obtain a more complete characterization, the axial ratio (AR) is used to quantify the purity of the polarization. The requirements on the purity of the CP are specified by a threshold, which is usually of 3dB but depends on the application. Therefore, to characterize spatially a CP antenna (of any kind), we need not only the directivity pattern but also the dependence of the axial ratio on the angle, usually quantified by the axial ratio beamwidth.

We use the same reference antenna as in Section 3.1.1 to show the CP patterns and AR aperture for the two main antenna cuts. The results are shown in Figure 45.

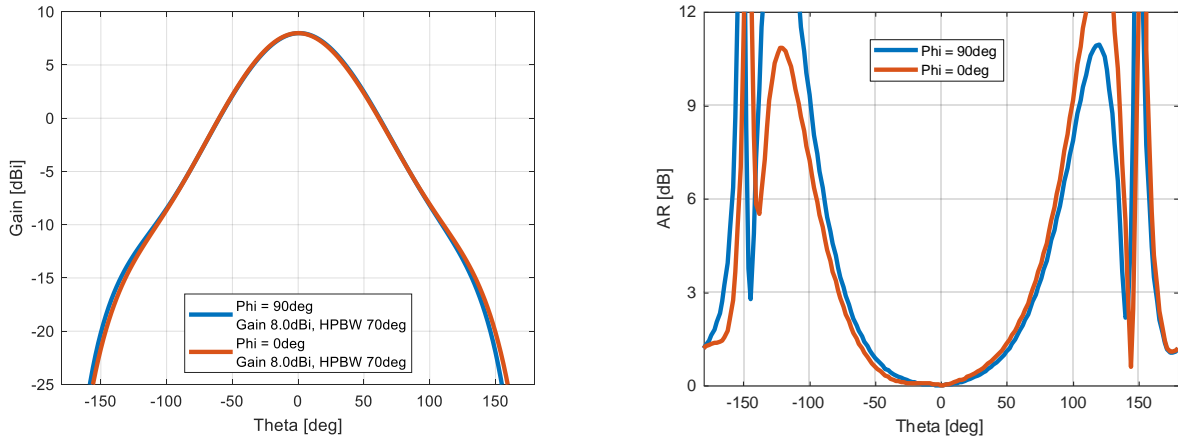


Figure 45. Radiation pattern in Copol (left) and its corresponding AR aperture (right) for the two main cuts of the antenna example used in Section 3.1.1

The AR beamwidth of microstrip antennas is limited in low elevation angles. To understand the cause of this effect, we can refer to Figure 43. For a CP antenna, the two perpendicular E field components in far field, E_1 and E_2 , are of the same magnitude and have a relative phase shift of 90° . If we observe these components in broadside, each orthogonal mode launched from the antenna can be easily tuned to fulfill these conditions. However, in low elevation angles, both components are smaller due to the limited effective aperture. The E_1 component will tend to increase for a reasonably large ground plane due to the boundary conditions of the metallic plane, while the E_2 , parallel to it, will be decreased. For smaller grounds, this effect will be less extreme but still will occur. This is a problem for a broad axial ratio beamwidth, as it is then difficult that the two polarizations in endfire are equal in amplitude for all observation angles.

The limit of the AR beamwidth is linked to the directivity beamwidth, but the different nature of these two parameters calls for different ways of enhancing the respective beamwidths. This is noticed in the literature, where usually the proposed techniques are very different to improve the directivity beamwidth or the AR beamwidth. In this thesis we focus mainly on the directivity beamwidth.

3.1.2 Fundamentals of the beamwidth of canonical microstrip antennas: summary

Below, a few conclusions on the beamwidth of microstrip antennas are summarized:

- **The antenna volumetry:** The ratio between the area of a microstrip antenna seen from broadside and endfire is in the range of 50. This is one of the reasons for the lower gain at low elevation angles.
- **The ground plane effect:**
 - The ground plane being a quasi-perfect electric conductor sets a limit to the amount of power the antenna can transfer to the horizontal component of the E field in far field in low elevation angles.
 - The size of the ground plane plays a key role in the beamwidth, increasing the peak gain in broadside.
- **Different types of beamwidths for CP antennas:** For CP antennas there are two beamwidths to be considered: the directivity beamwidth and the AR beamwidth. To improve the AR beamwidth in low elevation angle one should balance the two orthogonal components of the E field in far field, which are also affected by the boundary conditions of the ground. As this condition is not inherently linked to the directivity beamwidth, one could increase the AR beamwidth using techniques that do not increase the directivity beamwidth.

3.2 Analysis of the main parameters of a patch regarding its pattern

In this Section, we analyse the effect of the main parameters of a patch that affect their pattern. One of them is the ground plane size, which has a strong effect on the pattern (sidelobes, peak gain and back radiation). The thickness and permittivity of the substrate are also analysed as they are directly linked to the antenna effective aperture, and therefore to its gain and pattern.

For all the analyses in this Section, we use variations of a canonical rectangular antenna, to be coherent with Section 3.1. The results are specific realizations that help to quantify and illustrate the different effects of the parameters under analysis. We do not show the geometry in each of the individual analyses for the sake of brevity, but we specify the changes made to the geometry in each case.

3.2.1 Effect of the ground and substrate size

Following the premises explained in Section 3.1, the size of the ground plane is the cause of the directive pattern and the low gain in low elevation angles and thus its size is an important parameter regarding the pattern. For finite ground planes, the radiation from the edges of the PCB contributes in the total pattern, and it changes thus periodically with the ground size due to this effect depending on the interference with the radiation from the patch [59] [60].

In the results from Figure 46 we can observe that the back radiation is lower for the smaller ground plane which might seem counterintuitive. From the ripples on the radiation pattern for the largest ground plane at $\phi=90^\circ$, we can see how there is another radiation mechanism other than the patch that causes these effects. The cause

is the waves radiated from the board edges that come from the surface waves trapped in the substrate. These waves are diffracted by the ground and radiated by the edge, thus changing the shape of the pattern depending on the interference of the radiation from the edges and from the patch.

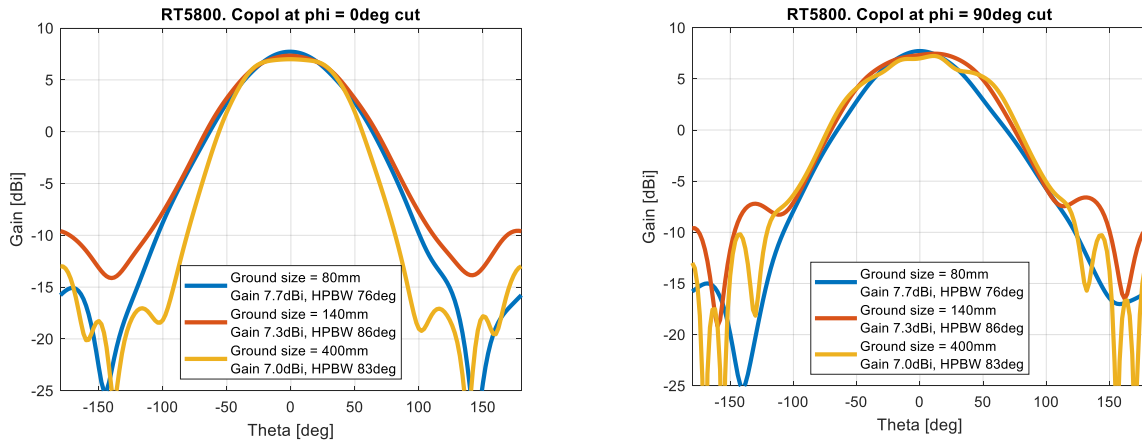


Figure 46. Radiation patterns for the two main cuts, $\phi=0^\circ$ (left) and $\phi=90^\circ$ (right) of a patch antenna.

The spurious radiation caused by the PCB edges occurs because of the surface waves in the substrate. Their decay is slower than for waves propagating in free space: inversely proportional to the distance, and not to the square of the distance as in free space. The surface waves are then not sufficiently attenuated when they reach the edges of the board. As their magnitude is non-negligible, the radiation from the edges interferes with the radiation of the patch, modifying the radiation pattern depending on the size of the board and the permittivity of the substrate. The latter also changes the propagation speed of the surface waves and therefore the phase shift between the radiation from the two radiating mechanisms: the patch and the edges of the board; therefore modifying their interference and shape of the total pattern [61]. Also, the low losses of the substrate (in the case of the results in Figure 47, the loss angle of 0.0009 for Rogers RT5880) are very low to sufficiently attenuate the surface waves.

Surface waves are usually an inconvenience for microstrip antennas, but if one wants to design a broadbeam antenna (standalone), they can be used to enhance the beamwidth, taking advantage from radiation on the edges of the substrate. The size of the ground plane allows to slightly change the shape of the pattern, but it is very often a parameter that is limited or set by the design requirements.

3.2.2 Effect of the substrate thickness

To increase the effective aperture of a patch seen from low elevation angles, one logical step is to increase the height of the substrate. The height of the patch, electrically, also depends on the substrate permittivity. We perform then the analysis using various substrate thicknesses from two commercial PCB materials with a low and high permittivity of 2.2 (RT5880), and 9.2 (TMM10), respectively.

First of all, changing the thickness of an antenna will have an important effect on the latter's bandwidth [62]. Therefore, even if it is not related to the beamwidth, it is important to get an overview of the compromise

bandwidth/beamwidth that we can make changing the substrate thickness. An increase of the height of a patch antenna leads to a broader bandwidth, and this is in line with the results obtained in Figure 48 and Figure 49. Changing the thickness moves slightly the resonant frequency, and this effect has been corrected for these simulations to perform a coherent comparison. The bandwidth is more limited as expected for higher permittivity materials, and the difference is less significant for thicker substrates.

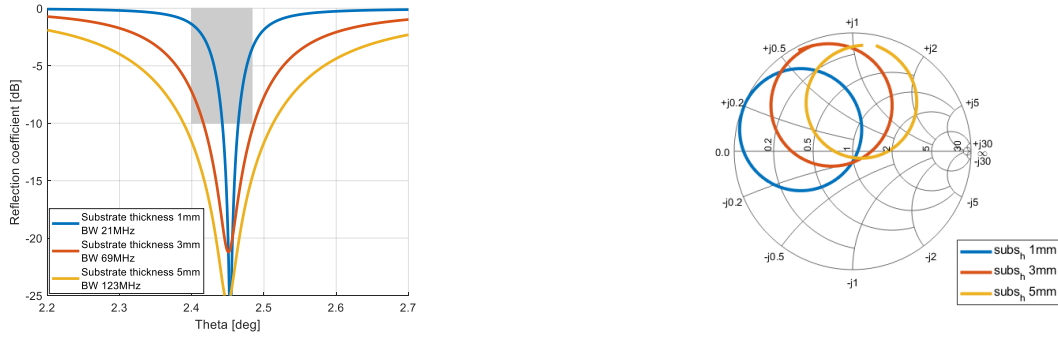


Figure 48. Reflection coefficient in magnitude (left) and Smith Chart (right) for various substrate heights. The substrate is Rogers RT5880.

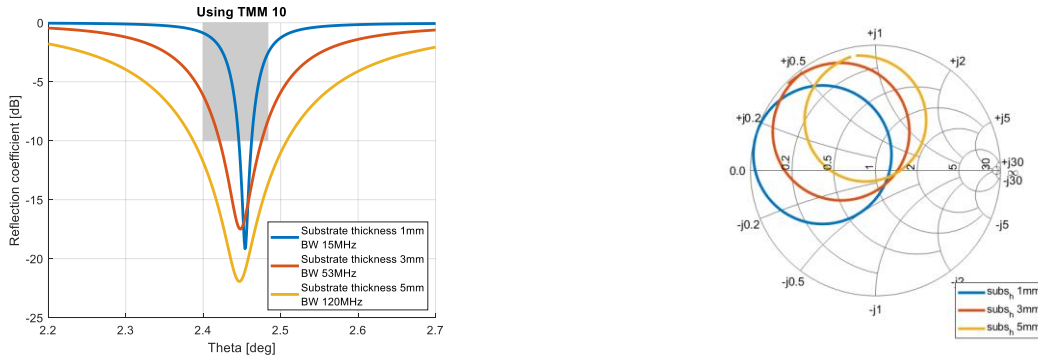


Figure 49. Reflection coefficient in magnitude (left) and Smith Chart (right) for various substrate heights. The substrate is Rogers TMM10.

Focusing on the radiation characteristics of the antenna, it is interesting to visualize the changes in the distribution of the fields for various thicknesses and the same antenna footprint. We can see this in Figure 50, where we compare the fields of a patch antenna on a substrate made of Rogers TMM10 for two different thicknesses of 1mm ($0.008\lambda_0$) and 5mm ($0.04\lambda_0$). We can observe that the shape of the fields is similar, with a couple of subtle differences: more power diffracted/reradiated at the edges of the thicker PCB, and a larger portion of the fields remains inside the substrate. The latter is a logical consequence of a thicker substrate, and has to be addressed carefully as it could increase the losses in a lossy substrate and diminish the antenna efficiency.

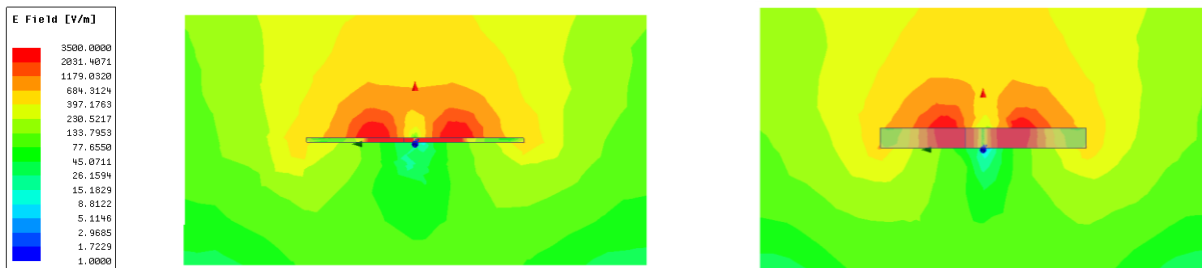


Figure 50. Side view of the E fields in complex magnitude in the two radiating slots of a patch with 1mm thickness (left) and 5 mm thickness (right). The substrate is Rogers TMM10, with a relative permittivity of 9.2. The fields are shown in the E-plane, to see the behaviour of the radiating edges of the patch.

We do not show the field distribution for the low permittivity substrate as it is too similar for the two thicknesses to be able to spot any difference. This is already a hint that the radiation pattern almost does not change when changing the thickness of a substrate with low permittivity, at least for thicknesses that are reasonable from the low-profile geometry and the commercially available panels. This can be confirmed from the results of the radiation patterns for the two substrates and various thicknesses are shown in Figure 51. We show only one of the two cuts, at $\Phi=90^\circ$, as the behavior in $\Phi=0^\circ$ is very similar. We can observe that the pattern is practically the same for the three variations of the thickness in both cases, but the change is almost negligible for the low permittivity substrate. The biggest change is between the two substrates, as higher permittivities lead to broader beamwidths, with better endfire gain and higher back radiation.

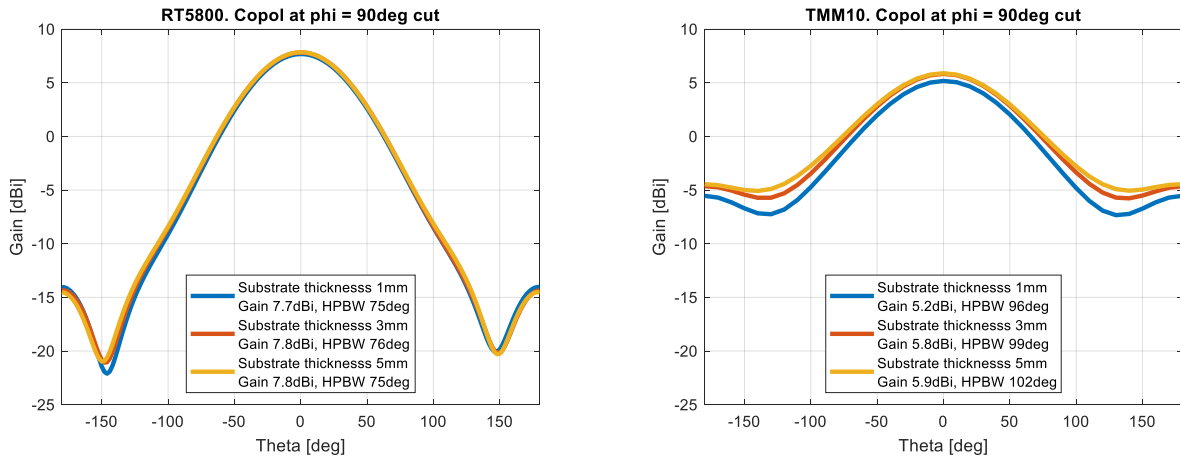


Figure 51. Radiation pattern of a patch antenna using RT5880 (left) and TMM10 (right) for various substrate thicknesses.

We can summarize the effect of the substrate thickness on a microstrip antenna as follows:

- Thicker substrates increase the bandwidth but can diminish the efficiency as a larger portion of the fields are confined inside the substrate.
- Thicker substrates can widen the beamwidth, but this effect is modest, and almost negligible for low permittivity substrates.
- Substrates with higher permittivities increase the beamwidth and the effect of the substrate height is then more sensitive. However, the back radiation is also increased, what further decreases the peak gain.

3.2.3 Effect of the substrate permittivity on the beamwidth. Relation to the effective area of an antenna

In this Section we analyse the influence of the substrate permittivity on the beamwidth, comparing results coming from several substrates. Following the results in Section 3.2.2, a high permittivity substrate increases the beamwidth. One of the reasons is the smaller antenna footprint thanks to the higher permittivity. The size reduction of the four patches in this Section are shown in Figure 52. For all the four cases we keep the same

substrate thickness of 1mm. These antennas have been adjusted to be resonant at the same frequency for a fair comparison, and their reflection coefficients are shown in Figure 53., from which we can see how the bandwidth is narrower for the higher permittivity substrates but the difference is not as large as for changing the physical thickness. An extended analysis of the effect of the permittivity on the radiation of patch antennas can be found in [63] and [64].

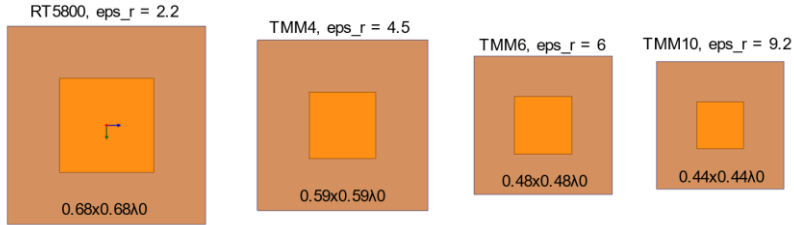


Figure 52. Top view of four patches using different substrates. The substrate thickness is of 1mm in all the cases. Antennas designed and simulated using Ansys Electronics Desktop [22].

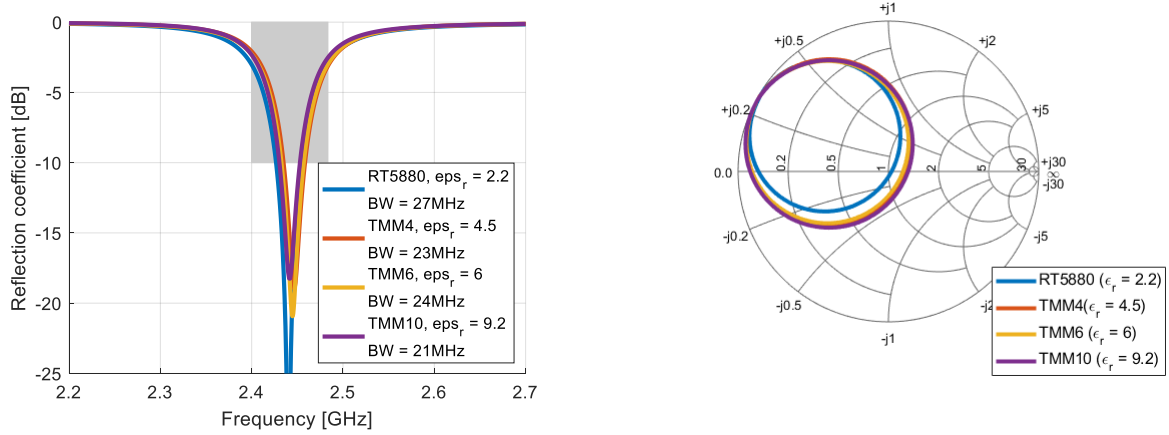


Figure 53. Reflection coefficient in magnitude (left) and Smith Chart (right) for various substrates with different permittivities.

The complex magnitude of the E field for the antennas with the highest and lowest permittivities, 2.2 and 9.2, are shown in Figure 54. We can observe how the radiation in the lower hemisphere and in the endfire direction are significantly higher for the higher permittivity patch. This is coherent with the variation of the radiation pattern with the permittivity, that is shown in Figure 55.

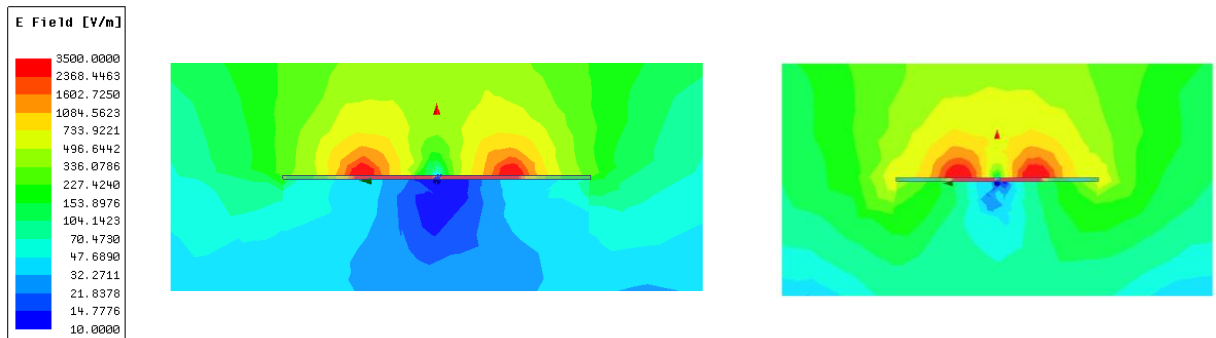


Figure 54. E-field complex magnitude for the lowest (left) and highest (right) permittivity substrates at $\phi=90^\circ$ cut, where we can see the behaviour of the radiating edges.

We can see how the beamwidth increases in direct relation to the increased permittivity. As a higher permittivity means a smaller antenna for the same resonant frequency, the physical area of the antenna is smaller and so is its effective aperture. This comes in line with the rule of thumb of higher effective aperture – higher gain, or smaller aperture – broader beamwidth [27]. For all the permittivity variations we have not changed the thickness, and then the ratio of the broadside to endfire effective aperture seen from far field is smaller for higher permittivity substrates. This also contributes to decrease the difference between the gain seen in broadside and endfire and thus leads to a smoother gain decay with angle and broader beamwidth.

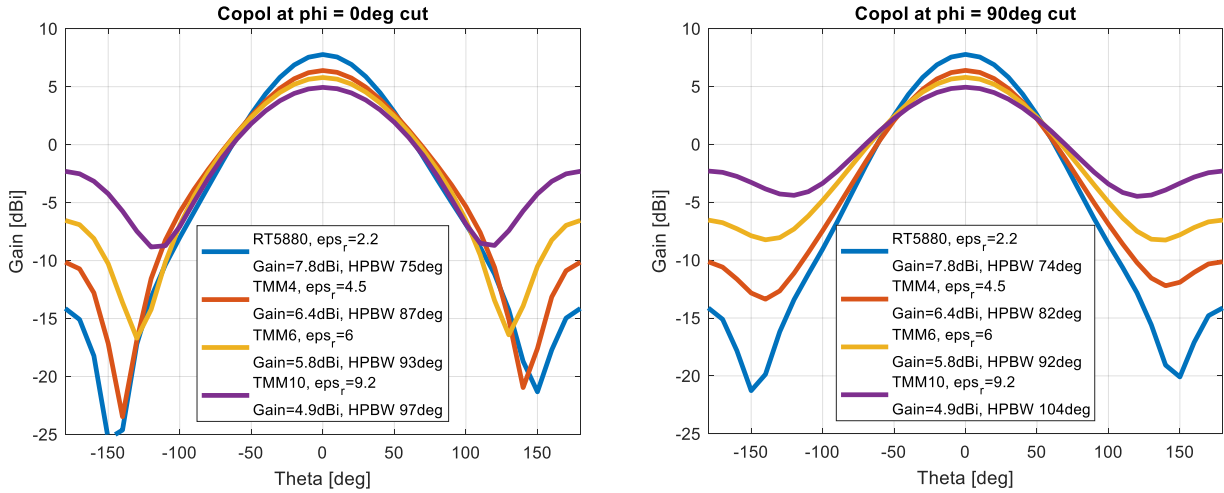


Figure 55. Radiation patterns in phi=0deg (left) and phi=90deg (right) cuts for the antennas in Figure 52.

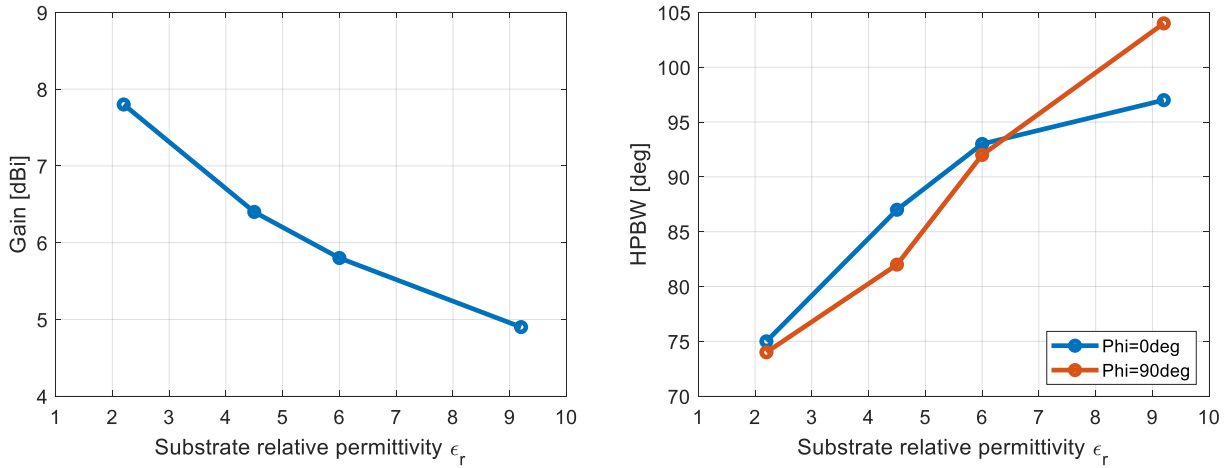


Figure 56. Variation of the gain (left) and HPBW (right) with the various substrate permittivities.

Another radiation mechanism that contributes to the higher endfire radiation using higher permittivity substrate is the effect of surface waves. These are reradiated from the edges of the board and contribute as well to a higher back radiation. This effect is more present in higher permittivity substrates as the permittivity difference between the air and the substrate is higher, trapping a higher ratio of the total power in form of surface waves. The effect of surface waves radiated by the edges of the board can be seen in Figure 54, where the diffraction on the edges is visible.

To summarize, the use of higher permittivity substrates:

- Decreases the antenna bandwidth.
- Reduces the antenna size.
- As the size is smaller, the achievable peak gain is also smaller, and the beamwidth larger.
- The smaller broadside to end-fire effective aperture ratio helps to obtain a broader beamwidth.
- The effect of reradiation and diffraction from the edges of the board is more significant, and it contributes to a broader beamwidth but also to a higher back radiation.

3.3 Techniques to increase the beamwidth changing the antenna geometry

We have seen how we can change the shape of the radiation pattern of a microstrip antenna by changing some of its main parameter, like the properties and geometry of its substrate and the size of its ground plane. In this section, we present some techniques that modify the canonical geometry of a microstrip antenna to increase its beamwidth.

3.3.1 Bending the substrate

One of the options to increase the beamwidth of a microstrip antenna is to bend its substrate. The principle is the same than for increasing the substrate thickness: to increase the antenna vertical section for a better effective aperture seen from endfire. To illustrate the effect of the bending, we use a design as an example, made with RT5880 substrate with a thickness of 1.57mm as an example. This design is shown in Figure 57. In Figure 58 we can see the top and side view of the design, from which we can already observe that the ratio between the effective aperture seen in broadside and endfire has changed from 35 to only 3.4. This means that the broadside gain should be lower and the endfire gain higher compared to the planar case. Bending the antenna also increases the impedance bandwidth by a factor 2. This is thanks to the antenna occupying more efficiently the space in the minimum sphere that can enclose it [65]. The antennas in this Section have been simulated using Ansys Electronics Desktop [22].



Figure 57. Regular patch (left) and bent patch (right). The bending radius is of 200 mm.

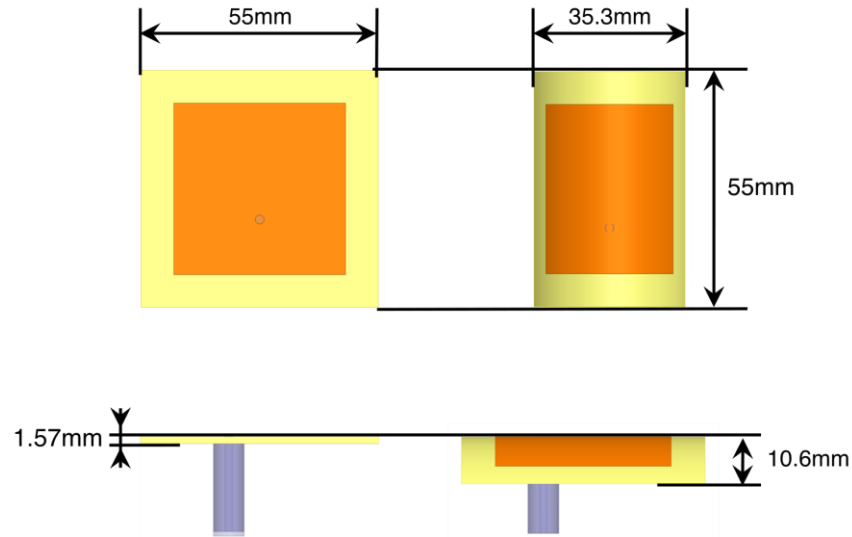


Figure 58. Effective aperture "equalization". Broadside to endfire ratio changes from 35 to 3.4.

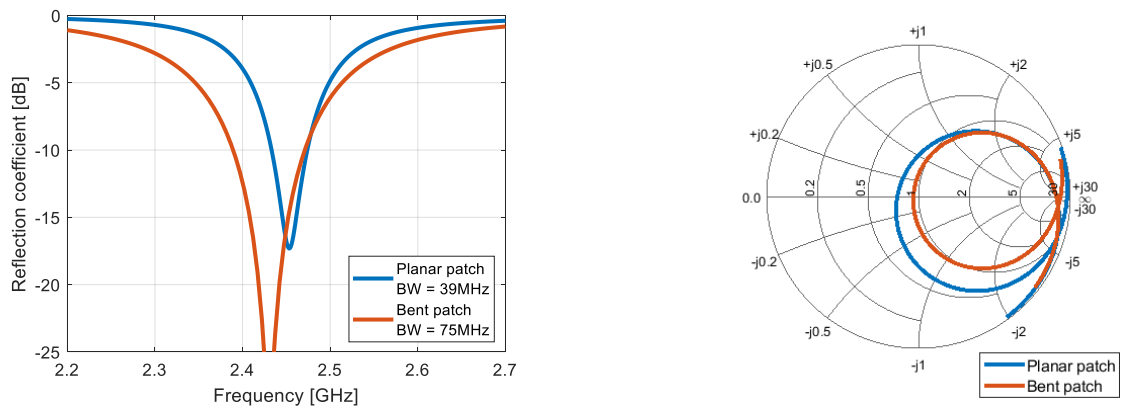


Figure 59. Reflection coefficient in magnitude (left) and Smith Chart (right) of a bent patch and a regular planar patch.

We can observe the effect of bending the substrate on the radiated fields in the Figure 60. The cut does not include the radiating edges, as the pattern is enhanced in the plane that does not include them. We can observe how the E field is much more uniformly distributed in the space for the bent antenna. This is coherent with the results of the radiation patterns in Figure 61. The HPBW is increased from 90° to 120° at $\phi=90^\circ$ thanks to the bending.

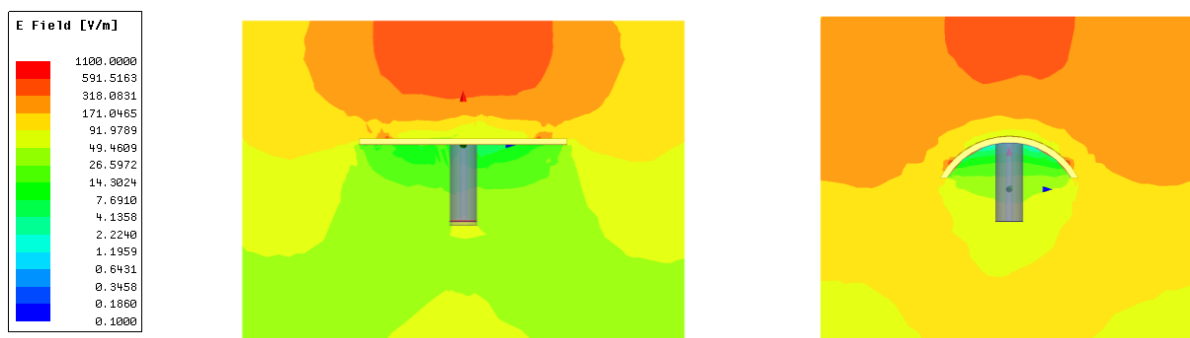


Figure 60. E field complex magnitude distribution for the planar (left) and bent patches (right). At 2.45GHz.

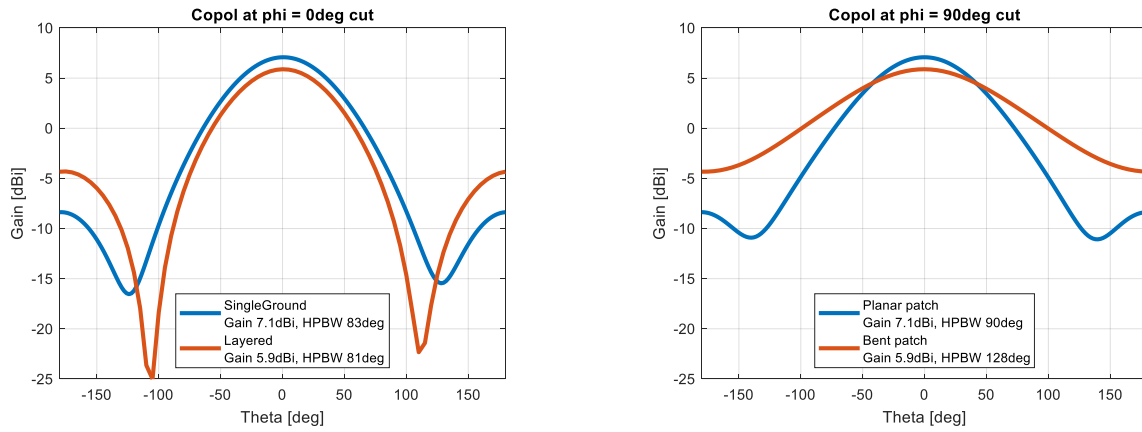


Figure 61. Radiation pattern $\phi=0$ (left) and $\phi=90$ (right)

Here we summarize the main aspects of this technique:

- We lose the advantage of having a low-profile geometry.
- More complicated to integrate the feeding structure underneath (depending on the bending radius).
- Only enhancing the pattern in one plane.
- The bending might not be a problem for some substrates that can be bent. Higher permittivity substrates like ceramics cannot be bent, however, and this should be considered in the design depending on the application and requirements.
- Significantly improved beamwidth in the plane of the bending, with a conceptually simple design.
- This geometry might be useful for certain applications, where a cylindrical bending and improvement in one plane could even be useful for the antenna integration.

3.3.2 Using 3D ground structures

Following the same idea of increasing the vertical section of the antenna, several works in the literature propose the use of 3D ground structures to enhance the beamwidth [66]–[68]. As the radiating mechanism of the patches rely on the fringing fields radiated by the radiating edges of the patch, a 3D ground changes the shape of the fringing fields to increase the vertical aperture of the antenna and improve its low elevation gain.

An example of a structures that uses 3D ground structures is proposed in [66] and is shown in Figure 62. With this antenna, the authors achieve a HPBW superior to 140° in the two main pattern cuts. It uses a parasitic patch to increase the bandwidth. As we can observe, this kind of antenna has a profile several times larger than a regular patch.

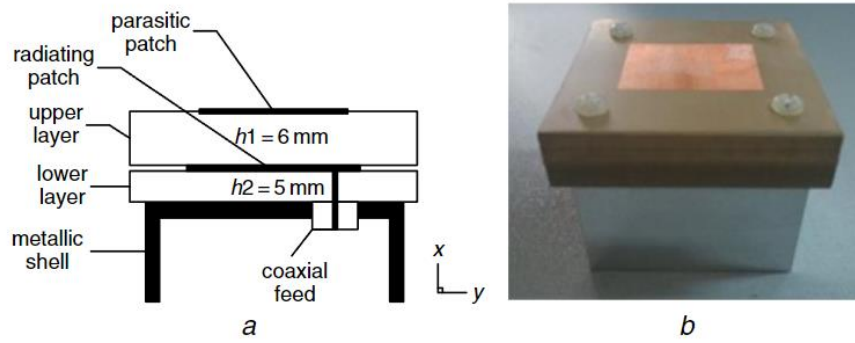


Figure 62. Example of a broadbeam microstrip antenna using 3D ground structure [66]

To illustrate the operation of this kind of antennas and their potential to increase the beamwidth, we propose a geometry using the same principle of redirecting the fringing fields to. It consists of a a multilayered ground structure that mimicks a 3D ground, and we compare it to the same antenna removing the extra layers of ground. Both structures are shown in Figure 63.

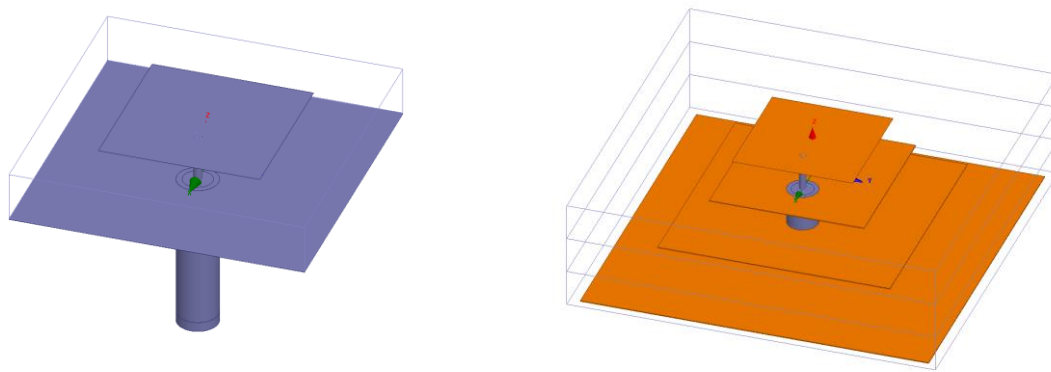


Figure 63. Proposed geometry mimicking a 3D ground structure using several substrate layers. Both use a substrate RO3210 with a permittivity of 10.2 and a loss angle of 0.003. Each substrate layer has a thickness of 5mm. Antenna designed and simulated using Ansys Electronics Desktop [22].

In Figure 64 we show the reflection coefficient of the two structures, where we can observe how the 3D ground antenna has improves significantly the bandwidth. This occurs because we are increasing the thickness of the ground and the fields are less confined in the cavity patch/ground, leading to a smaller Q factor.

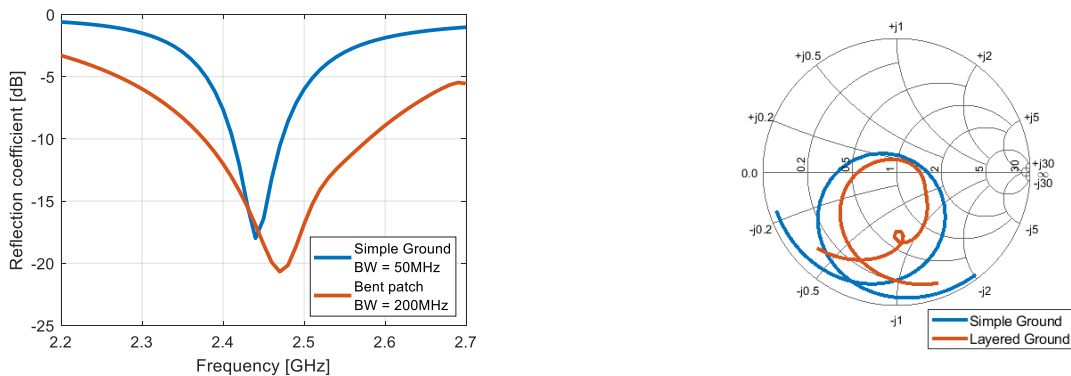


Figure 64. Refflection coefficient of the simple ground antenna and the layered ground antenna.

We can observe that the fields are more detached from the ground next to the antenna when we add the extra layers, and the back radiation is smaller. The closest ground to the patch is small enough to allow the fringing fields to get attached to the other layers of the ground, which leads to the more distributed E fields in the near field. The back radiation is reduced thanks to the larger ground plane surface compared to the patch. The lower back radiation is one advantage of this technique compared to the bent patch or to using high permittivity substrates. In Figure 66 we can observe the patterns, where at $\phi=90^\circ$, the plane orthogonal to the antenna polarization, the HPBW is increased from 113° to 144° .

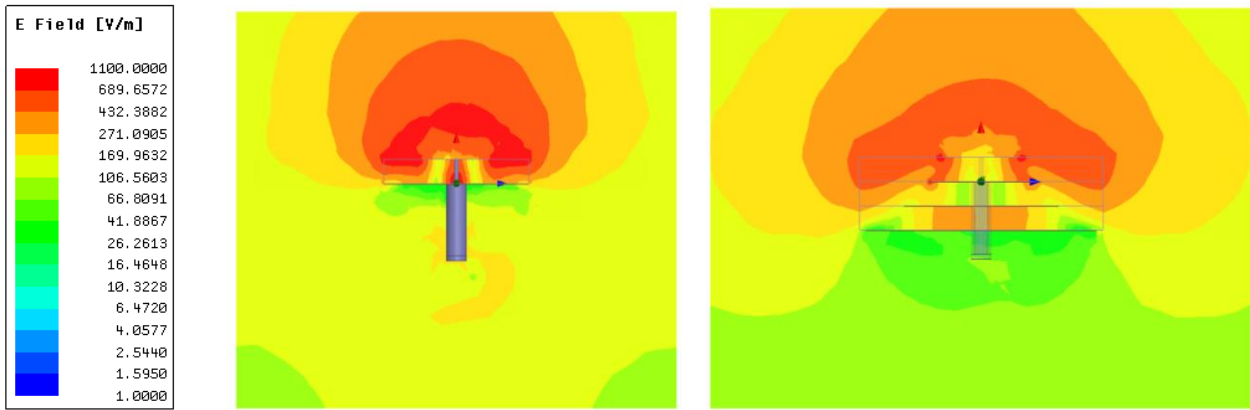


Figure 65. Complex magnitude distribution of the E field.

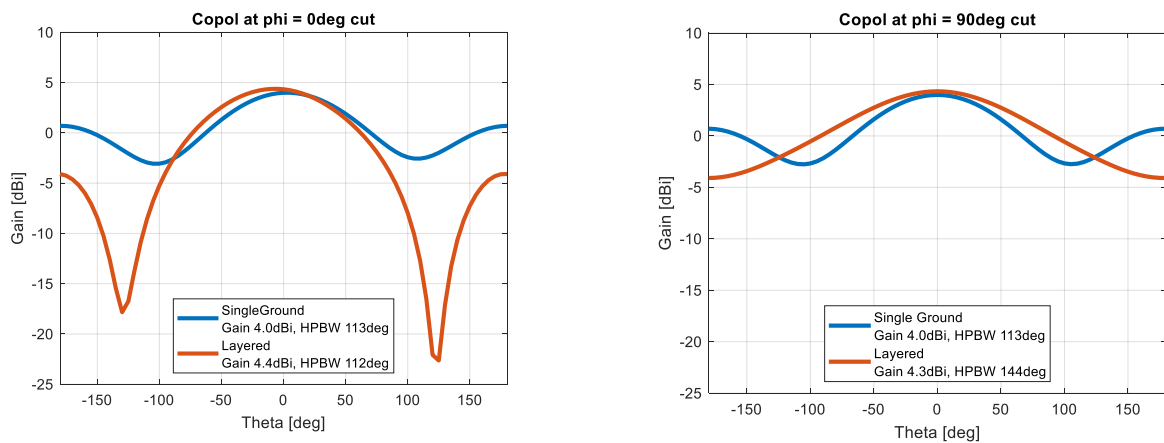


Figure 66. Radiation patterns for the cuts at $\phi=0^\circ$ (left) and $\phi= 90^\circ$ (right).

Here we gather some of the conclusions of using 3D ground structures to increase a microstrip antenna's beamwidth:

- The substrates should be thick.
- Very good beamwidth enhancement.
- It also enhances the bandwidth.
- The technique leads to structures significantly heavier and bigger than a regular patch and broadband patches using other techniques. It loses some of the main advantages of microstrip antennas: low profile and low weight.

- It offers a very good radiation performance as it enhances the beamwidth, bandwidth and low back radiation. For applications where volume or weight is not a problem, this approach is a suitable choice.

3.4 Using additional radiating elements for improved low elevation gain

The techniques we have seen in the previous Sections are based on modifying the geometry of the antennas without major conceptual changes in their functioning. Another approach to modify the behaviour of an antenna is to add more radiators that enable certain improvements with respect to the standalone antenna that are otherwise not possible or very difficult to achieve. For example, it is a common practice to use parasitic or stacked patches to extend the beamwidth of a single patch or to achieve multiband operation.

In [69], the authors summarize the idea of using additional elements along a patch to obtain the desired enhanced vertical section of the antenna. The idea is that the overall pattern consists not only on the patch contribution but also on these additional elements, as one can see in Figure 67. This antenna exhibits a HPBW of 236° in the E plane (where the vertical walls are located) and 130° in the H plane at 9GHz, clearly showing the potential of this approach. A similar approach is used in [56], where the authors combine a set of crossed dipoles instead of patches.

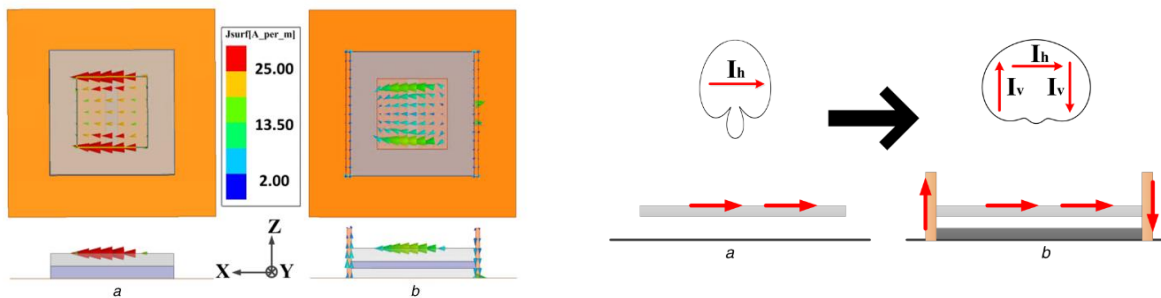


Figure 67. Additional radiating elements/current distributions for enhanced vertical effective aperture [69].

We can think of this type of antennas like an array with different individual elements and that are not necessarily all fed directly. The patterns of each elements should not have their maxima in the same direction like in usual arrays, as this will increase the peak gain and therefore decrease the beamwidth. The individual elements added to the patch open a huge set of possible geometries, and these should be chosen depending on the constraints of the application.

We summarize the approach of using additional elements to patch antennas as follows:

- These designs are also more complex and delicate. They require a careful design of the polarization of the patch and the individual elements together to achieve the desired polarization for the total pattern. This is especially critical for circularly polarized antennas.

- The type of the additional elements, position and feeding plays a key role on the total pattern. This adds a new layer of complexity to the design. If one chooses a compatible coplanar additional element, we can keep the advantage of the low profile and low weight. Also, depending on the extra element we can improve the bandwidth

This type of antennas offers a broad set of possibilities, depending on the various radiating elements, how they are excited, their individual patterns, etc. Depending on the individual element, one can adjust not only the bandwidth but also the beamwidth. This type of technique is very open, as it depends on the type of additional radiator that is used. We devote the Chapters 6 of this Thesis to beam broadening using this type of technique, more specifically using additional elements coplanar to the patch that help to keep the low-profile and minimize the weight of the antenna.

3.5 Summary and compromises on improving the beamwidth

Our objective with this Chapter is to provide a summary and an overview on the techniques to increase the beamwidth of microstrip patch antennas and the basic knowledge to decide which approach is better for a given design or application.

We can summarize the content very briefly as follows:

- **Causes to the narrow beamwidth:**
 - Presence of the ground plane.
 - Low effective area seen from endfire.
- **Solutions:**
 - Use a smaller ground and high permittivity substrates.
 - Decrease the ratio of effective area seen from broadside and endfire.
 - Increase the vertical section of the antenna by using 3D ground or bent structures.
 - Use additional radiators to complement the pattern of the patch.

The choice of the approach to increase the beamwidth will very much depend on the application and its specific requirements. There are then other parameters that are important to address to have a complete overview: size, weight and bandwidth, among others.

For our application, the most restrictive constraint for the antennas is the low weight and small size. Techniques like using high permittivity substrates (reduced antenna size) could be an acceptable option in terms of beamwidth, but would not offer a sufficient bandwidth. Using 3D ground structures increases too much the profile and the weight and is not an option for compact antennas. Our conclusion is that the most suitable approach amongst all presented in this Chapter are the antennas using into additional radiators as it seems the most versatile technique for low profile and light antennas. We devote the Chapter 4 of this thesis to the analysis,

design, and validation of antennas using coplanar additional elements for compact size, light weight and enhanced beamwidth.

	Mechanical	Bandwidth	Beamwidth	Remarks
Higher permittivity substrate	Excellent, very small	Reduced bandwidth	Good beamwidth enhancement	Back radiation More expensive substrates
Thicker substrate	Heavier	Improved	Slightly improved but only for high permittivity substrates	Too thick substrates can increase the surface waves and decrease the efficiency
Smaller ground	Better (smaller)	No changes	Depends on ground size and surface waves	Back radiation
Bending patch	Inconvenient to fabricate	Better than a regular patch	Very good but only in one plane	Back radiation
3D ground	Heavier but small footprint	Better than a regular patch	Very good beamwidth enhancement and low back radiation	Requires thicker antenna and smaller ground
Additional elements	Depends on the additional radiator. Bigger than regular patch	Can be improved depending on the additional element	Excellent beamwidth improvement	More complex, requires good knowledge of the patch and elements

Table 5. Comparative table of advantages and disadvantages of the different approaches.

4 Compact and lightweight LP and CP broad-beam microstrip antennas: compromises and explanation through designs and examples

In this Chapter, we describe the process of designing compact and lightweight, low-profile and broad-beam microstrip antennas using additional elements. We do it for various designs operating in linear and circular polarization. For these designs we apply the guidelines and knowledge from Chapter 3, and they serve to focus on the practical compromises to be made for a specific set of requirements. We present several designs of broad-beam microstrip antennas, focusing on the use of additional elements, both in linear and circular polarization. The use of additional elements allows to maintain a low-profile, while enhancing the beamwidth and the bandwidth.

We divide the Chapter in two groups of patches with additional elements: LP and CP antennas. We start with LP antennas as they are simpler to analyze and understand, and thus more useful to explain the techniques and designs proposed in the following sections. In Section 4.1, we summarize the requirements of our application, as the work in the rest of the Chapter is carried out in the search of an antenna that meets the requirements. In Section 4.2 we present an antenna that we use to understand the potential of using additional elements to increase the beamwidth. The antennas in Sections 4.3 and 4.4 are devoted to refining the same principle for smaller sizes and lower weight to meet the requirements of our application. We structure the work in these two Sections in three steps: explanation of the concept of operation, a specific design example to assess quantitatively the beamwidth widening, and the results from fabricated prototypes to validate the designs. The antennas in this Chapter have been designed and simulated using Ansys Electronics Desktop [22].

4.1 Summary on the antenna system constraints and requirements

The final design presented in this Chapter responds specifically to the needs of our application, which requirements we briefly remind here. The drone is protected by a carbon fibre cage, as shown in Figure 68, which makes it collision resilient and enables it to be used in many unprecedented scenarios. Carbon fibre is very light and robust, but also electrically conductive, and it is the material used by all the rods composing the protective structure. The cage perturbs significantly the antenna performance.



Figure 68. The signal radiated by the antennas inside of the cage is being attenuated by the cage, thus reducing the strength of the signal being emitted and therefore range of operation.

The proposed solution is to bring the antennas closer to the cage, to illuminate a smaller Section, which should reduce its effect on the antenna performance. This drone is flown indoors and in complex environments, where its position with respect to the controller is unknown and the multipath effect is significant. Therefore, we propose using a CP antenna, which should be more resilient to the polarization changes due to the different rods. Also, using CP on the antenna elements assures that the polarization mismatch with the linearly polarized antennas on the controller is maximum of 3dB.

The antenna requirements are summarized as follows:

1. **Matching:** better than -10 dB over the operating frequency range
2. **Operating frequency range:** 2.4-2.5 GHz (ISM band)
3. **Pattern:** As close as possible to hemispherical, as only 2 antenna elements can be used to cover the entire space. This is important to guarantee a **maximum gain variation around the drone of 10dB**.
4. **Polarization:** Circular polarization.
5. **Weight per antenna:** 10g max.
6. **Size:** Ideally 40x40mm max per antenna and a max volume of 8,000mm³ per antenna element.

Among these parameters, the weight is of critical importance, which inevitably sets a strong limitation in size as well. The antenna system should cover one hemisphere of the space with a gain variation in any direction around the drone smaller than 10dB, and ideally as small as possible. This implies using antennas with hemispherical patterns, which for microstrip antennas requires to broaden their typical beamwidth of approximately 70° in circular polarization. Ideally, as the cage changes the pattern of the antennas, it would be preferable to avoid its effect to have a better control on the pattern of our designs and also a better directivity. However, for our application it is not possible to remove this effect as the antennas must remain inside the cage and protected from potential collisions.

4.2 LP broadband patch using higher order modes

This antenna, reported more in detail in [70], condenses the concept of combining end-fire and broadside radiators. We investigated in the literature for end-fire radiators that could be integrated in the same layer as the patch, to maintain the low profile. In [46] the authors explain the behavior of higher order modes excited on circular patches. They address the topic from the theoretical point of view, providing insights on the distribution of the fields for the different modes, at which elevation the peak gain occurs, and all this for different substrates. In [43] they present also higher order modes excited in circular rings, providing a monopole-like radiation pattern with a null in the direction broadside to the antenna and higher gain at low elevation angles.

In this section we use this last idea, along the work in [44] to combine in the same plane a circular patch operating in its fundamental mode, TM₁₀, and an additional radiation element, a ring, that operates in a higher order mode. We take advantage of the naturally larger size of the ring to operate in a higher order mode to place it surrounding a central disk. We proposed the design in Figure 69, which explains this idea [70]. The geometry uses a circular disk and a ring, and a single coaxial feeding connected to the central disk. The ring is excited from the patch by a shorting strip. This short-circuiting strip has a very important effect on the antenna parameters, as it controls the contribution to the input impedance and the radiation for both elements. One can control the coupling between the two radiators by varying the width of the short connecting the two, or the separation between the patch and the ring. This antenna uses a Rogers Duroid 5880 substrate with 6.35mm of thickness, a relative permittivity of 2.2 and a loss tangent of 0.0009.

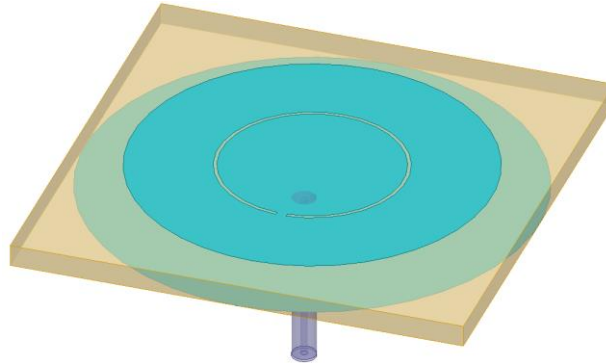


Figure 69. Geometry of the hybrid antenna using higher order modes. The antenna size is $140 \times 140 \times 6.35 \text{ mm}^3$ [70].

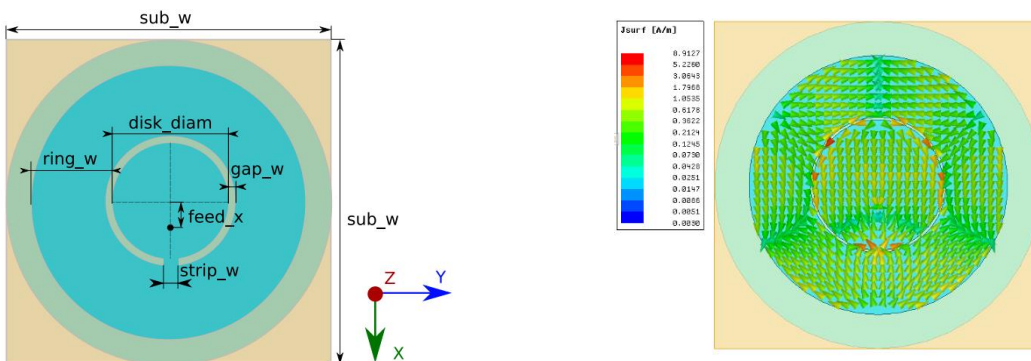


Figure 70. Geometry and main dimensions of the geometry proposed in Figure 69 (left), and the current distribution (right) [70].

Ring_w	Disk_diam	Gap_w	Feed_x	Strip_w	Sub_w
24.5mm	52mm	1 mm	7mm	3mm	130mm

Table 6. Dimensions of the geometry in Figure 70.

The distribution of the surface currents on the antenna are shown in Figure 70, in which one can distinguish the TM₁₀ mode excited in the central circular disk, and the TM₃₁ mode excited in the ring. The patterns of the two separate elements, the patch and the ring, operating at their respective modes, are shown in Figure 71. The radiation of the disk follows a typical broadside radiation from a patch, while the ring operating in the TM₃₁ mode has a null in broadside and a peak around 55°. The combination of these two patterns, with complementary radiation patterns, leads to an enhancement of the beamwidth in the optimized cut of up to 160°, as one can observe in Figure 72. In Figure 73, we show the co-pol and cross-pol patterns. In the optimized plane we can observe that the cross polar discrimination (XPD) is not very large at some angles (around 45°), because of the arrangement of the currents in the ring.

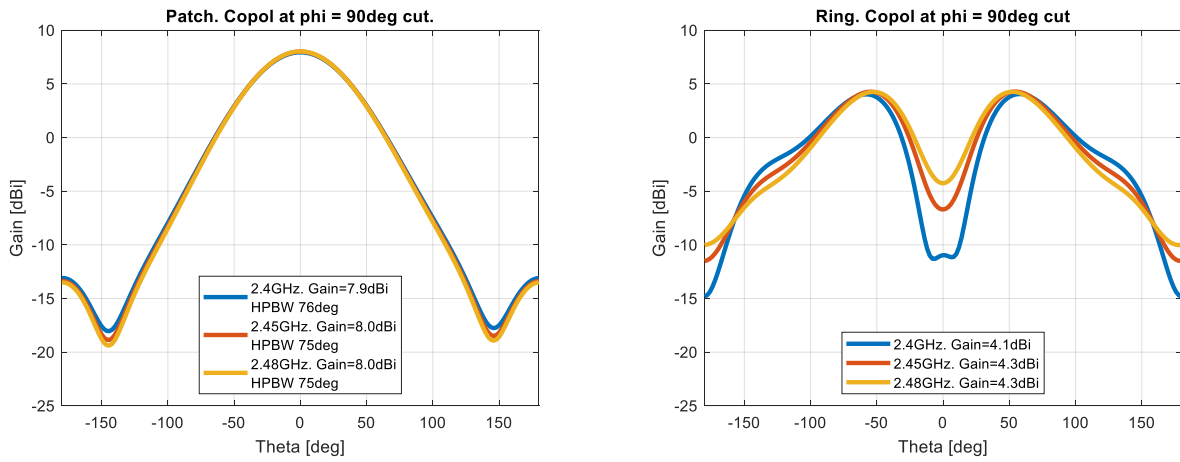


Figure 71. In this figure we show the $\Phi = 90^\circ$ pattern cuts (in copol) of the disk (left) and the ring (right). These two patterns complement each other to broaden the beamwidth.

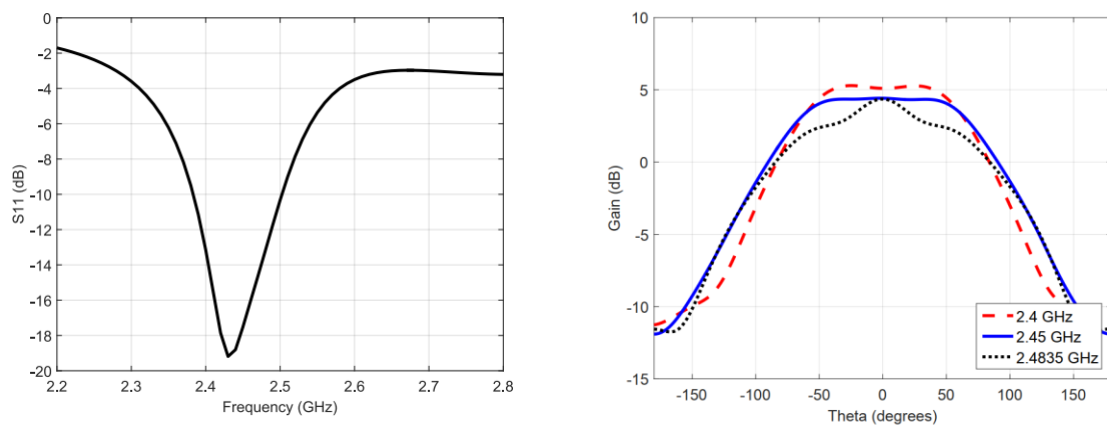
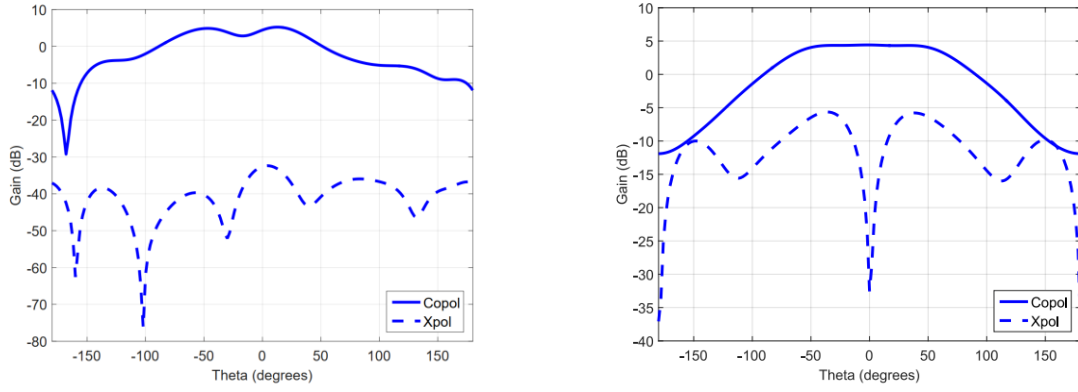
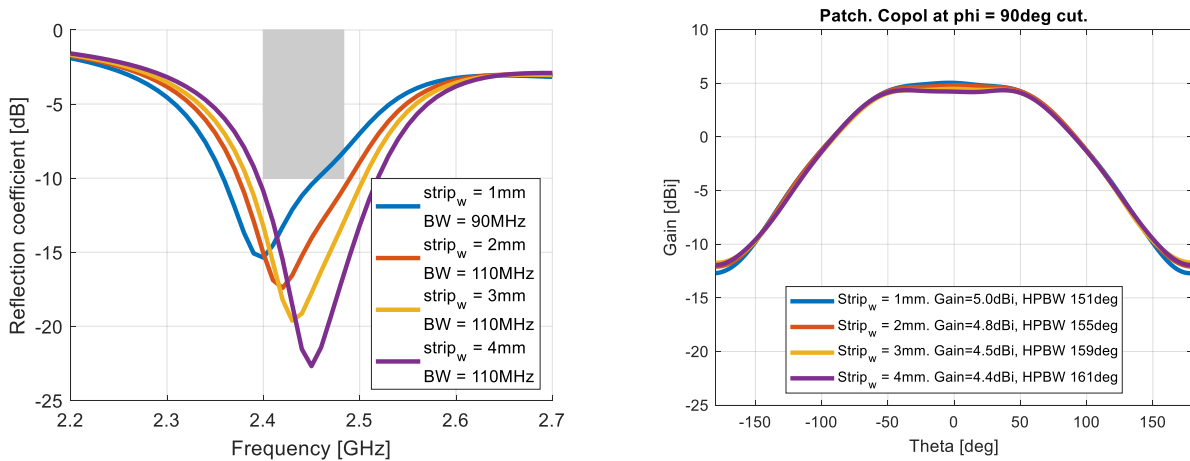


Figure 72. Reflection coefficient (left) and gain pattern over for the lower, center, and higher frequency of the band [70].


 Figure 73. Gain in Copol and Xpol for the antenna proposed in Figure 69. $\Phi = 0^\circ$ (left) and $\Phi = 90^\circ$ (right) [70].

Involving several elements and using the coupling between several elements to launch other modes provides interesting advantages to modify the pattern of a patch antenna. However, making the two radiators operate at the same frequency is not a simple task, as they are connected and operating together. As this design has many intercorrelated variables, an antenna of this type is more difficult to understand and to tune than a regular patch. This is especially true in designs intended for circular polarisation, where the purity of the modes is critical to achieve a stable CP. Ideally, the impedance bandwidth and the pattern should remain the same and stable over the frequency band, so that the total pattern of the total antenna is stable within this band. For the antenna presented here, the resonances of the two radiating elements are not exactly at the same frequency, but their resonances are tuned to be close together, and that is why, in Figure 72 we observe what seems to be a single resonance. One would need to separate the resonances as much as possible for a better impedance bandwidth, which would compromise the stability of the patterns, as one element dominates more in the lower part of the band, and the other in the upper part. This effect is easy to see in Figure 72, where the pattern is perfectly balanced at the center of the band, with a very flat pattern, and it tends to the shape the ring's or patch's pattern as we move away from it.

To better illustrate how some parameters affect the matching and the pattern, we show in Figure 74 and Figure 75 a few variations of the width of the strip connecting the two radiators, and the thickness of the substrate. These control how the two radiators are contributing to the input impedance and the total pattern.


 Figure 74. Effect of varying u_{strip_W} on the reflection coefficient (left) and the radiation pattern @2.45GHz (right).

By varying the width of the line, we can see how we can fine tune the matching and slightly the shape of the pattern, depending on which element dominates the other. In Figure 75, we can observe how thinner substrates lead to two clearly separated resonances when we look at the reflection coefficient. We then observe the radiation pattern at the lower, middle and higher frequencies of the band, for a slightly thinner substrate, but that still remains matched in the band of interest (4mm instead of 6.35mm). We see how it is more unstable, as the two radiating elements are not contributing equally over the band as their individual bandwidth is too narrow.

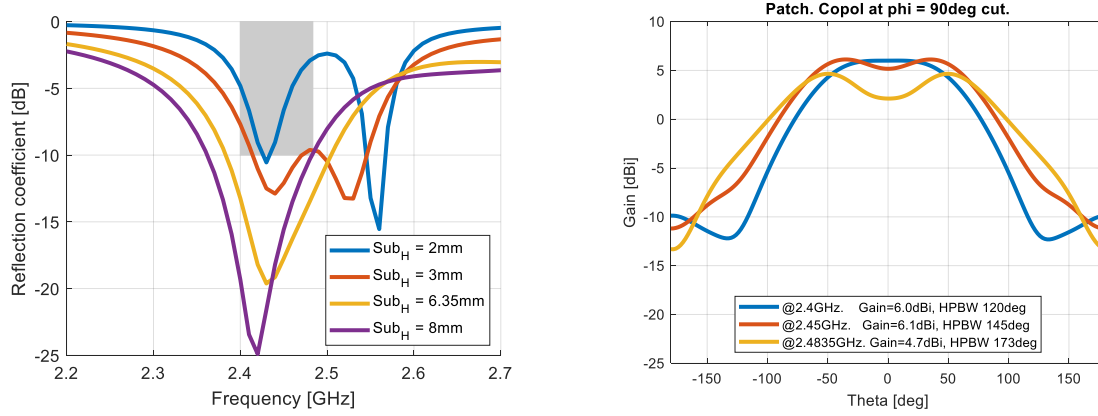


Figure 75. Effect of substrate thickness on the reflection coefficient (left) and how a thinner substrate leads to a more unstable radiation pattern over frequency (right), for a thinner substrate (4mm instead of 6.35mm).

Finally, we compare the performance of this antenna to a regular patch that serves as a reference for the typical performance of an antenna of the same type as the proposed, and a dipole, as a reference for omnidirectional coverage. The patterns in the two main cuts are shown in Figure 76, and the values of their HPBW and peak gain are gathered in Table 7. The proposed antenna establishes a good intermediate point between the two extremes, providing a HPBW of 160° in its optimized plane. One remark is that the peak direction of the ring is around 55° , and is lower closer to end-fire. Using this additional element can indeed be used to increase the beamwidth following the principle of increasing at end-fire. However, as its radiation pattern is not purely end-fire, and the potential to increase the beamwidth when combined with the patch is limited. This could be, however, an advantage, if we do not need to increase too much the beamwidth and it is more important to keep a low back radiation.

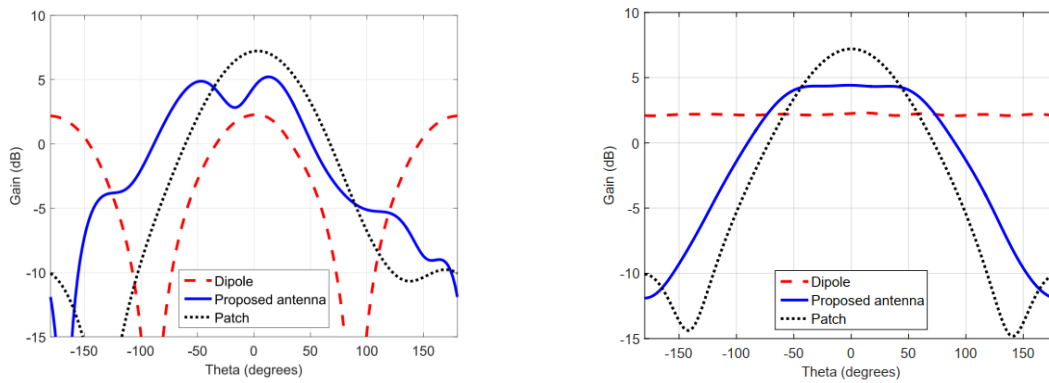


Figure 76. Gain in copol of the proposed antenna, a regular patch, and a dipole at cuts Phi = 0 (left) and Phi = 90 (right) [70].

Antenna	3dB beamwidth (deg)		Peak gain (dBi)	
	YZ cut	XZ cut	YZ cut	XZ cut
Dipole	360	76	2.3	2.7
Proposed antenna	159	115	4.4	5.2
Patch	70	68	8.5	8.5

Table 7. Comparison of the HPBW and peak gains for the YZ and XZ pattern cuts at 2.45GHz for various antennas

While this antenna using higher-order modes shows an excellent potential to increase the beamwidth, it is clear that it is not suitable for the requirements of our application. Its pattern is relatively unstable in frequency and is optimized only in one cut, it is only capable of radiating in linear polarization, and the most important: it exceeds significantly the size and weight requirements. We started thus looking for end-fire radiators that can be integrated with the patch, and that are potentially more compatible with CP.

4.3 Compact broadbeam LP patch antennas using ground slots

4.3.1 Concept of increasing the beamwidth using slots with end-fire patterns

To enhance the beamwidth using additional radiators, the radiation pattern generated by these has a strong impact on the achievable total beamwidth, as we could point out for the patch with a higher order mode ring in Section 4.2. The work in this Section focuses on finding radiators with a peak gain in end-fire, that does not much increase the antenna footprint. Apart from geometries using higher order modes, we found works like the one presented in [4], where they use Substrate Integrated Waveguide (SIW) antennas for end-fire radiation. Using this technology requires to add vias, complicates the fabrication and make it more expensive.

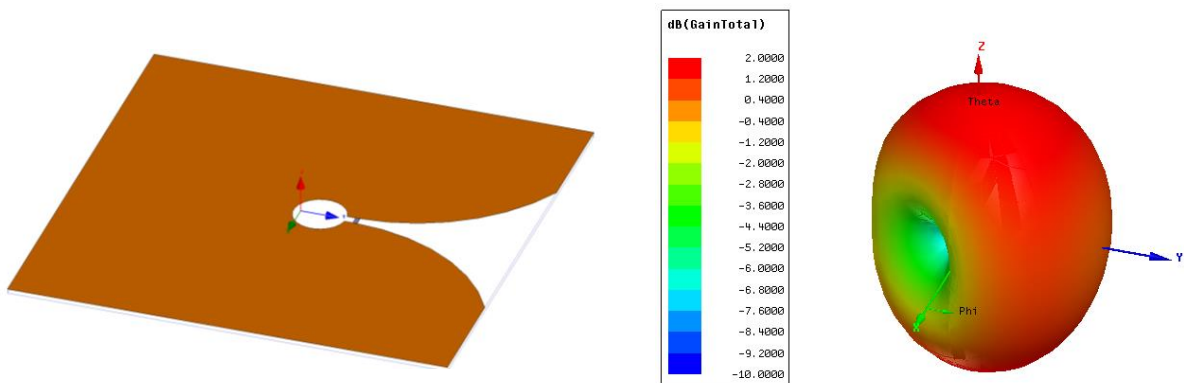


Figure 77. Standalone vivaldi antenna (left) and its corresponding pattern with good end-fire gain. The size is of 50x50mm and it operates at 2.4GHz.

Vivaldi antennas are simpler end-fire radiator and can be embedded in a single layer of substrate along with the patch. The geometry of a generic Vivaldi is shown in Figure 77. These antennas offer a much wider bandwidth as the ring operating in higher order modes. This means that if these are used as additional radiators to

a patch, the bandwidth of the antenna will be increased, and their pattern will be stable with frequency. In addition, these can easily be integrated in the structure, in a geometry as the one presented in Figure 78.

Combining four Vivaldi antennas, that are mainly radiating towards the lower elevation angles, we can generate an array that radiates a monopole-like radiation pattern if the elements are fed properly. This pattern has the desired shape to be combined with the patch, as the effect of the slots is to increase the gain in low elevation and decrease it in broadside. However, feeding several radiating elements with the right amplitudes and phase shifts, and especially in a small size, can be challenging.

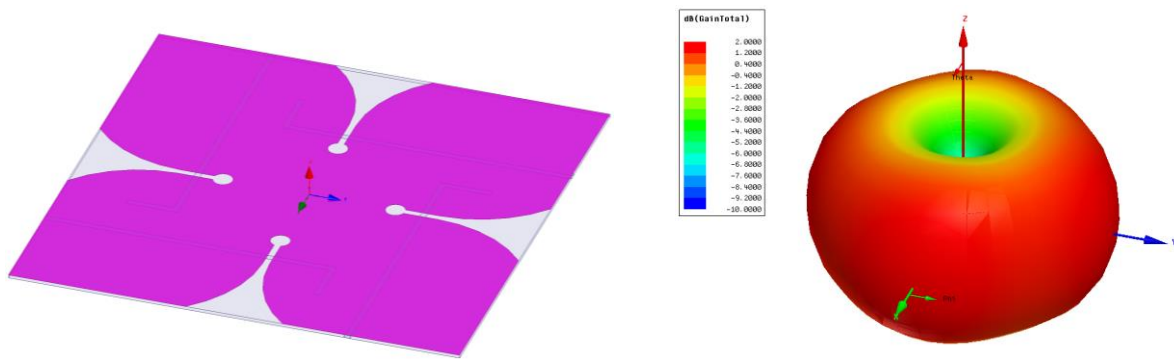


Figure 78. Combination of 4 Vivaldi antennas fed with microstrip lines (left) to achieve the desired monopole-like radiation pattern (right).

As all these radiators should be integrated together with a patch, five radiating elements have to be fed. The size of the radiators is therefore very important as they take much valuable space for the feeding network. Also, the ground should be sufficiently large to act as a good reference ground. Vivaldi antennas, due to their progressive aperture take a lot of surface off the metal, and are thus not suitable. We decided to reduce a Vivaldi to a simple rectangular slot that follows the same radiation principle and provides similar pattern, but with a narrower bandwidth. This evolution of the design is shown in Figure 80. These antennas still provide a bandwidth that largely covers the ISM band, as seen in Figure 81. We also observe and confirm that the broad bandwidth translates to a very stable pattern along the entire band of operation.

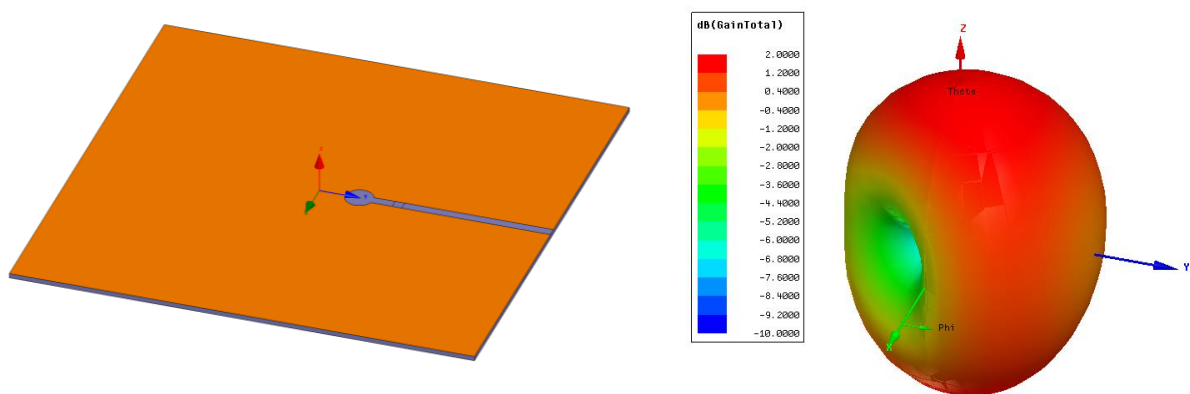


Figure 79. Slot antenna (left) on the same ground as the Vivaldi in Figure 77 and its corresponding radiation pattern (right).

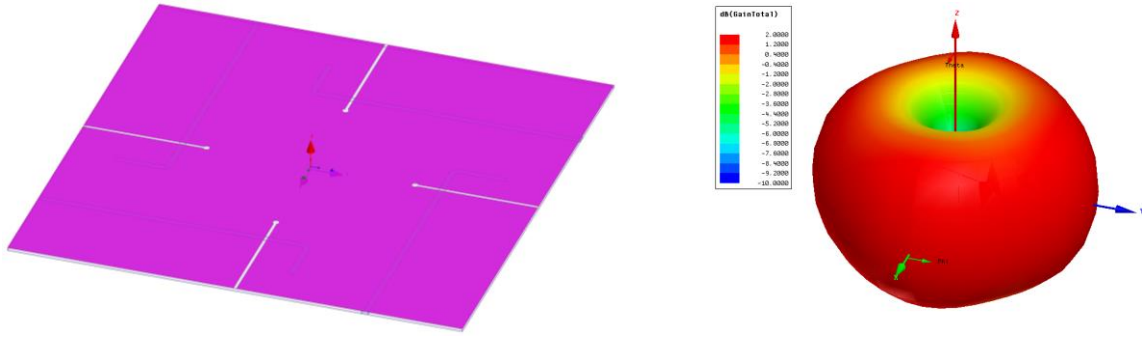


Figure 80. Evolution of the Vivaldi antennas to simple rectangular slots (left) to achieve the desired monopole-like radiation pattern (right)

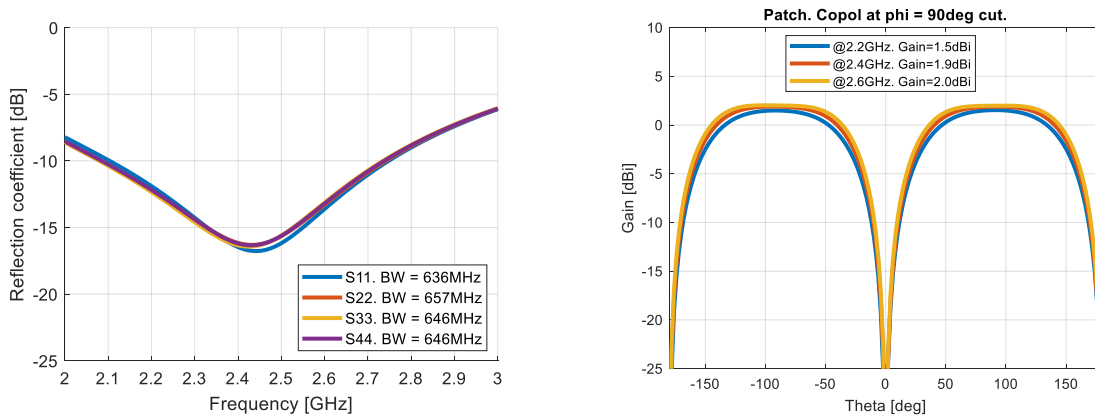


Figure 81. Matching (left) and radiation pattern stability over frequency (right) of the slots from the design in Figure 80.

In the design depicted in Figure 82, we combine four slots with a patch to illustrate this technique. The substrate used in this design is FR4 and the thickness is 1mm. The size is of 70x70mm, the length of the slots is 15mm and the size of the patch is 26.5x26.5mm². The slots are fed using lumped elements and the patch with a coaxial feed. All elements are fed in phase. The polarization of the patch is along the X axis, a same as the polarization of the slots to the left and right sides of the patch. In the plane at $\Phi=90^\circ$ or YZ, where the polarizations are aligned and the slots are combined to the patch, the pattern shows a very broad beamwidth of 220° in co-polarization. The slots contained in the plane XZ (along the X axis) have a polarization orthogonal to that of the patch. This explains the directional pattern in co-pol for that cut, which has a HPBW in the vicinity of 90° , not very different from a regular patch. In practice, these slots could be removed to gain some space with no significant change to the pattern. By applying this technique to a linearly polarized patch, it is only possible to optimize the beamwidth in one plane, but the potential to increase it is excellent.

While the performance looks very promising, as the size could still be shrunk using a higher permittivity substrate, there are a few problems to address. First of all, it is very complex to feed 5 elements in a small surface with the right phase shift, and even more complicated to achieve CP. Also, while the slots have a good frequency stability, the bandwidth of the patch is still limited and this can be a problem as we need to use a higher permittivity substrate.

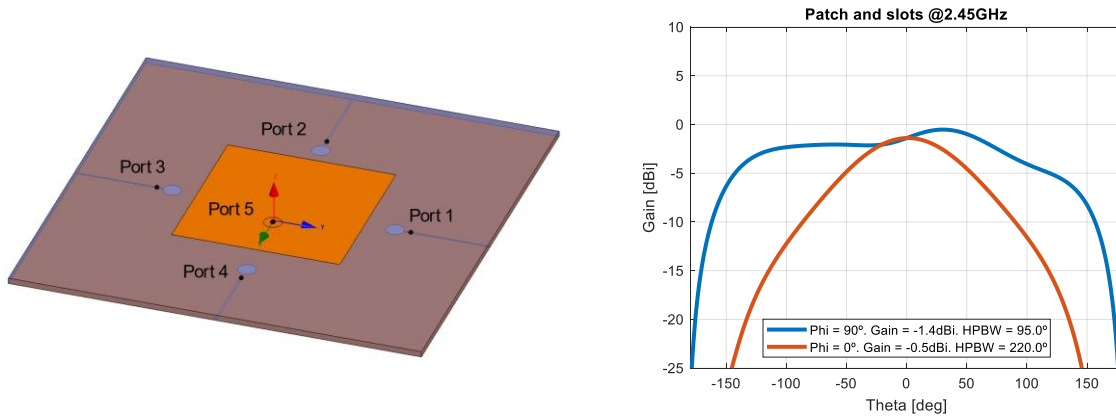


Figure 82. Adding a patch in the gap between the slots to combine their patterns providing a beamwidth of 220° .

4.3.2 Design of a LP patch antenna with slotted ground for a quantitative assessment of the performance

4.3.2.1 Description of the design and quantitative assessment of its bandwidth and beamwidth.

We analysed the behaviour of the patch to learn how we could feed this type of antenna and the slots together. The voltage difference created at both ends of the patch create a current flow in the patch and the ground, and an E field between the patch and the ground. The latter is ultimately the responsible of the radiation of a patch antenna. As the current also flows in the ground plane, if we place ground slots sufficiently close to the patch, the voltage difference between either side of the slots generates an E-field along the slot in the same polarisation as the patch. We use the antenna in Figure 83 to illustrate this effect, and we can observe in Figure 84 how the slots are excited passively from the patch.

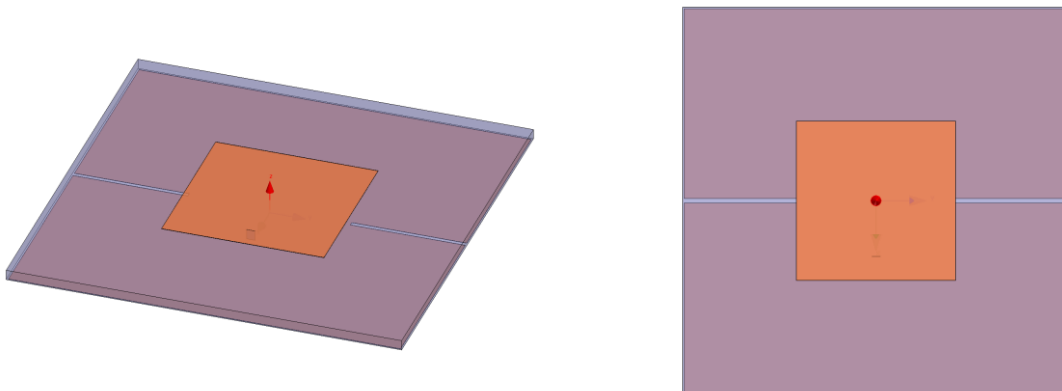


Figure 83. Patch antenna with ground slots. The substrate is Rogers TMM10 with a permittivity of 9.2, and a thickness of 1.27mm. The lateral size of the antenna is $47.8 \times 47.8 \text{ mm}^2$, and the dimension of the slots is of 14mm.

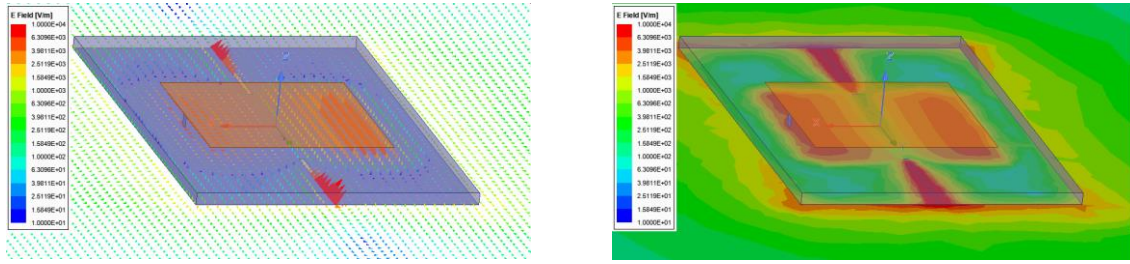


Figure 84. E fields of the LP antenna with slots in Figure 83. E-field vector (left) and complex magnitude (right).

For the architecture proposed in Figure 84, we can enhance the beamwidth significantly in the plane where the slots are placed. The effect on the beamwidth can be seen in Figure 85, where the pattern is quasi-omnidirectional with a HPBW of 190°.

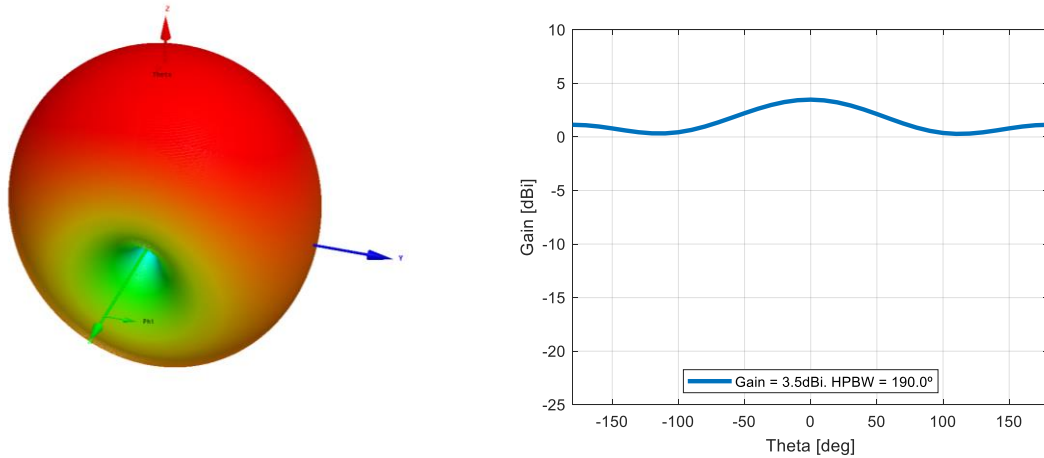


Figure 85. 3D LP pattern (left), and the co-pol cut in the YZ plane (right) with a HPBW of 190°.

Another of the advantages of such design is the effect of the slots on the antenna bandwidth. In Figure 86, we compare the bandwidth of exactly the same patch with and without slots. The bandwidth is increased by around 5 times thanks to the slots, due to the broad beamwidth of the slots. This is very desirable advantage of this technique, as we can choose a high permittivity and thin substrate to reduce the size and weight of the antenna. Also, we should remember that a good bandwidth for the modes that we combine in an antenna is important if we want to have a stable pattern over frequency.

This method has the disadvantage of increasing the back radiation but the advantages of having a simple feeding, enhanced beamwidth and bandwidth, and smaller footprint.

By controlling some parameters like the length of the slots and their proximity to the patch, one can tune how much the slots contribute to the radiation pattern and therefore how much the beamwidth is enhanced.

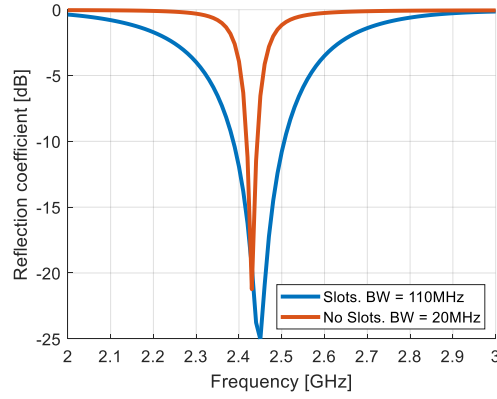


Figure 86. Bandwidth of a single patch (red) and the patch with slots 5% (yellow), for exactly the same size. The bandwidth is increased by x5 times

4.3.2.2 Analysis of the main parameters of a patch with a pair of ground slots

The objective here is to understand the effect of all main parameters, and their impact on the various figures of merit of the antenna. We use as a reference the patch with a pair of slots shown in Figure 83.

We can observe how the changes in the impedance are not significant when we change the width of the slots as seen in Figure 87. The changes in the pattern are negligible from the results in Figure 89.

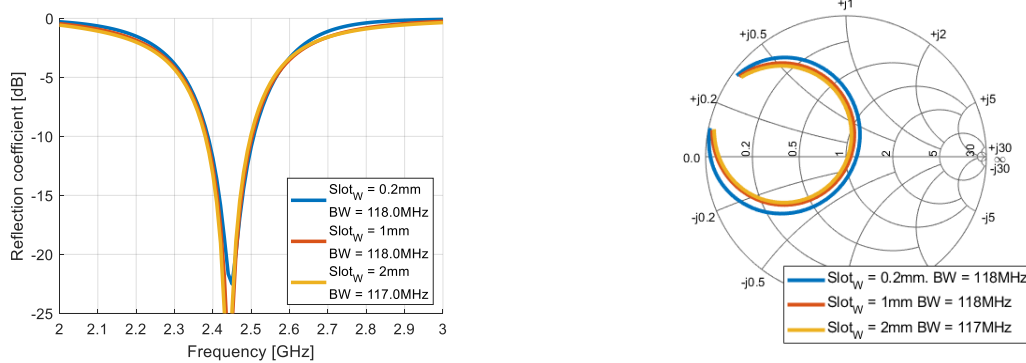


Figure 87. Effect of the **slot width** on the input impedance (left) and the radiation pattern (right). The variations are for a slot length of 14mm, a separation patch-gap of 0mm and a patch size of 19.8mm. These results refer to the antenna in Figure 88.

In Figure 90, we can see a spot where the two impedances are optimized to be matched for a slot length of 14mm. In fact, that point has a broad bandwidth that covers the entire band, thanks to the broader beamwidth of the slots. We can see in the Smith Chart how the impedance for the optimized values is significantly lower compared to the single patch. That means that for these antennas the feeding point of the patch should be moved closer to the edges of the patch. The pattern for various slot lengths is shown Figure 91

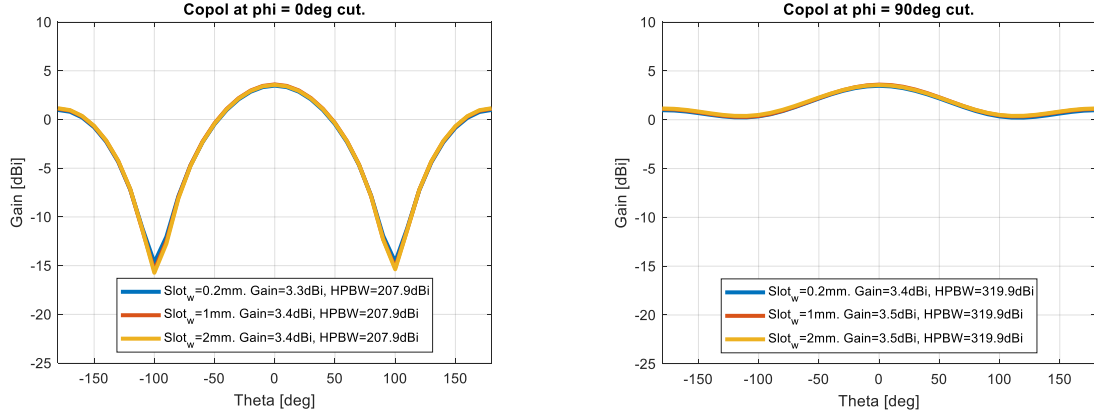


Figure 89. Radiation pattern cuts at $\phi=0^\circ$ (left) and $\phi=90^\circ$ (right) for various **slot widths**. The variations are for a slot length of 14mm, a separation patch-gap of 0mm and a patch size of 19.8mm.

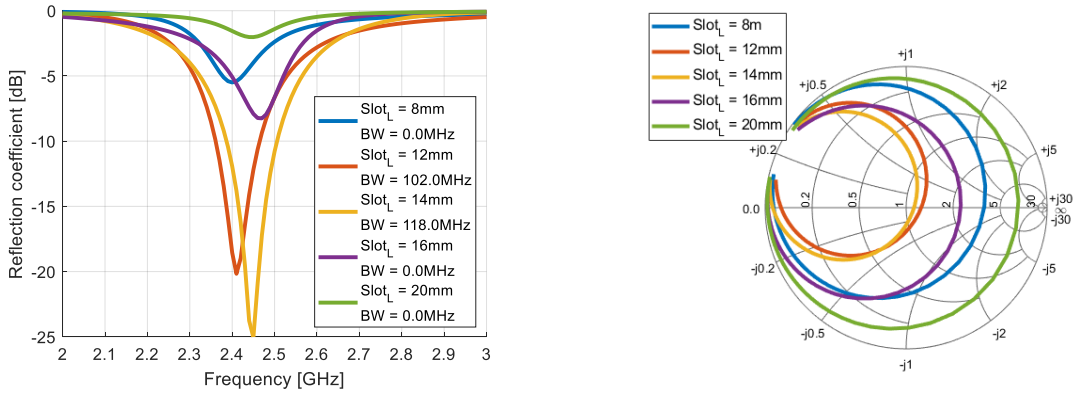


Figure 90. Effect of the **slot length** on the input impedance. The variations are for a slot width of 1mm, a separation patch-gap of 0mm and a patch size of 19.8mm.

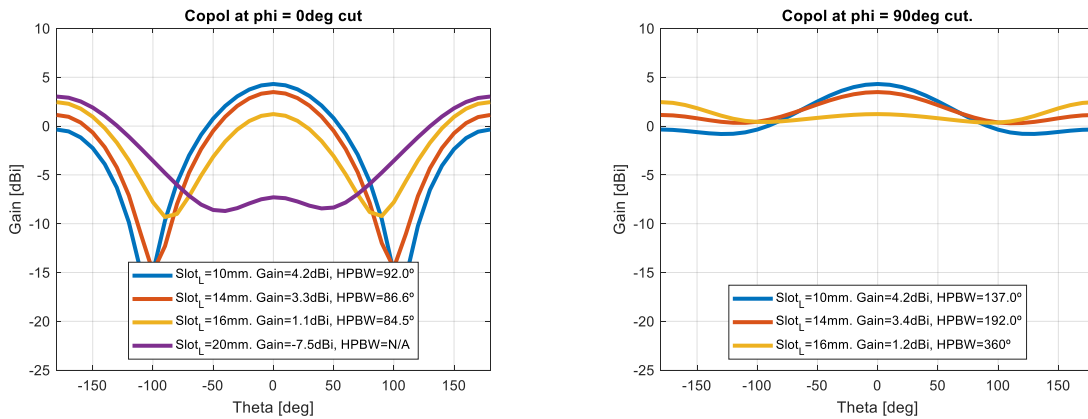


Figure 91. Radiation pattern cuts at $\phi=0^\circ$ (left) and $\phi=90^\circ$ (right) for various **slot lengths**. The variations are for a slot width of 1mm, a separation patch-gap of 0mm and a patch size of 19.8mm.

We can observe in Figure 92 the effect of the gap between the patch and the ground slots on the reflection coefficient. The input impedance of the antenna decreases when the slots are closer to the patch, and increase when they are further, converging to the usual input impedance of a standalone patch. This can be in some cases beneficial, as the impedance of the patch can be decreased closer to 50Ohm and use a simple microstrip

line to feed it. This would further decrease the size of the antenna, as there would be no need to for a quarter wavelength transformer between the connector and the antenna, which would require a larger footprint.

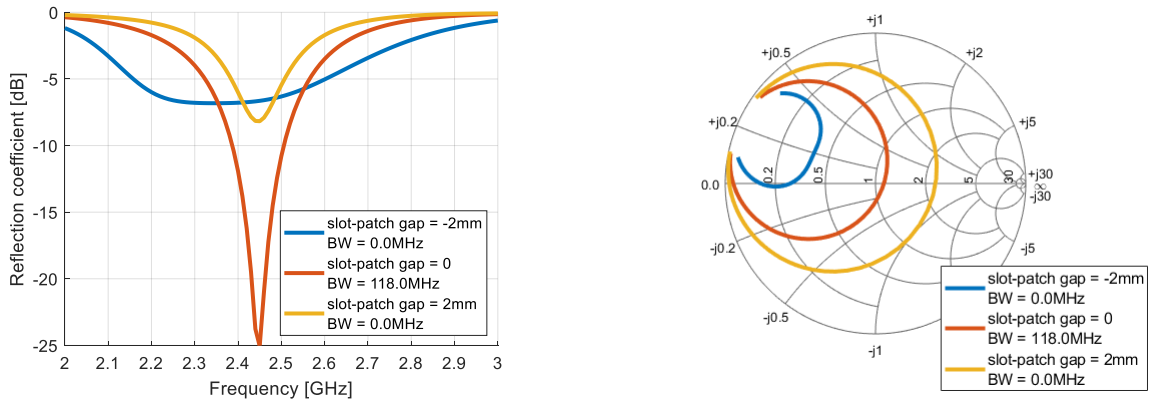


Figure 92. Effect of the **slot-patch gap** in the reflection coefficient.

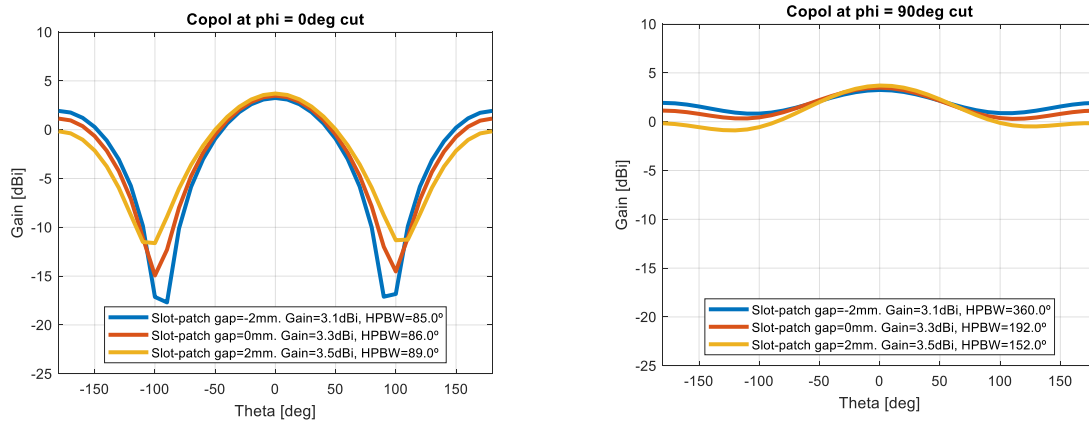


Figure 93. Effect of the **slot-patch gap** on the pattern. The variations are for a slot length of 14mm, a slot width of 1mm and a patch size of 19.8mm.

In Figure 93, we can observe how the beamwidth broadens when the slots are closer to the patch, as their contribution is more significant, and more directional when they are more distant from the patch. In Figure 94 we observe the effect of the substrate thickness. The resonant frequency does not move, but we can observe how the selected thickness, 1.27mm is the one that offers a sufficient bandwidth (>83MHz) to cover the band of interest.

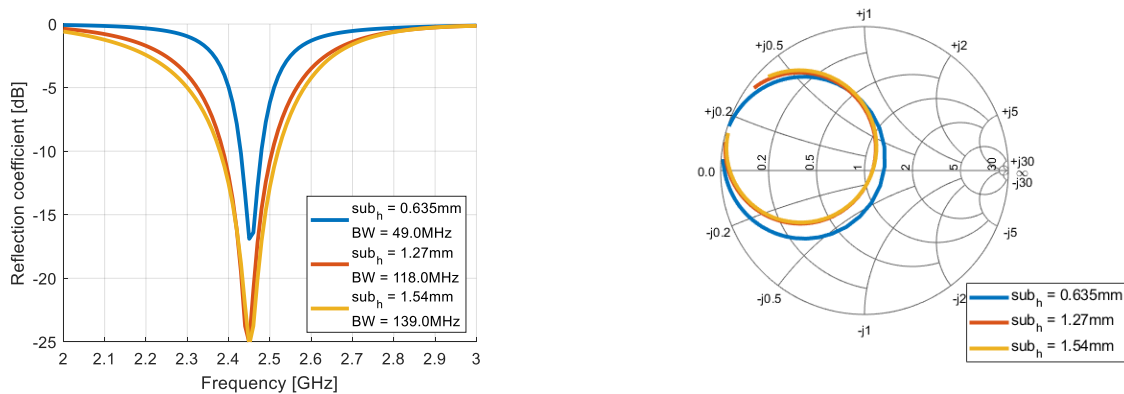


Figure 94. Reflection coefficient for various **substrate thicknesses**. The variations are for a slot length of 14mm, a separation of 0mm and a patch size of 19.8mm.

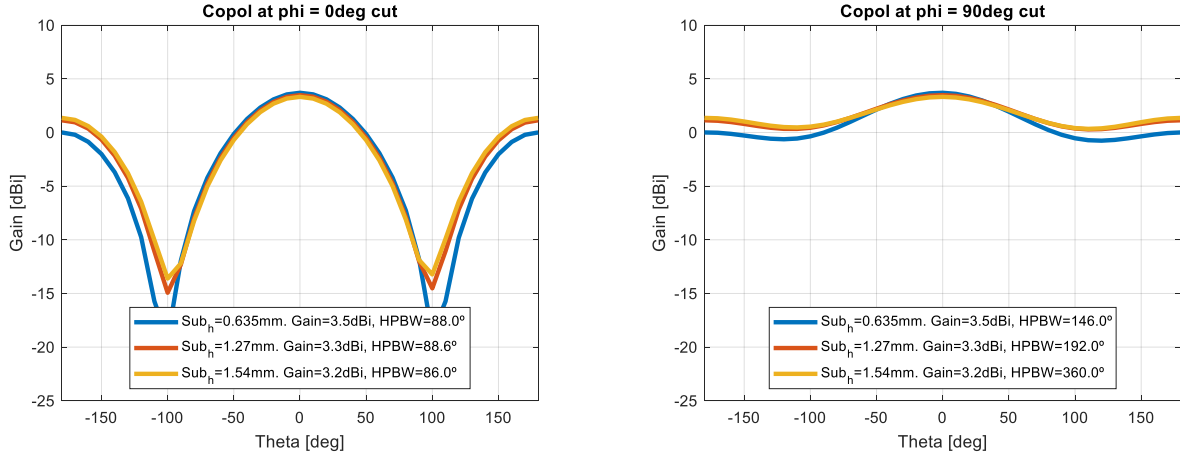


Figure 95. Radiation pattern cuts at $\phi=0^\circ$ (left) and $\phi=90^\circ$ (right) for various **substrate thicknesses**. The variations are for a slot length of 14mm, a separation of 0mm and a patch size of 19.8mm.

Some of the consequences of this design are a more sensitive design, the strong null at $\phi = 90^\circ$, and the back radiation. These are to the advantage of having a small and light antenna with a good bandwidth, a good beamwidth in the enhanced plane and a simplified feeding.

4.3.3 Prototype of a LP patch with ground slots

We fabricated and measured the antenna in Figure 96 to validate the proposed technique. We adjusted slightly the design using Rogers TMM 10i with a relative permittivity of 9.8 and a loss angle of 0.002, which makes the antenna smaller. The antenna size is $45.2 \times 45.2 \times 1.27 \text{ mm}^3$, the slots are 13mm and patch is $19.2 \times 19.2 \text{ mm}$. Among all the thicknesses available for this substrate, we selected 1.27mm, as the immediately thinner of 0.762mm does not provide sufficient bandwidth to cover the band of operation. This design allows us to solder directly a connector on the antenna to measure directly the input impedance of the antenna itself without a matching network. The fabricated prototypes are shown in Figure 96.

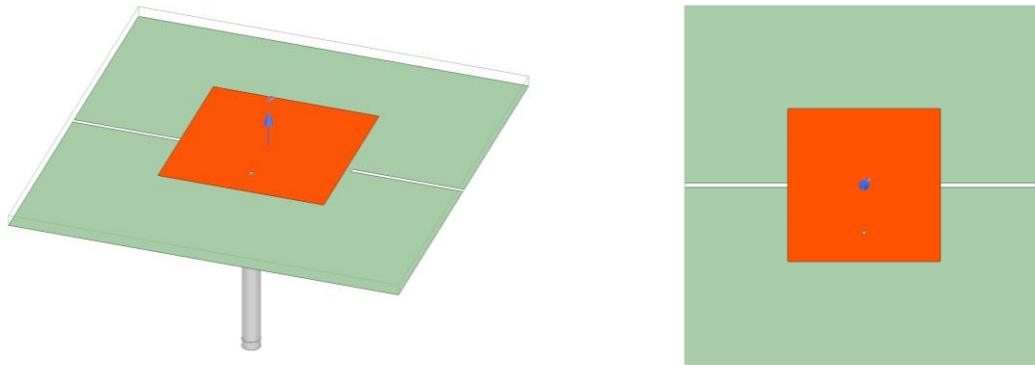


Figure 96. Geometry of the antenna prototype. The dimensions are $45.2 \times 45.2 \times 1.27 \text{ mm}^3$, with a Rogers TMM 10i substrate. The length of the slots is 13mm and the sides of the squared patch are 19.2mm.

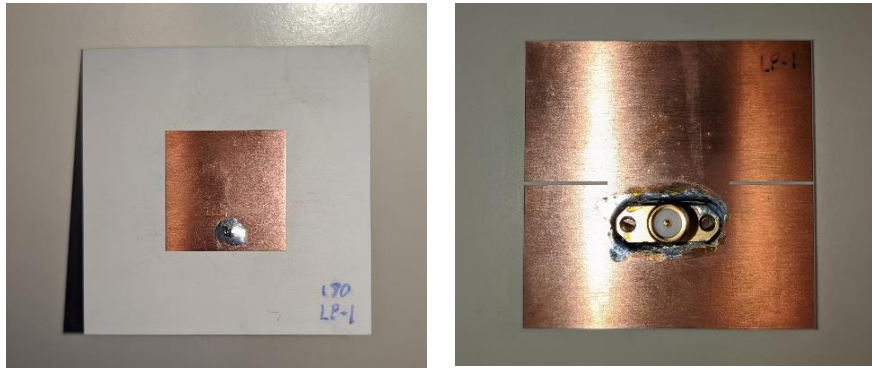


Figure 97. Fabricated LP patches. Top view (left) and bottom view (right).

The impedance bandwidth of this antenna covers the entire band of interest thanks to the interaction of the patch with the slots, which have a broader bandwidth. The sufficient bandwidth that we see here also makes us think that such antennas could be used in CP, as each of the two modes excited on the CP patches have a sufficient bandwidth separately.

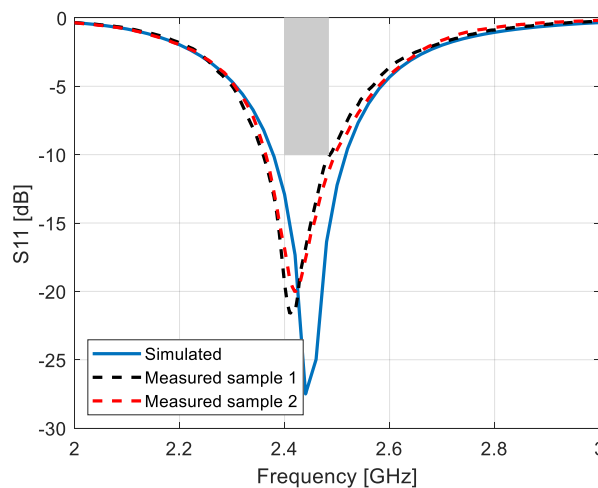


Figure 98. Measured and simulated S11 of the LP patches prototypes. Its bandwidth is of ~100 MHz, broader than the 83.5 MHz required in the band.

We measured the pattern and gain of the prototypes in the anechoic chamber and using the setups shown in Figure 99. As these antennas have a very broad beam and the ground slots are radiating, we have found that using a plastic slab to assemble them on the support can have an effect on the accuracy of the measurement. We avoid the use of the support by using tape to suspend the antennas in the middle of the support. We also add ferrites to the cable to eliminate any potential effect of cable currents on the measurements.



Figure 99. Measurement of the LP prototype in the anechoic chamber. The support introduces reflections that are ultimately seen in the measurement of the pattern as ripples.

The measured gain of 5.2dBi and 4.1dBi at the lower and upper frequencies, respectively, as we can see in Figure 100. The HPBW of this prototype is 190° in simulation for the optimized plane ($\phi = 90^\circ$), and we observe that the envelope of the pattern in simulations and measurements are very similar despite a ripple effect on the measurements, that from our experience is based on the measurement setup.

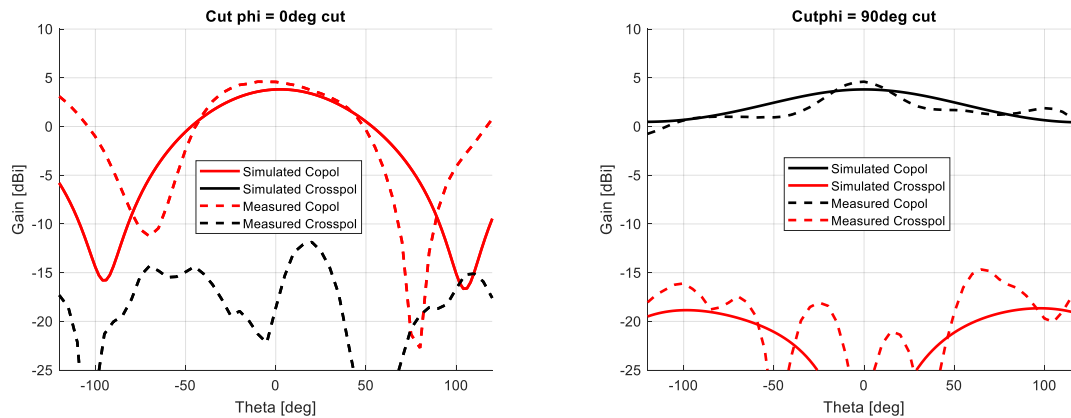


Figure 100. Measurement and simulation results in the $\phi=0^\circ$ cut (left) and $\phi=90^\circ$ cut (right). The HPBW is of 190° for the optimized plane. The patterns are shown @2.45GHz, and the peak gain is 4.6dBi

To summarize, combining a patch with ground slots, we can improve the bandwidth of the patch, and increase its beamwidth in a compact size and weight. However, antennas of the type presented in this Section only optimize the pattern in one plane, and in linear polarization. As the antennas in the drone require CP radiation and a broad pattern in all cuts, we devote the following Sections to developing this idea to meet the requirements.

4.4 Compact broadband circularly polarized patch antennas using ground slots

4.4.1 Concept. Broadbeam CP patches combining patches with ground slots

In this Section we use the ground slots to enhance the beamwidth in two planes and in circular polarization. A CP patch can be seen as the combination of two modes with the same amplitude that are shifted 90deg in phase, and placed perpendicular to each other. Following this idea, the patch with two slots from Section 4.3.2.2, is modified adding another pair of slots, one for each of the polarizations, resulting in the structure in Figure 101.

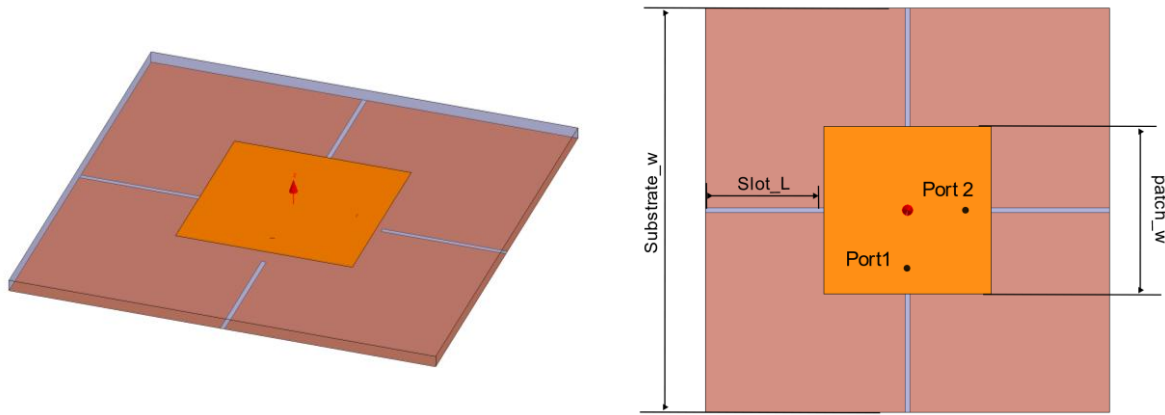


Figure 101. Patch with four ground slots and two lumped ports that excite circular polarization in the antenna.

To excite circular polarization in the patch, we use two lumped ports between the ground and the patch. One of the ports has a delay of 90deg with respect to the other. That means that at a phase of 0deg, ideally the current is purely horizontal or vertical along the patch, and only one pair of slots is excited. At 90deg and its multiples, the orthogonal polarization in the patch dominates and the corresponding pair of slots is active, as shown in Figure 102. Thanks to this behavior, this structure is compatible with exciting circular polarization, and the slots are coherently fed with the patch. This is important as it eliminates potential phase misalignments between the various radiating elements if we had to feed all of them.

From the distributions of the E fields and the currents in Figure 102, we observe that the slots are alternately activated depending on the mode that is excited on the patch (coming from port 1 or port 2). The combination of the two orthogonal modes in a patch allows to excite circular polarizations with patterns with revolution symmetry for regular patch antennas. For this type of modified antenna, due to the different interaction of the slots with the patch depending on the polarization, we need to analyze the patterns for each of the separate modes to understand how they can combine to radiate a CP pattern. In Figure 103 we show the pattern when we activate only port 1 on the antenna. In this case the antenna is equivalent to having a linearly polarized patch with its beamwidth enhanced in only one plane. If both ports are activated, the pattern in the enhanced plane combines with the non-enhanced pattern from the orthogonal polarization. The deep null from the non-optimized plane then reduces the beamwidth of the orthogonal mode and results in a limit to the achievable beamwidth of the total CP pattern.

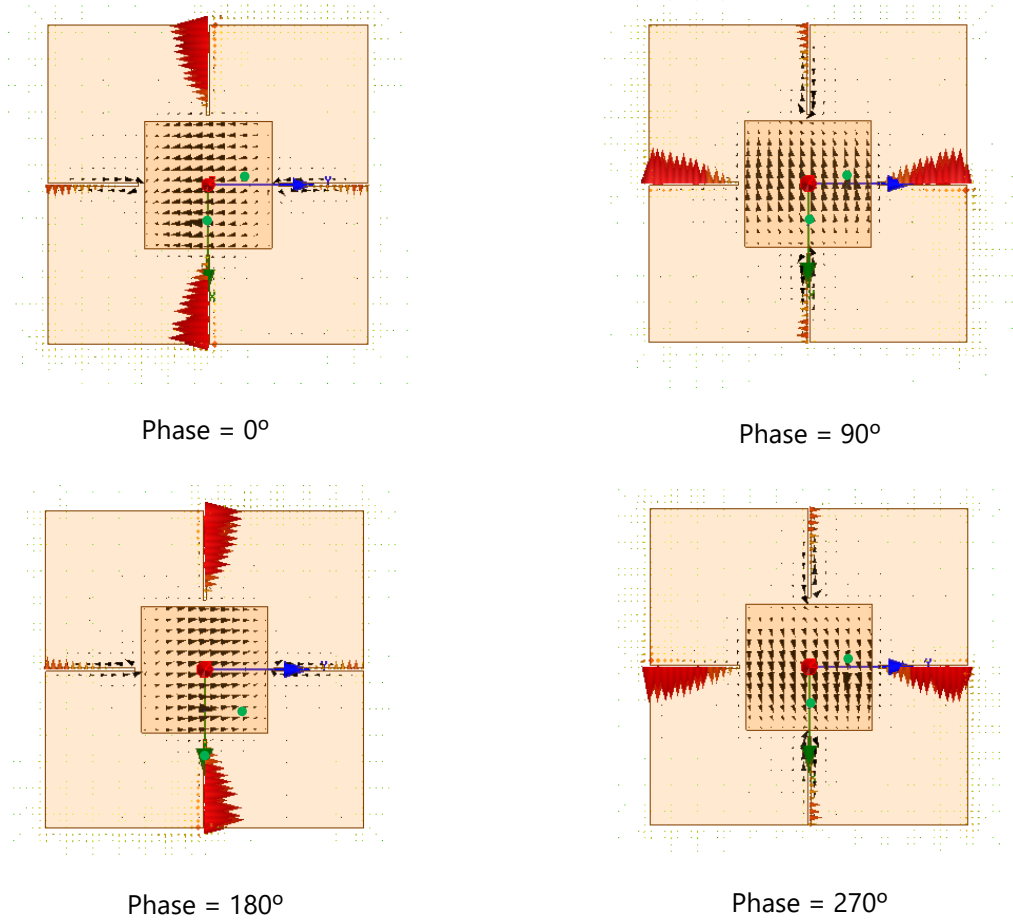


Figure 102. Illustration of the E field (red) and the current in the ground (black) in the antenna at different phases. The ports are marked with green circles.

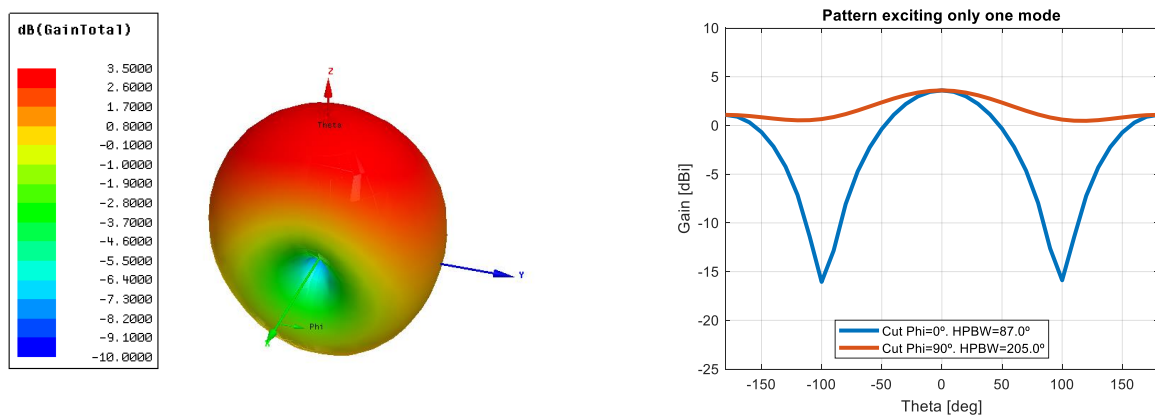


Figure 103. Pattern of the antenna from Figure 101 when exciting only one of its linear polarizations (current density along X axis). These results are obtained for an antenna of 47.1x47.1x1.27 made of TMM10. The patch is 19.5x19.5mm and the slot length 11.5mm.

In Figure 104 we can see the pattern in CP for the antenna from Figure 101, with the two ports activated. This solution offers a CP with enhanced beamwidth, small size and reduced weight, broad beamwidth and only two feeding points. As for the linearly polarized patch with two slots, the drawback is a stronger backwards

radiation. It is also important to note that higher gain (and narrower beamwidth) is expected for a CP antenna, as the antenna launches two modes [27] instead of only one.

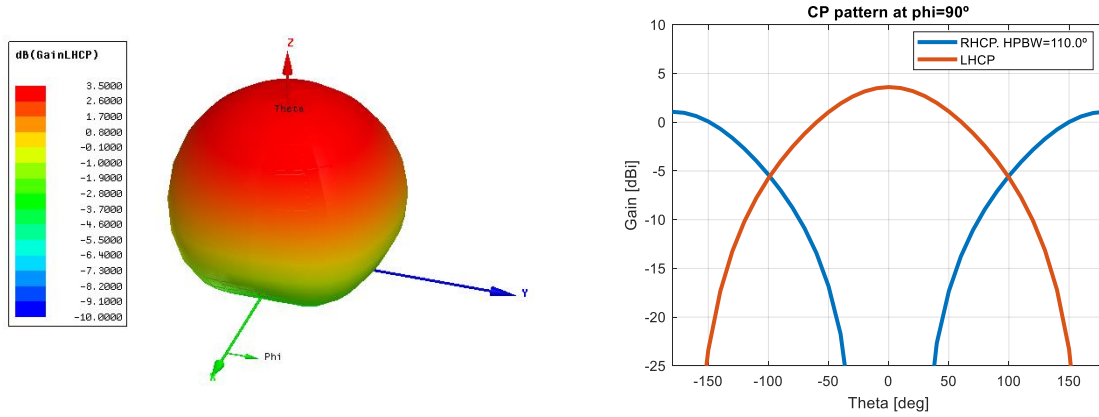


Figure 104. Pattern of the antenna from Figure 101 when exciting CP on it. These results are obtained for an antenna of 47.1x47.1x1.27 made of TMM10. The patch is 19.5x19.5mm and the slot length 11.5mm.

As the maximum tolerated gain variation around the drone is 10dB, and given the strong restrictions on size and weight, this solution offers a good compromise between performance and mechanical constraints.

4.4.2 Design of a CP patch antenna with slotted ground for a quantitative assessment of the beamwidth improvement

The proposed technique has several degrees of freedom, and many parameters that are interdependent. In this Section we analyse the performance of this technique and try to understand its potential to increase the beamwidth. We take as a reference the geometry in Figure 105, which has a reduced ground for lower weight and improved beamwidth. We keep using two lumped ports to feed the antenna.

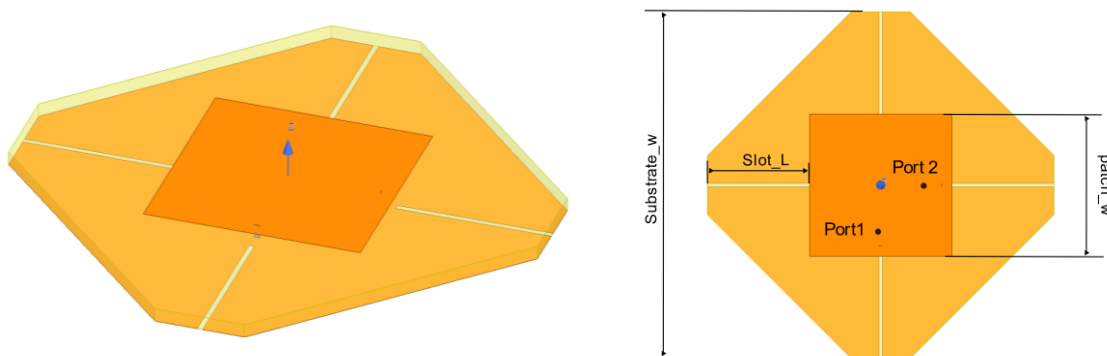


Figure 105. Antenna with optimized geometry to reduce its size and increase the beamwidth in both planes and circular polarization. The size of the antenna is of 48.2x48.2x1.27mm³, patch_w = 19.8mm, there is no gap between the patch and the slots, the corners are trimmed with a chamfer distance of 20mm and the feeding of the ports is located at 8.5mm from the center of the patch

To understand how the addition of the slots improves the beamwidth, we compare the performance of the geometry in Figure 105 with the exact same antenna without the slots. The gain patterns for these two variations are shown in Figure 106, where we can see that the HPBW is increased in the range of 15-20deg. As a direct consequence of the broader beam, the gain decreases from 3.1dBi to 2.5dBi.

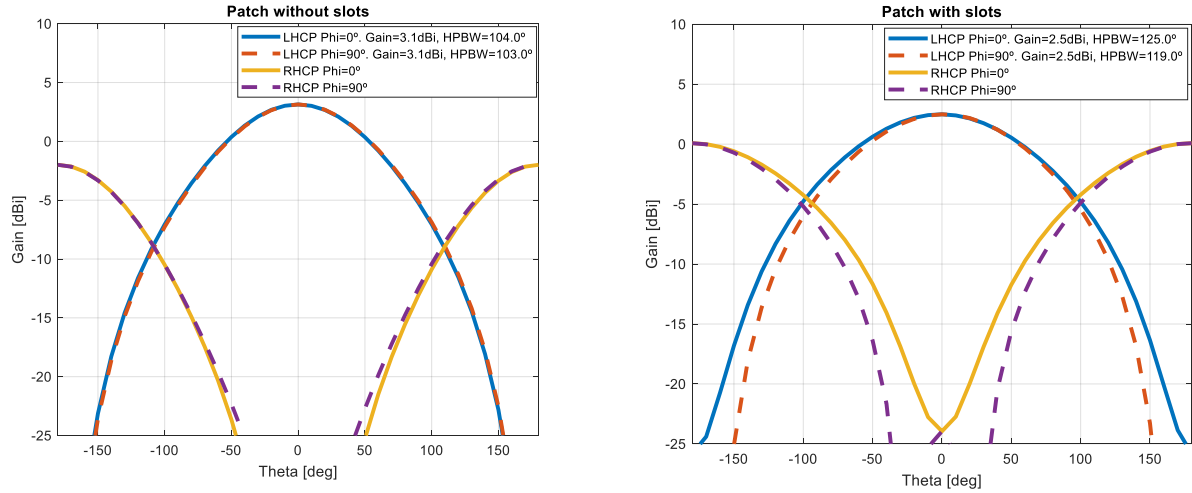


Figure 106. Realized gain patterns in copol and crosspol for the two main cuts, for the antenna without slots (left) and with slots (right). Results at 2.45GHz.

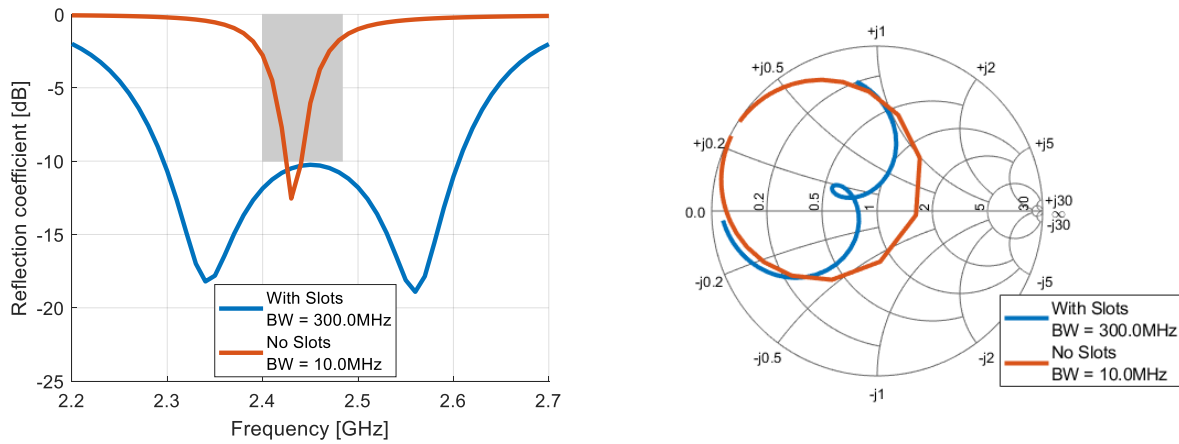


Figure 107. Reflection coefficient in magnitude (left) and in the Smith Chart (right).

The biggest improvement is in the bandwidth, as for the exact same size and thickness, it increases from 16MHz to 310MHz (see Figure 107). We should notice that the reflection coefficient is for one of the two ports of the circular polarization. When using a feeding network to deliver the power to the two ports from a single connector, the total bandwidth is likely to be broader. In that case, a broader bandwidth only means that there is less power coming back to the port from the antenna, in part due to the losses in the feeding network. Therefore, it is worth to verify the stability over frequency of antenna radiation, to confirm that this broad bandwidth is usable in practice with a stable pattern and gain. In Figure 108 we show the realized gain for the antenna with and without slots. The latter shows a very stable pattern in the entire band, with HPBW broader than 124°

and peak gain higher than 2.3dBi. The antenna without slots has a less stable pattern, due to its narrow bandwidth.

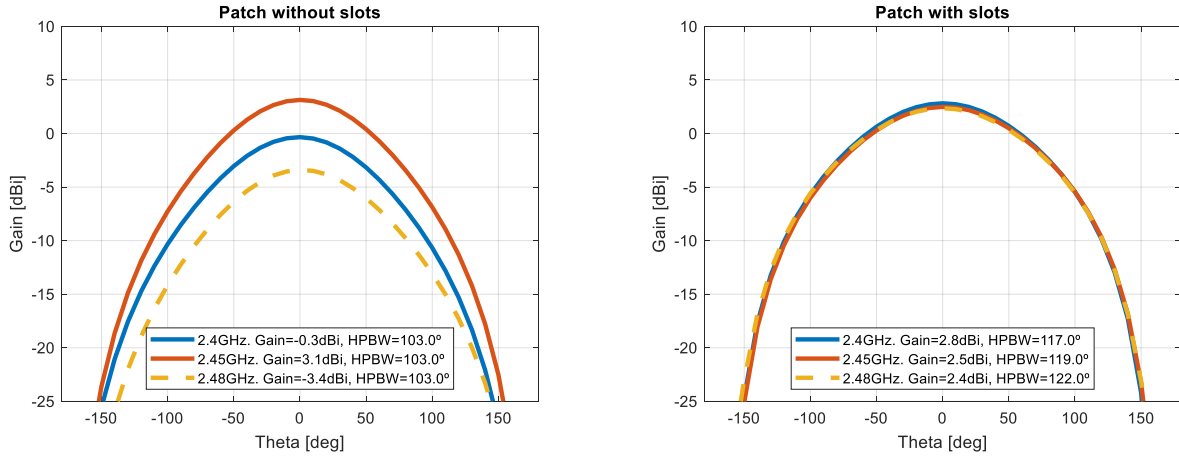


Figure 108. The realized gain pattern of the antenna without slots (left) and with slots (right). Both are obtained for the cut at $\Phi = 90^\circ$, the performance at $\Phi = 0^\circ$ is equivalent. Results at 2.45GHz.

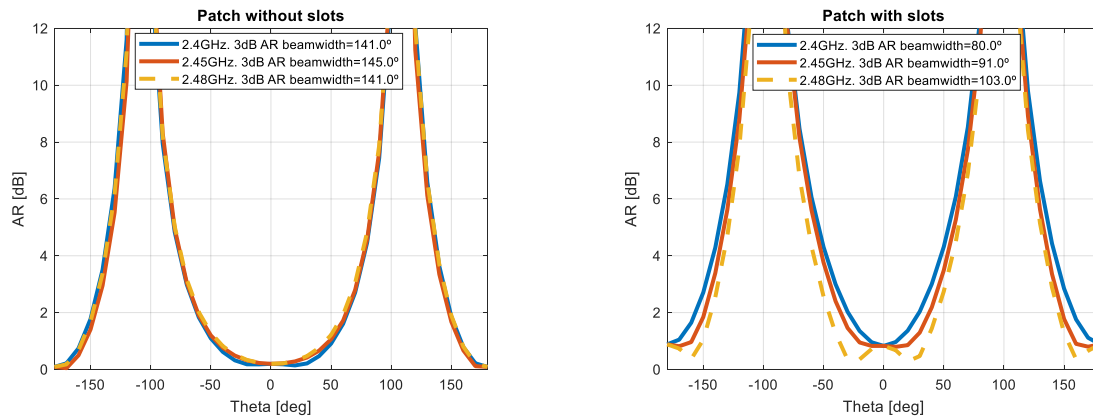


Figure 109. AR of the antenna without slots (left) and with slots (right). Results at 2.45GHz.

In Figure 109, we can observe the AR for the antenna with and without slots. The axial ratio aperture for the latter is broad thanks to the ideal feeding using the lumped elements and the small size of this antenna thanks to the high permittivity substrate. For the antenna with slots, the AR aperture is narrower, due to the more complex combination of the several radiators in all the directions of the space, which is compensated by the broader pattern, which results in a total a wider beamwidth. Other types of additional radiators can be explored for applications where the AR beamwidth is more important.

The narrower AR beamwidth and the higher back radiation are the downsides of using these additional elements. However, these disadvantages are not as important for our application as the broad total beamwidth the light weight and small size. This type of antenna offers a good compromise for our application.

4.4.3 Prototypes. CP patch with ground slots with feeding network

4.4.3.1 First prototype and cable currents

In this Section, we summarize the fabrication and measurements of a first prototype following the idea of the CP patch with four slots described in Section 4.4.2. We maintain the shape of the ground squared to add alignment holes and to reduce the number of degrees of freedom of the design. We should remember that as a direct consequence of the densely packed radiators (one patch and four slots), the design of the feeding network is no easy task, as the footprint should be small and should not be close to the slots. Options like a hybrid coupler would provide an excellent frequency stability, but it would require too much space. As the individual bandwidth of the two feeding points covers with a large margin the band of interest, we can use a simpler feeding network, like a T-junction power divider with a delay line in one of its arms to get the needed phase shift. We would like to mention that from all figures of merit, we prioritize weight over beamwidth, as long as the pattern of the two antennas combined still complies with the required gain margin of 10dB around the drone. The design of first prototype is shown in Figure 110.

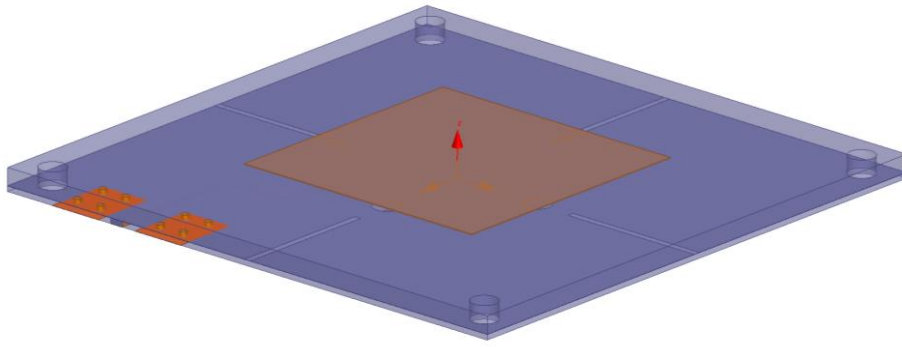


Figure 110. Geometry of the first prototype, including two substrate layers of Rogers TMM10.

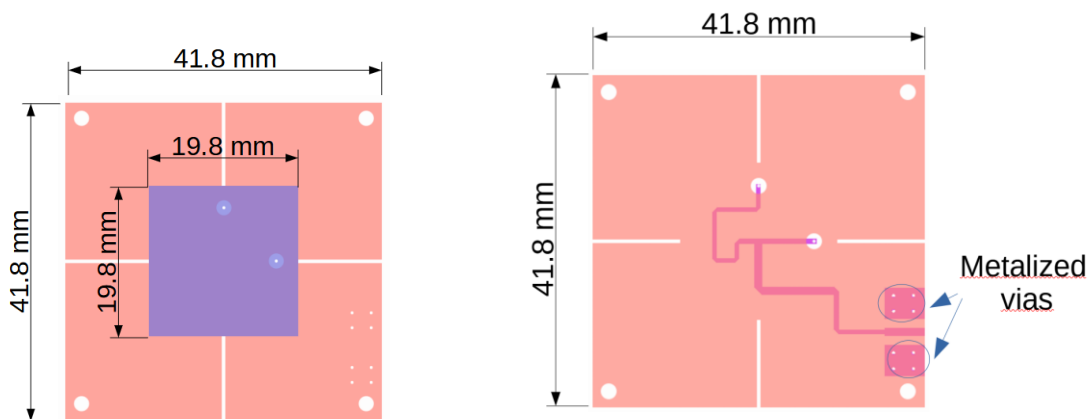


Figure 111. Top layer (left) and bottom layer (right) for the prototype.

To realize the design depicted on Figure 111, we fabricate the two PCBs separately and glue them together, as seen in Figure 112. The ground plane is included in both PCBs for a stable performance of the two separate

boards. The alignment of the two boards when assembled to avoid that the ground plane in one of the boards short circuits the slots on the other. This would unbalance the antenna and change the pattern or the polarization. We drill holes in the corners for a good alignment during the gluing process.



Figure 112. Gluing of the two PCBs (feeding network and antenna) together.

The next step is to solder a connector on the PCB. We prepared the feeding network PCB with copper pads connected to the ground through vias to properly ground the shield of the SMA connector. To diminish the proximity and potential effects of the connector on the slots, we chose an edge mount connector due to its small lateral size compatible with the total thickness of the antenna of 1.7mm. We consider the thickness of the two substrates (1.27mm and 0.381mm) and the copper layers at the connector pad ($0.035\text{mm} \times 3 = 0.105\text{mm}$). Once we soldered the connector to the socket the fabrication of the prototype is completed, with the results depicted in the Figure 113. The total weigh of this prototype, including the connector, is 10.85g, which is very close to the requirement of 10g per antenna.

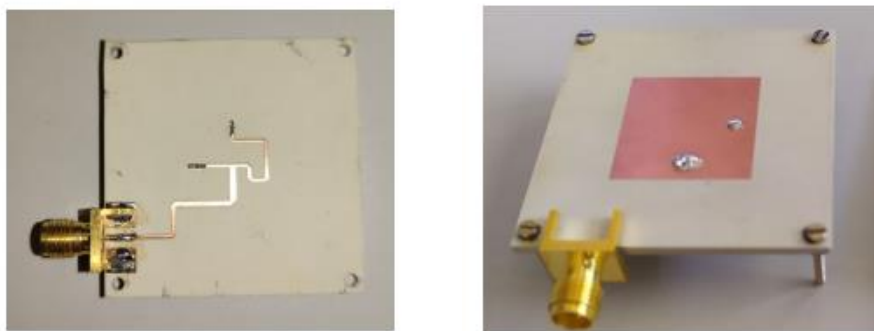


Figure 113. Fabricated prototype. Feeding network (left) and patch (right)

In the Figure 114, we see that the reflection coefficient is below the threshold of -10dB for the entire band of interest. However, we observe an shift down in frequency as compared to simulations. During the measurements, we could detect the appearance of cable currents, especially critical at lower frequencies in the range between 2.2 and 2.4 GHz. This phenomenon is a well-known effect that occurs to electrically small antennas, which can explain the presence of the cable currents along with the proximity of the radiators to the connector.

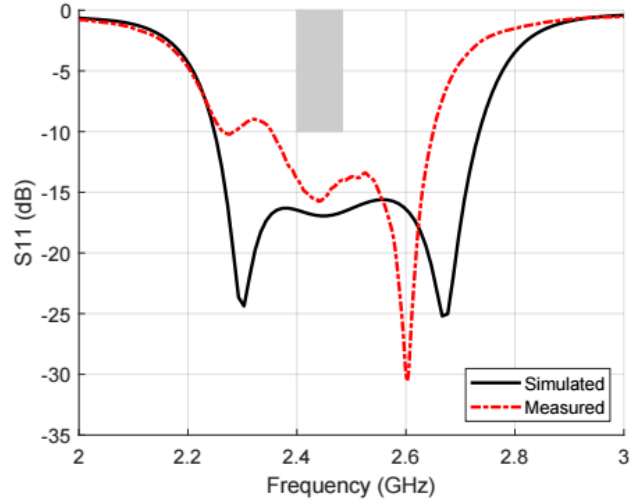
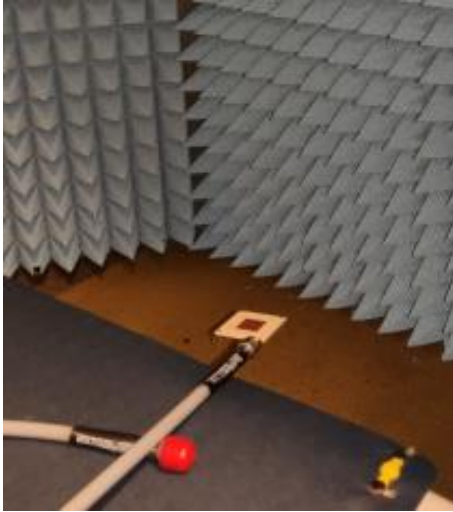


Figure 114. Reflection coefficient measurement setup (left) and results (right)

The radiation characteristics of the antenna were tested in the anechoic chamber. The most remarkable variation with respect to simulations is a shift of the AR minimum in the broadside direction of the antenna. As one can see in Figure 115, the AR is shifted down in frequency and is different for vertical and horizontal cuts. This shift does not occur in simulations and is not typical of patch antennas. It potentially comes from the asymmetrical design of the patch and the contribution of the cables to the radiation. We use this prototype as a starting point to debug these problems and produce a refined prototype.

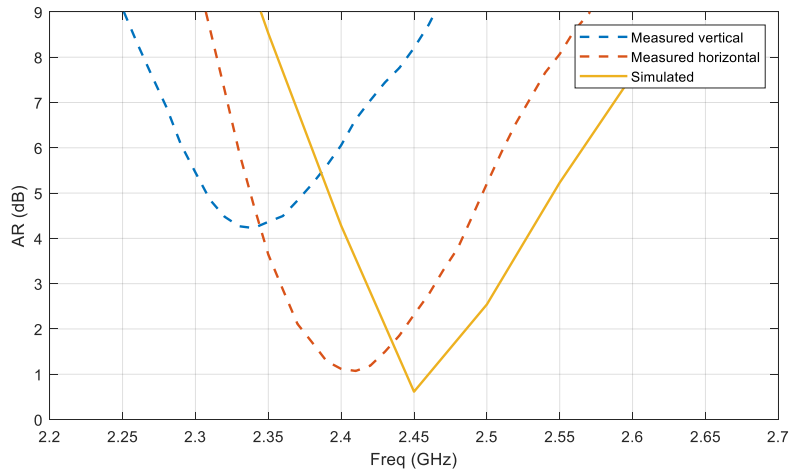


Figure 115. Axial ratio simulated and measured in both cuts

4.4.3.2 Prototype debugging. Addressing cable and ground currents

To debug and minimize the cable currents, we did several tests and variations in simulation on the first prototype to reduce the effect of the cable on the operation of the antenna. For the sake of simplicity, we only show a few of these tests.

One of the variations is to move the cable to the bottom of the PCB and away from the slots, as depicted in Figure 116. This allows to minimize the effect of the connector position on the pattern and its polarization. To assess the effect of the cable currents, we analyze the complex magnitude of the current density in the ground plane. We see in Figure 117, that indeed the cable changes the distribution of the currents in the ground and therefore also the excitation of the slots.

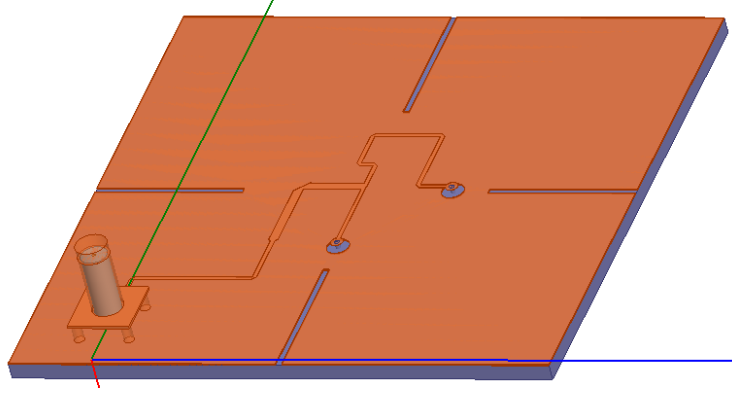


Figure 116. Modified design with the cable underneath the antenna

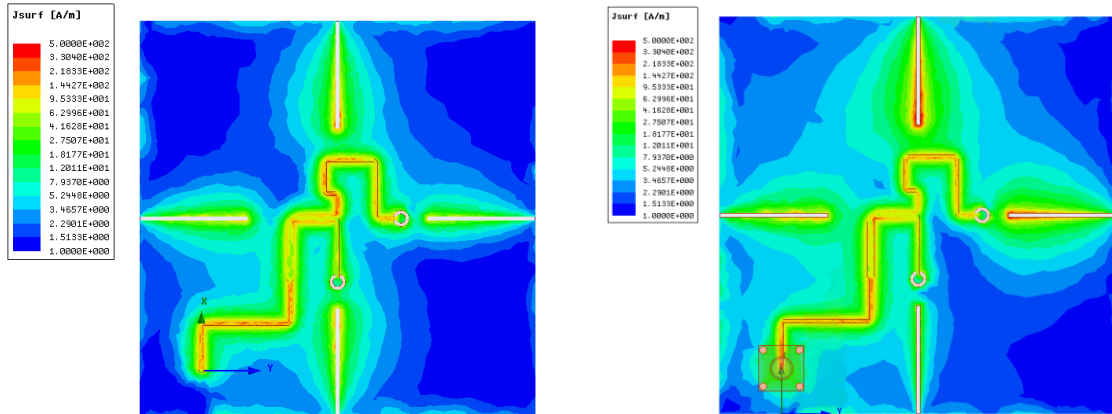


Figure 117. Complex magnitude of the current density at 2.35GHz with lumped port (left) and a cable with length of 20mm (right)

To continue our tests, we added a magnetic boundary on the cable shield, which artificially removes any the cable currents on the radiation. The reflection coefficient for different cable lengths with and without the magnetic boundary is shown in Figure 118. We can observe how the lower frequencies are very affected by the cable currents without magnetic boundary while this effect does not occur if we use a magnetic boundary. This confirms that the origin of the discrepancies between simulated and measured results from the prototype were due to the cable currents, and we explored various solutions to remove them.

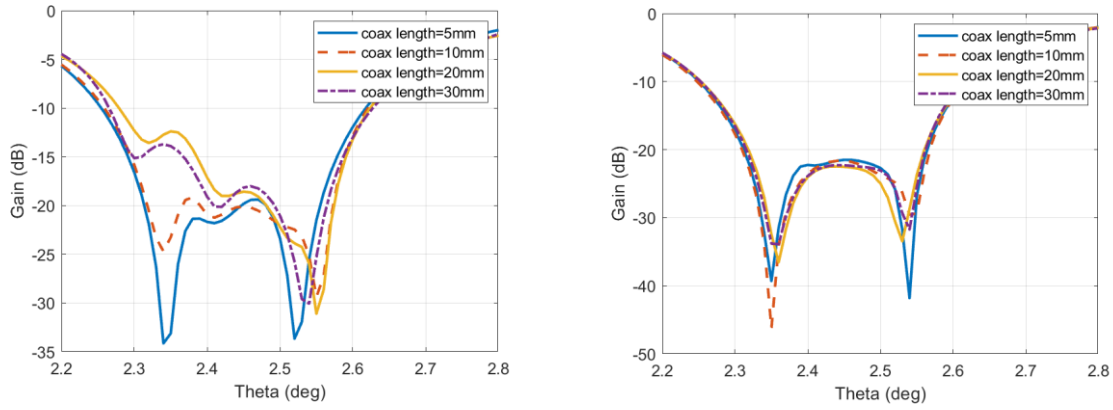


Figure 118. Effect of the cable in the lower frequencies without (left) and without (right) an H boundary on the cable for various cable lengths

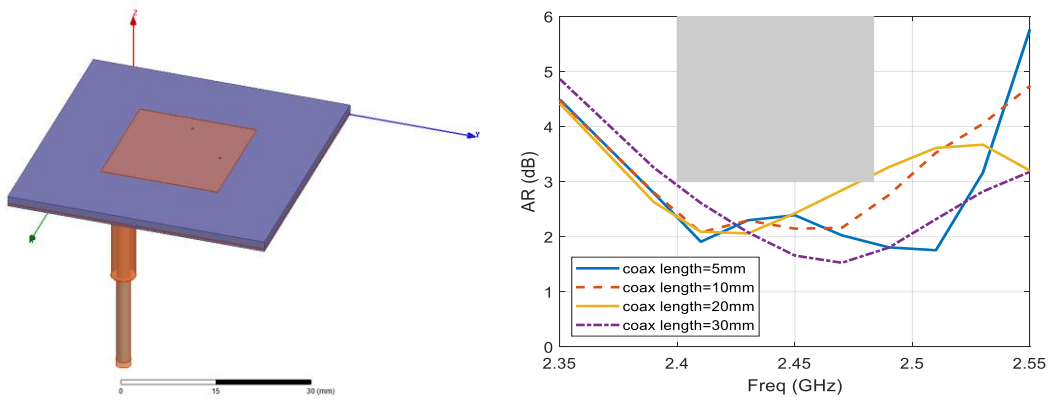


Figure 119. Design of antenna using bazooka balun on the coaxial cable (left) and its AR (right)

One of the practical solutions to diminish the cable currents is the implementation of a bazooka balun, that forces an open circuit at the interface between the cable and the antenna. The balun prevents the currents to circulate on the coaxial shield. We see in Figure 119 [1]. Indeed, the variation of the reflection coefficient depending on the cable length is reduced by the balun, maintaining a reasonably stable AR below the threshold. These results prove that a bazooka balun could be a potential solution to the cable currents. It would, however complicate the fabrication and add weight to the cable.

After the research on the cable currents, we decided to tune very carefully the feeding network and the antenna, to move the AR minimum to the band of interest and to bring the cable currents down in frequency and away of out band of interest.

4.4.3.3 Final prototype and validation

For the design of the final prototype, we gathered all the insight obtained through several iterations of prototypes and a thorough analysis in simulations. The adjustments made and considerations for the final prototype are the following:

- We optimize the feeding network separately. The substrate used for the feeding network is very thin (0.381mm) and therefore the impedance of the microstrip line is low. We change the connector for another with a smaller centre pin
- Due to the discrepancy in radiation characteristics in the two planes of the antenna, we modified the feeding network in order to bring the connector away from the slots. By doing this, the two perpendicular modes of the antenna are affected in a similar measure by the presence of the connector. This keeps the AR minimum in the same range of frequency for the two perpendicular planes of the antenna.
- One cannot define properly a port for electrically small antennas. Since the cable is included in the final antenna to be assembled on the drone, we decided to include the cable at its actual length to the antenna design. A system test of the antenna and the cable will be performed in Chapter 5.
- We considered the frequency shift of the AR seen in the previous prototypes in the design and compensated for it. We created two designs adjusting the AR minimum to slightly different frequencies to ensure to get more samples and compare them.
- We add a socket for the connector on one antenna corner, so that it can eventually be used to attach the antenna to the support on the drone.
- The ground shape has an effect on the potential improvement of the beamwidth enhancement. Trimming the corners increases the beamwidth and reduces the size. However, we should not trim it too much if we want to minimize the cable currents.
- We realized that the measurement support has a strong effect on the measurements, as it is very close to the antenna and is. A reflected wave in the backwards cross pol is reflected to the front in the coherent circular polarization.

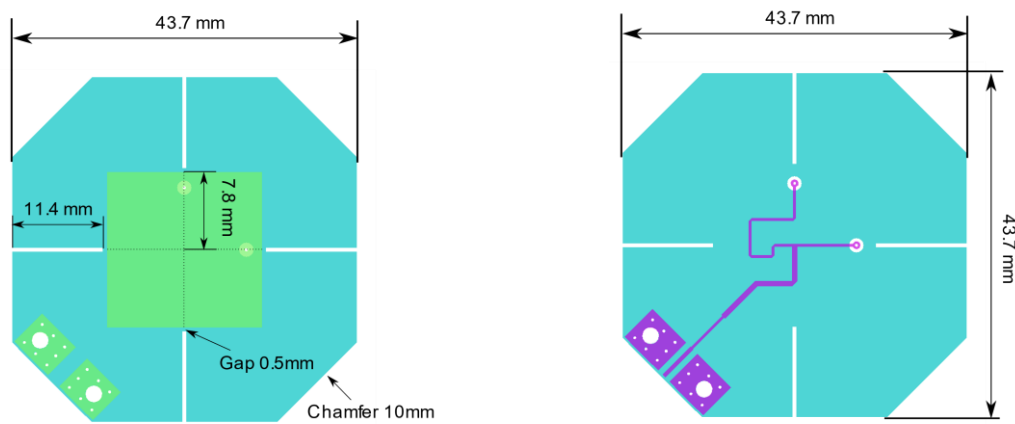


Figure 120. Design of the final prototype. Top (left) and bottom view (right).

The results from the simulations are shown in Figure 121. The impedance bandwidth is around 400MHz (16%) and the pattern is very stable in frequency, with a gain of 3.5dBi and a HPBW between 114° and 117° in its three main pattern cuts. The AR in frequency and angle is also satisfactory and as expected from the results in Figure 122.

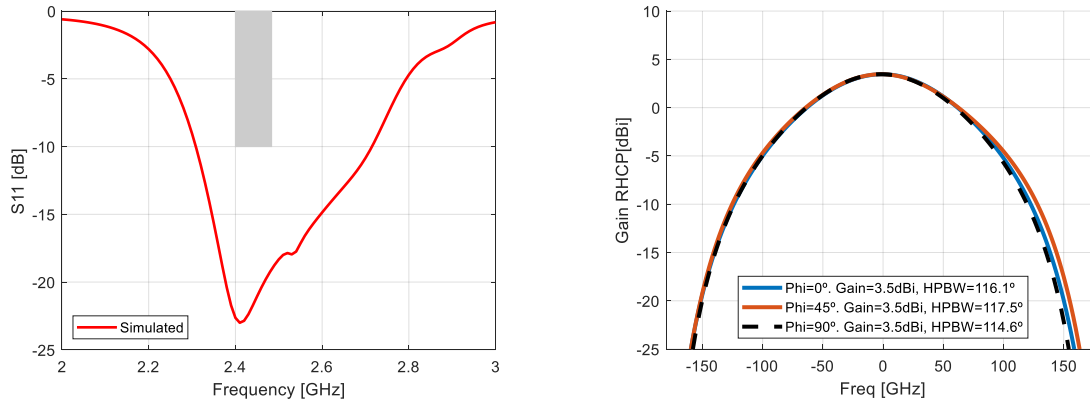


Figure 121. Simulation result. Reflection coefficient (left) and pattern (right) of the final designs.

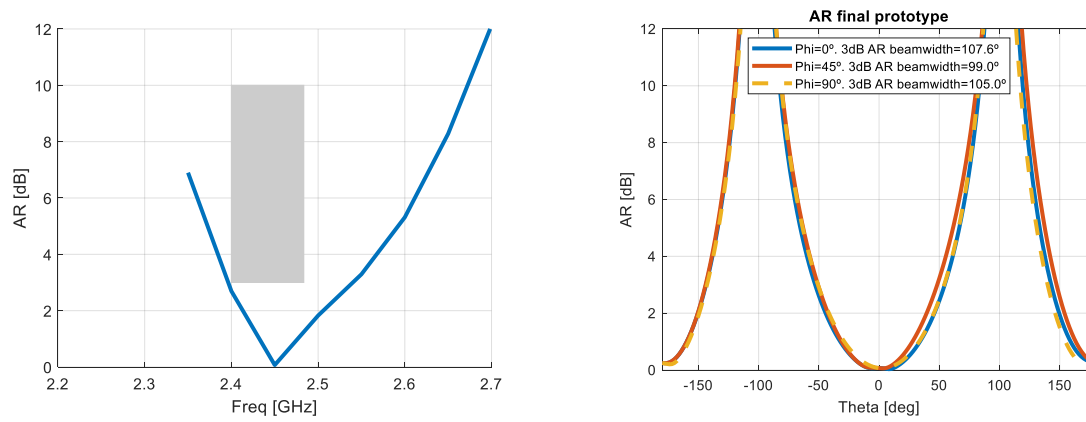


Figure 122. Simulation results. AR vs freq (left) and vs angle (right).

This antenna is composed of two layers of TMM 10 substrate: one for the antenna and another for the feeding network, of thicknesses 1.27mm and 0.381mm, respectively. We glue the two layers together, and we connect the feeding network and the patches by passing two pins through the substrates and soldering on either side. The resulting prototype is shown in Figure 123. For this antenna, we keep an SMA connector to measure the response of the antenna with the lab equipment.



Figure 123. Final prototype of the circularly polarized broad beam patch antenna

The size of the antenna is $43.7 \times 43.7 \times 1.7 \text{ mm}^3$, which slightly exceeds the requirements of $40 \times 40 \text{ mm}^2$, but, as the corners are trimmed its volume is 3250 mm^3 and it complies with a broad margin with the maximum requirement of 8000 mm^3 , thanks to its very low profile. The weight of the antenna and the connector is 13.16 g , were 4.2 g are due to the connector and 9 g for the antenna. As mentioned, this connector is temporary and a smaller one can be used, or the cable could be directly soldered to the antenna. This what would allow this antenna to comply with the weight limitation as well, even if it is close to it with the SMA connector.

	Size mm^3	Volume mm^3	Weight (g)
Requirements	$40 \times 40 \times 5$	8000 mm^3	10
Prototype	$43.7 \times 43.7 \times 1.7$	3250 mm^3	13.16 with connector and 9 (without connector)

Table 8. Mechanical requirements and actual values of the prototype.

In Figure 124 we can observe how f antenna is matched over a bandwidth of 250 MHz , including the band of interest.

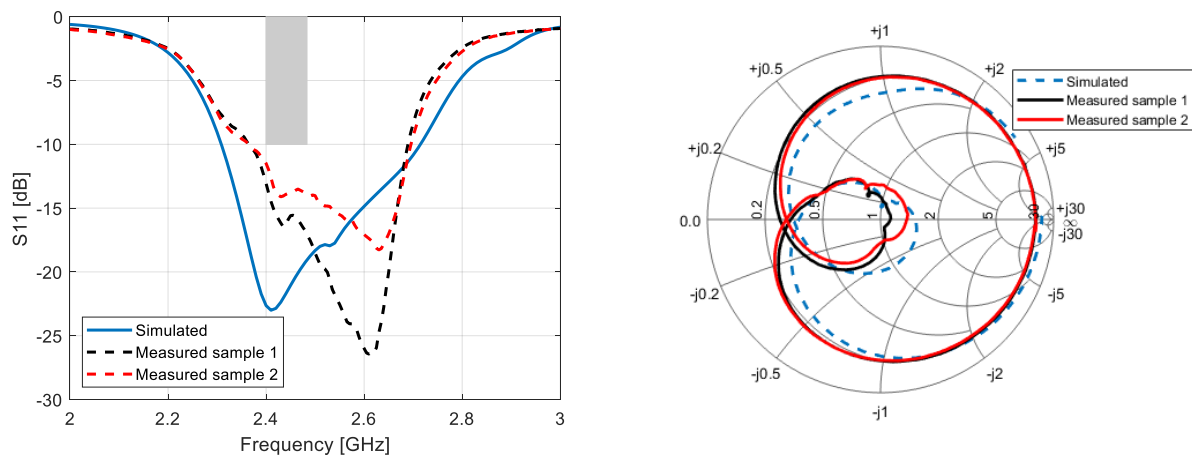


Figure 124. Measured and simulated S_{11} of the final prototype. Bandwidth $\sim 250 \text{ MHz} > 100 \text{ MHz}$

We measure the antenna in the anechoic chamber (see Figure 125). For the measurements we use tape to suspend the antenna and avoid using plastic support, as we could find that the setup affects the measurements due to the broad beam and the back radiation. In Figure 126 we can see the results for the gain and the patter. The pattern is broader than for a regular patch, for the three plane cuts of the pattern in which we measured the antenna. The shape of the pattern is not monotonously decreasing from broadside as it is for the simulations due to the effect of the support, but the variation of the gain in the range from -90° to 90° is in all the cuts less than 10 dB .

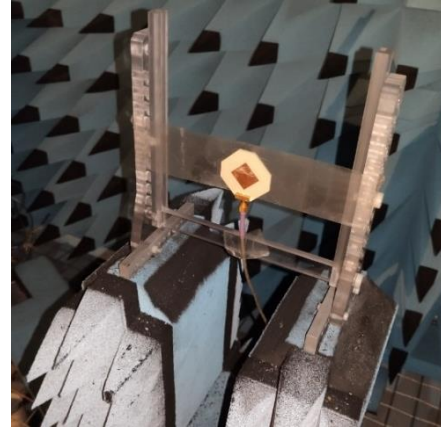
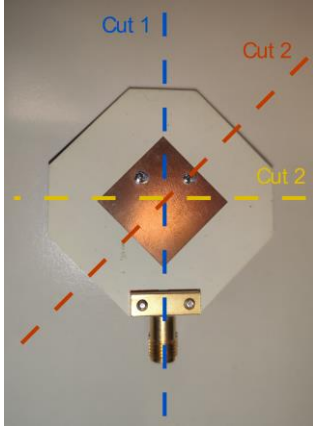


Figure 125. Final prototype of the CP broad-beam antenna in the measurement setup in the anechoic chamber.

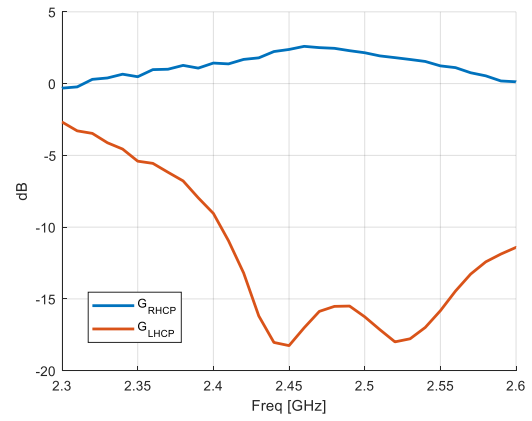
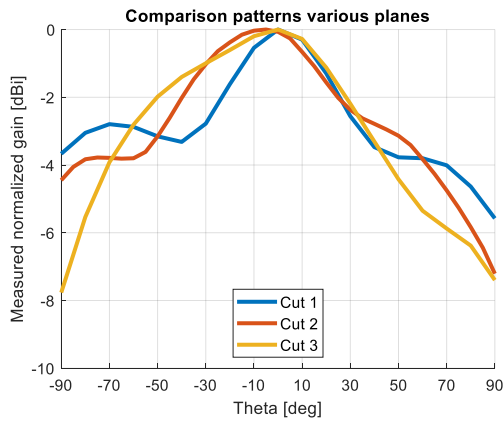


Figure 126. Measured pattern (left) and gain (right) of the final prototype. HPBW of 90°, and 6dB beamwidth of 150°. Gain of 2.1dBi @2.4 GHz, 3.2dBi @2.46 GHz and 3.1dBi @2.48 GHz. The gain variation with two antennas combined is of 6dB, below the maximum required of 10dB.

The AR in frequency is broad compared with regular CP patches [71], and the angular aperture below 6dB covers up to 140° for the three cuts that we have measured. We can observe how the 3dB AR beamwidth is larger than 120° in all the three samples. The AR bandwidth is also broad with a good margin.

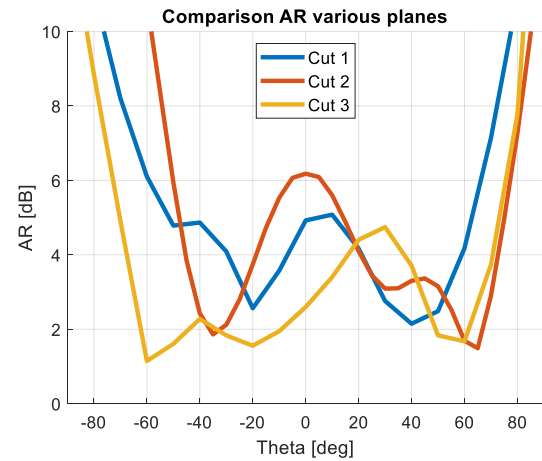
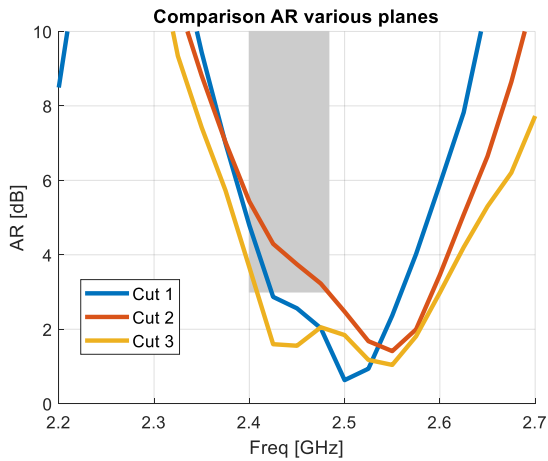


Figure 127. Measured axial ratio of the final prototype vs frequency (left) and vs angle (right). The AR bandwidth is of 200MHz and the AR is below 6dB for 120-140°.

We compare the results from the prototype to the normalized patterns of typical patches to assess how much we it reduces the variation in the upper hemisphere to the antenna. In Figure 128 we can see the normalized pattern for three cases:

- A regular patch antenna with a 5880 substrate with permittivity of 2.2 and a thickness of 1.27mm.
- A regular patch antenna with a TMM 10 substrate with permittivity of 9.2 and a thickness of 1.27mm. This one is physically smaller, and as we can observe, the beamwidth is broader than for the previous antenna. While its beamwidth is acceptable, its bandwidth is insufficient as the permittivity is very high. This is explained in detail in Section 4.3.2.1 for LP antennas and in Section 4.4.2.
- The measurement for the fabricated prototype CP antenna with four slots and including feeding network.

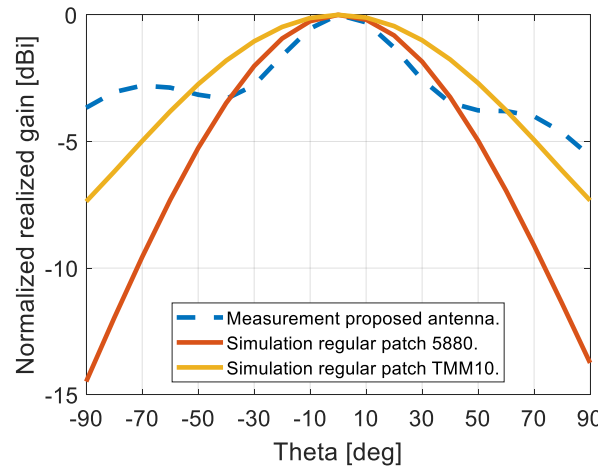


Figure 128. Comparison of the pattern of three antennas: proposed antenna (measured), and two regular patches using a substrate with a permittivity of 2.3 and 9.2.

The three results in Figure 128 the patch using a low permittivity substrate has the narrowest beamwidth among the three. For an antenna that has been miniaturized using a high permittivity substrate, the beamwidth is already very enhanced, as its effective aperture is smaller. The measurement of the proposed prototype adds the slotted ground technique to the miniaturized effective aperture to further increase the beamwidth.

We can conclude that the results are satisfactory for the standalone prototype, as the gain variation in one hemisphere is considerably diminished compared to the case of a regular patch, and meets the electrical and mechanical requirements for our application.

To assess the effect of the proximity of the cage to the antennas, we performed tests of the patches including the effect of the cage during the refining phase of the prototypes. In terms of reflection coefficient, the antenna remains matched as long as we keep it at a distance larger than 3cm from the cage (avoiding near field coupling). The pattern measurements in the anechoic chamber do not provide meaningful results as the phase center of the antenna is modified by the cage and the measurement is then not well defined. This is especially critical for axial ratio measurements, as this parameter is especially sensitive.

The measurements in the chamber only provide a qualitative check of the beamwidth, that only allows us to discard significant changes in the shape of the pattern that would invalidate the required hemispherical coverage of the antennas with less than 10dB variation. The characterization of these antennas should therefore consider not only the effect of the cage and antenna positioning, but also the multipath channel between the drone and the remote controller. The validation of these antennas becomes then a more complex problem, that can be seen as an antenna and propagation characterization, and to define a quantitative benchmark on the performance of these antennas should be done at system level. The system measurements to validate the performance of the antennas is presented in Chapter 5.

4.5 Conclusions from this chapter. Broad-beam LP and CP low profile antennas

We summarize here some conclusions extracted from the designs, fabrication and measurements of the antennas presented in this Chapter.

- Using additional elements is an effective solution to increase the beamwidth of microstrip patch antennas.
- We present a technique that makes use of slots as additional elements integrated in the antenna structure and passively activated by the patch, which is the only element that is connected to a feeding.
- One of the main advantages of using the ground slots is that this technique provides a very good bandwidth, that helps to achieve a better frequency stability for a smaller size.
- For linearly polarized designs using the passively activated slots, we can enhance significantly the beamwidth (more than 180°), but only in one plane.
- For circularly polarized designs using the passively activated slots, the achievable beamwidth is around 130° .
- The patches with ground slots, both in LP and CP, are robust to fabrication tolerances thanks to the coherent feeding of all the slots by the patch.
- With the presented technique we can increase the beamwidth and the bandwidth, but not the AR beamwidth due to the several elements contributing to the radiation.
- As expected for designs of broad beam microstrip antennas, the patch + slotted ground technique also increases the back radiation.
- The size of the ground should be considered carefully to avoid or minimize cable currents.
- The measurement setup for very broad-beam antennas should be carefully done and verified to get reliable measurements.

We also summarize in Table 10 and Table 9 the main antennas presented in this Chapter, to get an overview of their advantages and disadvantages, in terms of beamwidth, bandwidth and size.

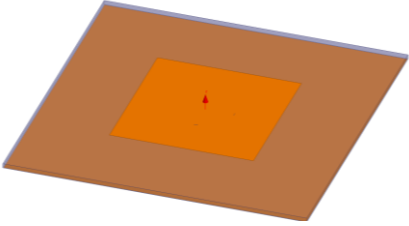
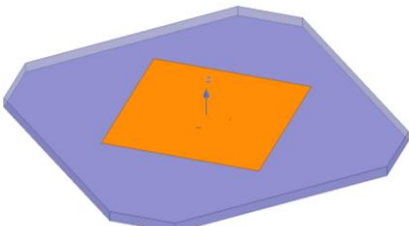
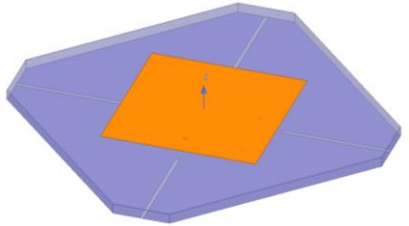
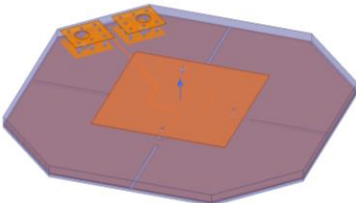
CP antennas	Substrate	Size	Bandwidth	HPBW and CP gain	Remarks
<p>Canonical patch</p> 	Rogers 5880 (2.2)	84x84x1.27mm ³	30 MHz	75° - 7.6dBi	
<p>Patch miniaturized with high permittivity substrate Section 4.4.2</p> 	TMM 10 (9.2)	48.2x48.2x1.27mm ³	21 MHz	104° - 3.2dBi	<p>Using ideal feeding with lumped ports</p> <p>Size smaller due to trimmed corners</p>
<p>Ideal CP + slotted ground Section 4.4.2</p> 	TMM 10 (9.2)	48.2x48.2x1.27mm ³	310 MHz	120° - 2.5dBi	<p>Using ideal feeding with lumped ports</p> <p>Size smaller due to trimmed corners</p>
<p>Real CP + slotted ground Section 4.4.3.3</p> 	TMM 10 (9.2)	43.7x43.7x1.7mm	410 MHz	110 – 115° - 3dBi	<p>Size smaller due to trimmed corners</p>

Table 9. Comparison of all the CP antennas presented in the Chapter

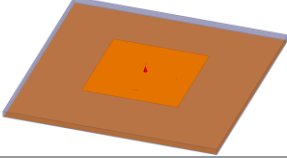
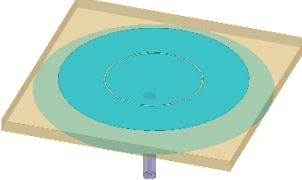
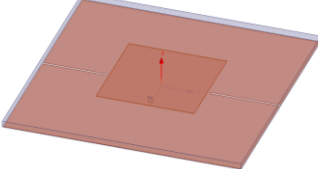
LP antennas	Substrate (ϵ_r)	Size	Bandwidth	HPBW and CP gain	Remarks
Regular patch 	Rogers 5880 (2.2)	84x84x1.27mm ³	30 MHz	90° - 7-9dBi	
Circular patch + higher order mode ring Section 4.2 	Rogers 5880 (2.2)	140x140x6.35mm ³	120 MHz	159° - 4.4-5.2dBi	Single feeding
Patch with slots Sections 4.3.2 and 4.3.3 	TMM10 (9.2)	47.8x47.8mm ²	100 MHz	220° - 4.7dBi	Single feeding Validated by measurements Tunable pattern (and gain)

Table 10. Comparison of all the LP antennas presented in the Chapter

5 Analysis of the cage and system measurements of the antennas assembled on the drone

In this Chapter, we focus on understanding the effect of the geodesic cage surrounding the drone on the antenna performance. This is structured in two parts which are intrinsic to the application: understanding the effect of the cage and evaluating the performance of the antennas with realistic system measurements. The goal is to provide a general qualitative understanding of the effect of the cage, and to validate the reliability of the antennas in LOS and NLOS environments, which is the most critical parameter for our application.

5.1 Analysis of the cage effect using canonical antennas and MoM

The wavelength at the frequency of operation of 2.45GHz is 122.5mm, and thus the diameter of the geodesic cage, of 400mm, is electrically large. To simulate the full cage, we use a Method of Moments (MoM) solver that simulates linear wires faster than other full-wave simulators (e.g Finite Element Methods), that discretize the geometries and therefore their complexity increases rapidly with the electrical size of the structures. The MoM solver that we use is *Numerical Electromagnetic Code 2*, NEC2 [72, p. 2]. We use this solver as a core, and control it using a MATLAB code that generates the input files and parses the output files. We also use as a support 4NEC2, a NEC2 distribution that adds a GUI to the solver and is very useful to debug and visualize the geometries and the results.

5.1.1 Analysis of the cage effect using canonical antennas and MoM

To analyse the effect of the cage on the radiation pattern, we place a canonical antenna, a resonant dipole, in the center of the cage, enclosed completely by the geodesic structure, as we can see in Figure 129. The dipole is oriented along the X axis, which means that there is a zero in the radiation pattern in this direction and it is omnidirectional in the YZ plane. We can see in Figure 130 the radiation pattern of the dipole when it is enclosed inside the cage. We observe that the pattern is not omnidirectional as it would be for the standalone dipole, with ripples that are caused by the interaction of the radiation with the pentagons and hexagons, given their different rod lengths. We observe that the gain is higher in the directions where there are pentagons in the structure, showing how each part of the cage affects the propagation of the waves.

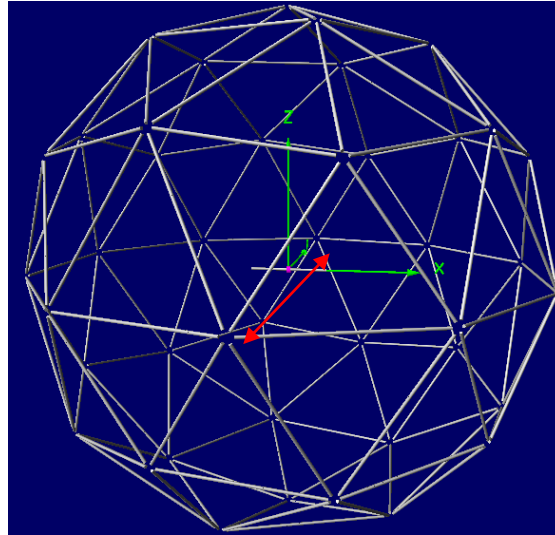


Figure 129. Cage with a resonant dipole that we move along the Y axis.

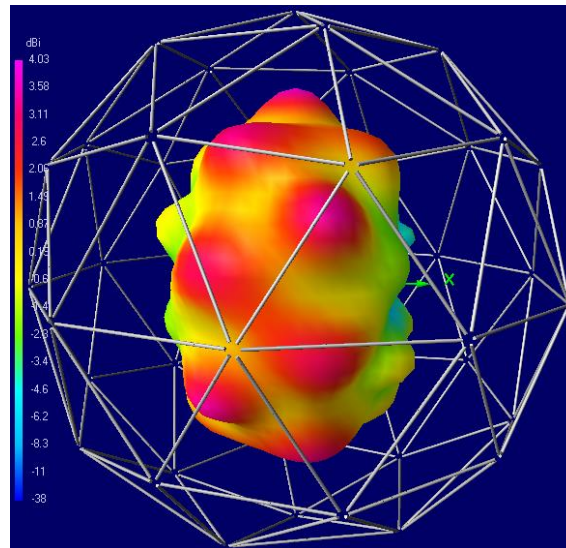


Figure 130. 3D radiation pattern of the resonant dipole along the X axis, centred in the cage (left) and moved 170mm from the centre, towards the cage and along the Y axis (right)

To assess the effect of the cage for different antenna positions, we move the antenna closer to the cage along the three different cartesian axes. In Figure 131, we use 2D plots for a clearer representation of the patterns, where we compare the pattern of the dipole moving along the Y axis inside the cage. The YZ plane is represented at $\Phi=90^\circ$, at the centre of each plots. We can see how the closer to the cage, the greater the variation in $\Phi=90^\circ$, due to the higher gain in the direction to which the antenna is approaching the cage. We can also observe the peaks of gain directed to the pentagons.

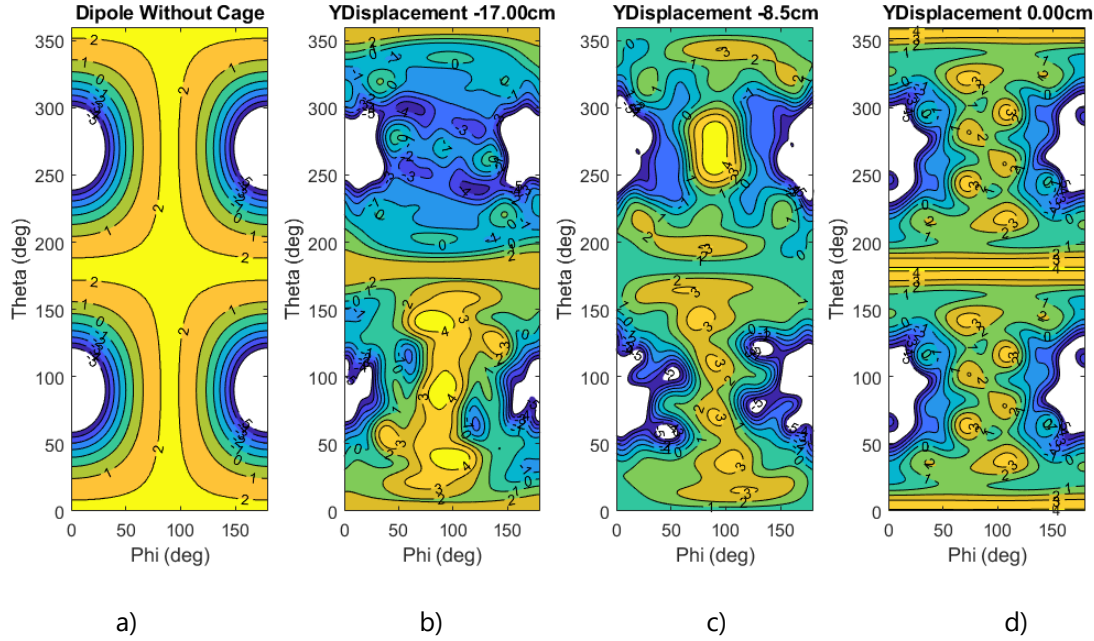


Figure 131. Gain of the dipole without cage (a), at -17cm from the centre (b), at -8.5cm from the centre (c), and at the centre (d). We are displacing the dipole in the hemisphere contained from theta 0° to 180°

To quantify how much the gain varies, we define as a figure of merit the gain variance, as the difference between the maximum and the minimum gain along the direction of max gain of the standalone dipole (at $\text{Phi}=90^\circ$). We can observe in Figure 132 that the gain variance is smaller when the antenna is at the centre of the cage, which comes from the fact that there is no focusing of the power towards one side of the cage. The gain variance is very similar when we move the dipole along the Z or Y axis. This is because these two axes are both perpendicular to the length of the dipole (direction of maximum gain), and thus the variation only depends on the different geometry of the cage along the two directions. The gain variance is smaller when we move the dipole along the X axis. The radiation of the antenna in this direction is minimum as there is the null in its pattern, and the interaction with the cage will be smaller as the dipole gets closer to it. We should note that the very small value in the blue trace in Figure 132 occurs because the dipole touches the cage and the simulation it is not valid.

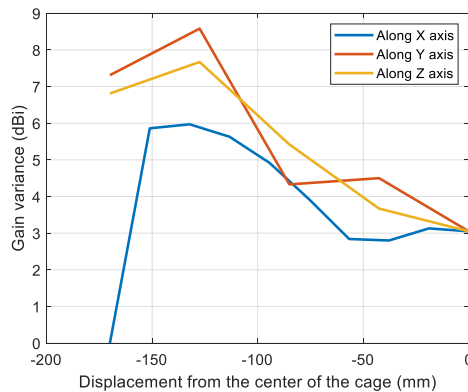


Figure 132. Gain variance computed moving the resonant dipole along the X, Y and Z axes of the cage, from its centre.

Let us now visualize the effect of the cage on the fields, looking at the near fields, which are represented in Figure 133, in the plane that contains the dipole. We can see how the dipole interacts more with the side of

the cage that is closer to it, and less with the opposite side. The magnitude of the fields induced in the segments of the cage is more significant as the antenna is closer to the cage. This effect is more significant in Figure 133 because all the cage segments are in the same plane as the dipole. The cage leads to the modification of the pattern of the dipole, transforming it into a directional pattern. Also, we observe how the interference pattern inside and outside the cage is very different in both cases, depending on the relative position of the antenna and the cage, and how the rods are excited.

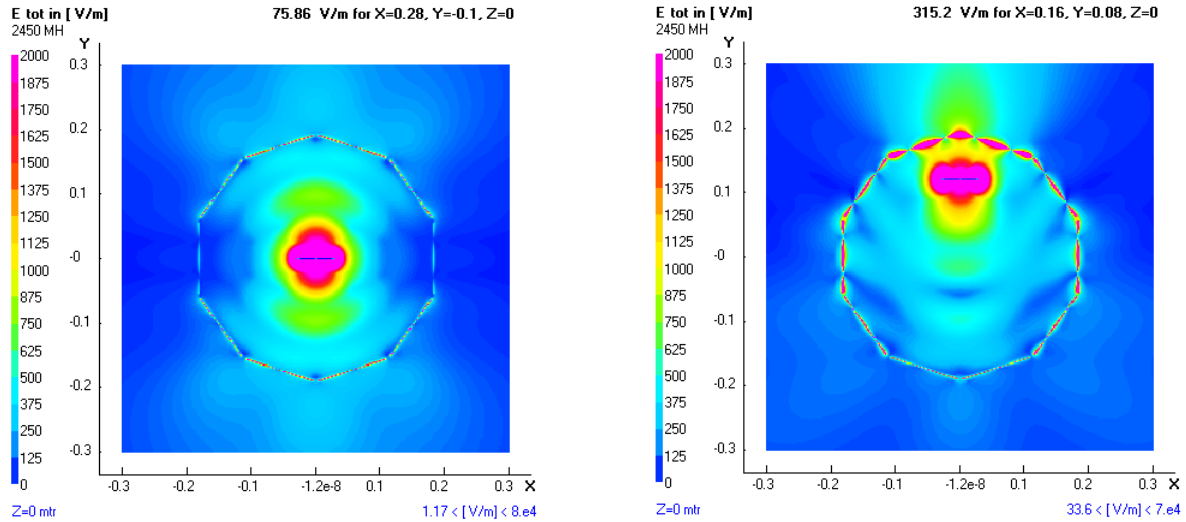


Figure 133. Near field plot of the dipole centred inside the cage (left) and at 12cm from the centre (right)

5.1.2 Analysis of a sector of the cage using a directional antenna

Once we have seen the effect of the entire cage, we analyse only one sector of the cage. Using only a portion of the cage allows us to use a Finite Element Based Simulator, provides a simplified vision of the effect of the cage, which allows us to modify it, understand, and isolate the effect of each change. The objective is to gain insight on the interaction between an antenna and the cage, and also on how the waves propagates through the structure. As we use a section of the cage, we use a directional antenna to illuminate the sector. In this case, we decide to use a Yagi as it a natural modification of the dipole to make it directional and is also linearly polarized.

In Figure 134 and Figure 135, we can see the distribution of the E field of the Yagi, and the effect of modifying the entire or parts of the cage with a perfect H boundary. We can see how adding a H boundary on the full cage significantly improves the transmission of the power from inside towards outside of the cage, which comes from the fact of forcing an open circuit boundary condition around the rods. This can also be seen when we add the H boundary to one of the rods, but the fields in the rest of the PEC rods remains as in the case with all the cage using PEC.

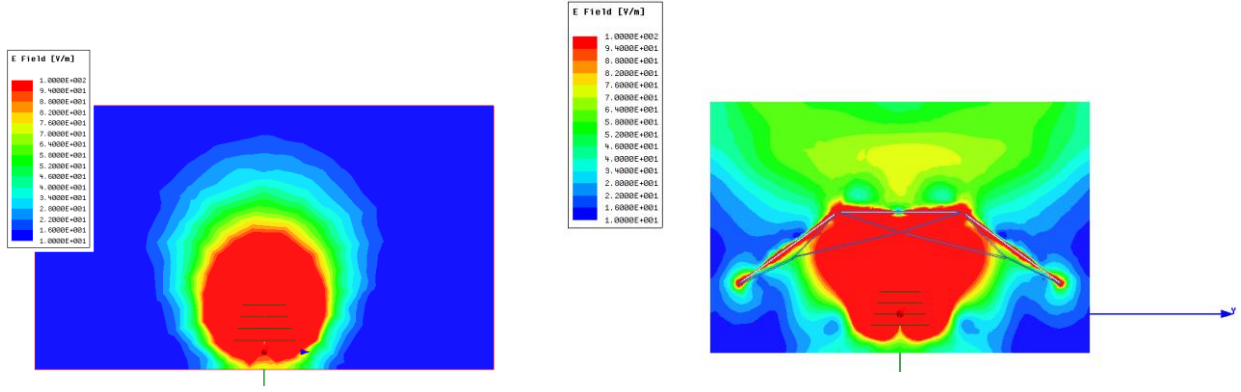


Figure 134. Fields distribution on the XY plane for a Yagi (left) and a Yagi with a portion of cage (right)

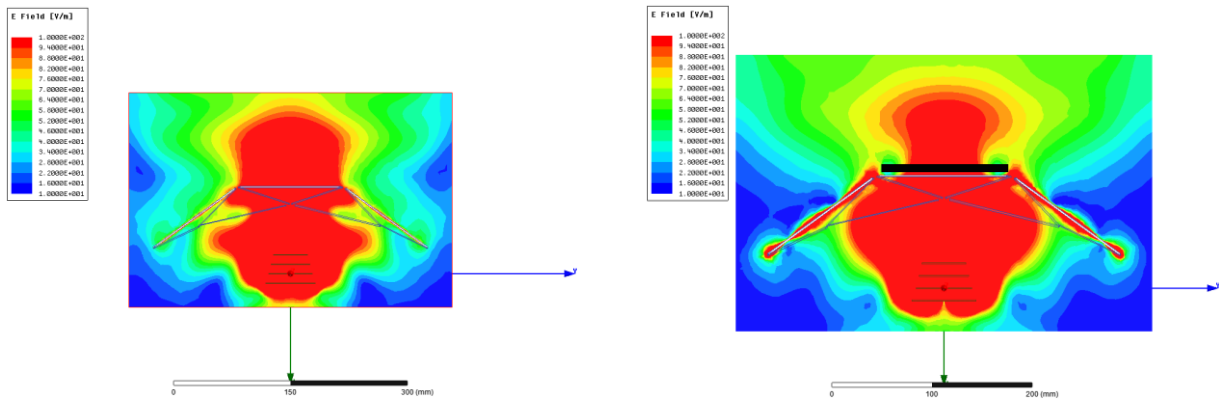


Figure 135. Fields distribution on the XY plane for a Yagi and full cage with H boundary (left) and with PEC cage and H boundary only on the rod parallel to the Yagi, in black (right)

We understand that modifying one rod allows to modify the transmission through the cage, but ultimately the contribution of all the rods generates an interference pattern outside and inside the cage that alters the propagation of the waves. From the results in Figure 134 and Figure 135, we can grasp that the propagation of the waves through the structure is complex. Not only are the rods reradiating, creating an interference pattern that changes the pattern, but also a part of the power is reflected back to the antenna. It is therefore important to understand how the cage reflects power back into the drone and how it perturbs the pattern and the polarization of the waves that manage to propagate through the structure.

5.2 Analysis of the power transferred through the cage and the polarization of the radiated wave using infinite periodic array theory

The radiation pattern of an isotropic antenna is, by definition, a sphere, as it radiates equally in all directions of the space. If we take as a source an **isotropic antenna** and place it inside that sphere, the radiated wave from the antenna arrives with same amplitude and phase to each part of a sphere surrounding the antenna. If we

assume that the cage is perfectly spherical, we can approximate the problem of the propagation through the cage by treating the cage as an **infinite periodic array**. This approximation is reasonable to get a qualitative assessment of the waves transmitted through the cage or reflected by it.

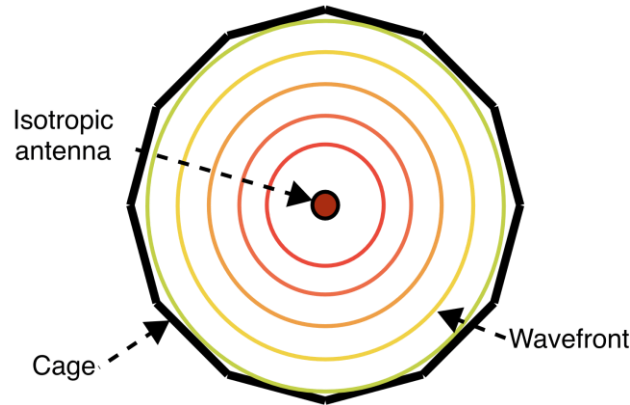


Figure 136. Illustration of a cut of the cage with an isotropic antenna in its center. We can assume that the waves have the same amplitude and phase when they arrive to the cage.

5.2.1 Definition of the experiment

To define the periodic structure, we need to separate it in planar irreducible unit cells, which are the minimum unit of the periodicity of the structure. An electrically large structure would support several transmitting modes, and therefore we need to reduce the size of the structure as much as possible. These cells can have various geometries, but it is mandatory that the faces along the dimension where there is repetition of the structure are parallel. To specify this repetition in *ANSYS Electronics Desktop*, we define Master and Slave boundaries on both sides of the cell to indicate the software how to generate the lattice of the structure [73]. A phase delay between the Master and Slave boundaries can mimic various angles of incidence in the structure of the impinging wave.

We analyse the geometry of the cage to define the cell, and we realise that we cannot use the cage's pentagons as not all its faces are parallel to each other. We can, however, use the hexagons that are created from putting various pentagons together. As for the analysis the cells should be planar, we generate an approximation of the cells within a plane and taking the longest size of the rods: $131\text{mm} \sim 1.07\lambda$ @ 2.45GHz . In Figure 138, we can see the final cell with parallel faces that we define for the experiment, and the assignment of one set of Master-Slave boundaries. We also assign the scanning Phi and Theta, that controls the incidence of the wave impinging on the cell. In our case we want to consider the incidences from all Phi angles, but only a small range of vertical incidence (in theta), from 0° (perpendicular incidence) to 40° . As the incidence angle in theta increases, the projection of the field on the structure is smaller and after a certain value of Theta_scan, the structure seen by the propagating fields changes significantly.

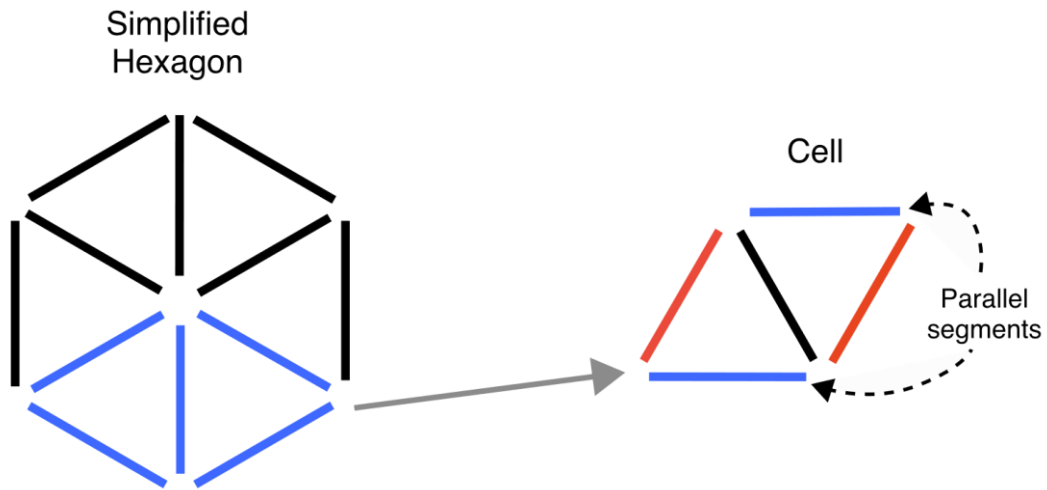


Figure 137. Simplification of a simplified hexagon to a smaller cell with parallel segments

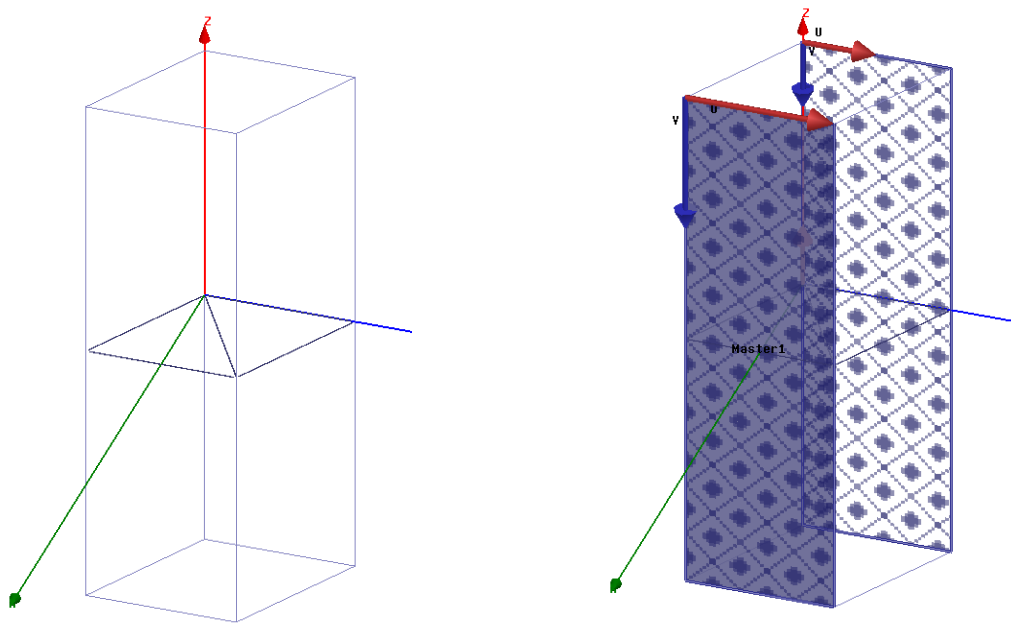


Figure 138. Definition of the cell on ANSYS Electronics Desktop (left), and definition of one pair of master/slave boundaries (right)

As we want to analyse the transmission and reflection of the waves through the structure, we define two Floquet ports as shown in Figure 139. As the cell is in the order of a full wavelength, and especially longer along its diagonal, a considerable set of modes is supported by the structure in our case. For an electrically smaller cell, the modes that propagate through the structure should be only the fundamental modes, and the attenuation of other higher order modes is not zero and they vanish.

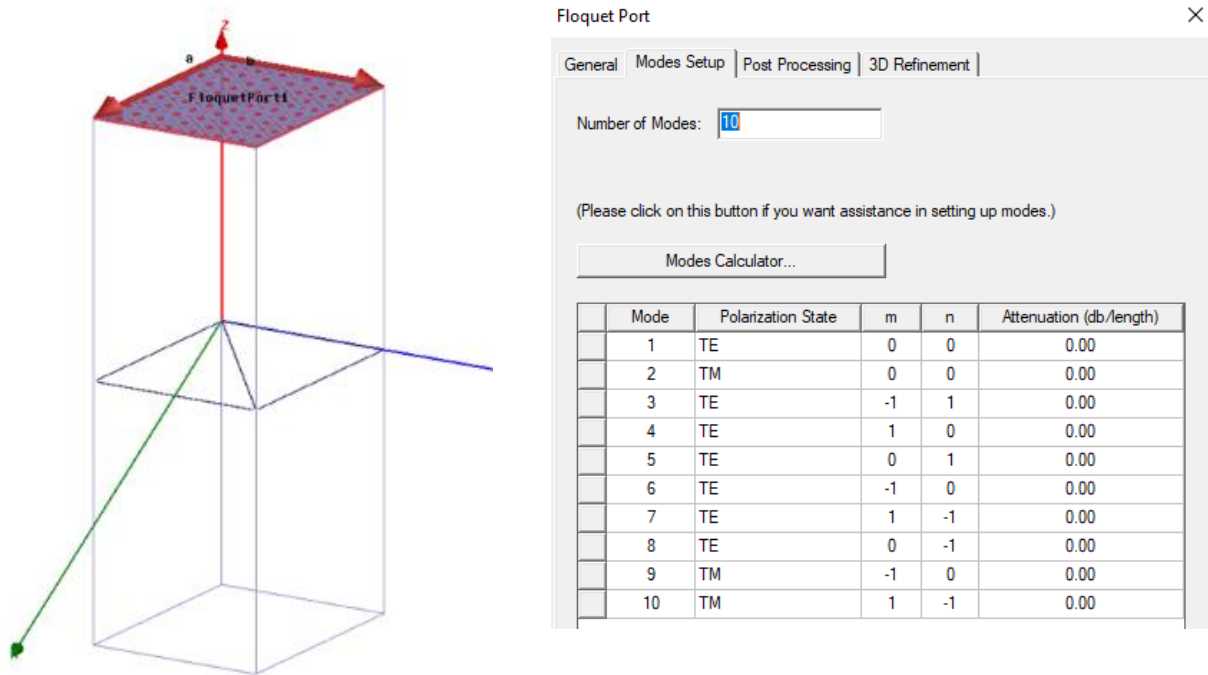
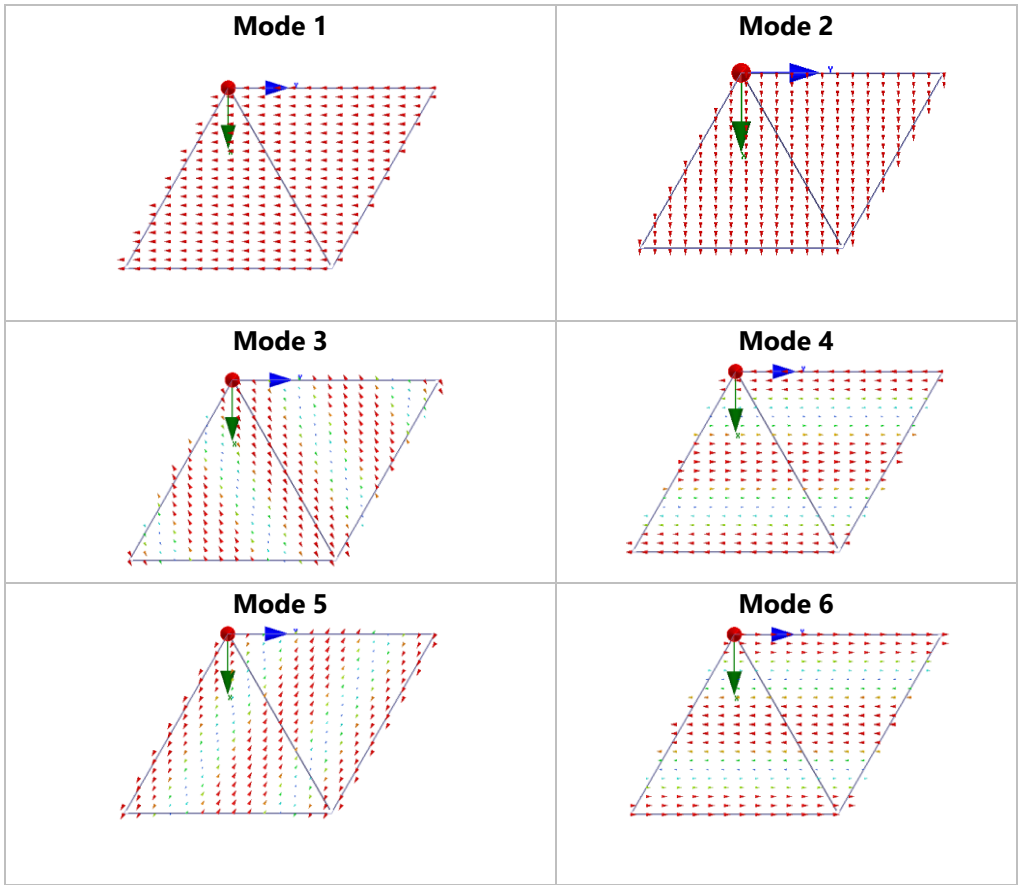


Figure 139. Definition of the Floquet ports and calculation of the 10 first modes analysed in the structure

The Floquet modes are depicted in Figure 140. We can see that some of them are equivalent but simply have a different phase, like the pairs 4-6, 5- 8 and 3-7.



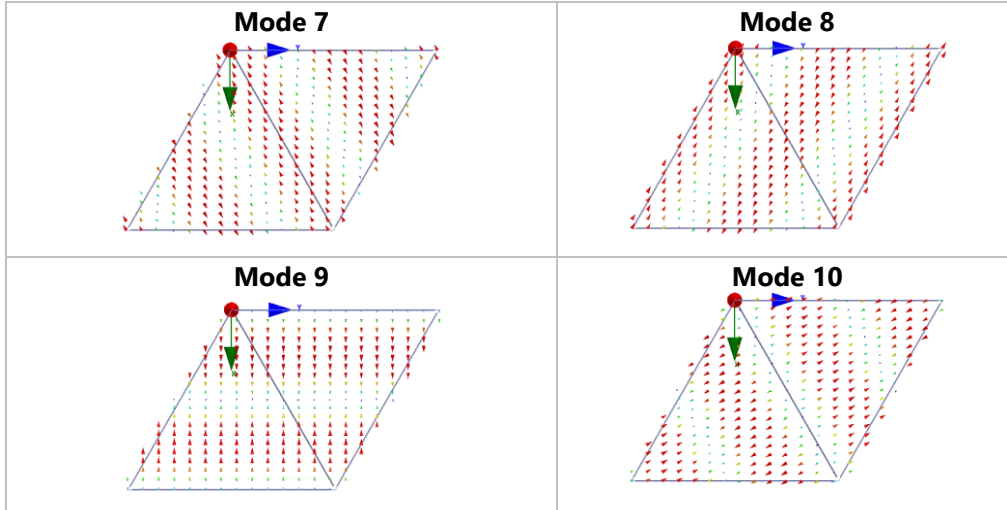


Figure 140. Modes modes excited by the two Floquet ports of the periodic structure.

Knowing the field distribution of these modes is important as it is needed to understand and interpret the results of the following sections.

5.2.2 Transmitted power through the structure. Perpendicular incidence

We analyse the transmission coefficient from port 1 to port 2 (S_{21}) for each mode in Figure 141. We can see that below 2.5GHz only modes 1 and 2 are transmitted through the structure as the transmission coefficient, is close to 0dB. Their behaviour is equivalent in terms of S_{21} , what comes in line with their similar field distribution (see Figure 140).

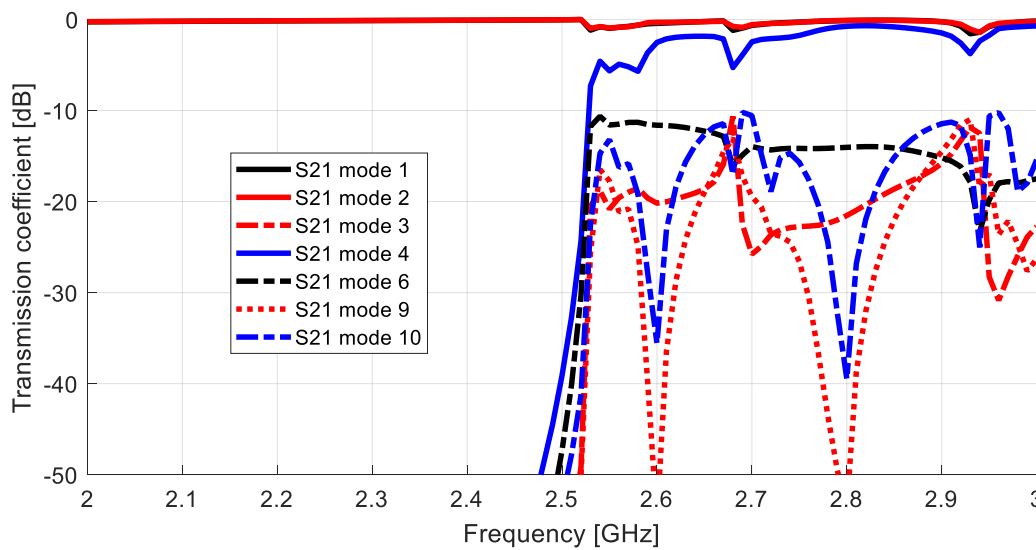


Figure 141. S_{21} for all 10 ports at a perpendicular incidence Theta scan= 0°

While the modes 1 and 2 have a cut-off frequency off the graph and below 2 GHz, all the other Floquet modes have a cut off frequency of around 2.5 GHz. We observe that above that frequency, the S21 for Modes 1 and 2 is more unstable. In our case, as we use PEC, there is no power lost or dissipated in the structure. Therefore, the power of one mode can be reflected back to the port, and we would see that in the S11; or it can be transmitted to the other port, and this can be seen in the S21. This means that the power is conserved as there is no dissipation. This is expressed in the next equation:

$$|S_{11}|^2 + |S_{21}|^2 = 1 \quad (5.1)$$

The condition of Equation (5.1) remains true within the same mode if there is no intermodal transmission. We can use it to assess if the structure modifies the waves in one mode and "transfers" part of its power into another mode. For example, if there is power transmitted from mode 1 to mode 2, that would mean a change of polarisation of the propagating wave that travels through the periodic structure.

We apply then the Equation (5.1) to the results of our analysis for the Mode 1. We can see in Figure 142 how there is no intermodal transmission below 2.5GHz. After 2.5GHz, the power of mode 1 transfers to other modes. We can see little reflections when the sum of S_{11}^2 and S_{21}^2 decreases. In some parts of the frequency spectrum the power transferred to other ports is as high as 30%. It is therefore important to understand this effect.

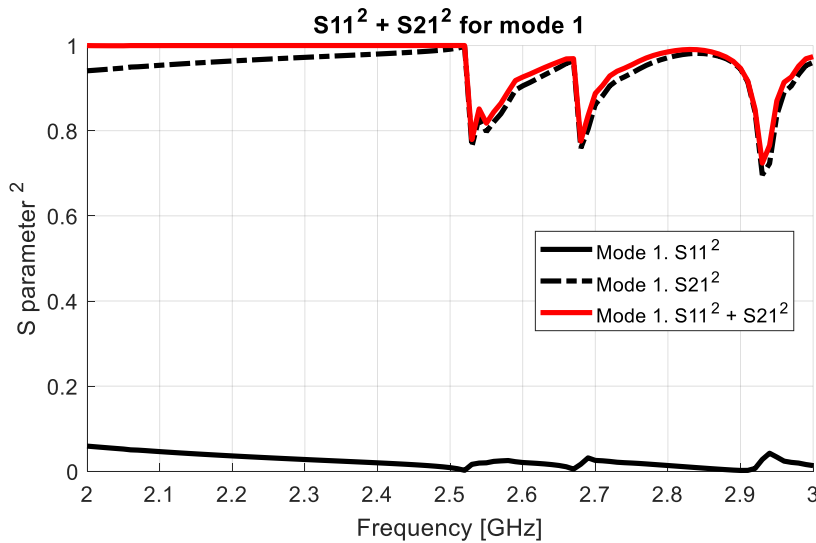


Figure 142. $|S_{11}|^2$, $|S_{21}|^2$ and $|S_{11}|^2 + |S_{21}|^2$ for mode 1

To assess how the power from mode 1 transfers to the other modes, we compute the ratio of the transmitted power to mode 1 in port 2 from all the modes in port 1. The result is depicted in Figure 143. We can see that the power is not transmitted to a single mode, but it is divided among various modes. We should notice the maximum transmission from mode 2, which is of approximately -35dB, lower than any of the other modes. That means that the portion of the power that changes the polarisation is very little for perpendicular incidence.

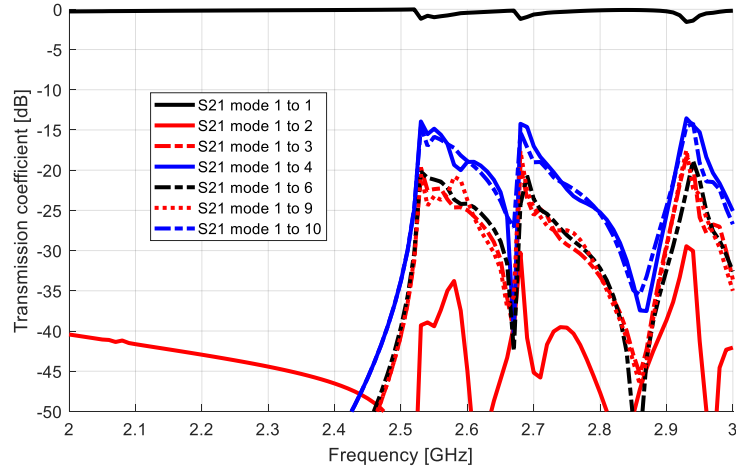


Figure 143. Intermodal transmission. It describes the power received in port 2 in mode 1 from all the other ports.

5.2.3 Transmitted power for non-perpendicular incidence

We have analysed until now the effect of the structure on a perpendicular wave incidence angle. That is a very specific case, and in practice the waves arriving to the cage impinge on its surface at broader incidence angles. In this section, we have done the analysis for an angle of incidence of 20° and 40° , and the results are in Figure 144 and Figure 145, respectively.

The main effect of the non-perpendicular incidence that we observe is that the modes that had an equivalent cut-off frequency are now moved up and down in frequency. These distinct trends are caused by the different imprints of the E field on the structure depending on the incidence. For higher incidences, the projection of the E field on the structure is different and therefore the electrical size of the structure varies. This effect changes depending on the incidence and on the orientation of the specific mode and becomes more significant as we increase the angle of incidence. We can observe that some of the modes that have a cut off frequency of 2.5 GHz for a perpendicular incidence, have their cut-off frequency increased above 3 GHz as their max in the range between 2 and 3 is very small.

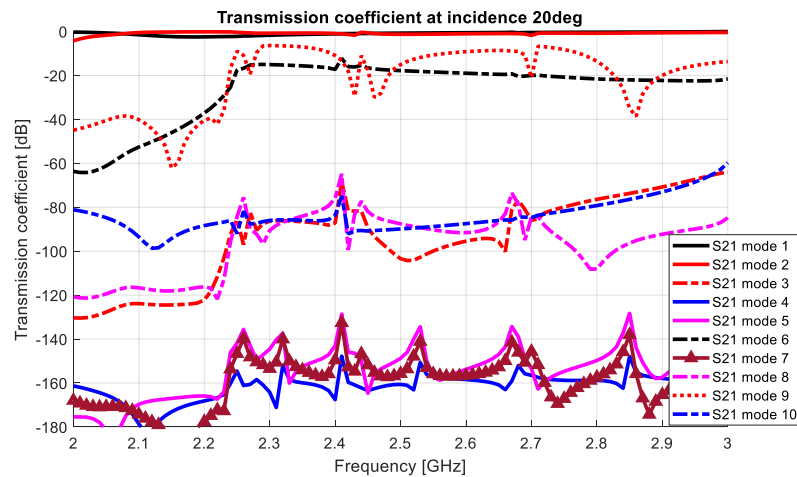
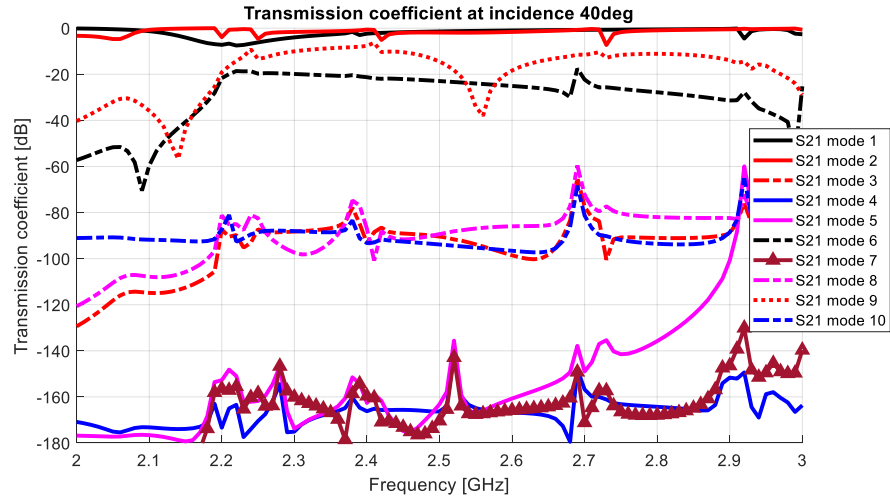
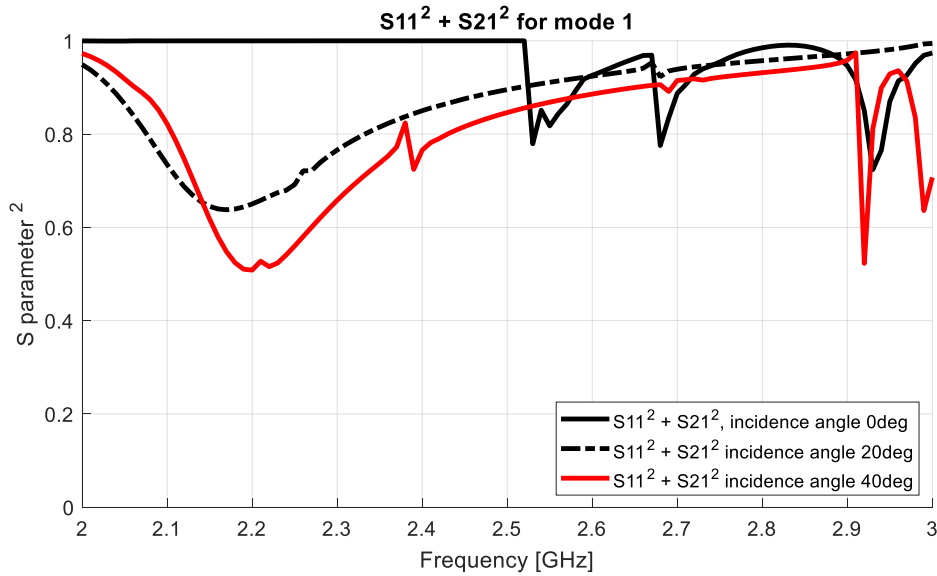


Figure 144. S21 for all 10 modes at an incidence of $\Theta_{\text{scan}}=20^\circ$


 Figure 145. S21 for all 10 modes at an incidence of $\Theta_{\text{scan}}=40^\circ$

We use the Equation (1) to compare the effect of the various angles of incidence. As we can see in Figure 146, as the angle of incidence increases, the intermodal transmission effect becomes more significant and also at lower frequencies, including the band between 2.4-2.5 GHz.


 Figure 146. $|S_{11}|^2 + |S_{21}|^2$ of mode 1 for various angles of incidence

5.2.4 Conclusions

For the real structure of the cage, the analysis is more complicated because the cage “cells” are not flat. Also, the antennas are not in the center, and there are rods with different lengths (for shorter rods, the cut off frequency moves to higher frequencies). However, this simplified analysis provides useful information on the propagation of the waves through the cage, that we can summarize as follows:

- The cage supports several modes propagating through it. Due to the several segments in different orientations, part of the power radiated from the antennas (their fundamental mode) is transferred to other modes, which contributes to the perturbation of the pattern.
- For incidence angles that are not perpendicular, the ratio of the usable power for a given polarization (mode) diminishes, becoming especially critical at lower frequencies, including the operating band of the transmission system.

5.3 System measurements. Validation of CP broadbeam patch with ground slots

In this Chapter we present the system measurements used to validate the performance of the lightweight CP broadbeam patch antennas designed in Chapter 4. We start defining the measurement setup, describing the placement of the drone and the controller, then the process is described step by step and the definition of the figures of merit to be used as benchmarks are given. We use the dipoles originally used in the drone as a reference, and we compare these with the proposed CP patches for different assemblies, which allows us to draw conclusions on the performance of each antenna, each positioning and of the effect on the cage and the environment in each case.

5.3.1 Definition of the system measurements

5.3.1.1 *Description of the measurement: environment and placement of the controller and drone*

The system measurements are made from point to point of the communication system, using both the drone and the remote controller. We place both on stands of around 1m of height to reduce the effect of the ground on the measurements. We create two setups, for LOS and NLOS conditions, which are described in Figure 147 and Figure 148 respectively. In both cases, we keep the controller facing the shortest path to the drone and place their two antennas (linearly polarized) in V-shape of polarisation diversity.

For the LOS setup, we place the remote and the drone at a distance of around 15m in a corridor full of metallic cupboards and metallic ceiling. In such a narrow environment, we expect to receive signal from reflected paths which are comparable to LOS.

In NLOS scenarios, the channel is more unpredictable as it relies on multiples reflections that arrive to the receiver with similar amplitudes and there is not a direct path. It is then more difficult to extract specific conclusions from the measurements of the SNR. However, we can see more easily which antenna performs better, as the differences between setups is more remarkable, as expected. This is the most representative scenario for our application, and also where the reliability is more degraded due to the multiple signals received with similar amplitude as there is not a clear direct path between the controller and the drone. It is for this scenario that we conceived the antennas presented in Chapter 4.

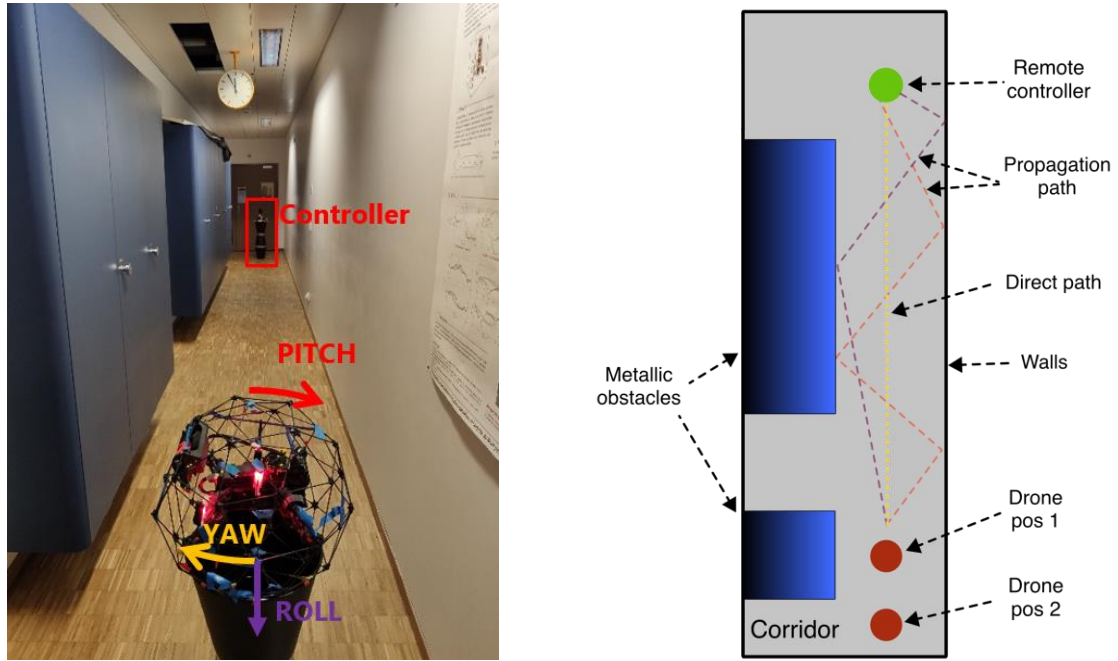


Figure 147. Setup LOS. Drone and controller in the corridor (left) and sketch of the measurement setup (right).

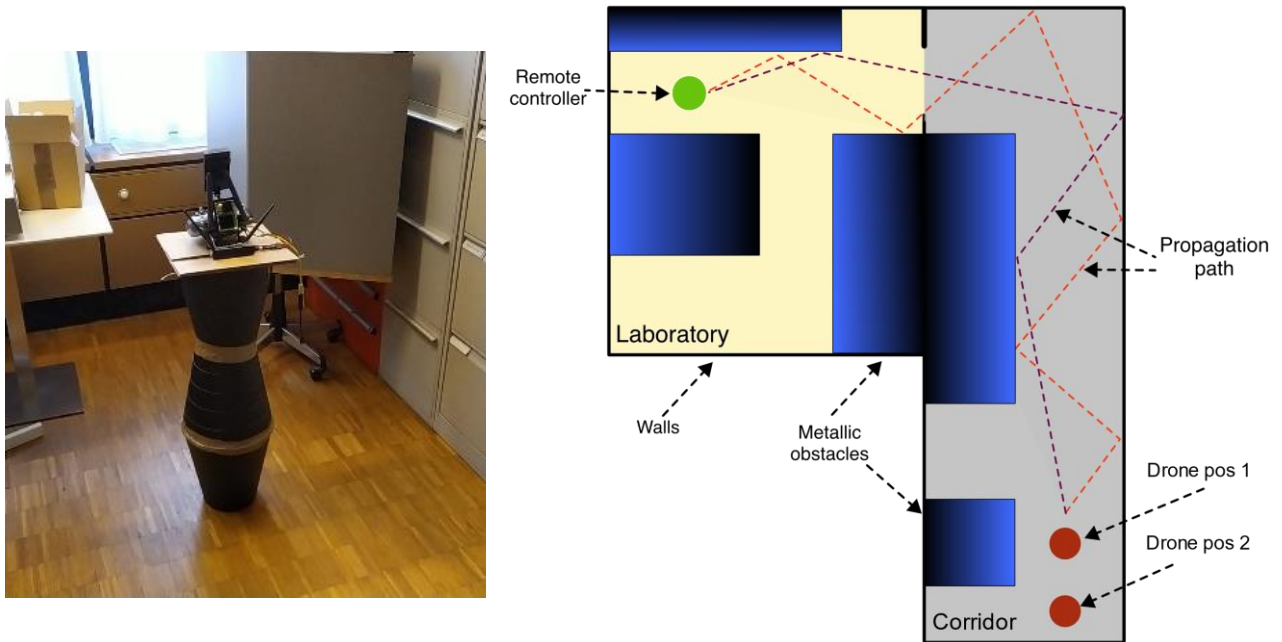


Figure 148. Setup NLOS. Remote controller inside a laboratory (left) and sketch of the measurement scenario (right).

5.3.1.2 Description of the procedure

With the controller and the drone put in place, we can start the measurements. The transmission system allows us to register the signal strength of each antenna and the total SNR of the radio link. We use the latter as a

single-value indicator of its quality, which already accounts for the two antennas combined. We start recording uninterruptedly the SNR on the drone, and then proceed as follows:

1. We rotate the drone in the three main axes of rotation (yaw, roll, and pitch), for 8 angles (0° , 45° , 90° , 135° , 180° , 225° and 270°) and for each angle we keep the drone steady for 10 seconds (see Figure 149). We calculate the average SNR in these 10 seconds, which gives us one set of 8 SNR values for each of the rotation axes and 24 in total for each measurement.

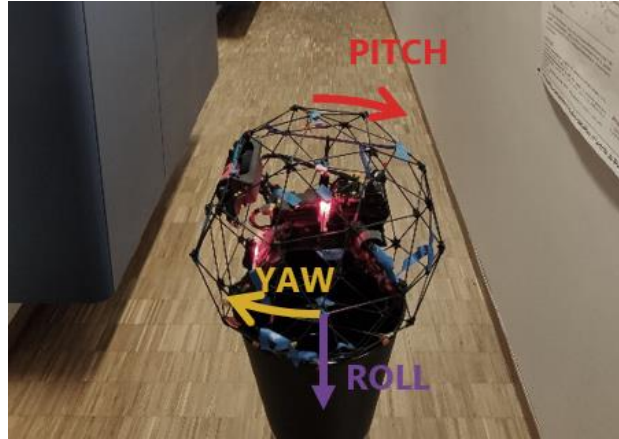


Figure 149. Drone prepared for measurements, with the three axes of rotation.

2. We repeat the measurements again moving the drone to another position a few wavelengths away (indicated by Drone Pos 2 in Figure 20.). We calculate the average for each rotation in the two positions to minimize the effect of potential fading effects caused by the multipath effect, as indicated in Figure 147 for LOS and Figure 148 in NLOS.

With this procedure we have a set of 8 values of SNR per rotation angle, and a total of 24 for a full measurement (3 rotation angles x 8 values).

5.3.1.3 Definition of the metrics

To assess the quality of the radio link we need to define metrics that allow to quantify the performance of the radio link. We propose two metrics of different nature that help us provide a quantitative measure of the **reliability** and **quality**. These two combined provide a good overview of the performance of each combination of antenna and positioning in the drone.

We define the **reliability metrics** as follow:

1. We calculate the average SNR value from the 8 rotation angles of each rotation axis, providing us 3 values. This gives an idea of the rotation axis that has the lower average SNR.
2. We take the lowest SNR from these averages and use it as a **worst-case threshold** to calculate the probability of the SNR being above it in all the measured positions. This gives us a single value (a probability) for each setup (antenna + position on the drone) and allows us to compare them quantitatively.

3. In some cases, the worst-case threshold is very low and does not allow to distinguish which setup is more reliable. To solve this, we increase the thresholds in steps of 1dB until we can distinguish which setup is better. Using this **adjusted threshold** is meaningful, as it shows how the system performs for SNR levels where the quality of the link is most unstable.

The reliability metrics allow us to quantify the reliability of the link and compare with other antenna types and assemblies in the drone. We propose a second metric that complements the previous, and that gives information about the improvement of the average SNR for each case. These two should be interpreted together to get a complete assessment of the performance of a specific setup. This new indicator, is a relative measure, that tells us how a given setup of antenna and orientation compares to another in terms of SNR. To calculate it, we calculate the average SNR difference, for each separate rotation axis and in total. This gives us an approximated value of the improvement in SNR for each rotation axis separately and of the entire system specifically. We do all these calculations always in natural units and transform then again to logarithmic units. With this indicator, we get an average increase (or decrease) of SNR. Using the Friis' formula we can translate that change of SNR to how much the range coverage would increase or decrease if the setup was in free space. The dependence of the increased EIRP (transmitted power or antenna gain) with the distance from the Friis' formula in free space is described by the relations between the increase of EIRP with distance [1]. In Figure 150 we can observe that relation between EIRP (in dB) and the relation between the ratio of EIRP and distance is described by equations (5.2)-(5.4).

$$EIRP(d_0) = P_{t_0} \cdot G_{t_0} = \frac{P_r}{Gr \cdot \left(\frac{\lambda}{(4 \cdot \pi \cdot d_0)^2} \right)} \quad (5.2)$$

$$EIRP(d_1) = P_{t_1} \cdot G_{t_1} = \frac{P_r}{Gr \cdot \left(\frac{\lambda}{(4 \cdot \pi \cdot d_1)^2} \right)} \quad (5.3)$$

$$EIRP_{ratio_dist} = \frac{EIRP_1(d_1)}{EIRP_0(d_1)}; \quad (5.4)$$

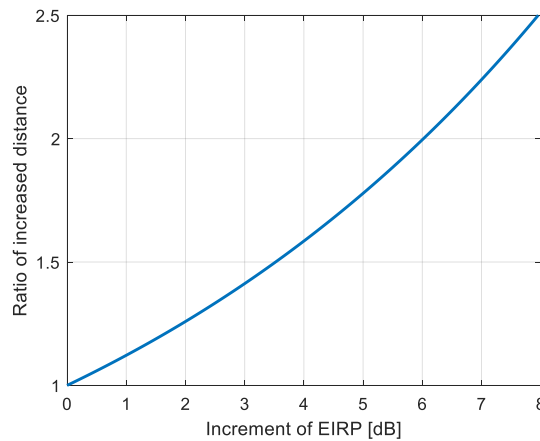


Figure 150. Ratio of increased distance in free space for an increment of EIRP (transmitted power, antenna gain or both).

The actual performance of the system will vary with respect to the measurements in this test, depending on the specific scenario. It is possible that the performance is better if the environment is more reflective, favouring a better reception, or it could be worse if the opposite happens. As the channel is unknown and will be very different for every flight, we find that the **free space equivalent improvement indicator (FSEII)** is a reasonable benchmark to understand and compare the performance of the various setups of the test.

Both the **reliability metrics** (worst-case and adjusted threshold) and the **FSEII** provide a good overview on the performance of each measurement setup (antenna + positioning).

5.3.1.4 Definition of the setups: Antenna type and positioning on the drone.

In this Section we describe the measurement assemblies, which has two variables: the **antenna** and the **placement on the drone**. We measure a total of 10 combinations in this Chapter, using three antennas: omnidirectional bowtie dipoles (**DPP**) used originally in the drone, and the broadbeam LP patches (**LPP**) and CP patches (**CPP**) fabricated and measured in Chapter 4. We should remember that the goal is to characterize and validate the CPP, and we use the BD and LPP antennas as a comparative reference. The description of the three antennas used in this test is summarized in Table 11, including three proposed abbreviated names that will simplify the naming of each setup.

(Antenna name) Antenna type	(BD) Bowtie dipoles	(LPP) LP patches designed and fabricated in Chap- ter 4	(CPP) CP patches patches de- signed and fabricated in Chapter 4
Polarisation	Linear	Linear	Circular
Gain within band	2 dBi	5.3 @2.4GHz 4.6 dBi @2.45GHz 4.2 @2.48GHz	2 - 3.2 -2.7 dBi (lower middle and higher part of the bands, respectively)
Pattern	Omnidirectional	Covers half space in one plane	Sectorial in 2 planes
HPBW	360 deg	180 deg	90-120 deg
Weight	2 g	7 g	9 g

Table 11. Comparison of all antennas included in the test

We describe each of the antenna assemblies in Figure 151 to Figure 160, providing a little description for each one, and an abbreviated name including the name of the antenna and a descriptive label for the assembly on the drone. For example, the setup in Figure 151 uses the original bowtie dipoles (BD) in the original orientation and positioning in the drone (labelled Orig), and the setup is called BD-Orig.


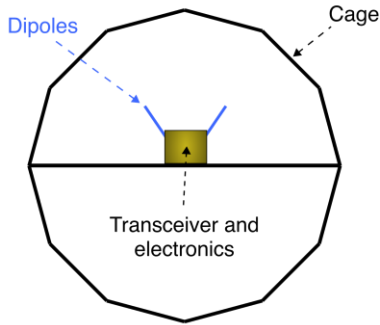
Setup BD-Orig Dipoles in original position and orientation, on inner frame	
Description: This position and orientation is important as that was the original setups of the antennas on the drone and it serves as a reference. The dipoles were placed in V shape for polarisation diversity in the centre of the cage, on the inner frame.	
	

Figure 151. Antennas in original orientation and position, on inner frame

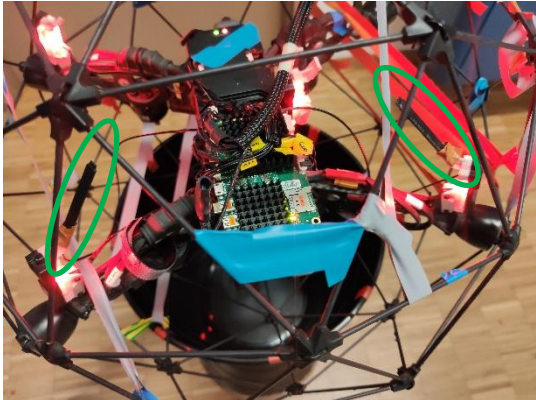
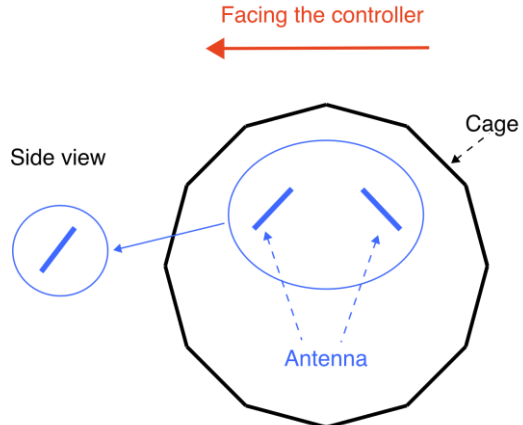
Setup BD-Sup Dipoles on support	
Description: This is the position and orientation of the antennas in the drone. It came as part of an analysis and optimisation performed during the project. The antennas are placed in V shape for polarisation diversity and separated for spatial diversity.	
	

Figure 152. Dipoles on support

Setup CPP-Sup CP Patches on support

Description: To cover one hemisphere each, the patches are placed on opposite sides of the cage. They are attached to the inner frame and are in front of one of the apertures. We leave a clearance from the cage avoid that near fields interacts with the segments. As these antennas are circularly polarised, we do not need to rotate one with respect to the other for polarization diversity.

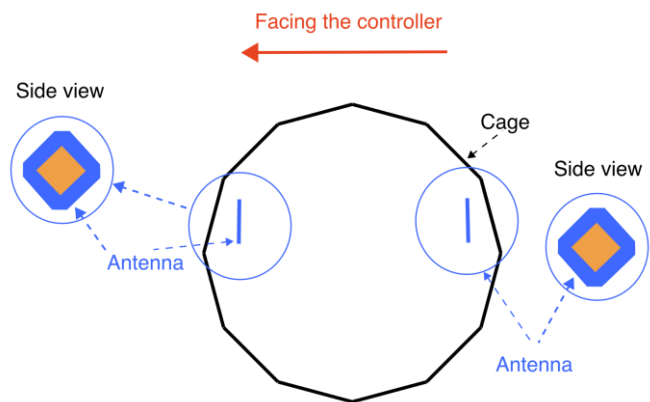
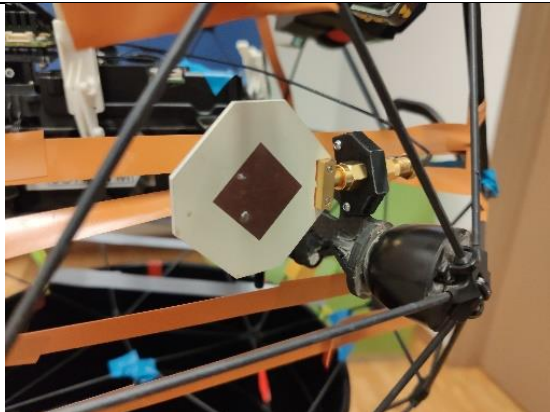


Figure 153. CP Patches on support.

Setup BD-Opt Dipoles optimal position and orientation

Description: The dipoles are placed on the upper and lower halves of the cage. We place them here to minimise the effect of the inner frame. The two dipoles are rotated for enhanced polarisation diversity.

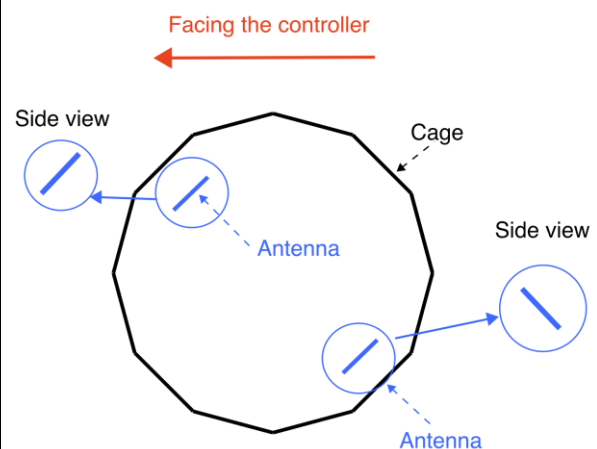
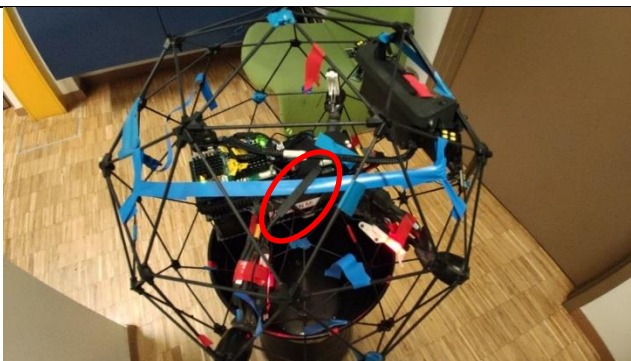


Figure 154. Dipoles optimal position and orientation.

Setup LPP-Opt LP patches optimal orientation

Description: These two antennas are placed in the same position as the dipoles. These are linearly polarised as the dipoles, but they cover only one hemisphere in the optimised plane. We place them orthogonal to each other for polarisation diversity and to cover apertures of 180deg in azimuth and elevation angles. This placement should reduce the risk of having a deep zero towards the top and/or bottom of the cage.

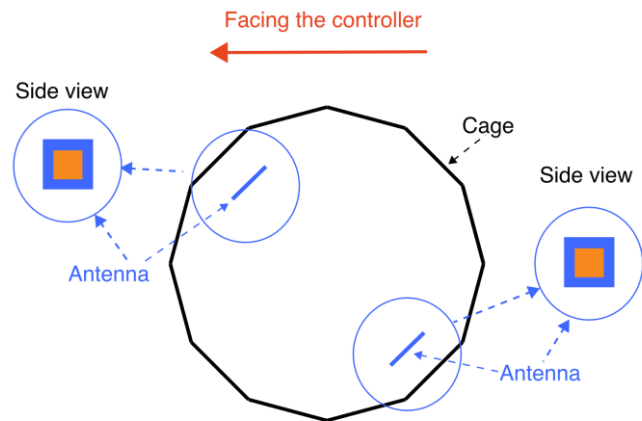
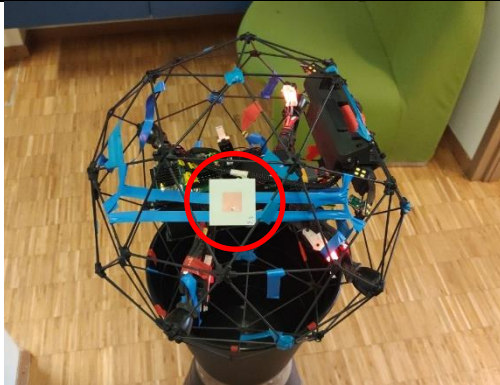


Figure 155. Positioning and orientation of the LP patches inside the cage for the tests.

Setup CPP-Opt CP patches optimal orientation

Description: The antennas are placed in the same position as the dipoles and the LP patches. They cover a narrower sector and have lower gain, but they radiate circularly polarised waves.

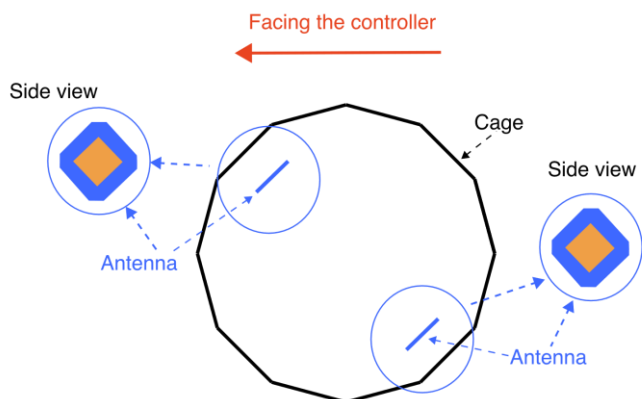
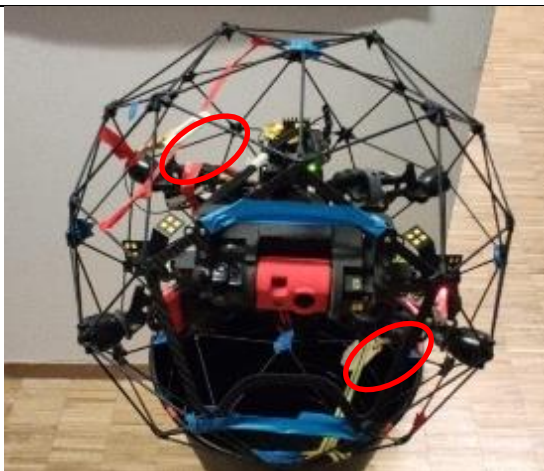


Figure 156. Positioning and orientation of the CP patches inside the cage for the tests.

Setup BD-Ins

Dipoles inside of cage

Description: The dipoles are placed inside the cage and orientated orthogonally to each other for polarisation diversity.

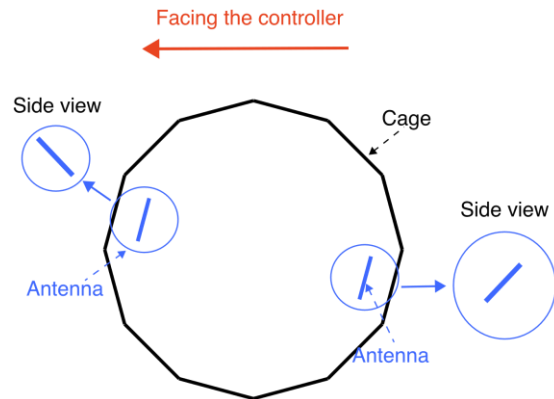


Figure 157. Dipoles inside cage.

Setup BD-Out

Description: The dipoles are placed outside of the cage, in the same orientation as in the setup BD-Ins.

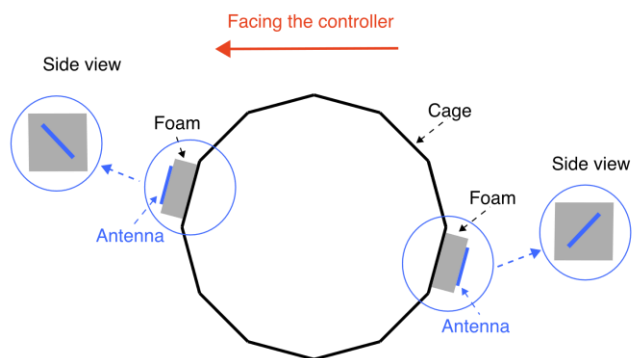


Figure 158. Dipoles outside cage.

Setup CPP-Ins Patches inside of cage

Description: The patches are placed inside the cage. As these are circularly polarised, we do not need to rotate them for polarisation diversity and both have the same orientation on both sides of the cage.

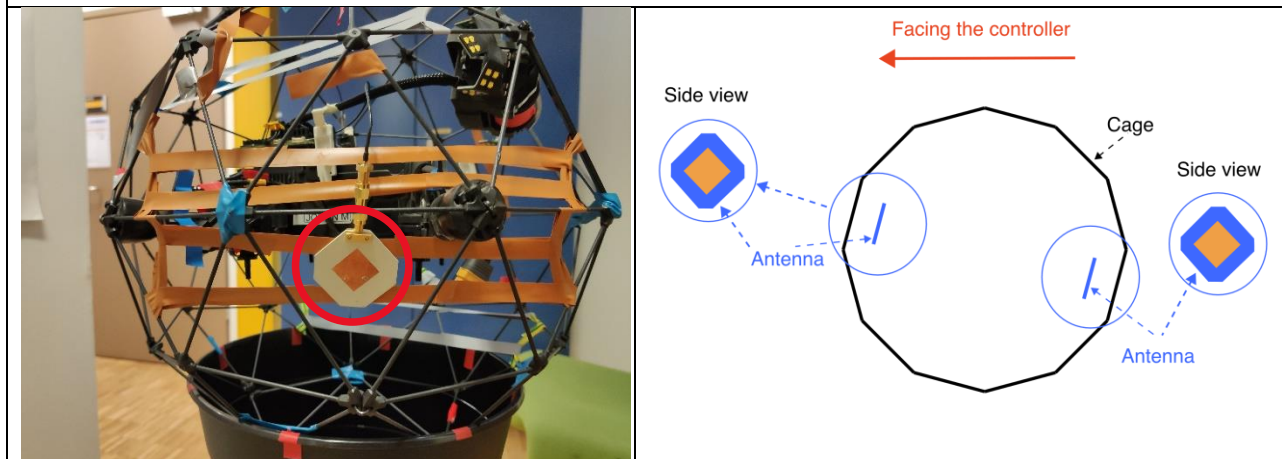


Figure 159. CP Patches inside cage.

Setup CPP-Out CP patches outside of cage

Description: The patches are placed outside of the cage, along the same radial distance from the center of the cage as the Setup D-Out. To place the antennas outside of the cage, we use foam to separate them enough and avoid any potential near field coupling with the segments nearby. We confirmed by measuring in the VNA that the foam and tape do not change the reflection coefficient.

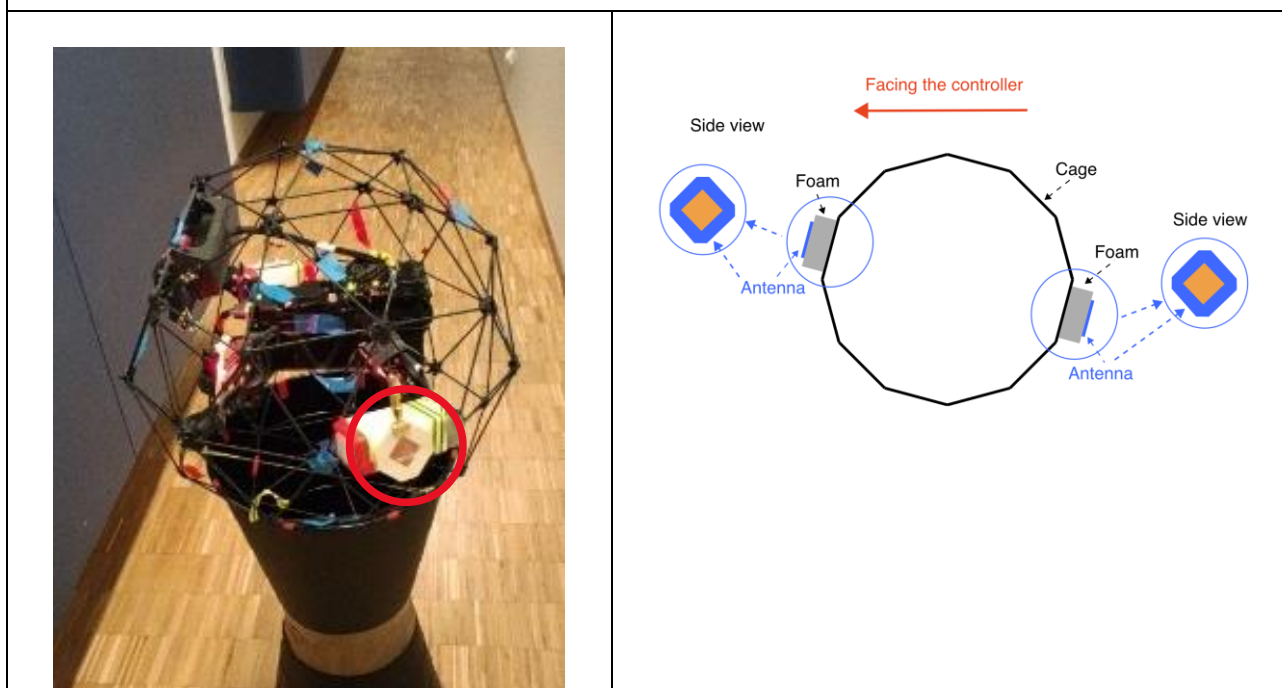


Figure 160. CP Patches outside cage.

5.3.2 Positioning of the antennas on the drone and comparison between dipoles and CP patches

In this Section we analyse first the results for the dipoles and patches in the positions proposed. These are not necessarily optimal, and they have been defined taking into each type of antenna and their radiation characteristics. **We compare the setups D-Orig (Figure 151), D-Sup (Figure 152) and CPP-Sup (Figure 153).** We divide the analysis in two scenarios using these three setups: LOS and NLOS.

5.3.2.1 Line of Sight (LOS) measurements and results

The test scenario is an environment with several reflective surfaces that favours multipath and resembles a real use case. For the measurement in LOS, we expect to receive reflected paths which are comparable to the main path in power, as the corridor is very narrow. We can see in Figure 161 the results of the averaged SNR for each rotation angle. The dipoles in the original orientation are more unstable in the PITCH rotation, as the SNR experiences two strong drops around 90° and 270° . At these two angles, the antennas are both contained in the horizontal plane, from which we can assume that the fields received are more vertically polarised than horizontally. In ROLL, there is a smaller drop but still significant at 90° , which is when the battery and the inner frame are shadowing the antennas. The big drop at 90° for this antenna setup could be explained from the fact that the front module of the camera blocks the LOS at this orientation.

We can extract some other conclusions for the setup BD-Sup as well. For the rotation in pitch, we can see a similar effect to what occurs for the dipoles in original orientation: two drops at around 90° and 270° . On the support and at these rotations the dipoles are also almost horizontal, but not completely, which explains why the dipoles the drop is smaller in this case.

There are two angles for which we see a similar effect for BD-Sup and for CPP-Sup: Roll at 90° and 270° . At 90° we have all the inner frame and the bottom of the cage occluding the LOS, and the CP patches have a lower gain in that point as it is the minimum gain plane of the two patches, what explains why they have a minimum also at 270° . Something similar happens with the dipoles, as these are almost parallel to the LOS direction at these rotations and this is the zero of their radiation patterns.

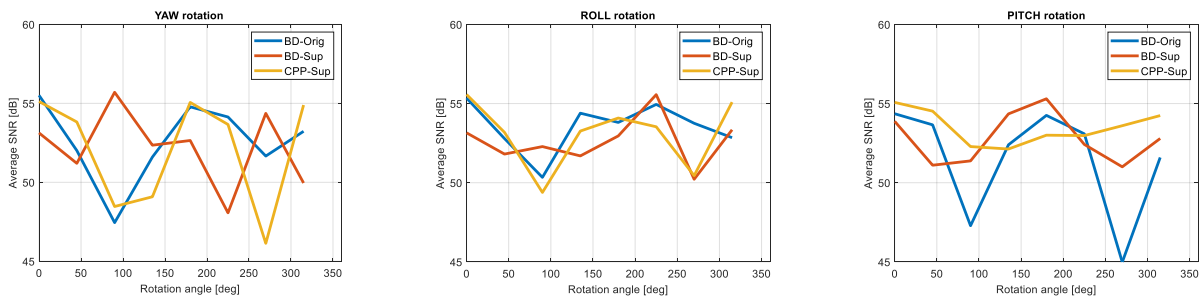


Figure 161. Average SNR over two measurements in the YAW, ROLL and PITCH rotation in LOS for the Setups BD-Orig, BD-Sup and CPP-Sup.

The results in Figure 161 do not provide a quantitative measurement of the reliability of each setup. We depict the reliability metrics in Figure 162. We can see that for the worst-case threshold the performance of the CPP-Sup and BD-Sup is not very different. This is what we expected for LOS as we have a direct path, which also makes LOS much less critical to optimize than NLOS. For our case, the reliability metric for the adjusted threshold is shown on the right part of Figure 162. As we cannot see a significant difference between the various setups, we can conclude that indeed this equivalent behaviour is due to the LOS.

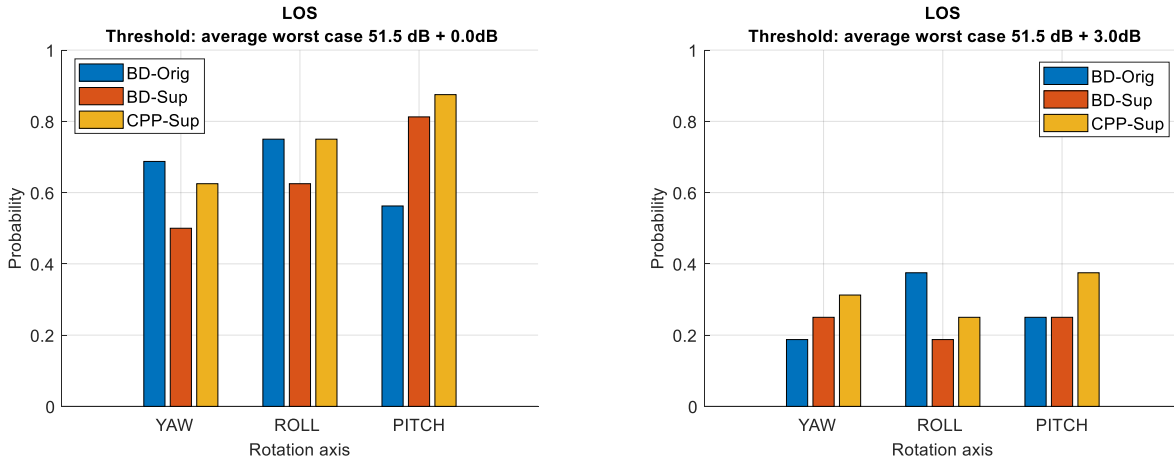


Figure 162. Reliability metrics for the worst-case threshold (left) and the adjusted threshold (right) for the three antenna setups in LOS, for the Setups BD-Orig, BD-Sup and CPP-Sup.

The results in Figure 162 allow us to spot if there is a problem with a specific rotation angle, and then with the help of the results in Figure 161 we can assess whether it is a problem of a specific angle and find an explanation for it. It is, however, useful, to gather all the probabilities in Figure 162 in a single value, which gives as a quantifier of the overall reliability of each antenna setup. The total reliability metrics are shown in Table 12 and as we expected from the previous results, all three setups show a similar reliability. However, we can notice that the CP patches are slightly better for both thresholds.

Disposition of the dipoles	Probability Threshold worst case	Probability Threshold: worst case + 3dB margin
Dipoles original (BD-Orig)	0.67	0.27
Dipoles support (BD-Sup)	0.65	0.23
CP patches support (CPP-Sup)	0.75	0.34

Table 12. Global probabilities for worst case threshold and worst case + margin in LOS, for the Setups BD-Orig, BD-Sup and CPP-Sup.

We gather in Table 13 the results of the *free space equivalent improvement indicator (FSEII)* of the proposed CP patches in comparison to the dipoles in the original orientation and to the dipoles on the support. We can notice that even if there is not a significant difference between the antenna setup as the measurements are in LOS, the variation of SNR is always positive in dB for all the cases, what means that, in average, the CP patches perform better than the dipoles in all cases.

	Compared to original dipoles (BD-Orig)		Compared to dipoles on support (BD-Sup)	
	Average SNR improvement	Free space equivalent improvement indicator (FSEII)	Average SNR improvement	Free space equivalent improvement indicator (FSEII)
YAW	0.35 dB	5%	2.20 dB	29%
ROLL	1.00 dB	10%	1.25 dB	15%
PITCH	3.80 dB	55%	1.45 dB	18%
TOTAL	2.00 dB	25%	1.65 dB	20%

Table 13. Average SNR improvement for the CP patches (setup CPP-Sup) compared to the dipoles in the setups D-Orig and D-Opt, and FSEII.

To validate the consistency of the assessment in LOS, we repeated some measurements in a larger place (a parking). In that case, there are yet multiple reflected paths, but their effect is less important than in the narrow corridor. The results from these new measurements were consistent with the conclusions that we present in this Section.

To summarise, the performance in LOS is not critically compromised as all the antenna setups receive a good SNR thanks to the direct path. In terms of FSEII, the CPP-Sup performs 25% and 20% better than the BD-Orig and BD-Sup, respectively. We can use the measurements in LOS to learn from the antenna positioning and to detect the effects of the drone structure. These conclusions can also be useful to understand the performance in NLOS, where the reliability is critical as the radio link is less stable and predictable.

The fact that we can spot some of the effects of the geometry that we intuitively expected, reinforces that the tests are meaningful, and we can extract consistent conclusions. This leads us to conclude that here we can identify features of the radiation that we would see in a radiation pattern, and therefore the LOS measurements can help us to understand the weak points of an assembly or an antenna setup.

5.3.2.2 Non-Line of Sight (NLOS) measurements and results

The results of the average SNR for the three setups under tests are shown in Figure 163. There is a clear difference of the results of the dipoles in original orientation with respect to the dipoles and patches in the support. That is something that we expected from our research on the cage: many segments of the cage interact with the antennas and affect the propagation.

If we compare the CPP-Sup and BD-Sup, we can see that, especially in pitch, the SNR of the CPP-Sup is superior and more stable for most angles. In roll their performance is very similar, except for at 0°, where CPP-Sup is superior to BD-Sup. There is a big drop for both setups at a rotation of 90°-135°. In yaw, CPP-Sup has a better SNR, excepting at 270°, where BD-Sup shows a large SNR peak. This is a localised peak, and CPP-Sup is more constant along all the rotation, being at a first glance the most reliable of all the setups in yaw.

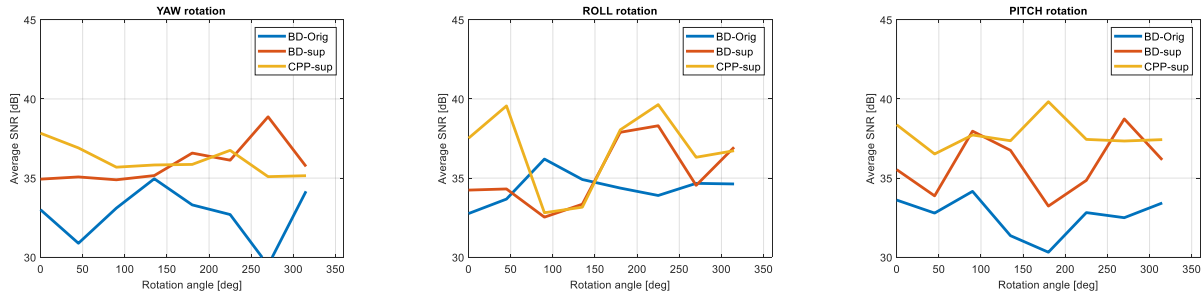


Figure 163. NLOS. Comparison of SNR for the Setups BD-Orig, BD-Sup and CPP-Sup.

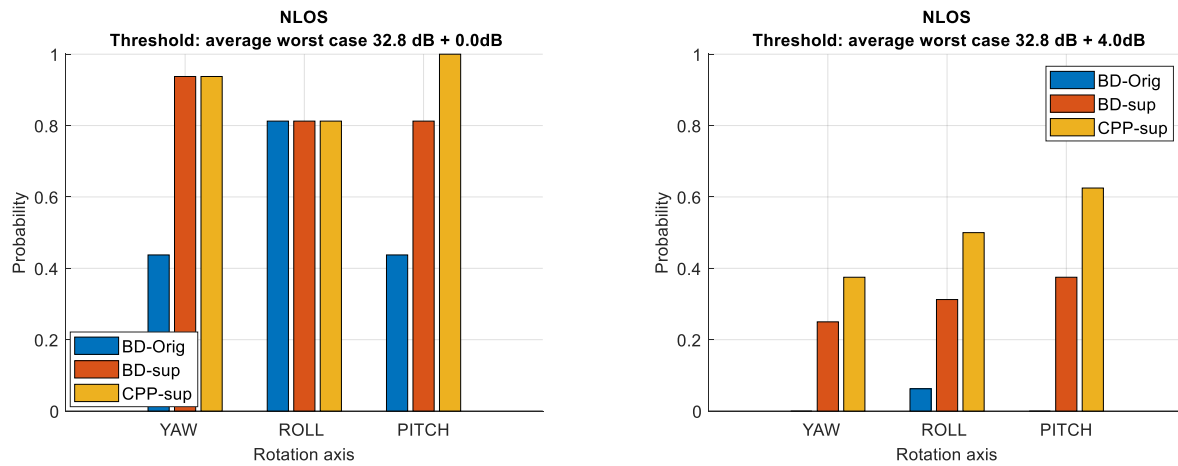


Figure 164. Comparison of reliability indicator for the Setups BD-Orig, BD-Sup and CPP-Sup.

In Figure 164, we can appreciate from the reliability metrics that CPP-Sup is consistently better than BD-Sup and BD-Orig in all the three axes of rotation. The global results are gathered in Table 14, where we can notice the remarkably worse performance of BD-Orig for both thresholds. For the worst-case threshold, we can see that CPP-Sup performs slightly better than BD-Sup, but it is for the modified threshold that we see a larger improvement of 20%. The fact that CPP-Sup maintains a greater probability for a higher threshold speaks also about their stability. If the probability decreases fast as the threshold ramps up, that means that the setup has a larger variability. In fact, we get a similar reliability with CPP-Sup as we would get with CP-Orig, but for a SNR 4dB higher. This is very positive, as the CPP suffer from 3dB of polarisation loss by default, and their gain is 1dB lower than for the BD.

NLOS		
Disposition of the dipoles	Probability Threshold worst case	Probability Threshold: worst case + 4dB margin
Dipoles original (BD-Orig)	0.58	0.02
Dipoles support (BD-Sup)	0.85	0.31
CP patches support (CPP-Sup)	0.92	0.50

Table 14. Global probabilities for worst case threshold and worst case + margin in NLOS, for the Setups BD-Orig, BD-Sup and CPP-Sup.

In Table 15, we can see the results of the FSEII for CPP-Sup compared to BD-Orig and BD-Sup. **In terms of FSEII, CPP-Sup improves by 70% and 29% compared to BD-Orig and BD-Sup, respectively.**

NLOS				
	Compared to BD-Orig		Compared to BD-Sup	
	Average SNR improvement	Free space equivalent improvement indicator (FSEII)	Average SNR improvement	Free space equivalent improvement indicator (FSEII)
YAW	3.9 dB	57 %	0.8 dB	10 %
ROLL	3.6 dB	52 %	2.4 dB	32 %
PITCH	5.8 dB	95 %	3.1 dB	43 %
TOTAL	4.6 dB	70 %	2.2 dB	29 %

Table 15. CPP-Sup compared to BD-Orig and BD-Sup.

The cross-polarization losses between a LP and a perfectly circularly polarized antenna are 3dB, which is very convenient to prevent higher losses that would compromise the reliability of the system. The CPP antennas under test do not have a perfect CP, with an axial ratio under 4dB in the frequency band. The CPP should experience cross polarization losses of around 3dB, which could vary depending on the alignment of the main component of the polarization. As the CPP antennas are penalized by the cross-polarization losses, they offer margin for improvement in the downlink (drone to controller), which is the most critical as it carries the video signal which requires a higher data rate. To exemplify this, we add 1dB to the measured SNR, which gives an idea about how much the performance could improve when we slightly increase the transmitted power. The results are shown in Figure 165. We do not see remarkable differences for the reliability metric by comparing the worst case in Table 14 and Table 16, and that shows how this metric might be misleading. The results for the adjusted threshold show an increase from 0.5 to 0.63.

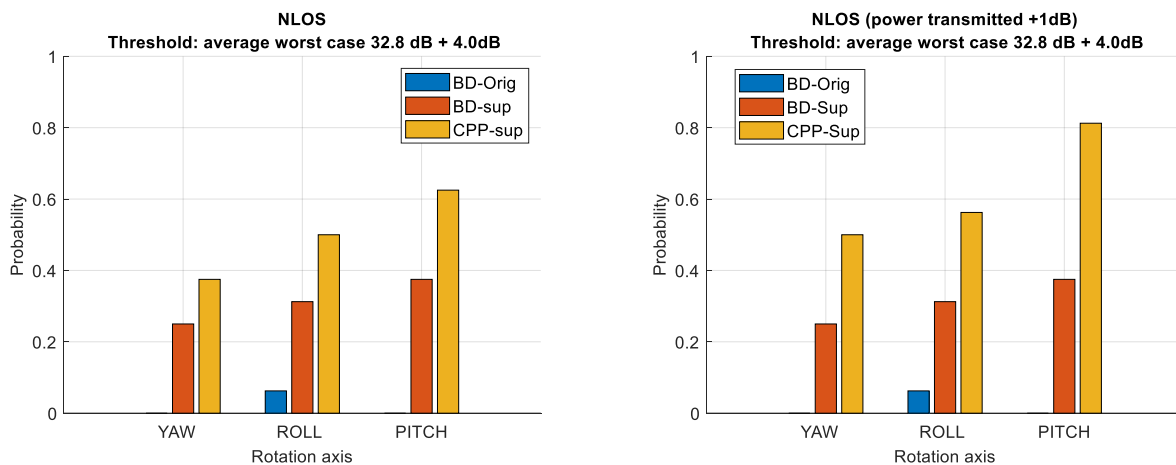


Figure 165. Comparison of reliability indicator before (left) and after adding 1dB to the measurements (right), for the Setups BD-Orig, BD-Sup and CPP-Sup.

The FSEII improves from 70% up to 90% for the CPP-Sup compared to BD-Orig. It increases from 29% to 45% percent compared to the BD-Sup. The results are shown in Table 17.

NLOS in downlink (+1dB added)		
Disposition of the dipoles	Probability Threshold worst case	Probability Threshold: worst case + 4dB margin
Dipoles original (BD-Orig)	0.58	0.02
Dipoles support (BD-Sup)	0.85	0.31
CP patches support (CPP-Sup)	0.96	0.63

Table 16. Global probabilities for worst case threshold and worst case + margin in NLOS +1dB, for the Setups BD-Orig, BD-Sup and CPP-Sup.

NLOS in downlink (+1dB added)				
	Compared to BD-Orig		Compard to BD-Sup	
	Average SNR improvement	Free space equivalent im- provement indicator (FSEII)	Average SNR improvement	Free space equivalent im- provement indicator (FSEII)
YAW	4.9 dB	76 %	1.8 dB	23 %
ROLL	4.6 dB	70 %	3.4 dB	48 %
PITCH	6.8 dB	120 %	4.1 dB	60 %
TOTAL	5.6 dB	90 %	3.2 dB	45 %

Table 17. CPP-Sup compared to BD-Orig and BD-Sup adding +1dB of extra transmit power thanks to lower gain of the patches.

5.3.2.3 Conclusions of the proposed antenna system

In conclusion, in LOS the SNR for all the antenna setups is very similar, but this is not critical as we have a direct path and stable radio link. However, the **CP patches (CPP)** perform better, especially in terms of *Free Space Equivalent Improvement Indicator* (FSEII), where they are **25% and 20% better than the dipoles in their original assembly (BD-Orig) and the dipoles on support (BD-Sup), respectively**. The measurements of LOS can help us understand how to improve the positioning and orientation of the antennas, as we can spot the main effects of the structure on the propagation of the waves as we rotate the drone.

The NLOS scenarios are the more unpredictable also more critical to the application. It is in NLOS where we see more differences between the different antenna setups that we have tested. While we can already significantly improve the performance of the dipoles by adjusting their position and orientation, we see from the results that **the circular polarisation of the CPP is key to further enhance the performance**. To get a complete overview on the performance of the CPP, we use both the reliability metric and the FSEII. **The CPP improve the reliability metric compared to BD-Sup by 20%, being as reliable as BD-Orig but for an increased SNR of 4dB. The Free Space Equivalent Improvement Indicator (FSEII) shows that CPP-Sup is in average 70% better than BD-Orig and ~30% compared to BD-Sup.** If we increase can increase the transmitted power of the air unit by 1dB to compensate for the polarization losses, **the downlink improves up to a FSEII of the CPP-Sup compared to BD-Sup from 30% to 45%, and the reliability for the adjusted threshold metric from 0.56 to 0.63.** The downlink is the most critical as it carries the video feed, and is what degrades first during a flight, as it carries more information and usually uses a less robust modulation.

NLOS in downlink (+1dB added)	
Disposition of the dipoles	Probability Threshold: worst case + 4dB margin
Dipoles original orien.	0.02
Dipoles support	0.31
CP patches support	0.63

Table 18. Final conclusions on the reliability of the dipoles and the CP patches

NLOS in downlink (+1dB added)	
	Free space equivalent improvement indicator (FSEII)
CP patches compared to original dipoles	+ 90%
CP patches compared to dipoles on support	+ 45%

Table 19. Final conclusions on the free space equivalent distance improvement of the CP patches compared to the dipoles

In this Section, we have summarised the results for the proposed antenna setups, but we add in the following sections a detailed report of all the measurements that we have performed and that provide useful information to the performance of the antennas and the effect of the cage.

5.3.3 System measurements. Comparison of dipoles, LP patches, and CP patches: effect of the polarization

With the measurements in this Section, we aim to assess how the proposed CP patches (CPP) compare to other broadband linearly polarized patches (LPP). We use the LP antenna designed, fabricated designed in Chapter 4. The setups used are: **BD-Orig (Figure 151)**, **BD-Opt (Figure 154)**, **LPP-Opt (Figure 155)**, **CPP-Opt (Figure 156)**. We test these antenna setups in LOS and NLOS.

5.3.3.1 Line of Sight (LOS) measurements and results

The results of the average SNR per axis of rotation for the four antenna setups are shown in Figure 166. We do not analyse here the setups 1, 2 and 4 as we analyse them already in other sections. We can see from the results how the average SNR of LPP-Opt clearly resembles the behaviour of BD-Opt, especially in the pitch rotation. That means that their channels are very similar, including their radiation characteristics and their interaction with the cage. We can also observe this effect also in Figure 166 and Figure 167, how their reliability indicators are very similar.

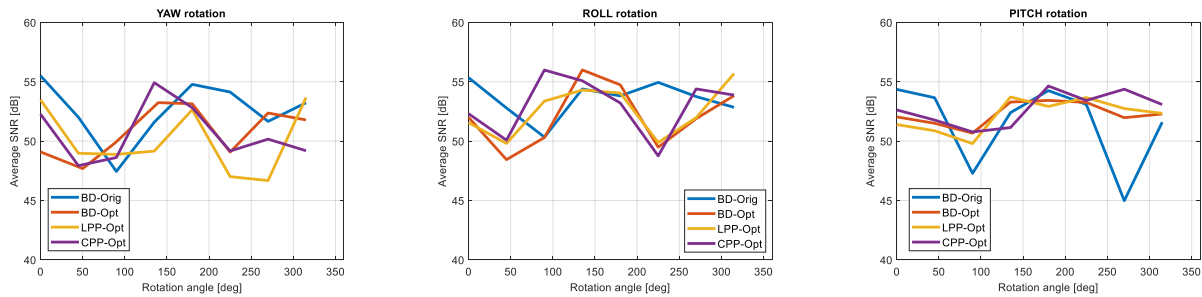


Figure 166. Comparison in LOS: average SNR over two measurements in the YAW, ROLL and PITCH rotation for BD-Orig, BD-Opt, LPP-Opt, CPP-Opt.

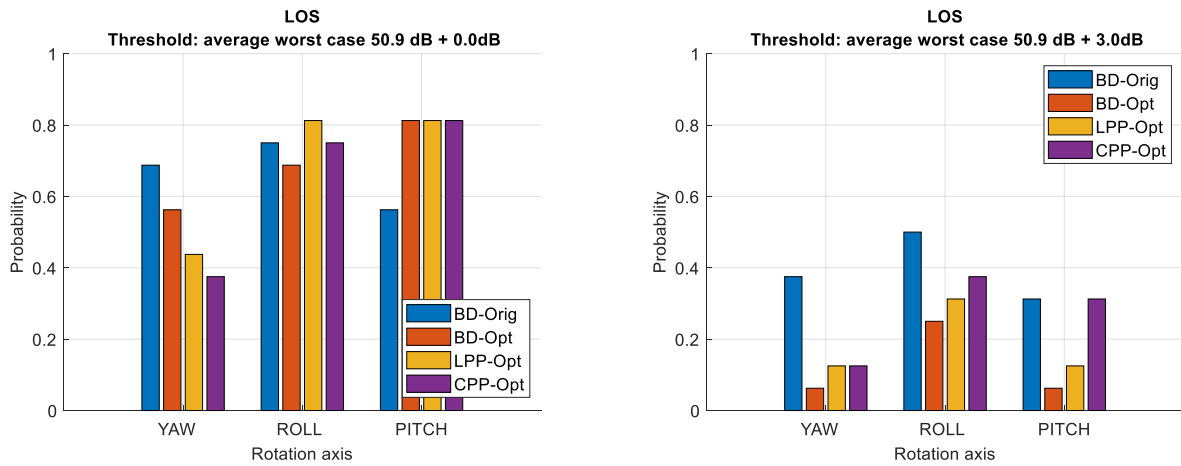


Figure 167. Comparison in LOS. Comparison of reliability indicator for BD-Orig, BD-Opt, LPP-Opt, CPP-Opt.

Setup LOS	Probability Threshold worst case	Probability Threshold: worst case + margin
Dip Original orien. (BD-Orig)	0.67	0.40
Dip Optimal pos. and orien. (updown) (BD-Opt)	0.69	0.13
LP patches (LPP-Opt)	0.69	0.19
CP patches (CPP-Opt)	0.65	0.27

Table 20. Comparison in LOS. Global probabilities for worst case threshold and worst case + margin in LOS, for BD-Orig, BD-Opt, LPP-Opt, CPP-Opt.

LOS	LPP-Opt compared to BDD-Opt		CPP Opt compared to BDD-Opt	
	Average SNR improvement	Free space equivalent distance improvement	Average SNR improvement	Free space equivalent distance improvement
YAW	+ 0.4 dB	+ 5 %	+ 0.4 dB	+ 5 %
ROLL	+ 1.3 dB	+ 16 %	+ 1.7 dB	+ 22 %
PITCH	+ 0.3 dB	+ 4 %	+ 0.9 dB	+ 11 %
TOTAL	+ 0.7 dB	+ 8 %	+ 1.0 dB	+ 12 %

Table 21. Comparison of LPP-Opt and CPP-Opt to BDD-Opt in LOS. Average SNR improvement and (FSEII).

As for all the tests in LOS, we can see how the performance does not change significantly from one setup to another. Yet, we could confirm here that the CP of the CPP-Opt slightly improves the performance, as we compare it with other LP patches (LPP-Opt) that in fact have a better gain.

5.3.3.2 Non-Line of Sight (NLOS) measurements and results

We can distinguish from the reliability metrics in Figure 169 and in Table 22 that, while the BD-Orig and CPP-Opt are different, the results from BD-Opt and LP-Opt are similar. For BD-Orig, and as we have seen in the other analyses in this report, these results confirm that the BD-Orig is the least reliable in NLOS due to the

position of the antennas in BD-Orig. The positioning of the BD-Opt, LPP-Opt and CPP-Opt is the same with respect to the cage, and therefore it is the circular polatization of CPP-Opt what improves the performance compared to BD-Opt and LPP-Opt. Therefore, the similar performance of BD-Opt and LPP-Opt comes from the fact that they are linearly polarised.

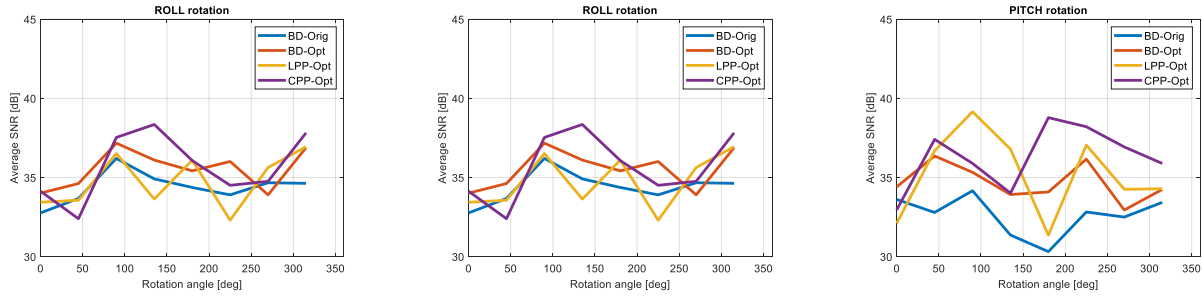


Figure 168. Comparison in LOS: average SNR over two measurements in the YAW, ROLL and PITCH rotation for various positions and orientations

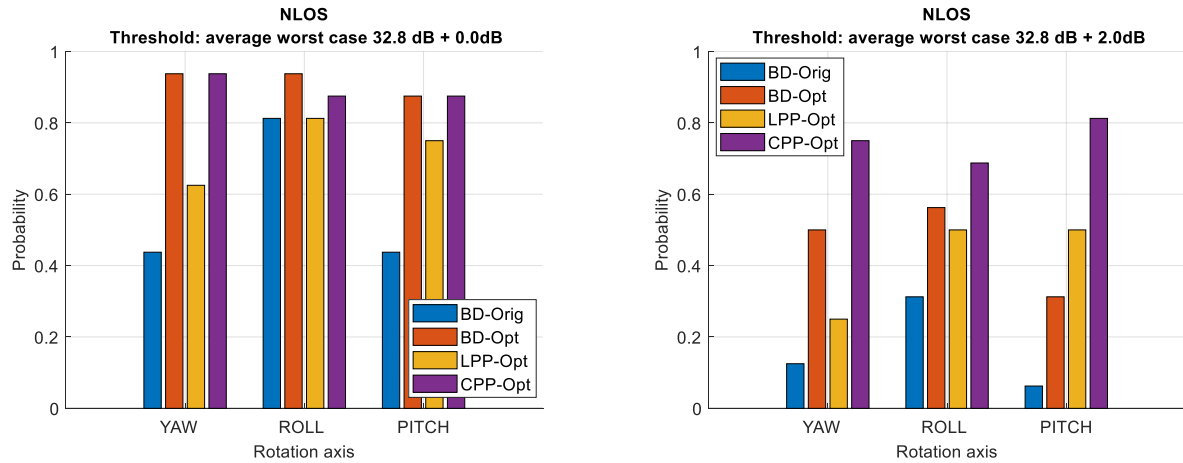


Figure 169. Comparison in NLOS. Comparison of reliability indicators for BD-Orig, BD-Opt, LPP-Opt, CPP-Opt.

Setup NLOS	Probability Threshold worst case	Probability Threshold: worst case + 2dB margin
Dip Original orien. (BD-Orig)	0.56	0.17
Dip Optimal pos. and orien. (updown) (BD-Opt)	0.92	0.46
LP patches (LPP-Opt)	0.73	0.42
CP patches (CPP-Opt)	0.90	0.75

Table 22. Comparison in NLOS. Global probabilities for worst case threshold and worst case and adjusted thresholds, for BD-Orig, BD-Opt, LPP-Opt, and CPP-Opt.

We compare the CP patches and LP patches to the same setup to see how these two behave differently. In Table 23, we can see that in terms of *free space equivalent distance improvement*, both the CP and LP patches improve the performance compared to the dipoles up-down the cage. However, and as we can anticipate from the results in Table 23, the performance using the LP patches improve only by 6% while it grows 18% for the

CP patches. We also need to consider that the peak gain of the LP patches is higher than the dipoles, so the transmitted power should be decreased to maintain the EIRP and comply with the certification limits. This would lead to a further degradation of the performance using the LP antennas compared to the results in Table 23.

NLOS	LP patches up-down compared to dipoles up-down		CP patches up-down compared to dipoles up-down	
	Average SNR improvement	Free space equivalent distance improvement	Average SNR improvement	Free space equivalent distance improvement
YAW	0 dB	0 %	1.2 dB	+ 15 %
ROLL	-0.2 dB	-2.3 %	0.6 dB	+ 7.5 %
PITCH	1.5 dB	+ 19 %	2.3 dB	+ 30 %
TOTAL	0.5 dB	+ 6 %	1.4 dB	+ 18 %

Table 23. Comparison of LPP-Opt and CPP-Opt to BDD-Opt in NLOS. Average SNR improvement and (FSEII).

5.3.3.3 Conclusions

This experiment shows the importance of using polarization diversity and circular polarisation in NLOS and multipath scenarios. The CP is the key advantage of the patches, and this is especially true as they present other limiting factors inherent to the restriction on the number of antennas: they have lower gain and narrower beam than the LP patches and dipoles.

5.3.4 System measurements: Comparison of antennas inside and outside the cage: effect of the cage

We have seen in previous Sections that using CP antennas is beneficial for the reliability of the radio link. This benefit can come from two sources: the cross polarisation between the antennas of the controller and the drone is diminished, and that the circular polarisation is more resilient to the effect of the cage. The latter effect could be generated from the fact that a CP antenna can "listen" in two orthogonal polarisations. We expect that these two are modified by the cage similarly as we have many cage segments around the antenna for many different rotations.

With the tests in this Section, we expect to understand to what extent the better performance of the CP patches is due to a better resilience to the effect of the cage. The measurement setups used in this Section are BD-Ins (Figure 157), BD-Out (Figure 158), CPP-Ins (Figure 159) and CPP-Out (Figure 160), and consist on placing the BD and the CPP patches along exactly the same radial distance inside and inside the cage, as sketched in Figure 170. We analyse only the results in NLOS for the sake of brevity, as we have confirmed repeatedly for all the tests that in LOS the differences between antenna setups are not significant.

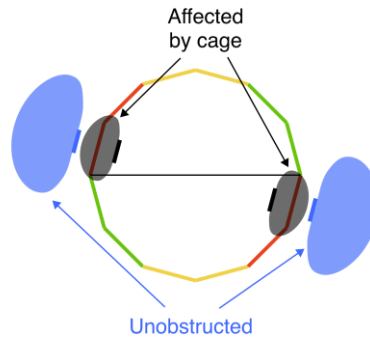


Figure 170. Sketch of the interaction of the antennas inside and outside the cage, and their placement for the tests. The cage cross section shows the various pentagons highlighted with different colors.

In Figure 171, we can see that BD-Out have a better SNR for most angles than the BD-Ins. The average SNR of the CPP-Out is more unstable than CPP-Ins, which could come from a shadowing at some rotations of the cage as we rotate, that is especially noticeable in yaw.

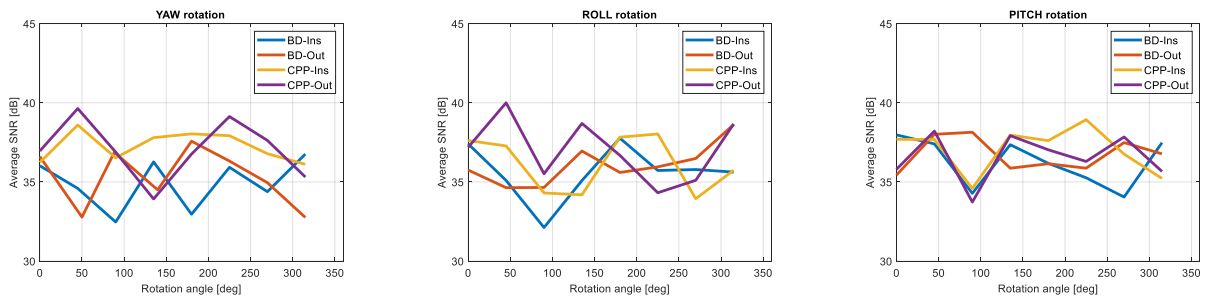


Figure 171. Comparison in NLOS: average SNR over two measurements in the YAW, ROLL and PITCH rotation for various positions and orientations

It is not obvious to glimpse in Figure 171 if SNR is better for CPP-Ins or CPP-Out. We can spot clearer differences using our reliability metric, in Figure 172 and Table 24. Especially for the worst-case threshold, the reliability of CPP-Ins and CPP-Out is almost identical, while the change is more remarkable for the BD. In fact, the reliability of CP-Ins is as good as BD-Out.

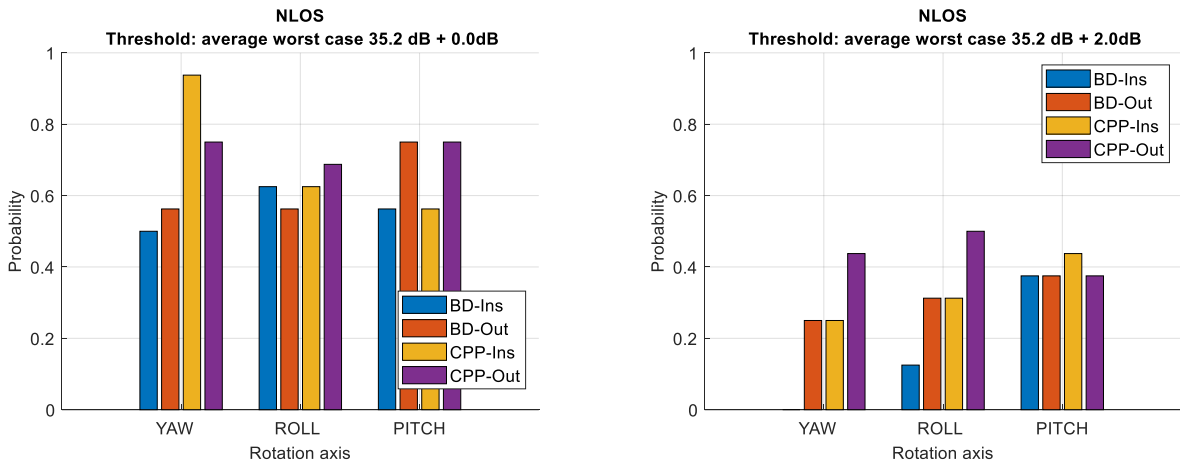


Figure 172. Comparison in NLOS. Comparison of reliability indicators for BD-Ins, BD-Out, CPP-Ins, CPP-Out.

NLOS	Probability Threshold worst case	Probability Threshold: worst case + 2dB margin
Dipoles in cage (BD-Ins)	0.56	0.17
Dipoles outside of cage (BD-Out)	0.63	0.31
CP patches inside cage (CPP-Ins)	0.71	0.33
CP patches outside cage (CPP-Out)	0.73	0.44

Table 24. Comparison in NLOS. Global probabilities for worst case threshold and worst case + margin, for BD-Ins, BD-Out, CPP-Ins, CPP-Out.

While the difference is not enormous, these results suggest that indeed the BD are a bit more affected by the cage than the CPP. We can then consider the changes in terms of FSEII to obtain a clearer picture. In Table 25, we calculate the *FSEII* of the BD-Out compared to BD-Ins and CPP-Out compared to CPP-Ins. We see that the overall improvement of the BD is 20 % against the 13 % of the CPP, confirming that the BD are more affected by the cage. In yaw, which is the most important rotation axis in a drone, CPP change significantly less (5%) than BD (19%).

NLOS				
	BD-Out compared to BD-Ins		CPP-Out compared to CPP-Ins	
	Average SNR improvement	Free space equivalent improvement indicator (FSEII)	Average SNR improvement	Free space equivalent improvement indicator (FSEII)
YAW	1.5 dB	19 %	0.4 dB	5 %
ROLL	1.4 dB	17 %	1.7 dB	22 %
PITCH	1.9 dB	24 %	1.0 dB	12 %
TOTAL	1.6 dB	20 %	1.1 dB	13 %

Table 25. Average change of SNR and FSEII, comparing BD-Out to BD-Ins and CPP-Out to CPP-Ins. The bigger the change, the more significant the effect of the cage.

The results in this section have shown consistently that the CPP are more resilient to the effect of the cage than the BD. Along with the reduced cross polarisation losses thanks to their CP, the better resilience of the patches to the cage contributes to the better reliability of the CPP that we have observed throughout the tests.

5.3.5 Conclusions

We can extract the following conclusions from this Chapter:

- The antenna closer to the cage suffers a focusing effect, thus only one sector of the cage is significantly interacting with the antenna. Using a directional antenna allows to minimize the sector of rods interacting with it, but then more antennas are needed.
- The effect of the several cage rods leads to power reflected back to the antenna and power transferred to other modes.

- The positioning of the antennas is very important due to the effect of the structure. A closer placement of the antenna to the cage leads to a stronger iteration of that sector of the cage but a clever positioning can improve significantly the reliability of the link (using several antennas).
- In LOS scenarios, the choice of the antenna system does not affect significantly the reliability of the system as there is a direct path between the drone and the controller.
- In NLOS, the reliability of the radio link is more unstable, and it is in this case when the CP patches perform consistently better than the LP dipoles. The proposed CP patches (CPP) improve the **reliability of the link compared to the dipoles in their original assembly (BD-orig) by 70%**. They also improve the average SNR of the system in all the NLOS configurations that we have tested. We can translate this SNR increase to the **equivalent distance that the range would increase in free space, improving the downlink up to 90% when compared to BD-Orig**.
- From all the tests we could also understand the importance of using the CP for a better reliability in NLOS indoors (multipath environments), and also for a better resilience to the effect of the cage. It shows more resilience to the structure and to cross polarization losses.

6 Broadening the beamwidth of microstrip antennas using multiple elements for larger footprint antennas

This Chapter has the goal of extending the use of additional elements for larger footprints, for applications where the size and weight are not as critical as they are for drones. A larger antenna allows more degrees of freedom and to explore the potential of different additional radiators. Also, it is more straightforward to understand the separate contributions of each element, which ultimately allows to provide a more structured and formal overview of the use of additional radiators in a more general scope.

The Chapter starts by refreshing the basics of array theory, and uses this as a starting point and reference to understand the functioning of patches as additional radiators. We use parasitics identical to the active antenna, which simplifies the formulation of the problem and allows to understand the effect of each element. This allows to provide guidelines and a more didactic explanation about the technique. We provide the mentioned detailed explanation with guidelines to use this approach to design LP and CP antennas with a single-feeding.

We finalize by presenting an antenna using parasitic elements for a specific application in satellite communications. This new application works requires dual band operation and a different frequency band (1.5-1.56GHz for downlink and 1.6-1.66 GHz for uplink). These changes present new challenges and compromises to be made between bandwidth, beamwidth and AR beamwidth, and gives a more realistic example of an antenna for a specific application. To be consistent with the rest of the Thesis, we use the ISM band at 2.4GHz for the analysis and explanations in Sections 6.1 and 6.2, and we modify it for the antennas in Section 6.3, according to the new frequency band required by the application.

6.1 Basic array theory as an analogy to increase the beamwidth with additional elements

In this Section, we tackle the broadening of the beamwidth of microstrip antennas using additional elements starting from basic array theory. We start with an illustration of the simplest array possible, using only two patches. If we combine two of these arrays side by side, we can generate a broadened or even isoflux pattern using an array of three elements. To finalise, we disconnect two of the patches in the 3-element array, resulting in a single fed patch antenna with parasitic elements, that still follows the same principle as the array to generate a broad-beam radiation pattern.

6.1.1 Basic two-elements array. Directing the beam towards a given direction.

Using antennas in arrays allows to radiate patterns that are not achievable using a single element. Among its advantages, the pattern can be more directive, or it can point to a direction different than the peak of its individual elements. The total pattern created by any array of identical antennas can be separated into two contributions: the array factor and the antenna individual pattern. One simple architecture of are 1D arrays with linear phase delay between its elements, which allow to generate an array factor that directs the beam in a given direction and in the plane along which the elements are located. The pointing of the array is controlled by the phase and magnitude at which the elements are fed, and their separation.

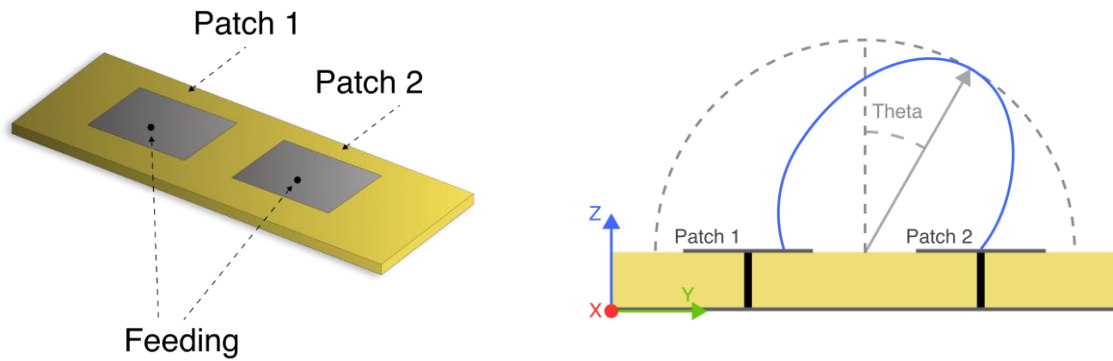


Figure 173. Two elements array, pin-fed with lumped ports (left), and illustration of the pointing of the radiation pattern when using a linear array with a phase delay between elements (right)

A simple array of two patches is shown in Figure 173. These are fed with lumped ports, exciting a mode on the patches with polarization along the X axis. If we feed both antennas with the same amplitude but with a given phase delay between each other, the pattern is tilted in the plane YZ following the idea shown in Figure 173.

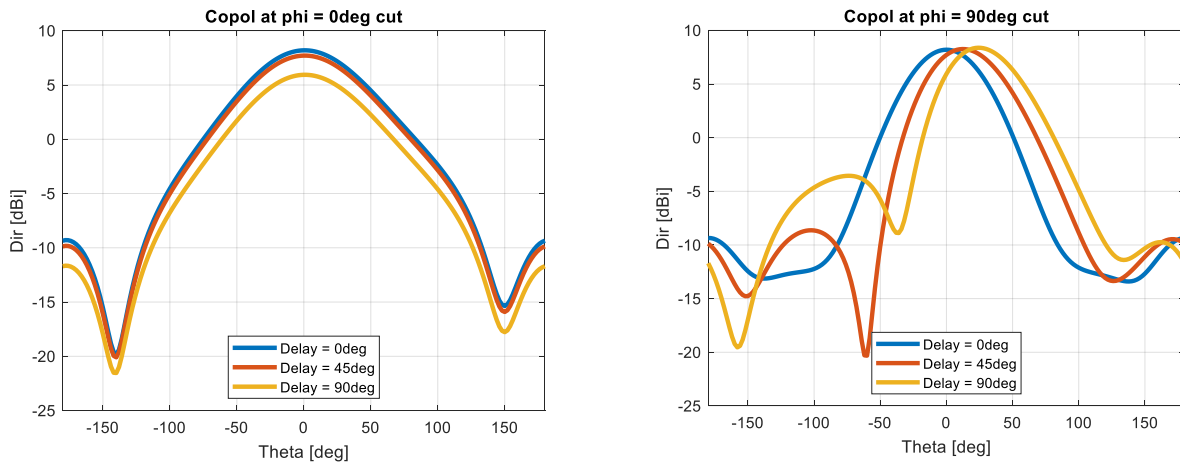


Figure 174. Radiation pattern in of a two-element patch array in the two main cuts at $\phi = 0^\circ$ (left) and $\phi = 90^\circ$ (right). The results are at @2.45GHz.

In Figure 174 we show how the pattern generated by the two patches for different phase delays allows to tilt the gain in the plane XZ ($\Phi = 90^\circ$). These patches use FR4 as substrate. This means that the use of arrays allows us to some extent to increase the gain in low elevation angles for patch antennas.

6.1.2 Three element patch arrays to tune the beamwidth

A common use of arrays is to increase the directivity in a given direction. In arrays of patches, as the pattern of the elements has its peak in broadside, the achievable gain decreases as the pointing angle increases. Depending on the requirements, it might be needed to increase the number of elements to radiate the desired pattern. A 3-element array as the one in Figure 175 that is fed with a progressive phase delay, generates a pattern tilted to one direction as happens for the 2-element array, but with better gain in the main beam.

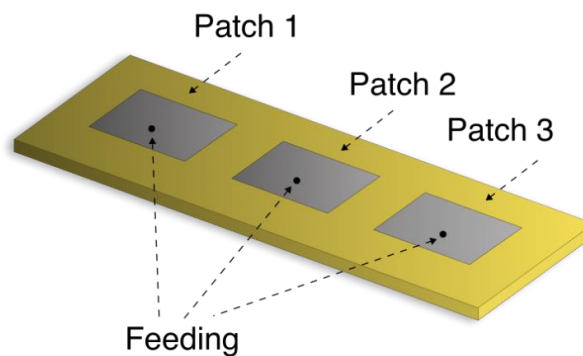


Figure 175. Array of three patches. The substrate is made of FR4 and its thickness is of 2.4mm.

Let us see the array from the perspective of several elements that interfere with each other to provide a certain array factor. Based on that idea, we can think of a 3-element array as the one shown in Figure 175, as the combination of two 2-element arrays side by side sharing the central patch. If we take the latter as a reference, and add the same phase delay to the lateral patches as described in Section 6.1.1, two beams directed in opposite directions are generated, as shown in Figure 176. The combination of both radiation patterns generates two lobes pointing to symmetric elevation angles (θ), and create a broadbeam or isoflux pattern when the separation between elements and the phase delay are properly tuned.

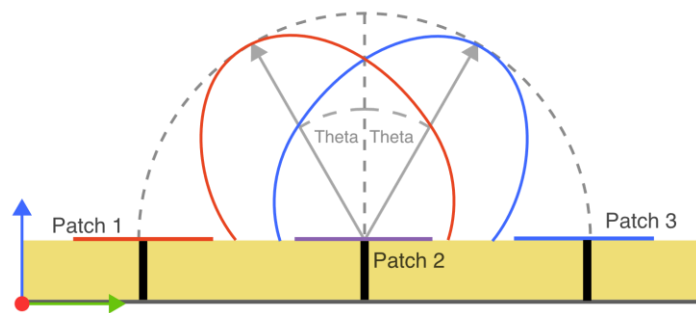


Figure 176. Patterns generated by the combination of Patch 1 and 2 in absence of patch 3 (red) and by the combination of Patch 2 and 3 in absence of Patch 1 (blue).

In Figure 177 we show the results for the two main cuts of the radiation pattern of the 3-element array and for different delays between the elements. We can observe how, for the plane YZ ($\phi = 90^\circ$) there are two lateral lobes that increase the HPBW up to 149° for a delay between elements of 135° . The feeding of the three patches to obtain these results is shown in Table 26.

	PATCH 1	PATCH 2 (CENTRE)	PATCH 3
AMPLITUDE (W)	0.1	1	0.1
PHASE (DEG)	+Delay	0	+Delay

Table 26. Feeding of the three patches to obtain the results of Figure 177.

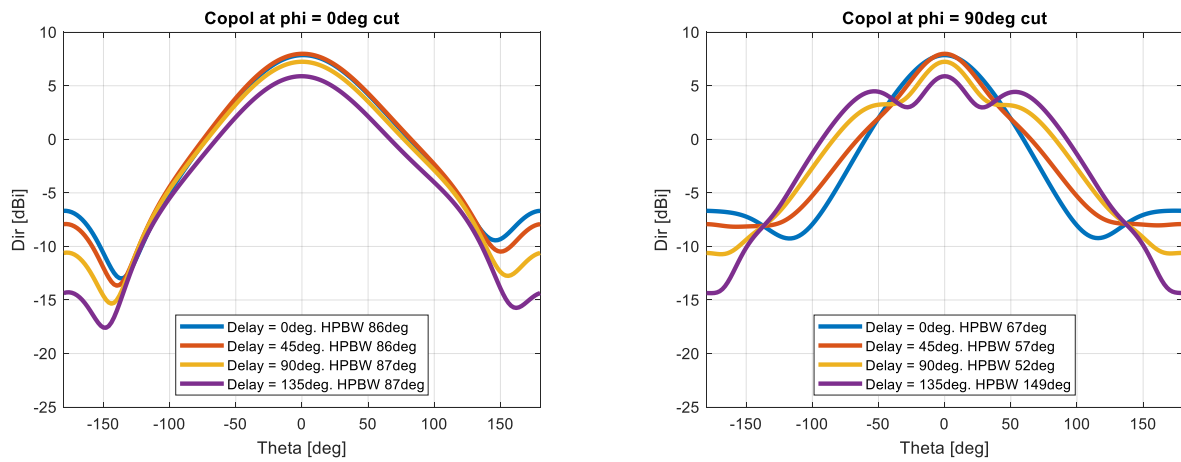


Figure 177. Radiation pattern of the 3-element array for its two main cuts at $\phi=0^\circ$ (left) and $\phi=90^\circ$ (right). This is made for the two lateral antennas with a 10% of the power of the central patch.

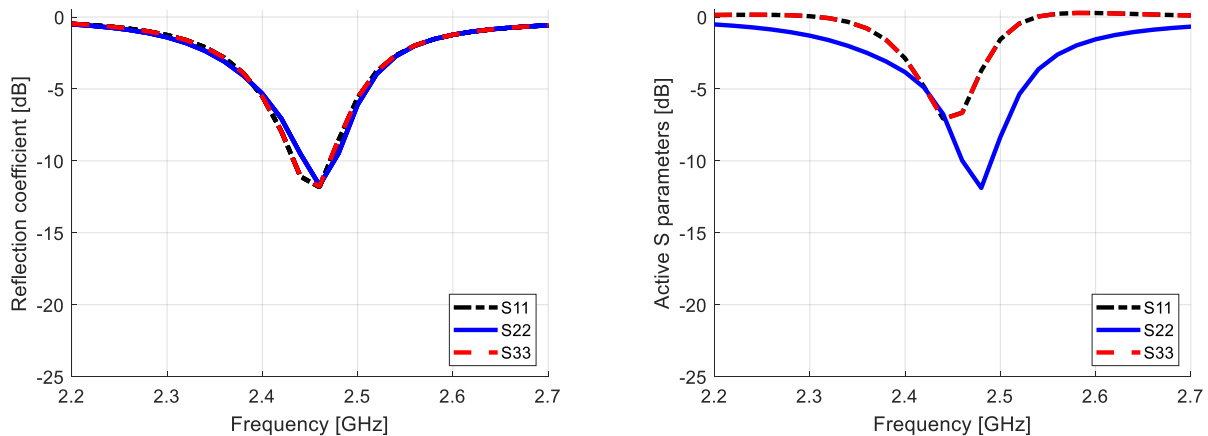


Figure 178. Normal S11 and Active S11 to show coupling

Another important aspect in arrays is the mutual coupling between the elements. As the antennas share the same substrate, the surface waves launched from each element propagate inside the substrate and affect the others. The power of the surface waves decays more slowly than the waves propagated in free space and thus they should be treated carefully. The effect of mutual coupling for the 3-element array can be seen through

the Active S-parameters in Figure 178. The reflection coefficient using traditional S parameters is the same for all the three antennas as they are identical, and the different Active S-parameters show that each of the three antennas are affected by the other two.

In conclusion, arrays can be used to change the shape of the radiation pattern with a proper feeding and spacing between the elements. A feeding network is required to feed the three elements as desired, and the effect of the surface waves should be addressed to obtain the expected results. While mutual coupling in arrays is usually negative and complicates the design, surface waves can also be used as an advantage as, for example, exciting parasitic elements with a single-fed patch.

6.1.3 Patch antenna with two parasitic elements for broad beamwidth

An evolution of the 3-element array of patches consists of disconnecting the two lateral patches and feeding only the central patch, as shown in Figure 179. This cannot be considered an array as there is only one feeding point, and it should be taken as an antenna with parasitic elements. However, it follows the same idea to increase the beamwidth using two pairs of elements with a symmetric phase delay, which is provided by the distance between elements. In this case, the surface waves in the substrate excite the parasitic patches, and the phase delay is controlled by the separation between the elements, as shown in Figure 180.

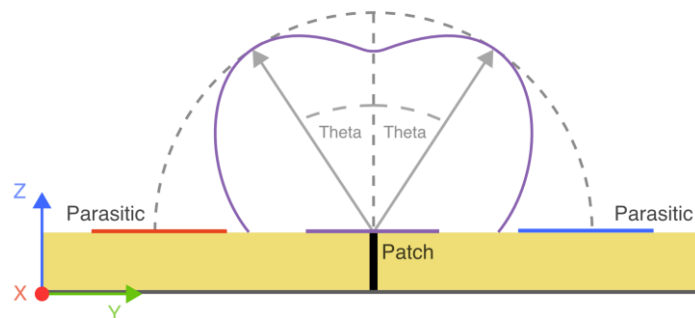


Figure 179. Total radiation pattern for a patch with parasitic elements designed to achieve broad beamwidth. The pattern results from combining the effect of the two sub-antennas (patch + parasitic elements).

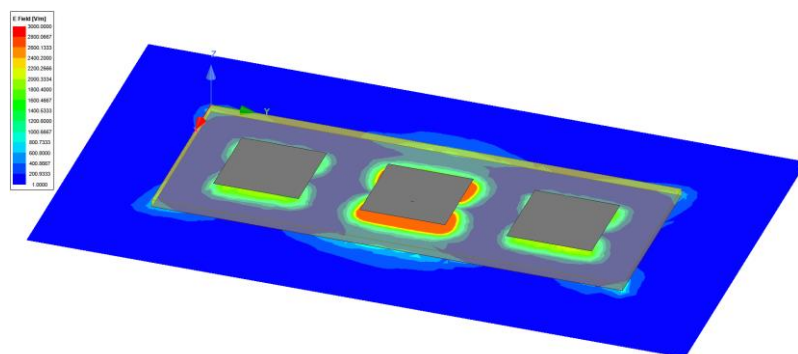


Figure 180. Central patch antenna is active and the two lateral patches are identical but not fed.

This design change leads to the following consequences compared to the 3-elements array:

- The feeding is simpler, consisting of a single point feeding as a coaxial cable.
- The needed phase shift between elements is delivered to the two parasitic patches directly by the coupling between the elements as they are all at the same distance between each other. It is important to mention that the patches can be arranged only along the axis orthogonal to the polarization of the antenna, as seen in Figure 181.
- The amplitude and phase of the parasitic elements is dependent on the separation between the elements. This simplifies the design but decreases its degrees of freedom.
- As the two parasitic elements are not fed, the matching is easier to tune, and it only changes slightly the matching of the central patch.

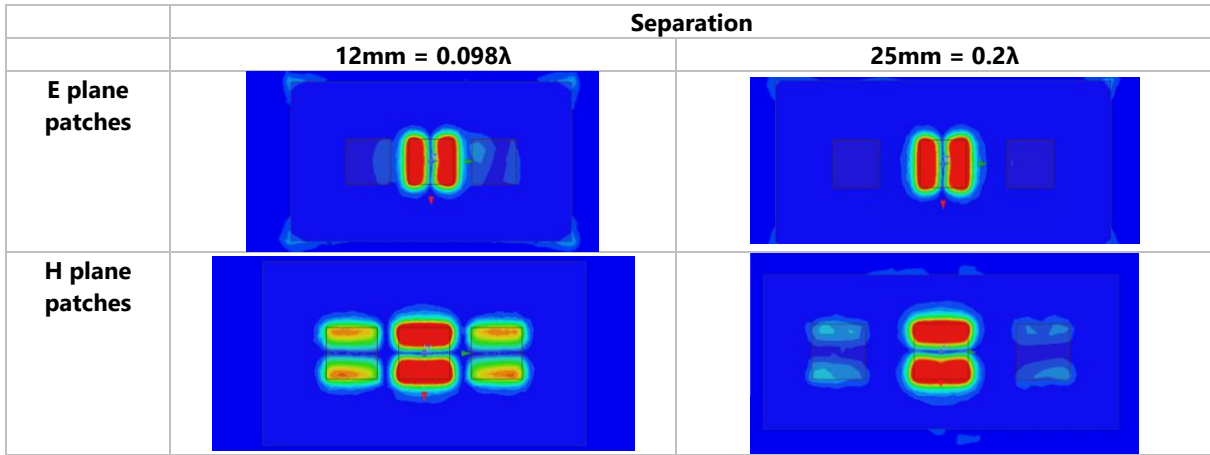


Figure 181. Different arrangement of the patches and the dependence with the element separation.

In Figure 182, we can see the results of the radiation pattern for the patch with parasitic elements for a set of different separations. The effect described in Figure 179 is clearly visible as there are two symmetric lobes around the broadside directions. This type of antenna allows then to achieve HPBW in the range of 140°.

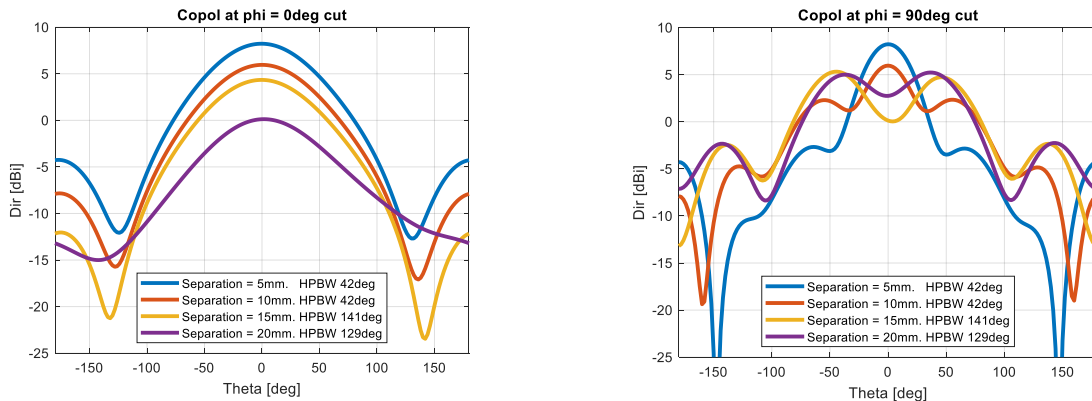


Figure 182. Phi = 0° (left) and Phi = 90° (right) pattern cuts for a patch with parasitic elements identical to the patch placed along the Y axis.

The example presented in this Section is for an ideal case and for a specific variation of the antenna with parasitic elements, where we do not modify parameters like the geometry of the latter. The technique requires a deeper and more detailed understanding to design the patch antenna and the parasitic elements.

6.2 Broadbeam patch using parasitic elements – concept and design rules

In this Section we explain more in detail how to use parasitic elements to increase the beamwidth of patch antennas, and to provide a quantitative assessment of the performance achievable using this technique. We also explain how a different type of the additional element and their individual patterns are another aspect to consider. For example, while the use of patches allows to increase the beamwidth to a certain level, using parasitic elements without a ground plane below them can provide a broader beamwidth thanks to the different individual pattern of the additional elements. We also show how this technique can be used to design CP antennas. The work in this Section uses the contribution in [74].

6.2.1 Description and analysis of the beamwidth enhancement

To start, we define the geometry of the parasitic elements and its parameters that we use throughout the Section. In this example we use patches without ground for a broader beamwidth. The pattern of the additional elements is therefore more omnidirectional, and contributes to improve the radiation in the end-fire direction. This technique is applicable for similar antennas with other types of parasitic elements. We can see the geometry in Figure 183 and the specific values of its parameters in Table 27. The antenna beamwidth is optimized the plane YZ ($\Phi=90^\circ$) by placing the parasitic elements along the Y axis.

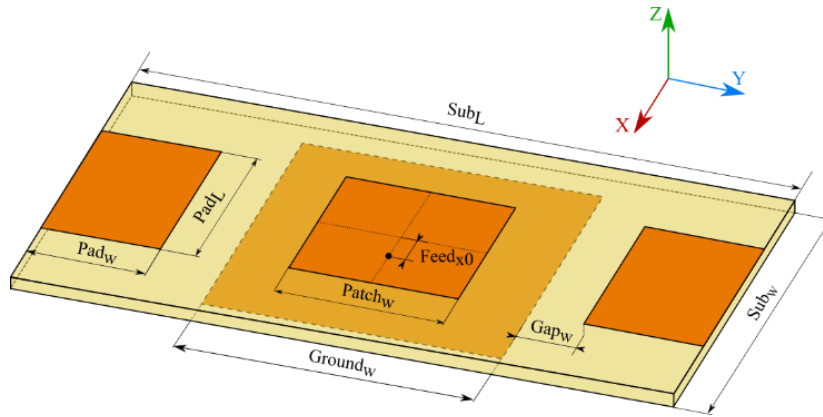


Figure 183. Example of a rectangular patch with parasitic elements to enhance the beamwidth in the YZ plane [74]

Ground_w	Gap_w	Pad_w	Pad_L
50 mm	10 mm	20mm	30mm
Sub_L	Sub_w	Feed_{x0}	Patch_w
110 mm	60 mm	7mm	28.2mm

Table 27. Values used in the example

To feed the antenna a lumped port is used, connected only to the central patch, and the lateral patches are passively activated by the central patch. The reflection coefficient of the antenna is shown in Figure 184. The bandwidth covers the entire 2.4-2.48 GHz ISM band, and the effect of the parasitics is negligible in the reflection coefficient if they are placed sufficiently separated from the patch.

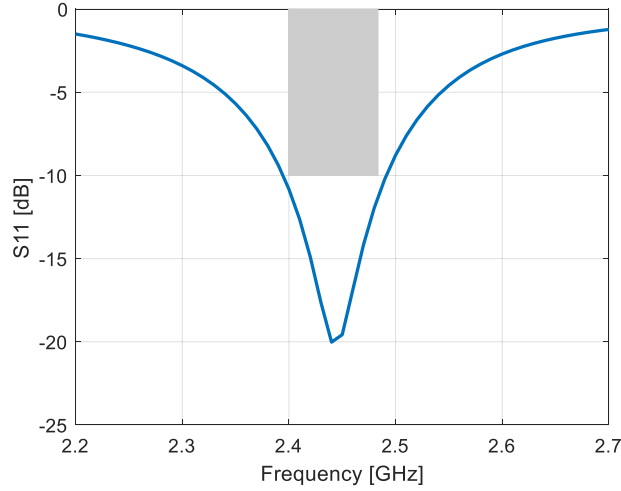


Figure 184. Reflection coefficient. Bandwidth of 97 MHz [74]

As this design is made to show the concept and validate it with measurements, we use as a substrate a low cost FR4 with 2.4mm of thickness. This material has a relative permittivity $\epsilon_r = 4.4$ and a loss angle $\tan\delta = 0.02$. As our focus is on the shape of the pattern, and the high losses of the FR4 decrease the gain, we use the directivity as a figure of merit. Using a substrate with lower losses is a safer option for a design that requires better gain.

With the geometry in Figure 183 and Table 27, we obtain HPBW of 220° in the YZ plane. In Figure 185, we can see how the directivity drops at the center, and the maximum peak occurs at $\theta = -55^\circ$ and 55° . This pattern is very stable in the frequency band, with very small variations of 0.3dBi at $\theta = 0^\circ$.

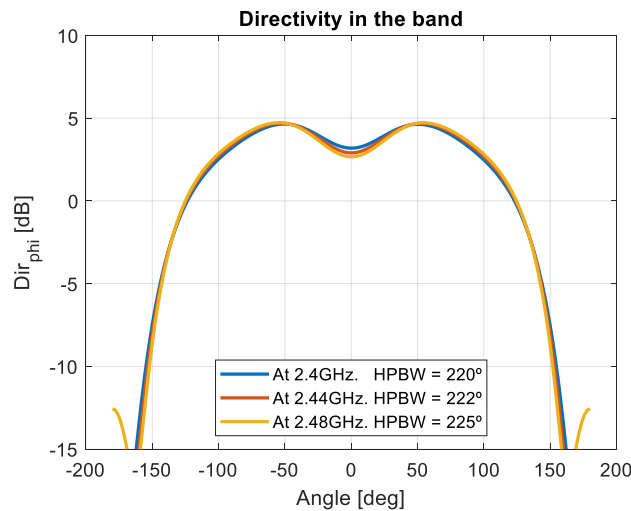


Figure 185. Directivity for the lower, middle, and upper frequencies within the band [74].

The parasitic elements are fed by the active patch and therefore in the same polarization, providing a large cross polar discrimination (XPD) higher than 30dB in the upper hemisphere as we can observe in Figure 186.

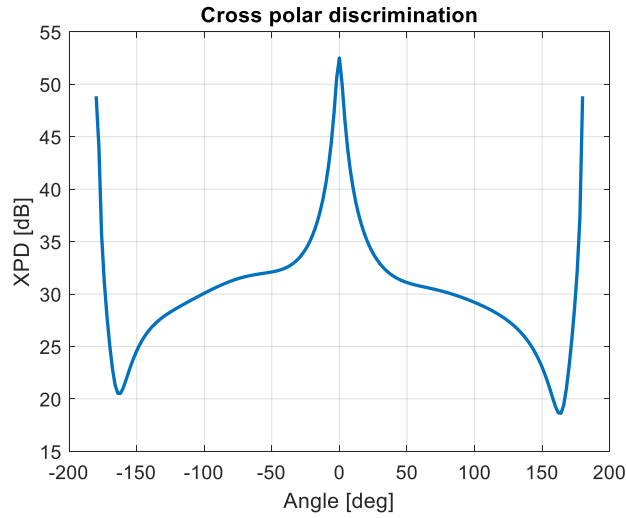


Figure 186. Cross polar discrimination in the YZ plane. XPD is larger than 30dB in the entire upper hemisphere [74].

We fabricated and measured the antenna in Figure 183 and with the values in Table 27. The simulated and measured results of the pattern are collected in Figure 187, showing a good agreement in the shape of the pattern and the HPBW. The ripples in the measurements are caused by the measurement setup, as the antenna has a broad beamwidth, it is very sensitive to the surrounding elements.

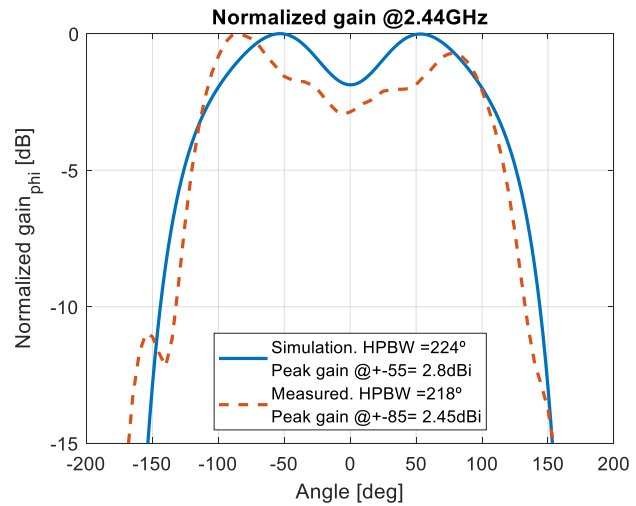
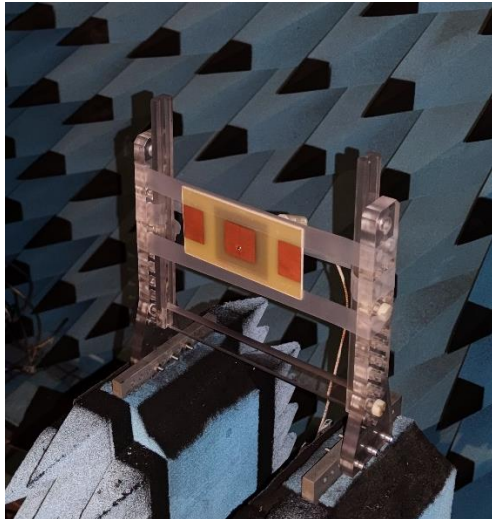


Figure 187. Fabricated prototype (left) and comparison of normalized pattern in simulation and measurements at the center of the band and in the YZ plane (right) [74].

The antenna is composed of various radiating elements, and therefore the interaction between elements should be treated carefully. The most critical parameters to look at are: the distance between the elements

(gap_w) and the size of the parasitic strips (pad_l and pad_w). By tuning these parameters, the pattern can be modified substantially, and the beamwidth can be increased as much as the application requires.

6.2.2 Modifying the pattern by tuning critical parameters: gap_w , pad_w and pad_l

The inter-element separation is critical to change the shape of the radiation pattern, and the contribution of the parasitic elements to the total radiation also decreases when these are more separated from the active patch. We can see this antenna as a simplified version of an array of three elements: the separation controls the amplitude but also the phase shift between elements leading to different total radiation patterns. In Figure 188, we observe how one can achieve isoflux patterns when the separation is small ($gap_w = 10\text{mm}$), and it evolves to more directive pattern as it increases.

The results for several variations pad_l are collected in Figure 189, in which we can observe how this parameter has also a strong effect on the shape of the pattern. When it is shorter than the central patch ($\lambda/2$ on FR4), the effect on the pattern is less noticeable. When the size is close to $\lambda/2$, the pattern has a minimum in broadside which leads to a very broad HPBW. For longer length values, above $\lambda/2$, the back radiation increases and the pattern is more directional in broadside.

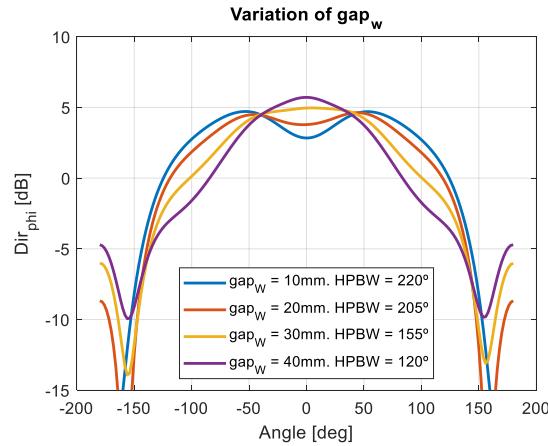


Figure 188. gap_w sweep [74]

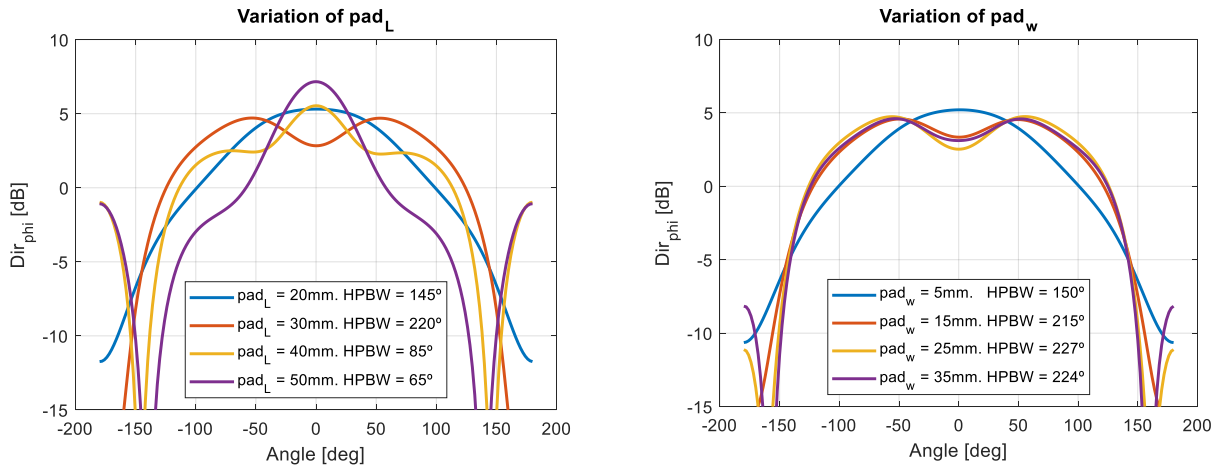


Figure 189. pad_l (left) and $Strip_w$ sweeps (right) [74]

The parameter pad_w does not have a significant effect on the pattern, as long as it is larger than 10mm, as seen in Figure 189. This parameter has a direct effect on the antenna footprint, so our recommendation is to keep it small enough to reduce the size but sufficiently large to enable substantial changes on the pattern.

The size of the ground plane is also an important parameter of importance to the beamwidth of microstrip antennas in general. In all the results presented in the Section, the ground size remains unchanged. Smaller ground sizes lead to higher back radiation and the beamwidth is also more prone to increase. The operation of the parasitic elements depends on the ground size and therefore one should consider it in the design. We recommend to keep it large enough for a stable and reliable impedance matching.

6.2.3 Compromise between size, performance and compatibility for CP antennas

The technique is useful to improve the beamwidth in one plane, but can also be extrapolated to two orthogonal planes circular polarization. To this aim, one needs to add another pair of the parasitic pads in the perpendicular plane, resulting in the geometry shown in Figure 190.

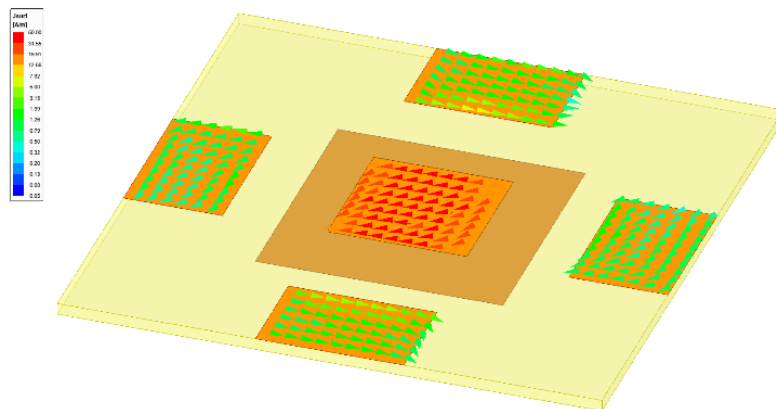


Figure 190. Surface currents on the geometry with additional pads, to excite circular polarisation and extend the beamwidth in the XZ and YZ planes [74]

In Figure 190, the current density in all the radiating elements when CP is excited in the central patch via two lumped ports. The pads in the YZ plane are in orthogonal polarization to those in the XZ plane, thanks to the two orthogonal modes of the CP. Each mode (along X and along Y axes) excites a pair of parasitic elements and broadens the beamwidth in one axis.

To understand the operation of the antenna in CP, it is important to understand the radiation from the two separate two orthogonal and linearly polarized modes excited on the geometry. The pattern radiated by one of the modes (polarization along X axis) is shown in Figure 191. The results show that for the XZ plane, the beamwidth is not increased and the directivity decreases rapidly with angle. As the CP radiation pattern combines two orthogonal modes, each of them broadening the beamwidth in only one plane, the narrower pattern of the non-enhanced planes sets a limit to the achievable beamwidth broadening. However, one can tune the two separate LP modes to radiate isoflux patterns, as the one in Figure 191, to compensate for this effect, leading to reasonably flat gain for a very broad angle. We observe in Figure 192 that the HPBW of the CP

antenna is of 200° for both the XZ and YZ planes. The peak directivity is of 2.7dBi, lower than for the linearly polarized case, as in this case we are broadening the beamwidth in two planes. The XPD is low around 90° , which also causes the reduced co-pol directivity in these directions, that is compensated in this case also by the isoflux pattern of the two orthogonal modes composing the CP radiation pattern.

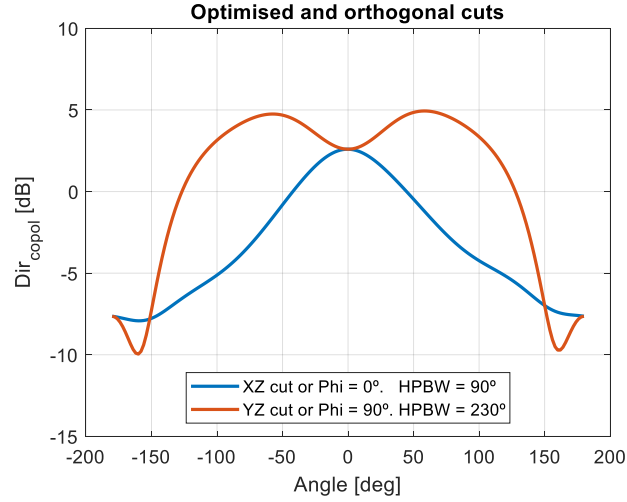


Figure 191. Copol of the XZ and YZ cuts with only one mode activated in the geometry of Figure 190 [74]

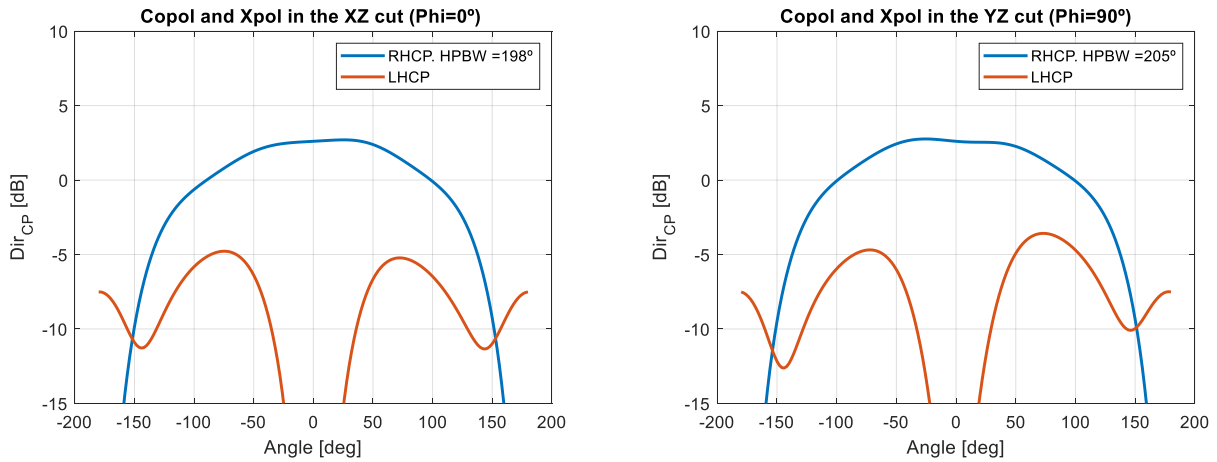


Figure 192. RHCP (Copol) and LHCP (Xpol) for the XZ cut (left) and YZ cut (right). The peak directivity is 2.7dBi [74]

6.2.4 Summary of the results

We can summarize this Section as follows:

- We can conclude from the analysis on the circular polarization that with a clever optimization of both orthogonal planes using conical patterns, one could design antennas with radiating CP patterns with HPBW as broad as 200° .

- We present a technique that allows to enhance the HPBW of conventional microstrip antennas to the range of 200° both in linear and circular polarization.
- We provide guidelines to use and understand some key parameters and obtain very distinct pattern shapes.
- We also explain in detail the effect of the parasitic elements, and use this knowledge to adapt the idea to obtain a circularly polarized broadbeam patch antenna. As the beamwidth can be increased substantially, using this technique opens a broad spectrum of options to establish compromises between the antenna size, gain, and beamwidth.
- Additionally, the technique does not increase the fabrication or feeding complexity, and it keeps the low profile that is critical for a broad range of applications.

The analysis in the Section is made for patches with rectangular parasitic pads, operating in a single band and in the ISM band at 2.4GHz.

6.3 Broadbeam patch using parasitic elements. Modification of the parasitic elements and dual band operation

In this Section, we extend the analysis of the parasitic elements to broaden the beamwidth of a patch antenna to a design applied to a specific application. The design consists of a cost-efficient low-profile CP dual-band IoT terminal antenna with improved beamwidth. The latter is a key requirement for Satellite-IoT applications as it has a direct effect on the system latency. Emphasis is placed on simplicity and antenna profile, while improving the radiation characteristics in both frequency bands.

This design gives us the chance to explain how to tune patches with parasitic elements to operate in dual band by modifying the shape of the parasitic elements, and to test this technique in the L band (1.5-1.56GHz for downlink and 1.6-1.66 GHz for uplink) instead of the S band. A dual band design with a small Frequency Ratio (FR) is obtained with a simple modification of a conventional CP single-fed patch antenna. This Section uses the work in [75].

6.3.1 Modification of the dual-band CP element

A conventional way of exciting circular polarization for single-fed patch antennas with a small frequency ratio is to generate two orthogonal degenerate modes of the patch resonator, using various geometric asymmetries (trimmed corners, diagonal slots, etc.). Using these techniques, the quality of the CP is optimal only in a single frequency point between the resonance of the two modes, and the impedance matching is widened. If dual band operation is required, the geometric asymmetry can be accentuated until the antenna resonances are separated to cover the two desired bands. This reduces the quality of the CP (increases the AR), but allows to

cover two bands with good impedance matching for a relatively small frequency ratio and zero increase in complexity. Other dual-band antenna geometries with closely spaced frequencies either use a multi-layered structures [16] or have a limited achievable frequency ratio [76]. This approach is applicable only to single-fed patch antennas.

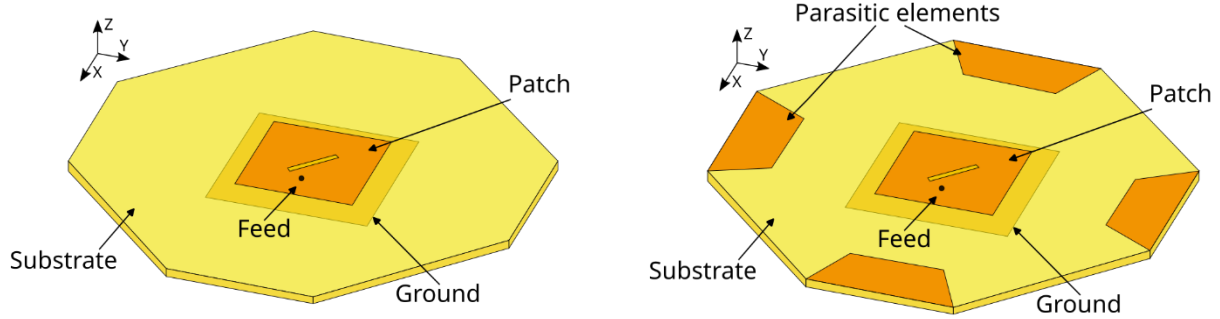


Figure 193. Proposed antenna geometry without parasitic elements (left) and with parasitic elements (right). The shape of the parasitic elements is modified and diagonal slots to excite dominant CP and dual band operation.

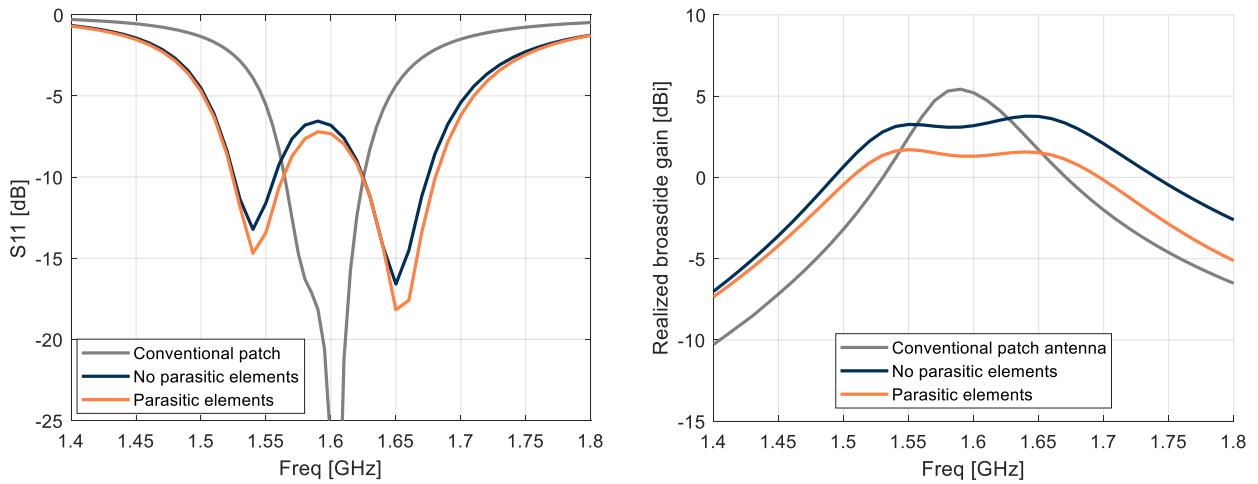


Figure 194. Simulated (left) S_{11} parameter and (right) broadside realized RHCP gain of (gray) a conventional patch antenna (not shown here), and the proposed antenna: (blue) without and (orange) with parasitic elements.

The antenna in Figure 193 uses parasitic elements to achieve a dominant CP component and a realized gain of several dBi in broadside in dual band operation. The AR values are around ~ 15 dB and the XPD ranges between 4-5 dB for the two frequencies. The low cost and complexity of this technique is preferred over the higher AR for low-bandwidth Satellite-IoT applications, as the antennas on the satellite side typically radiate very pure CP and the polarization losses of the remain low (typically 1.5 dB).

To demonstrate the principle, a CP patch antenna is designed on a low-permittivity substrate ($\epsilon_r=3.66$, $\tan\delta = 0.003$, $h=3$ mm) and tuned to the mobile-satellite frequencies of 1.54 and 1.64 GHz (see Figure 193). The S_{11} parameter and broadside CP realized gain are shown in Figure 194. The antenna exhibits a broadbeam pattern, with its peak in broadside and stable radiation patterns in both bands. The following Section describes the modifications that improve the antenna beamwidth at both frequency bands.

6.3.2 Beamwidth Improvement - Results

The beamwidth of the antenna should be broadened in both frequency bands and all azimuth angles. To this aim, four parasitic elements, coplanar to the patch and with trapezoidal shape, are added on the top layer of the patch substrate. The elements are placed with a 45° angular offset with respect to the polarization of the two degenerate modes of the active patch. This arrangement allows each of the patch modes to efficiently couple to all parasitic elements. This presence of the latter slightly improves the antenna matching at both frequency bands, as seen in Figure 194.

The antenna beamwidth is determined by the shape and size of the parasitic elements, as well as their distance from the patch. These parameters are optimized to have a stable pattern at two frequencies, necessary for an efficient two-way communication, and the trapezoidal shape of the parasitic elements improves their frequency stability. Placing the parasitic elements further away from the patch or making them longer increases the beamwidth, and can generate even conical radiation patterns. For our application, a HPBW beamwidth broader than 160° is not practically useful, as the IoT terminals usually cannot establish a link with the satellite at elevation angles lower than 10° above horizon. A compromise between the total antenna dimensions, gain, and pattern broadening is made to have a HPBW of around 150° in the two frequency bands. It is critical to carefully tune the two resonances created on the patch by the presence of the slot to achieve a stable pattern and beamwidth in both frequency bands.

The radiation patterns of the antenna, are shown in Figure 195, and the HPBW for the two frequencies and angular planes is shown in Table 28, also showing the the same antenna without parasitics. The average HPBW on all planes is of 133° and 146° at 1.54 and 1.64 GHz, respectively.

Frequency	1.54 GHz		1.64 GHz	
Angle ϕ	0°	90°	0°	90°
Without parasitic elements [°]	99	97	99	96
With parasitic elements [°]	148	160	128	148

Table 28. Antenna beamwidth (in $^\circ$).

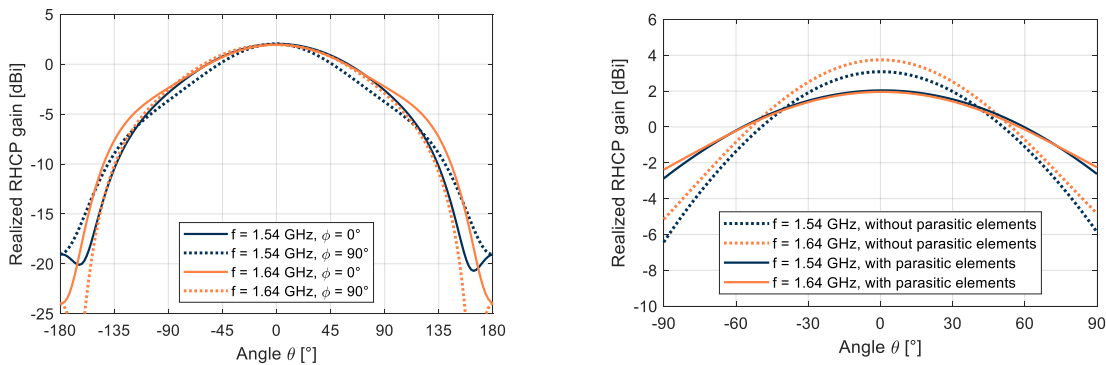


Figure 195. Radiation patterns of the proposed antenna at two frequencies and angular cuts (left), and comparison with the antenna without parasitic elements (right). Note the gain improvement of 1 – 2 dBi at angles $60 - 75^\circ$

6.3.3 Discussion on the results

We present a simple technique to design cost-efficient dual-band patch antennas with a small frequency ratio and a dominant CP sense, for Satellite-IoT terminals. The slot of the conventional rectangular CP patch antenna generates two separate resonances enable dual-band operation without increasing the complexity. This technique is convenient for dual-band CP communication systems with a small FR between both bands, as the AR of the proposed design deteriorates with the increase of the FR.

Four parasitic elements, placed around the patch antenna and coplanar to it, significantly broaden the antenna beamwidth at both frequency bands and all angular planes. The disposition around the patch, separation with respect to it, and their shape is modified to provide the desired compromise between pattern stability and antenna dimensions. The antenna has an average HPBW in all cuts of 140° , and it serves as a good example to illustrates the capabilities of the proposed patch antenna modification. The same principle can be applied to patch antennas having different substrate properties, opening more degrees of freedom to increase the beamwidth.

Despite its mechanical simplicity, the antenna placement and its integration with the IoT terminal should be carefully addressed. The lack of ground plane below the parasitic elements can lead to the perturbation of the antenna radiation depending on its placement. To address this limitation in the future, parasitic elements with a ground plane could be used, to the cost of reducing the achievable HPBW. Alternatively, a more elaborated positioning of the parasitic elements with respect to the patch can be considered, integrating them, for example, in a custom antenna radome. Moving the parasitic elements vertically would also increase the vertical section of the antenna, favouring higher gains in end-fire direction.

This type of antenna is presented as a response to a growing need for antennas with a wide beamwidth in the field of full-duplex dual-band IoT satellite communication. Improving the beamwidth of these antennas allows to reduce the time between satellite contacts and consequently, an improvement of the IoT message latency. A low profile of the presented design makes it especially interesting in the Satellite-IoT domains where terminal aerodynamics are crucial, such as commercial fleet management for land transport (cars, vans), and tracking of drones.

6.4 Conclusions

We can summarize this Chapter as follows:

- A 3-element patch array can be used to radiate a broad beamwidth by feeding the patches symmetrically with respect to the central patch.
- A single patch with parasitic elements can increase the beamwidth following the same principle of the 3-element array.
- We provide a set of guidelines and explanation on the how to design broadbeam patch antennas using parasitic elements, for linear and circularly polarized designs.

- The shape of the parasitic elements is crucial to tune the pattern. Different shapes can be used, for example, to increase the frequency stability of the pattern which is advantageous for wideband or dual band designs.
- The presented technique allows to generate patterns with HPBW larger than 200° in one plane in linear polarization and of up to 200° in two planes in circular polarization
- The antennas designed with this technique maintain a low profile and low fabrication complexity.
- These designs without ground plane need to be well tuned for the axial ratio beamwidth, and to find a compromise with the directivity beamwidth.
- With ground plane the back radiation is better and the AR beamwidth does not change as much as for the parasitic elements with no ground.

7 Conclusions

7.1 Summary and conclusions

Patch antennas have a directive pattern, with a typical HPBW of 70° due to the combined radiation of its two radiating edges in the broadside direction and their ground plane. Their low profile, low weight and easy fabrication makes them convenient for many applications despite their limited bandwidth. Therefore, the literature on increasing bandwidth or gain for patch antennas is very mature, but this is not the case with the broadening of their beamwidth. As their nature is intrinsically directive, increasing their beamwidth means pushing their limits, which calls for innovative and inventive solutions. These usually require a good understanding of each technique and of the patches themselves.

In this Thesis, the increase of the beamwidth of microstrip antennas is tackled from a didactic perspective, which is needed to reach a sufficient level of understanding of each technique that allows to use them to design broadbeam patch antennas. One can classify the various techniques surveyed in the State-of-the-Art in different groups into two large groups: modifying the canonical geometry of patch antennas, or using additional elements to extend the pattern of the patch. One modification in common to most of the contributions is to increase the profile of the antennas as much as the mechanical requirements allow, especially if significantly broadened pattern is needed. Thicker antennas have better bandwidth, and increase their vertical section and therefore their effective aperture seen from low elevation angles. This helps to increase the achievable gain at low elevation angles.

From all the techniques, the focus of the Thesis is on using additional elements beside the main patch, which is, from our experience, one of the options with a better potential and versatility to broaden the beamwidth of microstrip patches maintaining a low profile. This technique is very versatile as it has many degrees of freedom, one of the most important being the intrinsic radiation pattern of the additional elements. For a significant beamwidth improvement, one should use additional elements with good gain in low elevation angles, as, for example, tapered slot antennas.

A design of a patch antenna with crossed ground slots is presented, which establishes a compromise between weight (volume) and beamwidth. The designed patch embeds four slots in its ground plane, that are passively fed by the patch thanks to the currents induced in the ground. With a feeding network that excites CP on the patch, one pair of slots is activated with each of the two orthogonal modes needed for the CP, radiating a broadbeam pattern. The slots increase significantly the bandwidth of the patch, which allows to cover the band of operation with a good margin and to have a good pattern stability over frequency. The increased bandwidth is key to this design, as we can use a very high permittivity substrate to reduce the size of the antenna, meeting the size and weight requirements and achieving an enhanced HPBW ranging between 110° and 120° , which is an improvement of 40° - 50° compared to canonical patches. The antenna was measured and fabricated, showing a good performance that complies with the requirements. These antennas operate integrated inside of a geodesic conductive cage that serves as a collision protector for a drone. As the cage perturbs the performance of the antennas, we performed system measurements to validate their reliability. Through these tests, we can validate the superior performance in terms of reliability of the proposed broadbeam CP patches and extract useful conclusions on the interaction of the structure of the drone with different types of antennas.

To continue with the work on broadening the beamwidth of microstrip antennas using additional elements, we propose several designs with a larger footprint than the antenna for the drone. A bigger footprint allows to analyse more systematically the potential of this technique, and to provide a set of guidelines for the design of broadbeam patch antennas using this technique. These antennas can provide very broad patterns (even isoflux) if they are tuned properly. One of these versions was fabricated and measured, showing a good agreement between simulations and measurements and HPBW of 220° .

We summarize the work and main conclusions of the various Chapter as follows:

- **Chapter 2: State of the Art**

In this Chapter we provide a survey of the State-of-the-Art on broadbeam patch antennas. We can identify that there are two types of contributions: optimizing the directivity beamwidth or the AR beamwidth. In our case we focus on the optimization of the directivity beamwidth. This Chapter helps to have a compilation and overview on the different techniques to broaden the beamwidth of microstrip antennas that one can find in the literature. We provide a comparative table of all the techniques classified in two categories: using modification of the canonical structure of a patch (and its fringing fields), and using additional radiators.

A common trend of all the antennas is to increase their vertical section or to add vertical posts, to enlarge the vertical component of the fields and mitigate the effect of the low gain at low elevation angles.

- **Chapter 3: On the beamwidth of microstrip antennas and how to increase it**

This Chapter offers a thorough analysis of the main categories of the techniques identified in the State of the Art. Having a good understanding is necessary for a successful antenna design, and this is especially true for less canonical design as the case of broadbeam patches. We start with a brief explanation on the principle of operation of patches from the point of view of their pattern, as this serves as reference to understand the rest of the techniques.

The main conclusions that we can obtain about the beamwidth broadening from this Chapter are the following:

- **The antenna volumetry:** The ratio between the area of a microstrip antenna seen from broadside and endfire is in the range of 50, explaining the fact that the gain is limited in low elevation angles.
- **The ground plane effect:**
 - The ground plane being a quasi-perfect electric conductor sets a limit to the amount of power the antenna can transfer to the horizontal component of the E field in far field in low elevation angles.
 - The size of the ground plane plays a key role in the beamwidth, increasing the peak gain in broadside.

- **Different types of beamwidths for CP antennas:** For CP antennas there are two beamwidths to be considered: the directivity beamwidth and the AR beamwidth. To improve the AR beamwidth in low elevation angle one should balance the two orthogonal components of the E field in far field, which are also affected by the boundary conditions of the ground. As this condition is not inherently linked to the directivity beamwidth, one could increase the AR beamwidth using techniques that do not increase the directivity beamwidth.
- **Techniques to improve the beamwidth:**
 - Use a smaller ground and high permittivity substrate to decrease the ratio of effective area seen from broadside and endfire.
 - Increase the vertical section of the antenna by using 3D ground or bent structures.
 - Use additional radiators to complement the pattern of the patch.

The choice of the approach to increase the beamwidth depends on the application and its specific requirements. There are then other parameters that are important to address to have a complete overview: size, weight and bandwidth, among others.

- **Chapter 4: Compact and lightweight LP and CP broad-beam microstrip antennas: compromises and explanation through designs and examples**

In Chapter 4, we explain how additional elements can be used to modify the pattern of a patch without increasing its profile. The use of this technique is very versatile and it has many degrees of freedom, depending on the design requirements. With this Chapter we want to expand the knowledge on this technique and to provide novel designs with which we can explain how to establish compromises between beamwidth, bandwidth, size and weight, putting the focus on the latter.

We summarize here some conclusions extracted from the designs, fabrication and measurements of the antennas presented in this Chapter.

- We present a technique that makes use of slots as additional elements integrated in the antenna structure and passively activated by the patch, which is the only element that is connected to a feeding.
- One of the main advantages of using the ground slots is that this technique provides a very good bandwidth, that helps to achieve a better frequency stability for a smaller size.
- We present a design and prototype of a LP patch with ground slots, which increases the HPBW to 220° in one plane.
- We present a design and prototype of a very small CP patch with a HBBW of around 130° .

- The patches with ground slots, both in LP and CP, are robust to fabrication tolerances despite the combination of multiple radiators in the same structure. This happens thanks to the coherent feeding of all the slots by the patch.
- With the presented technique we can increase the beamwidth and the bandwidth, but not the AR beamwidth due to the several elements contributing to the radiation.
- As expected for designs of broad beam microstrip antennas, the patch + slotted ground technique also increases the back radiation.
- The measurement setup for very broad-beam is very sensitive and should be addressed carefully to get reliable measurements.

- **Chapter 5: Analysis of the cage and system measurements of the antennas assembled on the drone**

Chapter 5 focuses on the assessment of the antennas proposed in Chapter 4 through system measurements that include the effect of the protective cage. This Chapter gathers several analyses that can help to set benchmarks to assess the reliability of antennas in indoor environments and affected by any surrounding structure. Also, it is useful as it gives hints on how to integrate microstrip antennas in complex structures in general, and for a broad and stable coverage in particular.

We can extract the following conclusions from this Chapter:

- The antenna closer to the cage interacts with a smaller sector of the cage. Using a directional antenna allows to minimize the sector of rods interacting with it, but more antennas are needed.
- The effect of the several cage rods leads to power reflected back to the antenna and power transferred to other modes, which means that the purity of the polarization is degraded.
- A closer placement of the antenna to the cage leads, as is logical, to a stronger integration of that sector of the cage, but the interaction happens only with a small section. A clever positioning can improve significantly the reliability of the link.
- In LOS scenarios, the choice of the antenna system does not affect significantly to the reliability of the system as there is a direct path between the drone and the controller.
- In NLOS, the reliability of the radio link is more unstable, and it is in this case when our proposed CP patches perform consistently better than the LP dipoles. The proposed CP patches (CPP) improve the **reliability of the link compared to the dipoles in their original assembly by 70%**. They also improve the average SNR of the system in all the NLOS configurations that we have tested. We can translate this SNR increase to the **equivalent distance that the range would increase in free space, improving the downlink up to 90% when compared to the dipoles in their original assembly**.

- From all the tests we could also understand the importance of using the CP for a better reliability in NLOS indoors (multipath environments), and also for a better resilience to the effect of the cage. It shows more resilience to the structure and to cross polarization losses.

- **Chapter 6: Broadening the beamwidth of microstrip antennas using multiple elements for larger footprint antennas**

Finally, Chapter 6 focuses on the detailed explanation of the technique using additional radiators to enhance the beamwidth of patches. This approach is very versatile but it can also get very complex to understand and tune due to the several radiators interacting with each other and creating many interdependent parameters. The objective of the Chapter is to provide a structured analysis that allows to get a deeper understanding of the main parameters to tune these designs.

We can summarize this Chapter as follows:

- A 3-element patch array can be used to radiate a broad beamwidth by feeding the patches symmetrically with respect to the central patch.
- A single patch with parasitic elements can increase the beamwidth following the same principle of the 3-element array.
- We provide a set of guidelines and an explanation on how to design broadbeam patch antennas using parasitic elements, for linear and circularly polarized designs.
- The shape of the parasitic elements is crucial to tune the pattern. Different shapes can be used, for example, to increase the frequency stability of the pattern which is advantageous for wide-band or dual band designs.
- The presented technique allows to generate patterns with HPBW larger than 200° in one plane in linear polarization and of up to 200° in two planes in circular polarization
- The antennas designed with this technique maintain a low profile and low fabrication complexity.

7.2 Future work

The antenna system on the drone can be improved with new solutions that take advantage of the already gained knowledge about the structure. Modifying the cage was not possible during the project, as it is an essential part of the drone and its material and geometry are optimized for collision resilience. However, we can envision a more intelligent use of the cage and the antenna system, as making use of the cage (or portions of it) as radiators, or implementing using more antennas in a MIMO. The latter would allow for a higher

directivity of each antenna element, increasing the range or saving battery for the same range (less transmitted power to comply with certification limits).

The antennas with parasitic elements open a very broad range of possibilities and applications. However, they have many degrees of freedom, which sometimes can make their use very challenging. One direction to go with these designs is to find a way to simplify their formulation following the same idea as the designs on Chapter 5. These antennas can also be used to design reconfigurable patterns, where we selectively activate or deactivate parasitic elements. Also, exploring options with a better integration resilience would be very useful, even if this comes at the cost of a narrower beamwidth.

The broadbeam patch antennas using higher order modes presented in Chapter 4 were discarded during the design of the antennas for the drone due to their large size. The idea would be to explore more in that direction and how to excite circular polarization on them. This is useful for other applications that do not have such a strong weight restriction as the antennas for the drone.

References

- [1] C. A. Balanis, *Antenna Theory: Analysis and Design*, 3rd Edition. Hoboken, NJ: Wiley-Blackwell, 2005.
- [2] M. J. Arpaio, F. Fuschini, E. M. Vitucci, V. Degli Esposti, M. Barbiroli, and D. Masotti, 'Lightweight Microstrip Patch Array for Broadband UAV Applications over 5G networks', in *2019 Conference on Microwave Techniques (COMITE)*, Apr. 2019, pp. 1–5. doi: 10.1109/COMITE.2019.8733547.
- [3] M. S. Sharawi, O. A. Rawashdeh, and D. N. Aloji, '2.4 GHz Printed Antennas Embedded in Small UAV Wing Structures', *J. Electromagn. Waves Appl.*, vol. 24, no. 4, pp. 463–474, Jan. 2010, doi: 10.1163/156939310790966097.
- [4] M. Esquius Morote, 'Horn Antennas and Dual-Polarized Circuits in Substrate Integrated Waveguide (SIW) Technology', EPFL, Lausanne, 2014. doi: 10.5075/epfl-thesis-6421.
- [5] W. L. Williams, L. A. Anderson, and A. M. Kroening, 'Lightweight agile beam antennas for UAVS using advanced injection-molded materials', in *2007 IEEE Antennas and Propagation Society International Symposium*, Jun. 2007, pp. 21–24. doi: 10.1109/APS.2007.4395420.
- [6] P. Chandhar, D. Danev, and E. G. Larsson, 'Massive MIMO for Communications with Drone Swarms'. arXiv, Dec. 08, 2017. doi: 10.48550/arXiv.1707.01039.
- [7] N. Boisbouvier, F. Le Bolzer, and A. Louzir, 'A compact radiation pattern diversity antenna for WLAN applications', in *IEEE Antennas and Propagation Society International Symposium (IEEE Cat. No.02CH37313)*, Jun. 2002, vol. 4, pp. 64–67 vol.4. doi: 10.1109/APS.2002.1016927.
- [8] 'Isoflux antenna coverage'. https://www.esa.int/ESA_Multimedia/Images/2018/11/Isoflux_antenna_coverage (accessed Oct. 05, 2022).
- [9] X. Ren and H. Wong, 'A Circularly Polarized Shaped Beam Antenna with Isoflux Radiation Pattern', in *2019 International Conference on Microwave and Millimeter Wave Technology (ICMMT)*, May 2019, pp. 1–2. doi: 10.1109/ICMMT45702.2019.8992304.
- [10] E. Pittella *et al.*, 'Reconfigurable S-band patch antenna system for cubesat satellites', *IEEE Aerosp. Electron. Syst. Mag.*, vol. 31, no. 5, pp. 6–13, May 2016, doi: 10.1109/MAES.2016.150153.
- [11] 'Flyability — Drones for indoor inspection and confined space'. <https://www.flyability.com> (accessed Oct. 05, 2022).
- [12] J. Fagerberg, 'The Satellite IoT Communications Market', Gothenburg, Sweden, 2021.
- [13] 'Astrocast: The first Swiss CubeSat IoT Constellation'.
- [14] Maxtena, 'M1600HCT12-UFL Thuraya helical antenna'. Rockville, MD, 2021.
- [15] J. Ye and Y. Wang, 'A broad-band circularly polarized microstrip antenna for Thuraya satellite communication', *2010 9th Int. Symp. Antennas Propag. EM Theory ISAPE 2010*, pp. 105–107, 2010, doi: 10.1109/IS-APE.2010.5696407.
- [16] W. Chujo, M. Fujise, H. Arai, and N. Goto, 'A Two-Layer Self-Diplexing Antenna Using A Circularly Polarized Ring Patch Antenna', *Antennas Propag. Soc. Symp. 1991 Dig.*, 1991, doi: <https://doi.org/10.1109/APS.1991.174845>.
- [17] D. M. Pozar, 'Basic Microstrip Antenna Elements and Feeding Techniques', in *Microstrip Antennas: The Analysis and Design of Microstrip Antennas and Arrays*, Accessed: Feb. 08, 2022. [Online]. Available: <https://ieeexplore.ieee.org/document/5263416>
- [18] Krauss, *Antennas and Wave Propagation: Fourth Edition*. Tata McGraw Hill, 2006.
- [19] F. Croq and D. M. Pozar, 'Millimeter-wave design of wide-band aperture-coupled stacked microstrip antennas', *IEEE Trans. Antennas Propag.*, vol. 39, no. 12, pp. 1770–1776, Dec. 1991, doi: 10.1109/8.121599.
- [20] O. Staub, 'Electrically small antennas', 2001, doi: 10.5075/epfl-thesis-2311.
- [21] P. Salonen, L. Sydanheimo, M. Keskilammi, and M. Kivikoski, 'A small planar inverted-F antenna for wearable applications', in *Digest of Papers. Third International Symposium on Wearable Computers*, Oct. 1999, pp. 95–100. doi: 10.1109/ISWC.1999.806679.
- [22] 'Ansys HFSS | 3D High Frequency Simulation Software'. Accessed: Oct. 20, 2022. [Online]. Available: <https://www.ansys.com/products/electronics/ansys-hfss>
- [23] E. Choi, J. W. Lee, and T.-K. Lee, 'Modified S-Band Satellite Antenna With Isoflux Pattern and Circularly Polarized Wide Beamwidth', *IEEE Antennas Wirel. Propag. Lett.*, vol. 12, pp. 1319–1322, 2013, doi: 10.1109/LAWP.2013.2285231.

- [24] D. V. N. Méndez, L. F. C. Suárez, and M. B. Escudero, 'Circular polarization patch antenna with low axial ratio in a large beamwidth', in *2013 7th European Conference on Antennas and Propagation (EuCAP)*, Apr. 2013, pp. 3330–3333.
- [25] Y. Luo, Q. Chu, and L. Zhu, 'A Miniaturized Wide-Beamwidth Circularly Polarized Planar Antenna via Two Pairs of Folded Dipoles in a Square Contour', *IEEE Trans. Antennas Propag.*, 2015, doi: 10.1109/TAP.2015.2438334.
- [26] R. F. Harrington, 'Effect of antenna size on gain, bandwidth, and efficiency', *J. Res. Natl. Bur. Stand. Sect. Radio Propag.*, vol. 64D, no. 1, p. 1, Jan. 1960, doi: 10.6028/jres.064D.003.
- [27] R. Harrington, 'On the gain and beamwidth of directional antennas', *IRE Trans. Antennas Propag.*, vol. 6, no. 3, pp. 219–225, Jul. 1958, doi: 10.1109/TAP.1958.1144605.
- [28] L. C. Paul, M. S. Hosain, S. Sarker, M. H. Prio, M. Morshed, and A. K. Sarkar, 'The Effect of Changing Substrate Material and Thickness on the Performance of Inset Feed Microstrip Patch Antenna', *Am. J. Netw. Commun.*, vol. 4, no. 3, Art. no. 3, May 2015, doi: 10.11648/j.ajnc.20150403.16.
- [29] E. S. Neves, 'CHALMERS ANALYSIS OF CONFORMAL ANTENNAS FOR AVIONICS APPLICATIONS', 2007. <https://www.semanticscholar.org/paper/CHALMERS-ANALYSIS-OF-CONFORMAL-ANTENNAS-FOR-Neves/2bf3daa76b2695fdd6e58dc48025a381d3bd1d2d> (accessed Mar. 04, 2022).
- [30] L. Jiang, F.-S. Zhang, F. Zhang, Y.-L. Yao, and T. Li, 'Wide-Beamwidth Circularly Polarized Antenna and ITS Application in a Sequential-Rotation Array with Enhanced Bandwidth', *Prog. Electromagn. Res. C*, vol. 67, pp. 127–134, 2016, doi: 10.2528/PIERC16051601.
- [31] Nasimuddin, Y. S. Anjani, and A. Alphones, 'A Wide-Beam Circularly Polarized Asymmetric-Microstrip Antenna', *IEEE Trans. Antennas Propag.*, vol. 63, no. 8, pp. 3764–3768, Aug. 2015, doi: 10.1109/TAP.2015.2438397.
- [32] J.-Y. Deng, Y.-Z. Yin, Y.-H. Huang, J. Ma, and Q.-Z. Liu, 'Compact circularly polarized microstrip antenna with wide beamwidth for compass satellite service', *Prog. Electromagn. Res. Lett.*, vol. 11, Jan. 2009, doi: 10.2528/PIERL09080801.
- [33] X. Zhang, L. Zhu, and N.-W. Liu, 'Pin-Loaded Circularly-Polarized Patch Antennas With Wide 3-dB Axial Ratio Beamwidth', *IEEE Trans. Antennas Propag.*, vol. 65, no. 2, pp. 521–528, Feb. 2017, doi: 10.1109/TAP.2016.2632728.
- [34] L. Dou, S. Li, and W. Cao, 'Research of Wide Beam Antenna', in *2019 International Symposium on Antennas and Propagation (ISAP)*, Oct. 2019, pp. 1–3.
- [35] D. P. Fan, Z. X. Wang, B. Huang, and W. Zhang, 'Design of broad beam circular-polarized microstrip antenna', in *2013 Proceedings of the International Symposium on Antennas Propagation*, Oct. 2013, vol. 01, pp. 439–441.
- [36] Y. Liu, S. Xiao, and B. Wang, 'A RHCP Microstrip Antenna with Ultrawide Beamwidth for UHF Band Application', *Int. J. Antennas Propag.*, vol. 2014, p. e472397, May 2014, doi: 10.1155/2014/472397.
- [37] X. L. Bao and M. J. Ammann, 'Dual-frequency dual circularly-polarised patch antenna with wide beamwidth', *Electron. Lett.*, vol. 44, no. 21, p. 1233, 2008, doi: 10.1049/el:20082284.
- [38] Nasimuddin, X. Qing, and Z. N. Chen, 'A Compact Circularly Polarized Slotted Patch Antenna for GNSS Applications', *IEEE Trans. Antennas Propag.*, vol. 62, no. 12, pp. 6506–6509, Dec. 2014, doi: 10.1109/TAP.2014.2360218.
- [39] M. Saravanan and M. Rangachar, 'Design of Wide Beam Hexagonal Shaped Circularly Polarized Patch Antenna for WLAN Application', Jan. 2018, pp. 142–150. doi: 10.1007/978-3-319-60618-7_15.
- [40] C. Zhang, X. Liang, X. Bai, J. Geng, and R. Jin, 'A Broadband Dual Circularly Polarized Patch Antenna With Wide Beamwidth', *IEEE Antennas Wirel. Propag. Lett.*, vol. 13, pp. 1457–1460, 2014, doi: 10.1109/LAWP.2014.2333760.
- [41] M. Saravanan, 'An L-Shaped Slot Circularly Polarized Patch Antenna for Wireless Communication', *J. Inst. Electron. Comput.*, vol. 2, no. 1, pp. 1–11, Jan. 2020, doi: 10.33969/JIEC.2020.21001.
- [42] T. Mondal, S. Maity, R. Ghatak, and S. R. B. Chaudhuri, 'Compact Circularly Polarized Wide-Beamwidth Fern-Fractal-Shaped Microstrip Antenna for Vehicular Communication', *IEEE Trans. Veh. Technol.*, vol. 67, no. 6, pp. 5126–5134, Jun. 2018, doi: 10.1109/TVT.2018.2824841.
- [43] J. C. Batchelor, 'Microstrip ring antennas operating at higher order modes for mobile communications', *IEE Proc. - Microw. Antennas Propag.*, vol. 142, no. 2, p. 151, 1995, doi: 10.1049/ip-map:19951826.

- [44] J. Tak and J. Choi, 'Circular-ring patch antenna with higher order mode for on-body communications', *Microw. Opt. Technol. Lett.*, vol. 56, no. 7, pp. 1543–1547, Jul. 2014, doi: 10.1002/mop.28374.
- [45] J. Liu, Q. Xue, H. Wong, H. W. Lai, and Y. Long, 'Design and Analysis of a Low-Profile and Broadband Microstrip Monopolar Patch Antenna', *IEEE Trans. Antennas Propag.*, vol. 61, no. 1, pp. 11–18, Jan. 2013, doi: 10.1109/TAP.2012.2214996.
- [46] J. Huang, 'Circularly polarized conical patterns from circular microstrip antennas', *IEEE Trans. Antennas Propag.*, vol. 32, no. 9, pp. 991–994, Sep. 1984, doi: 10.1109/TAP.1984.1143455.
- [47] T. Tan, Y. Xia, and Q. Zhu, 'A novel wide beamwidth and circularly polarized microstrip antenna loading annular dielectric superstrate with metal ring', in *2014 IEEE Antennas and Propagation Society International Symposium (APSURSI)*, Jul. 2014, pp. 1883–1884. doi: 10.1109/APS.2014.6905268.
- [48] Z.-K. Pan, W.-X. Lin, and Q.-X. Chu, 'Compact Wide-Beam Circularly-Polarized Microstrip Antenna With a Parasitic Ring for CNSS Application', *IEEE Trans. Antennas Propag.*, vol. 62, no. 5, pp. 2847–2850, May 2014, doi: 10.1109/TAP.2014.2307348.
- [49] J. Kornprobst, K. Wang, G. Hamberger, and T. F. Eibert, 'A mm-Wave Patch Antenna with Broad Bandwidth and a Wide Angular Range', *IEEE Trans. Antennas Propag.*, vol. 65, no. 8, pp. 4293–4298, Aug. 2017, doi: 10.1109/TAP.2017.2710261.
- [50] Y. Yuan, M. Wang, Y. Yin, and W. Wu, 'Wide-beam circularly polarized microstrip antenna with high front-to-back ratio for CNSS application', in *2017 Sixth Asia-Pacific Conference on Antennas and Propagation (APCAP)*, Oct. 2017, pp. 1–3. doi: 10.1109/APCAP.2017.8420318.
- [51] Q. Li, Y. Yin, and X. Chen, 'A parasitic surface based wide beam width patch antenna', *AIP Adv.*, vol. 11, no. 11, p. 115320, Nov. 2021, doi: 10.1063/5.0069428.
- [52] S. Yoo, G. Byun, and H. Choo, 'Design of microstrip patch antennas with improved low-elevation gain for CRPA applications', *Microw. Opt. Technol. Lett.*, vol. 58, pp. 170–174, Jan. 2016, doi: 10.1002/mop.29517.
- [53] X. Chen, D. Wu, L. Yang, and G. Fu, 'Compact Circularly Polarized Microstrip Antenna With Cross-Polarization Suppression at Low-Elevation Angle', *IEEE Antennas Wirel. Propag. Lett.*, vol. 16, pp. 258–261, 2017, doi: 10.1109/LAWP.2016.2571303.
- [54] X. Chen, Z. Wei, D. Wu, L. Yang, and G. Fu, 'Low-cost and compact 3D circularly polarized Microstrip antenna with high efficiency and wide beamwidth', *Int. J. Microw. Wirel. Technol.*, vol. 9, no. 7, pp. 1533–1540, Sep. 2017, doi: 10.1017/S1759078717000101.
- [55] M.-S. Wang, X.-Q. Zhu, Y.-X. Guo, and W. Wu, 'Compact Circularly Polarized Patch Antenna With Wide Axial-Ratio Beamwidth', *IEEE Antennas Wirel. Propag. Lett.*, vol. 17, no. 4, pp. 714–718, Apr. 2018, doi: 10.1109/LAWP.2018.2813160.
- [56] W. J. Yang, Y. M. Pan, and S. Y. Zheng, 'A Low-Profile Wideband Circularly Polarized Crossed-Dipole Antenna With Wide Axial-Ratio and Gain Beamwidths', *IEEE Trans. Antennas Propag.*, vol. 66, no. 7, pp. 3346–3353, Jul. 2018, doi: 10.1109/TAP.2018.2829810.
- [57] M. Sahal, V. TIWARI, D. Yadav, D. BHATNAGAR, and T. Jhahhria, 'A Broadband Circularly Polarized Antenna with Low-Profile and Wide Axial Ratio Beamwidth', *Walailak J. Sci. Technol. WJST*, vol. 18, May 2021, doi: 10.48048/wjst.2021.18741.
- [58] J. D. Kraus, *Antennas and Wave Propagation, 4th edition*. Accessed: Jan. 09, 2020. [Online]. Available: <https://www.biblio.com/book/antennas-wave-propagation-4th-edition-john/d/496321301>
- [59] M. T. Nguyen, B. Kim, H. Choo, and I. Park, 'Effects of ground plane size on a square microstrip patch antenna designed on a low-permittivity substrate with an air gap', in *2010 International Workshop on Antenna Technology (iWAT)*, Mar. 2010, pp. 1–4. doi: 10.1109/IWAT.2010.5464869.
- [60] A. K. Bhattacharyya, 'Effects of finite ground plane on the radiation characteristics of a circular patch antenna', *IEEE Trans. Antennas Propag.*, vol. 38, no. 2, pp. 152–159, Feb. 1990, doi: 10.1109/8.45116.
- [61] J.-F. Zürcher and F. E. Gardiol, *Broadband Patch Antennas*. Artech House, 1995.
- [62] S. Fatima Farida, P. M. Hadalgi, P. V. Hunagund, and S. Rafath Ara, 'Effect of substrate thickness and permittivity on the characteristics of rectangular microstrip antenna', in *1998 Conference on Precision Electromagnetic Measurements Digest (Cat. No.98CH36254)*, Jul. 1998, pp. 598–599. doi: 10.1109/CPEM.1998.700074.
- [63] A. Hoorfar and A. Perrotta, 'An experimental study of microstrip antennas on very high permittivity ceramic substrates and very small ground planes', *IEEE Trans. Antennas Propag.*, vol. 49, no. 5, pp. 838–840, May 2001, doi: 10.1109/8.929638.

- [64] S. I. Latif and L. Shafai, 'Pattern Equalization of Circular Patch Antennas Using Different Substrate Permittivities and Ground Plane Sizes', *IEEE Trans. Antennas Propag.*, vol. 59, no. 10, pp. 3502–3511, Oct. 2011, doi: 10.1109/TAP.2011.2163775.
- [65] A. K. Skrivervik, 'Classic electrically small antennas versus In/On-Body antennas: similarities and differences', in *2019 13th European Conference on Antennas and Propagation (EuCAP)*, Mar. 2019, pp. 1–3.
- [66] H. Jiang, Z. Xue, W. Li, and W. Ren, 'Broad beamwidth stacked patch antenna with wide circularly polarised bandwidth', *Electron. Lett.*, vol. 51, no. 1, pp. 10–12, 2015, doi: 10.1049/el.2014.3783.
- [67] C.-L. Tang, J.-Y. Chiou, and K.-L. Wong, 'Beamwidth enhancement of a circularly polarized microstrip antenna mounted on a three-dimensional ground structure', *Microw. Opt. Technol. Lett.*, vol. 32, no. 2, pp. 149–153, doi: 10.1002/mop.10116.
- [68] S. Noghanian and L. Shafai, 'Control of microstrip antenna radiation characteristics by ground plane size and shape', *Antennas Propag. IEE Proc. - Microw.*, vol. 145, no. 3, pp. 207–212, Jun. 1998, doi: 10.1049/ip-map:19981819.
- [69] G. Yang, J.-Y. Li, D. Wei, S. Zhou, and J. Yang, 'Broadening the beam-width of microstrip antenna by the induced vertical currents', *IET Microw. Antennas Propag.*, vol. 12, no. 2, pp. 190–194, 2018, doi: 10.1049/iet-map.2017.0295.
- [70] I. V. Trivino and A. K. Skrivervik, 'Broadbeam microstrip patch antenna using higher order modes', in *2019 13th European Conference on Antennas and Propagation (EuCAP)*, Mar. 2019, pp. 1–4.
- [71] L. Xie, Y. Li, and Y. Zheng, 'A wide axial-ratio beamwidth circularly polarized microstrip antenna', in *2016 IEEE International Conference on Ubiquitous Wireless Broadband (ICUWB)*, Oct. 2016, pp. 1–4. doi: 10.1109/ICUWB.2016.7790495.
- [72] 'Numerical Electromagnetics Code NEC2 unofficial home page'. <https://www.nec2.org/> (accessed May 14, 2021).
- [73] J. Perruisseau-Carrier, 'Microwave periodic structures based on MicroElectroMechanical Systems (MEMS) and micromachining techniques', *Infoscience*, 2007. <https://infoscience.epfl.ch/record/112718> (accessed May 15, 2021).
- [74] I. V. Triviño and A. K. Skrivervik, 'Enhancing the beamwidth of low profile single-fed microstrip antennas using parasitic elements', in *2022 16th European Conference on Antennas and Propagation (EuCAP)*, Mar. 2022, pp. 01–05.
- [75] I. Vico Triviño, M. Veljovic, and A. K. Skrivervik, 'Cost-effective, dual-band and broadbeam antennas for satellite IoT networks', *Rev. EurAAP Vis.*, 2022.
- [76] W. Liao and Q. X. Chu, 'Dual-band circularly polarized microstrip antenna with small frequency ratio', *Prog. Electromagn. Res. Lett.*, vol. 15, pp. 145–152, 2010, doi: 10.2528/PIERL10052101.

Curriculum Vitae

CONTACT INFORMATION

Ismael Vico Triviño
École Polytechnique Fédérale de Lausanne [EPFL]
School of Engineering [STI]
Microwaves and Antennas Group [MAG]
Lausanne (Switzerland)
Email: ismael.vicotrivino@epfl.ch

EMPLOYMENT HISTORY

- Doctoral Student (Microwave and Antenna Group, EPFL, Lausanne) (March 2018 - Today)
Main tasks: Research on broadbeam microstrip antennas, design of antennas for drones and teaching assistant.
- Antenna and RF Electronics Engineer (Flyability SA, Lausanne) (September 2017 – March 2018)
Main tasks: Antenna design, industrialization of antennas and RF systems and RF tests for system validation.
- Internship as Antenna Engineer (Flyability SA, Lausanne) (March 2017- September 2017)
Main tasks: Design, prototyping and implementation of optimized antennas for isotropic coverage.

EDUCATION

- Master Degree in Telecommunication Engineering (University of Granada, Spain)
 - Final Project in Microwave and Antenna Group (MAG, EPFL, Lausanne) entitled "Simplified electromagnetic models for Wireless Body Area Networks".
- Bachelor Degree in Telecommunication Engineering (University of Granada, Spain)
 - Final Project entitled "Seismic Signals Polarization Analysis to Enhance First Phase Arrival".

PROFESSIONAL QUALIFICATIONS

- Computer Skills: ANSYS Electronics Desktop, NEC, CST, Matlab, LabView, Spice.

LANGUAGES

- Spanish: Native
- English: Full working proficiency
- French: Full working proficiency

PUBLICATIONS

V. Trivino, Z. Sipus, M. Bosiljevac, and A. K. Skrivervik, 'Design Tools for Small Implantable antennas', Jan. 2018, pp. 591 (4 pp.)-591 (4 pp.), doi: [10.1049/cp.2018.0950](https://doi.org/10.1049/cp.2018.0950).

I. V. Trivino and A. K. Skrivervik, "Broadbeam microstrip patch antenna using higher order modes," in *2019 13th European Conference on Antennas and Propagation (EuCAP)*, Mar. 2019, pp. 1–4.

AJM Montes, IV Trivino, M Bosiljevac, MJ Veljovic, Z Sipus, AK Skrivervik, "Antenna for a Cranial Implant: Simulation Issues and Design Strategies," in *2020 14th European Conference on Antennas and Propagation (EuCAP)*.

A. J. M. Montes, I. V. Trivino, M. Bosiljevac, M. Veljovic, and Z. Sipus, A. K. Skrivervik, "Antenna design for a cranial implant," in *2020 International Workshop on Antenna Technology (iWAT)*, Feb. 2020, pp. 1–4, doi: [10.1109/iWAT48004.2020.1570609528](https://doi.org/10.1109/iWAT48004.2020.1570609528)

I. V. Triviño and A. K. Skrivervik, 'Enhancing the beamwidth of low-profile single-fed microstrip antennas using parasitic elements', in *2022 16th European Conference on Antennas and Propagation (EuCAP)*, Mar. 2022, pp. 01–05.

I. V. Trivino, M. Veljovic, and A. K. Skrivervik, 'Single-Layer Dual-band Satellite-IoT Terminal Antennas with Increased Beamwidth', in *Reviews of Electromagnetics Vision (RoE) EurAAP*. *Under minor revision*

V. Trivino and A. K. Skrivervik, "Small antennas with broad beamwidth integrated on a drone enclosed in a protective structure". Submitted to *2023 17th European Conference on Antennas and Propagation (EuCAP)*, Mar. 2023.

G. A. Ramírez, H. Bartle. I. V. Trivino, Anja K. Skrivervik, "Circularly polarized planar antenna with axially symmetric beamwidth reconfigurability". Submitted to *2023 17th European Conference on Antennas and Propagation (EuCAP)*, Mar. 2023.